UNIVERSIDADE D
COIMBRA

Neeraj Kumar

Si-Sn and Si-Sn-X (X = Ti, Cu, and Zn) systems for humidity sensing applications fabricated by non-equilibrium techniques

PhD thesis in Mechanical Engineering, Surface Engineering and Nanomaterials, supervised by Professor Doctor Bruno Miguel Quelhas de Sacadura Cabral Trindade and Professor Doctor Pedro Manuel Gens de Azevedo de Matos Faia, submitted to the Department of Mechanical Engineering, Faculty of Sciences and Technology of the University of Coimbra.

December 2022

Faculty of Sciences and Technology
University of Coimbra

Si-Sn and Si-Sn-X (X = Ti, Cu, and Zn) systems for humidity sensing applications fabricated by non-equilibrium techniques

Neeraj Kumar

PhD Thesis in Mechanical Engineering, Surface Engineering and Nanomaterials, supervised by Professor Doctor Bruno Miguel Quelhas de Sacadura Cabral Trindade and Professor Doctor Pedro Manuel Gens de Azevedo de Matos Faia, submitted to the Department of Mechanical Engineering, Faculty of Sciences and Technology of the University of Coimbra.

December 2022

UNIVERSIDADE D
COIMBRA

This research was supported by MATIS project “Materials and Sustainable Industrial Technologies” (reference: Centro-01-0145-FEDER-000014), co-financed by European Regional Development Fund (ERDF) of the European Union, through the Programa Operacional Regional do Centro 2014-2020 (Centro 2020) Portugal 2020 (PT2020), and national funds through the Portuguese Foundation for Science and Technology (FCT), under the project UID/EMS/00285/2020.

Acknowledgements

I want to take this opportunity to express my sincere appreciation to my supervisors, Professor Bruno Miguel Quelhas de Sacadura Cabral Trindade and Professor Pedro Manuel Gens de Azevedo de Matos Faia, for providing me with continuous support, guidance, motivation, knowledge and valuable time. It was a great honour and a valuable experience for me to work under their invaluable supervision.

A special thanks to Dr. Manuel António Peralta Evaristo for his assistance during the preparation of thin films through RF magnetron sputtering equipment and for his generous support and suggestions throughout the course of this work. I would also like to thank Professor Albano Augusto Cavaleiro Rodrigues de Carvalho for his scientific advice and recommendations throughout this research work.

I would also like to express my appreciation to Dr. João Carlos Barbas de Oliveira, Dr. Ricardo Gil Henriques Serra, Dr. Filipe Daniel Fernandes, and Dr. Todor Vuchkov from Surface Engineering Group at the Centre for Mechanical Engineering, Materials and Processes, the University of Coimbra for their technical discussions and support on various types of equipment.

I gratefully acknowledge the financial support by MATIS project "Materials and Sustainable Industrial Technologies" (reference: Centro-01-0145-FEDER-000014), co-financed by the European Regional Development Fund (ERDF) of the European Union, through the Programa Operacional Regional do Centro 2014-2020 (Centro 2020) Portugal 2020 (PT2020), and national funds through the Portuguese Foundation for Science and Technology (FCT), under the project UID/EMS/00285/2020.

I am also thankful to my family and closest friends for always encouraging and supporting me, particularly my mother, who is a constant source of inspiration.

Finally, I would like to acknowledge everyone who has directly or indirectly contributed in any way to this work or provided me with any assistance over the years.

To all, my honest and sincere

Thank you!

Abstract

Humidity (the amount of water vapour in the air) has always impacted human comfort levels. In the last few decades, the need for controlled and regulated environmental conditions has skyrocketed for various industrial applications. Humidity is one of the major contributing factors that must be continuously monitored and controlled for advanced industrial processes and better instrument productivity. Humidity sensor industries are constantly required to innovate in order to produce sensors with better sensitivity, enhanced stability, fast response time, reproducibility, repeatability, and long-life expectancy.

The first study on the use of porous silicon for humidity-sensing applications dates back to the early 1990s, in which an increase in the capacitance response of 440 % was claimed in the relative humidity range from 0 to 100 % RH, at room temperature. The shape and size of pores play an important role in water condensation, with the ones near the mesoporous region exhibiting higher electrical response with humidity variations. Tin is also a well-known material used for sensing-based applications. The incorporation of tin into the silicon matrix forms a strong inter-penetrating microstructure that helps to stabilise the system and to increase the component life.

This thesis aimed to produce different mesoporous Si-Sn and Si-Sn-X (X = Ti, Cu, and Zn) alloy systems and to correlate their chemical, structural, morphological, and mechanical properties to the electrical response to changes in relative humidity (RH) in the range of 10 to 100 %. To achieve these objectives two non-equilibrium production techniques (magnetron sputtering and high energy mechanical alloying) were used and the samples were analysed by means of different characterisation techniques, *i.e.* X-ray diffraction (XRD), scanning electron microscopy (SEM), energy dispersive X-ray spectroscopy (EDS), transmission electron microscopy (TEM), mössbauer spectroscopy (MS), atomic force microscopy (AFM), hardness, mercury intrusion porosimetry (MIP), particle size distribution (PSD), and complex impedance spectroscopy (CIS).

The results showed that the best humidity-sensing properties depend upon several factors, including chemical composition, morphology, surface roughness, structure, and mesoporosity. Among all the systems produced in this thesis, the Si-Sn one obtained by

sputtering presented the most promising response toward humidity sensing. The film with composition $Si_{72}Sn_{28}$ (at. %) deposited at 1 Pa presented a *p*-type conduction behaviour in a relative humidity range from 10 to 100 %. The impedance modulus values obtained at 1 kHz for this sample showed a stable and linear variation of the impedance modulus as a function of relative humidity content with a trendline slope of 83 Ω/RH(%). Moreover, the humidity tests performed 1 and 6 months after the first run revealed that the electrical response of this sensor is quite stable over time.

From the Si-Sn-Ti system, the film with chemical composition $Si_{71}Sn_{23}Ti_6$ deposited at 1 Pa showed a *p*-type humidity sensing behaviour in a relative humidity range from 10 to 90 %. However, this sample suffered from the ageing effect after 1 and 6 months from the first measurement. Si-Sn-X (Cu, and Zn) films did not show any promising behaviour towards the humidity changes. Despite, the sample with the chemical composition $Si_{48}Sn_{44}Zn_8$ displayed a small *p*-type conduction behaviour to increase relative humidity from 10 to 100 %. However, these variations were not significantly enough to be considered for humidity sensing behaviour.

Keywords: Humidity sensors, Magnetron sputtering, Mechanical alloying, Impedance spectroscopy, Mesoporosity, Porous silicon.

Resumo

A humidade (quantidade de vapor de água no ar) sempre teve impacto nos níveis de conforto humano. Nas últimas décadas, a necessidade de existência de condições ambientais controladas e regulamentadas é fundamental em várias aplicações industriais, sendo a humidade um dos principais fatores que devem ser continuamente monitorados e controlados para aumento da produtividade. Tal como noutros casos, as indústrias de produção de sensores de humidade são constantemente obrigadas a inovar de forma a obter sensores com melhores sensibilidade, estabilidade e reprodutibilidade, bem como tempos de resposta mais rápidos, e longa expectativa de vida.

O primeiro estudo sobre o uso de silício poroso para aplicações de deteção de humidade data do início dos anos 1990, no qual é referido um aumento de capacitância de 440 % na gama de humidade relativa entre 0 e 100 %, à temperatura ambiente. É sabido que a forma e o tamanho dos poros desempenham um papel importante na condensação da água, e que os situados na região mesoporosa apresentam uma maior resposta elétrica às variações do teor de humidade. O estanho é também um material promissor para aplicações em sensores. A incorporação de estanho numa matriz de silício forma uma microestrutura interpenetrante que ajuda a estabilizar o sistema e a aumentar a vida útil do componente.

Esta tese teve como objetivo produzir diferentes ligas mesoporosas de Si-Sn e Si-Sn-X (X = Ti, Cu e Zn) e correlacionar suas propriedades químicas, estruturais, morfológicas e mecânicas com a resposta elétrica a mudanças na humidade relativa entre 0 e 100 %. Para atingir esses objetivos, foram usadas duas técnicas de produção “fora do equilíbrio” (pulverização catódica e síntese mecânica de alta energia). As amostras produzidas foram analisadas por diferentes técnicas de caracterização: difração de raios X (DRX), microscopia eletrónica de varrimento (MEV), espectroscopia de raios X por dispersão de energia (EDS), microscopia eletrónica de transmissão (MET), espectroscopia Mössbauer (MS), microscopia de força atómica (AFM), dureza, porosimetria de intrusão de mercúrio (MIP), distribuição de tamanho de partícula (PSD) e espectroscopia de impedância complexa (CIS).

Os resultados mostraram que a capacidade de deteção de humidade depende de vários fatores, tais como composição química, morfologia, rugosidade da superfície, estrutura e mesoporosidade. Dentre todos os sistemas produzidos nesta tese, o sistema Si-Sn obtido por pulverização catódica apresentou a resposta mais promissora para deteção de humidade. O filme fino de composição $Si_{72}Sn_{28}$ (% at.) depositado a 1 Pa apresentou um comportamento de condução do tipo *p* na faixa de humidade entre 10 e 100 %. O módulo de impedância obtido a 1 kHz para esta amostra mostrou uma variação estável e linear do módulo de impedância em função do teor de humidade relativa com uma inclinação da linha de tendência de 83 Ω/RH(%). Para além disso, os testes de humidade realizados 1 e 6 meses após a primeira medição revelaram que a resposta elétrica desse sensor é bastante estável ao longo do tempo.

No que se refere ao sistema Si-Sn-Ti, o filme fino com composição química $Si_{71}Sn_{23}Ti_6$ depositado a 1 Pa apresentou um comportamento de deteção de humidade do tipo *p* numa faixa de Humidade relativa entre 10 e 90%. No entanto, esta amostra sofreu envelhecimento 1 e 6 meses após a primeira medição. Os filmes finos de Si-Sn-X (Cu e Zn) não apresentaram nenhum comportamento promissor face à mudança de humidade. A amostra com a composição química $Si_{48}Sn_{44}Zn_8$ apresentou um ligeiro comportamento de condução do tipo *p* entre 10 e 100 % de humidade relativa. No entanto, essas variações não foram suficientemente significativas para serem consideradas adequadas para a sua aplicação em deteção de humidade.

Palavras-chave: Sensores de humidade, Pulverização catódica, Síntese mecânica, Espectroscopia de impedância, Mesoporosidade, Silício poroso.

List of Publications

- N. Kumar, P. Sanguino, S. Diliberto, P. Faia & B. Trindade, *Tailoring thin mesoporous silicon-tin films by radio-frequency magnetron sputtering*, Thin Solid Films, 704 (2020) 137989, https://doi.org/10.1016/j.tsf.2020.137989. Impact factor: 2.358.
- N. Kumar, M. Evaristo, B. Trindade & P. Faia, *Humidity sensing properties of thin silicon-tin films prepared by magnetron sputtering*, Sensors and Actuators B: Chemical, 321 (2020) 128554, https://doi.org/10.1016/j.snb.2020.128554. Impact factor: 9.221.
- N. Kumar, P. Sanguino, P. Faia & B. Trindade, *Porous Si-Sn alloys produced by mechanical alloying and subsequent consolidation by sintering and hot-pressing*, Materials and Manufacturing Processes, 37 (2) (2022) 169-176, https://doi.org/10.1080/10426914.2021.1967979. Impact factor: 4.783.

List of Conferences

- N. Kumar, A. Cavaleiro, B. Trindade, & P. Faia, *Si-Sn films deposited at different vacuum pressure using RF magnetron sputtering as possible candidates for application in Li-ion batteries*, XVI ECerS Conference 2019.
- P. Faia, N. Kumar, B. Trindade, & A. Cavaleiro, *Porous silicon-tin thin films for humidity sensors deposited by RF magnetron sputtering*, XVI ECerS Conference 2019.
- N. Kumar, P. Faia, A. Cavaleiro, & B. Trindade, *Production of silicon-tin alloys with stearic acid for humidity sensing application*, MATERIAIS 2019.

List of Abbreviations

AC	Alternating Current
AFM	Atomic Force Microscopy
a.m.u.	atomic mass unit
a-Si	amorphous silicon
BSE	Back-scattered Electrons
CEMMPRE	Centre for Mechanical Engineering, Materials and Processes
CIS	Complex Impedance Spectroscopy
CL	Cathode luminescence
c-Si	crystalline silicon
DC	Direct Current
DEEC	Department of Electrical and Computers Engineering
DEM	Department of Mechanical Engineering
EDS / EDX	Energy dispersive X-ray spectroscopy
FCT	Faculty of Sciences and Technology
FWHM	Full Width at Half Maximum
HEMA	High Energy Mechanical Alloying
HR-TEM	High-resolution Transmission Electron Microscopy
ICDD	International Centre for Diffraction Data
ICs	Integrated Chips
IEC	International Electrotechnical Commission
INCO	International Nickel Company
IPN	Instituto Pedro Nunes
IR	Infra-red
JCPDS	Joint Committee on Powder Diffraction Standards
LD	Laser Diffraction
LED&MAT	Laboratory for Wear, Testing and Materials
MA	Mechanical Alloying
MFC	Mass Flow Controller
MIP	Mercury Intrusion Porosimetry
MS	Mössbauer spectroscopy
PCA	Process Control Agent
PDF	Powder Diffraction File

ppm	parts per million
PSD	Particle Size Distribution
p-Si	porous silicon
PVD	Physical Vapour Deposition
RF	Radio Frequency
RH	Relative Humidity
rpm	revolutions per minute
SAED	Selected Area Electron Diffraction
SE	Secondary Electrons
SEM	Scanning Electron Microscopy
TEM	Transmission Electron Microscopy
TSD	Target-to-Substrate Distance
UC	University of Coimbra
VOCs	Volatile Organic Compounds
W-H	Williamson-Hall
XPPA	X-ray Peak Profile Analysis
XRD	X-ray Diffraction

List of Symbols

A_a	Area under amorphous peaks of diffraction	[m^2]
AB	Absolute humidity	[g/m^3]
A_c	Area under the crystalline peaks of diffraction	[m^2]
d	Diameter of capillary pore	[µm] [nm]
D PT	Dew point	[°C] [°F] [K]
f	Frequency	[Hz] [kHz] [MHz]
F PT	Frost point	[°C] [°F] [K]
I	Current	[A]
m	Mass	[g] [kg]
M_a	Mass of dry air	[g] [kg]
M_w	Mass of water vapour	[g] [kg]
ø	Phase shift	[°]
P	Pressure	[bar] [Pa] [atm.]
P_a	Actual partial pressure of vapour in air	[bar] [Pa] [atm.]
ppm_V, ppm_W	Volumetric concentration	[m^3/m^3] [g/g]
P_s	Saturated pressure of fully humidified air	[bar] [Pa] [atm.]
Q	Specific humidity	[%]
r	Mixing ratio	[g/g] [kg/kg]
R	Resistance	[Ω]
R_a	Arithmetic mean roughness value	[µm] [nm]
RH	Relative humidity	[%]
R_q or R_{rms}	Root-mean-squared roughness	[µm] [nm]
t	Time	[s] [min]
T	Temperature	[°C] [°F] [K]
v	Volume	[m^3]
V	Voltage	[V]
Z	Impedance	[Ω]
γ	Surface tension	[N/m]
θ	X-ray incidence angle	[°]
λ	X-ray wavelength	[Å]
χ_c	Degree of crystallinity	[%]
ω	Angular frequency	[Hz] [kHz] [MHz]

Table of Contents

List of Figures

List of Tables

Outline of the thesis

In this research work, Si-Sn and Si-Sn-X (X = Ti, Cu, and Zn) alloys were produced by two non-equilibrium manufacturing techniques (sputtering and mechanical alloying) and their structural, chemical, morphological, mechanical, and electrical (response towards changes to relative humidity) were evaluated. The main goal was to study the influence of tin and other transition metals on porous-Si in order to produce improved systems for humidity-sensing applications.

This work was performed at the Departments of Mechanical Engineering (DEM) and Electrical and Computers Engineering (DEEC) of the University of Coimbra (UC), in the Centre for Mechanical Engineering, Materials and Processes (CEMMPRE), a research unit from the Portuguese Foundation for Science and Technology (FCT). Some characterisations were also carried out at the Laboratory for Wear, Testing and Materials (LED&MAT) of the Instituto Pedro Nunes (IPN), Coimbra.

This thesis is organised into five chapters; the schematic of the outline of the thesis is shown in Fig. 1.

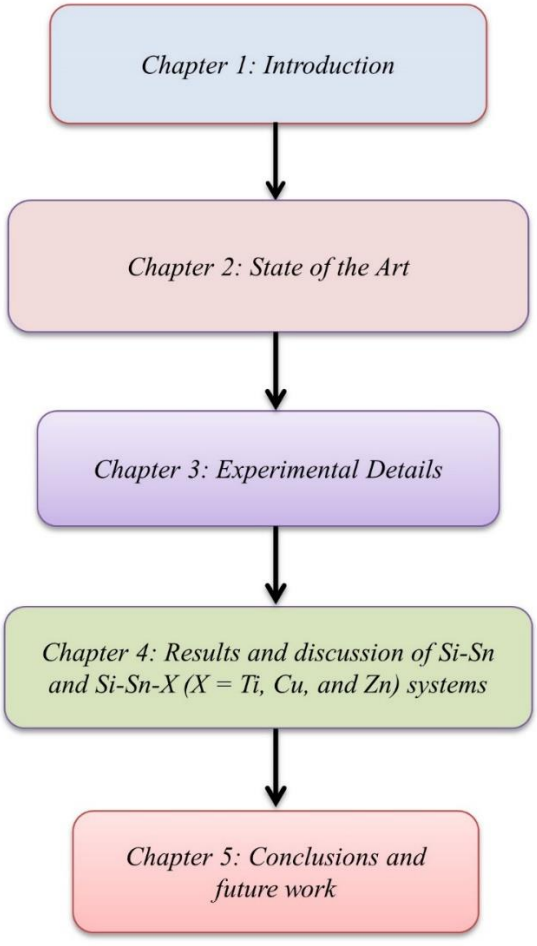

Figure 1. Outline of the thesis.

Chapter 1: Introduction is the first chapter of this thesis and aims to provide a general introduction and background about the research work performed in this thesis. The motivation, work objectives and work methodology are also mentioned in this chapter.

Chapter 2: State-of-the-art is divided into specific sub-sections accounting for the literature review, such as characterisation of the desired properties for humidity sensing applications, humidity sensors and their classification, materials used for humidity sensing, introduction to porous silicon, silicon-tin system, and alloying elements to improve the humidity sensing properties.

Chapter 3: Experimental details contains all the methods and methodologies adopted for the preparation and characterisation of the produced materials. This chapter is divided into two sections: (i) Alloy preparation and (ii) Characterization of the alloys. Each subsection has a theoretical description and methodology of the processes used for the alloy preparation and characterisation techniques.

Chapter 4: Results and discussion of the Si-Sn and Si-Sn-X (X = Ti, Cu, and Zn) is dedicated to the fabrication and characterisation of the Si-Sn and Si-Sn-X (X = Ti, Cu, and Zn) alloys produced by two different non-equilibrium techniques: sputtering and mechanical alloying. The structural, morphological, chemical, mechanical and electrical characterisation results are presented separately, for each system. The electrical measurements were performed to study the behaviour of the samples towards changes in relative humidity, ranging from 10 to 100% RH. The time stability response of the sensor displaying the best humidity sensitivity after 1 and 6 months is also included in this chapter.

Chapter 5: Conclusions and future work present the main conclusions of the research work, and some future perspectives to improve physical properties (structural, chemical, and morphological) favouring towards response to humidity sensing and detection.

CHAPTER 1: Introduction

This chapter aims to provide a general introduction and background about the research work performed during this thesis. The motivation, objectives, and methodology used throughout the course of the research work are also presented in this chapter.

1.1 Introduction and background

Materials have always been deep-seated in the development of human civilisation. History reveals that the advancement of human societies from the stone age to the bronze age and later to the iron age was possible only because of the ability to discover, produce and manipulate materials to fulfil the needs of the civilisation.

The utilisation of materials in a particular application is based on their properties, which are defined by their chemical composition, atomic structure, and microstructure. The advancement in material science and engineering, i.e., the knowledge about structure-property correlation, has led to the developments and improvements in these materials to serve various modern applications required in complex human societies.

With the increased requirements for controlled environmental conditions in many advanced industrial processes and better instrument productivity, the demand for accurate and reliable measurement of quantities using various sensors has grown exponentially in the last few decades.

Sensor technology is essential for life awareness, monitoring, safety, security, and surveillance. Sensors play a significant role in industries related to process control, diagnostics, monitoring, critical care, or public health. The International Electrotechnical Commission (IEC) [1] defines "a sensor as a measuring element that is a part of a measuring instrument or a measuring chain, which is directly affected by the measurand and generates a signal suitable for the measurement". Grandke *et al.* [2] also categorise a sensor as an element with housing and electrical connections included" or "a sensor system as being a sensor which incorporates signal processing (from analog to digital)".

According to the principle of operation, sensors can be classified into two major groups: physical and chemical sensors. Physical sensors are based on physical effects like piezoelectric, magnetic, ionisation, thermoelectric, photoelectric, etc., and include optical sensors, pressure sensors, temperature sensors, magnetic sensors, acoustic sensors, etc. Chemical sensors involve some chemical/physical adsorption, electrochemical reactions, etc. Gas, humidity, ionic, and biochemical sensors are in this group. The slightest change in the quantity being measured in the sensors is converted into an electrical signal and displayed in a form understandable to the user.

Humidity is defined as the amount of water vapour in the air or some given mixture of gases (atmosphere), while the sensor for measuring humidity is referred to as a humidity sensor. The term 'moisture' is often mistaken for "humidity". Moisture generally refers to the water

content of any material. Still, for practical reasons, it is usually applied only to liquids and solids, while the term humidity is reserved for the water vapour content in gases.

The measuring and control of humidity are required in many industrial manufacturing processes, such as paint, paper, or leather production; food packaging (storage of bakery items); plantation and soil moisture monitoring in the agriculture industry; respiratory equipment, incubators, sterilisers in the medical sector; packaging of medicines and biological products in the pharmaceutical industry; meteorological analysis for climate change and weather forecasting in environmental-based research institutes and industries. Figure 2 shows in detail the sectors of application for moisture and humidity sensors.

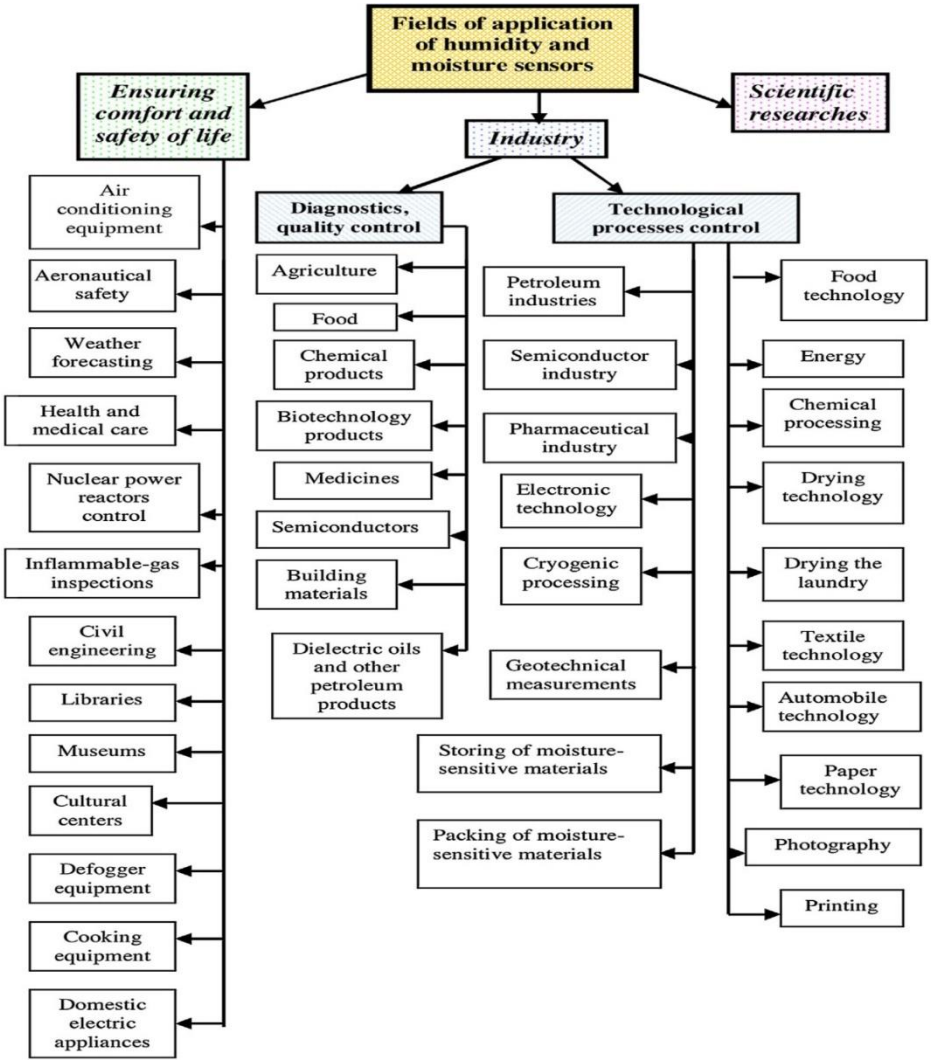

Figure 2. Fields of applications of moisture and humidity sensors [3].

Figure 3 presents the optimal environmental conditions (including relative humidity, %RH, and temperature) required for everyday applications in several industries and in living areas.

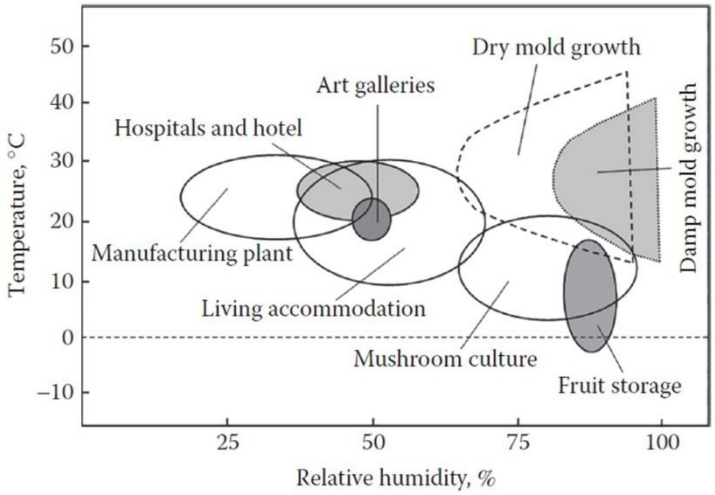

Figure 3. Graphical representation of optimal environmental conditions in different industries and living areas [4].

With such a wide range of applications, newer technologies, and environmental regulations, humidity sensors must be able to work under a variety of climatic conditions, ensuring their functioning with better sensitivity, improved stability, fast response times, with long life expectancy. Hence, the development of new humidity sensors or improvements to the old ones is still an ongoing process.

It is common sense, that in general, the amount of water vapour adsorbed by materials significantly affects their properties. In the case of hygroscopic materials, the length, weight and conductivity of organic materials can change due to water molecules adsorption. For impedance sensors, these changes are responsible for the shift in the impedance measurements of the sensing material. Therefore, currently, many approaches are used for measuring humidity, based on different measuring methods, different sensing materials, and different sensing technologies. This makes the classification and categorisation of humidity sensors a tricky process, which will be discussed in-depth in Chapter 2.

1.2 Motivation

The current technological and industrial development is becoming more and more demanding towards multi-functionality and excellence in performance. With such high stakes, even small changes in working conditions can dramatically affect a material's physical, chemical, mechanical, and technological properties that, in turn, impact its performance. For instance, in the semiconductor industry, integrated chips (ICs) are strictly manufactured under a controlled atmosphere. Hence, measuring, controlling, and monitoring humidity levels with better performance are essential for various research and industrial applications. This is where the requirement of humidity sensors for accurate and reliable measurement has gained a lot of importance in the last few decades. Humidity sensors should provide high performance, accuracy, reliability, short response time, repeatability, reproducibility, long-term stability, resistance to contaminants, and low production and maintenance costs.

In recent years, the use of Si-based gas sensors has increased extensively due to their wide range of properties such as relatively large contact surface and internal area, very high theoretical energy density, high photoluminescence, structural stability, biodegradability, and biocompatibility [5]. The porous silicon-based interface provides the ability to control and transform the interactive sensing properties by varying pore size distribution, pore morphology and surface roughness [6,7]. Due to these advantages, porous silicon has been used in several electronic industries to develop microprocessors, solar cells, optoelectronics, photovoltaics, chemical sensors and batteries [8]. Tin is also a well-known material used for sensing-based applications. Tin dioxide (SnO_2) is used to monitor and control different gases in the atmosphere [9]. Silicon-tin (Si-Sn) based alloy systems have mainly been used in electronic industries as electrodes in lithium-ion batteries. The incorporation of tin into the silicon matrix forms a strong inter-penetrating microstructure that helps to stabilise the system and increases the component's life [10].

However, its use as a porous material with the potential for humidity sensing is scarcely mentioned in the literature. Hence, this thesis aims to produce porous (Si-Sn) based alloy systems by non-equilibrium techniques (sputtering and mechanical alloying) and to correlate their chemical, structural, morphological, and mechanical properties with the electrical response to changes in relative humidity (RH), in the range of 10 to 100%. Moreover, different transition metals (Ti, Cu, and Zn) were used as dopant elements to the Si-Sn system with the aim of increasing their performance to humidity sensitivity. These alloying elements provide better structural stability to silicon and assist the formation of pores suitable for sensing-based applications [11–14]. Therefore, the idea was to take advantage of these alloying elements in

order to study the structural and electrical response for Si-Sn-X (X = Ti, Cu, and Zn) systems fabricated using non-equilibrium techniques. Additionally, there wasn't much information in the literature about how these systems might be employed for humidity-sensing applications.

1.3 Work objective and methodology

The objective of this work was to fabricate Si-Sn and Si-Sn-X (X = Ti, Cu, and Zn) alloys by non-equilibrium processes: (a) RF-magnetron sputtering for co-deposition of thin films and (b) mechanical alloying (MA) of powders followed by compaction and sintering to synthesise bulk materials. The produced materials were characterised using various structural, chemical, mechanical, and electrical methods to find the best-suited system for humidity sensing applications. The methodology used for the synthesis of Si-Sn and Si-Sn-X (X = Ti, Cu, and Zn) alloys is summarised in Fig. 4.

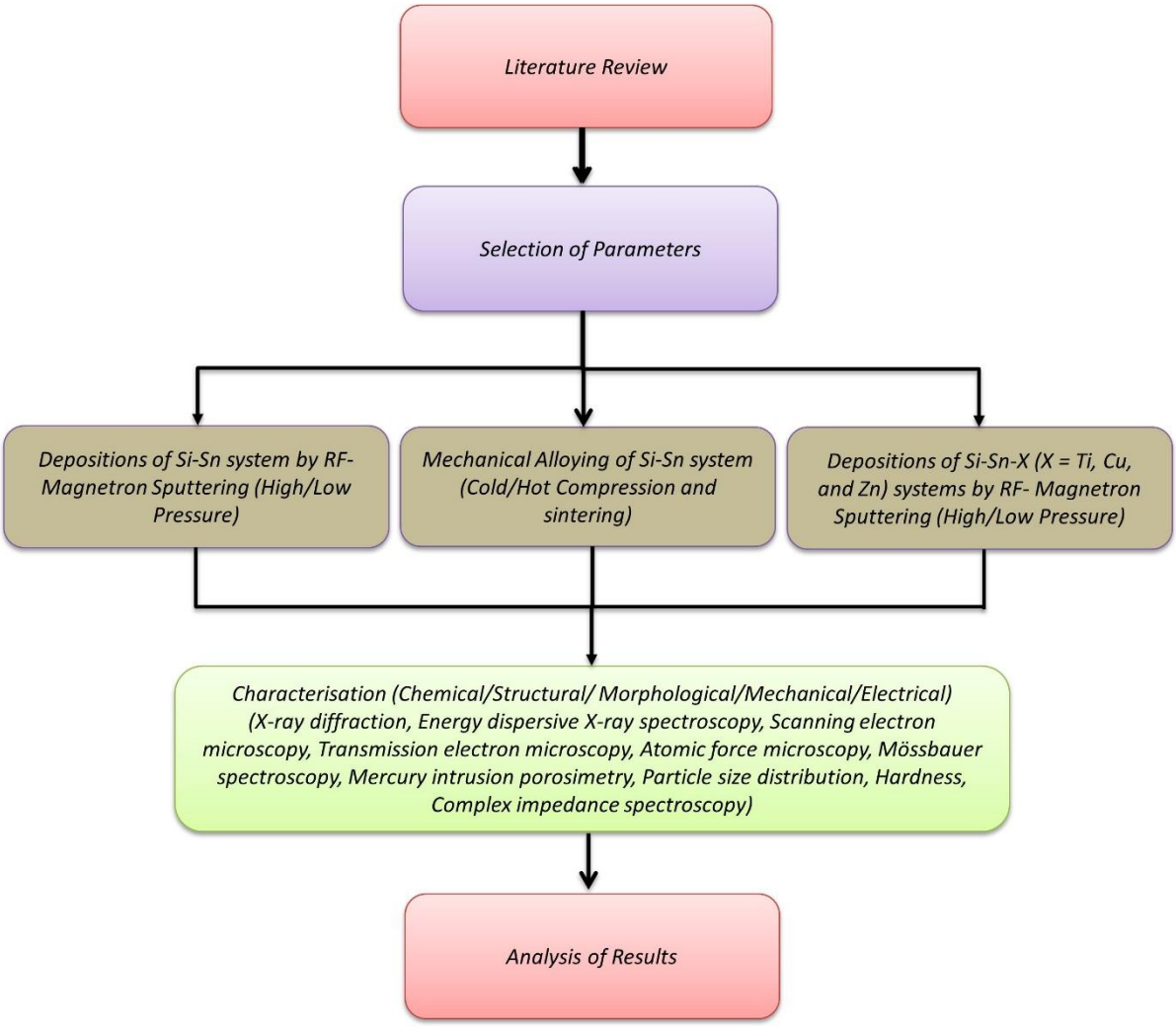

Figure 4. Schematic of the methodology used in this work for the synthesis and characterisation of the Si-Sn and Si-Sn-X (X = Ti, Cu, and Zn) systems.

CHAPTER 2: State of the art

This chapter is divided into sub-sections. The first one concerns the introduction, the measuring parameters, and the classification of the humidity sensors. Materials used for humidity sensing, with a special focus on porous silicon and its properties that favour gas and vapour sensing behaviour are addressed in the second sub-section. The later sections are dedicated to a literature review of the silicon-tin system and how doping with different elements could improve the humidity sensing properties. This will be addressed mainly for Ti, Cu, and Zn.

2.1 Introduction and measuring parameters for humidity

Water is a special substance that makes the planet earth unique across the universe. Water covers around 70% of the earth's surface and its co-existence in solid, liquid, and gaseous state make it suitable for the survival of all the life forms on earth. The water molecule is a non-linear compound, with the chemical formula H_2O. Properties of water include electrical dipole moment, surface tension, capillary action, and relatively high melting and boiling points.

Humidity is described as the amount of water vapour in the air or among other gases. In the environment, water and water vapour are constantly encompassed in the processes like evaporation, deposition, condensation, and sublimation. These parameters in addition to atmospheric conditions like temperature, pressure, time of day, and latitude also affect the levels of water vapour. Due to these variables, the humidity levels are significantly affected and constantly changing. Hence, the need to measure and monitor humidity levels requires considerable attention from the research and development community. Humidity also affects human comfort in terms of quality of life, efficiency and safety of manufacturing processes, packaging, and the storage of various products.

Humidity measurement determines the amount of water vapour in the air, or in some given mixture of gases within a closed environment. Humidity parameters are expressed in numerous ways, and the corresponding units are established considering the measurement technique. Therefore, humidity can be categorised into absolute, specific humidity, mixing ratio, dew point, and relative humidity. Table 1 shows the list of humidity parameters and their respective units used to determine humidity levels.

Table 1. List of humidity parameters and their respective units.

Humidity parameter	**Unit**
Absolute humidity (*AB*)	g/m^3
Mixing ratio (*r*)	g/g or kg/kg
Specific humidity (*Q*)	%
Dew point (*D PT*)	ºC or ºF
Frost point (*F PT*)	ºC or ºF
Volumetric concentration	ppm_V, ppm_W
Relative humidity (*RH*)	% RH

Absolute humidity (*AB*), also known as vapour density, is described as the ratio of the mass of water vapour to per unit volume of moist air:

$$AB = \frac{m}{v} \tag{1}$$

Where *m* is the mass of water vapour (g), and *v* is the volume of the air (m^3).

The mixing ratio (r) is defined as the ratio between the mass of the water vapour and the mass of dry air and is expressed as follows:

$$r = \frac{M_w}{M_a} \tag{2}$$

Where M_w and M_a are the water vapour and the dry air masses (g or kg), respectively.

The specific humidity (Q) is expressed as the ratio of water vapour to the total mass of the gas. It is usually expressed in percentage (%). The empirical formula for specific humidity is given as:

$$Q = \frac{M_w}{M_w + M_a} \times 100 \tag{3}$$

Where M_w is the mass of the water vapour, and M_a is the mass of dry air.

Absolute humidity (*AB*), mixing ratio (r), and specific humidity (Q) do not consider temperature and therefore, the values obtained from these humidity measuring parameters are hard to interpret. For example, warm air (at 30º C) can hold a maximum of 30 g of water vapour, and this will account for an *AB* value of 30 g/m^{3,} whereas cold air (at 0º C) can carry up to a maximum of 5 g of water vapour resulting in maximum *AB* value of 5 g/m^3. Therefore, humidity sensors based on these humidity parameters are rarely used in research and industrial applications.

Humidity sensors based on Dew / Frost point (*D/F PT*), volumetric concentration (*ppm*) and relative humidity (*RH*) are the most used for humidity measurements.

Dew point is defined as the temperature above 0 ºC at which the water vapour in gas or air condenses to liquid water, i.e., the temperature at which air or gas gets saturated (i.e., 100% saturation). Frost point is the temperature below 0 ºC at which water vapour condenses to ice. Dew/Frost Points (*D/F PT*) depends on the air or gas pressures, but they are independent of temperature and hence, are sometimes defined as absolute humidity measurements.

Volumetric concentration or parts per million (*ppm*) is sometimes referred to under an absolute humidity measurement. It represents the ratio of water vapour content ($\times 10^6$) in terms of either volume or weight to that of volume or weight of dry gas. Therefore, they can be either expressed as ppm_V or $ppm_{W,}$ respectively. This humidity unit is primarily used for measuring traces of humidity.

In contrast, relative humidity (*RH*) is defined as the ratio between the water vapour present in the air (or gas mixture) and the maximum water vapour content at the same temperature, when the air or gas is saturated. It is expressed in percentage (%), where 0% RH refers to absolute dry air or zero moisture content, whereas 100% RH, implies full saturation or dew point (ºC)

achieved. A state of full saturation is defined as a level of moisture content in the air above which any additional moisture will precipitate (condense) in the form of water droplets, i.e.:

$$RH = \frac{P_a}{P_s} \times 100 \quad (4)$$

Where P_a is the actual partial pressure of vapour in the air (bar), and P_s is the saturated pressure of fully humidified air (bar) at the same temperature.

With so many humidity measuring parameters, there is a lot of confusion around the correlation between these humidity units. Figure 5 shows one of the scales for easy conversion between units like dew/frost point, parts per million and relative humidity.

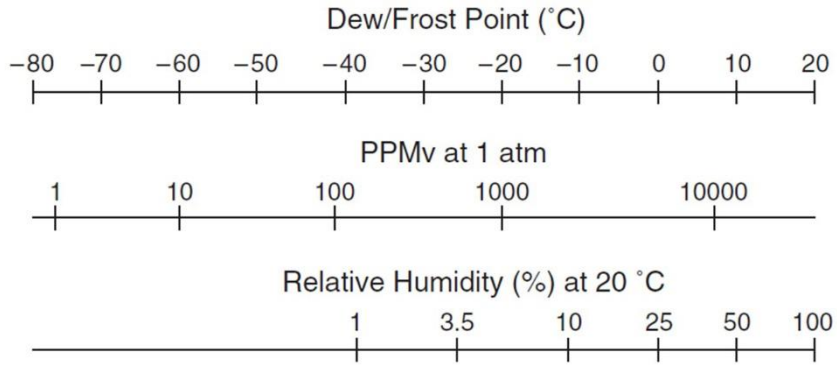

Figure 5. Humidity unit conversion scale between dew/frost point (ºC), parts per million (ppm_V) at 1 atm. and relative humidity (%) at 20ºC [15].

The correlation between the humidity measurements can also be performed using the psychrometric charts. These are complex graphs plotted at a constant pressure to understand the relationship between various parameters like temperature, vapour content and energy. A psychrometric chart also defines a relationship between temperature, and absolute and relative humidity values. Figure 6 illustrates a psychrometric chart of the mixing ratio *r* values from 0 to 30 g/kg.

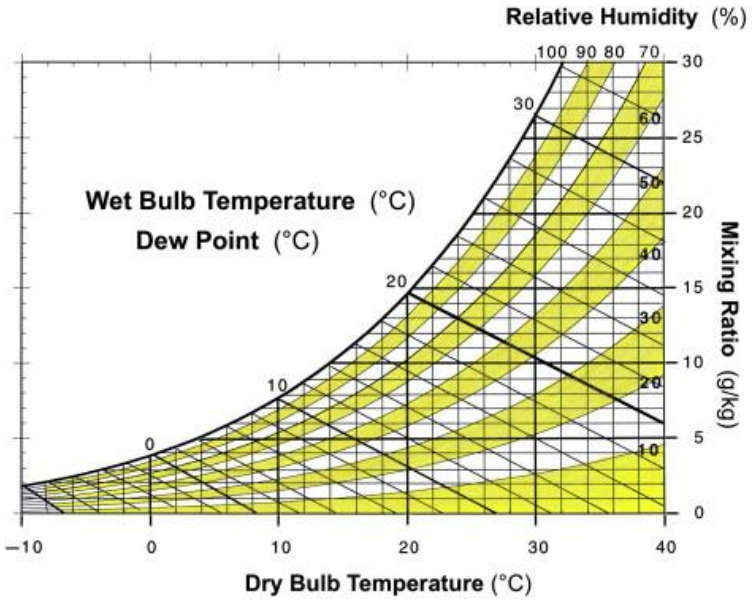

Figure 6. Psychrometric chart for the mixing ratio *r* values from 0 to 30 g/kg [16].

Amongst the various humidity parameters and units, absolute and relative humidity are the most prevalent. For commercial and industrial purposes, generally, relative humidity (RH %) measurements are preferable to absolute humidity ones because they are easier to read and interpret.

2.2 Humidity sensors and their classification

Numerous and different processes in manufacturing, production, and storage create high demand for humidity sensors. Hence, humidity sensing studies at different environmental conditions have progressed rapidly, and humidity sensors, regardless of their fabrication routes, have been widely employed in various industrial and household applications. Due to constantly changing operating conditions from different environments, various humidity sensing devices have been developed based on different hygroscopic materials that operate on distinct working principles and mechanisms. The constant increase in the requirements of controlled environmental conditions in various sophisticated industrial applications has caused researchers to come up with new, more accurate, reliable, and cost-effective humidity sensors. One way to classify humidity sensors is based on the water adsorption mechanisms used to identify the humidity levels. Table 2 shows some common types of humidity sensors with their working principles.

Table 2. Some types of humidity sensors and their working principles [17].

Principle	**Working mechanism**
Capacitance	The dielectric constant of a material varies with the amount of water absorption.
Coulometer	Electrolyte formation by water absorption which is proportional to current.
Infra-red (IR) radiation	The amount of water vapour adsorption by IR radiation depends on the level of humidity.
Microwave radiation	The radiation at the receiving end attenuates as the amount of water content increases.
Resistance	Conductivity of a material changes with amount of water vapour adsorption.
Gravimetric	The weight of a drying agent changes with the amount of water adsorbed.
Psychrometric	The change in temperature of the wet bulb when humid air is introduced depends on the amount of water vapour present in humid air.
Radio frequency	Radio frequency current produced by the dielectric change depends on humidity level.
Thermal conductivity	Self-heated transistors are connected in a Wheatstone bridge circuit. The presence of moisture content creates an imbalance in the bridge as the heat dissipation in the reference and measuring thermistors
Dew Point	The temperature corresponding to the condensation evaporation equilibrium at a cooled surface varies with the amount of water present.

Humidity sensors based on relative humidity measurements are temperature dependent. Nevertheless, they are cheap and easy to interpret, and therefore they are the most widely used. Based on employed sensing material, the classification of these sensors has been attempted by many authors in the past [18,19]. Recently, Chen and Lu [15] categorised them into three major classes: ceramic, semiconductor and organic polymer types. Humidity sensors exploit changes in the physical and electrical properties of the sensing material when subjected to the different environmental conditions and present a measure of the amount of humidity due to adsorption and desorption of water vapour molecules.

Humidity sensing in these types of sensors is based on the electrolytic properties of sensing matter by taking the advantage of inner water electrolytes. Humidity sensing based on nanowires, nanorods, nanofibers and *p-n* heterojunctions are classified under the ceramic type. Ceramic humidity sensing elements with different intrinsic properties can be classified into either semiconducting or dielectric metal oxide composite. Polymeric types are based on conducting or non-conducting polyelectrolytes.

These sensors are based on the changes in the physical and electrical properties of the sensitive elements when exposed to different atmospheric humidity levels. Ceramic materials are

more popular due to their unique structure comprising grains, grain boundaries, surface contact areas, and porous microstructures, making them ideal candidates for electrochemical sensing applications. The humidity sensing mechanism behind all-ceramic sensors is water vapour adsorption based on chemisorption (chemical adsorption), physisorption (physical adsorption), and capillary condensation processes [20,21]. Adsorption of water vapour on the surface affects the electrical conduction, and this change encompasses the resistance, capacitance, or electrolytic conduction depending upon the sensor type. Adsorption of water vapour on the ceramic surface is promoted by its porous nature [22,23]. Water is a polar molecule, and the negatively charged oxygen is electro statistically attached to the positively charged ions of the sensor material.

Consequently, the initial monolayer (chemisorbed) formation is caused by the chemical bond between the positive ion of the sensor material and the oxygen of the water layer formed under the influence of a high electrostatic field. Once this monolayer is formed, it is no longer affected by continuous exposure to humidity. Thus, the concentration of the chemisorbed water will be the same as that of outermost positively charged ions on the surface of the ceramic material. At low humidity concentrations, water vapour chemisorbs by a dissociation mechanism, forming hydroxyl ions at the surface, until a single layer is formed. Usually, an additional monolayer is formed by around 20-40% RH, due to the physical adsorption (physisorbed) between the initial layer and the additional water molecules present at the sensing material surface. After the first physisorbed layer, new ones get formed on top of each other, as the amount of water molecules near the surface keeps on increasing. Contrary to the chemisorbed layers, these physisorbed ones can be easily removed by decreasing the humidity.

With a further increase in the humidity concentration, the layers of physisorbed water molecules tend to condense inside the capillary pores, which have dimensions below the Kelvin radius. The increase in the physisorbed water vapour layers increases the concentration of H^+ ions. The neck of the pores filled or unfilled depends on the radius and the thickness of the physisorbed layer, i.e., on RH%. It has been reported that capillary condensation of water vapour with a significant impact on conduction changes only occurs for a specific pore radius range, generally referred to as the mesopore range [24].

Figure 7 illustrates the formation of the chemisorption and physisorption layers onto the surface of an alumina-based film [25].

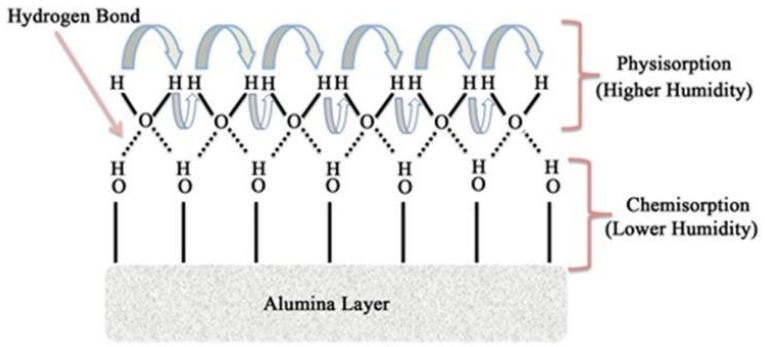

Figure 7. Schematic of chemisorbed and physisorbed layers on an alumina-based sensor surface [25].

The charge transportation occurs by a proton hopping mechanism between the chemisorbed hydroxyl groups in the atmosphere, moving from dry air to low humidity levels. The physisorbed water molecules start appearing by slowly increasing the humidity values, and the hydronium ions, H_3O^+, act as charge carriers. When a high concentration of humidity is reached, the H_3O^+ ions are hydrated and originate H^+ ions and H_2O. Each water molecule will be slightly bonded with one hydroxyl group. The transportation of the charges occurs when H_3O^+ ions release a proton to neighbouring water molecules, which accept it while releasing another proton and so on. This phenomenon is known as the Grotthuss's chain reaction, represented in Fig. 8.

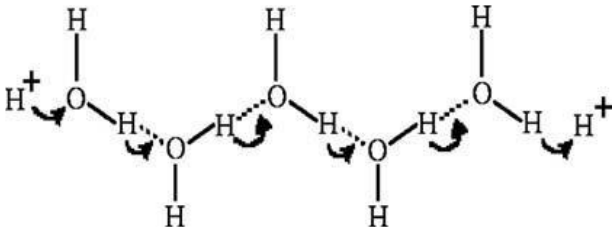

Figure 8. Illustration of Grotthuss chain mechanism [15].

At high humidity concentrations, the behaviour of physisorbed water layers is liquid-like, and the H^+ ions move freely. If micropore condensation takes place, the conduction mechanism through the pores is electrolytic in nature and will occur in addition to the Grotthuss mechanism. Electrolytic conduction in the condensed water within the pores combined with charge diffusion at the walls of the pores originates a sort of Warburg impedance, described by a power dependence. This succession of mechanisms leads to a rapid increase in conduction (i.e., decrease in resistance) with increasing humidity content. This fact occurs only in an *n*-type sensing element. For *p*-type sensing elements, holes are filled, and the conduction will decrease with increasing humidity because of the decrease in free electrons which participate in conduction mechanisms [26].

2.3 Materials used in humidity sensors for sensing

As mentioned before the most popular materials used for sensing applications are metal oxides. They have excellent thermal and environmental stability, fast response, and good reversibility of electrical conductivity. Metal oxide sensors usually also have good mechanical properties, like high mechanical strength, they are applied in a wide range of working temperatures, and they have low fabrication costs.

Among the metal oxides, the ones with spinel (ferrites and other magnetic oxides) and perovskite (ferroelectric and superconducting oxides) structures are of particular interest in this kind of applications. Metal oxides having a spinel-type structure are often used as model systems due to their structural features, which facilitate the tailoring of relevant properties. Many physical and chemical properties of these materials are a function of the cation distribution and most of the metal oxide's functionalities are connected to the degree of non-stoichiometry and structural defects. The structure of spinel compounds contains a tetrahedral framework with a high density of defects and is semi-conductive in nature. The perovskite oxides with a ABO_3 formula, where A is a rare earth or alkaline earth metal susceptible to humidity, and B is a transition metal. Such materials have higher activity than normal metal oxides and therefore show better humidity sensing even at high temperatures [27]. The key factor influencing humidity sensing for perovskite oxides is the semiconducting nature of ceramic materials. As a result, these oxides are less susceptible to their porous features [28].

Spinel and perovskite-type oxides, as well as hybrid materials that contain them, are used to fabricate electrochemical humidity sensors. Besides metal oxides, there are other materials which have been used for humidity sensing, such as titanate-based, phosphate-based, tungstate-based, bismuth-iron molybdate, some oxygen compounds, glass-ceramic composites and zeolites, among others [29].

Ceramic humidity sensors including single crystal, porous solid bodies, and thick (thickness between 10 to 25 μm) and thin films (thickness between 0.1 to 10 μm) have been fabricated by different processing techniques, in different shapes such as disks, pellets, rectangular bars, plates, and thimble-shaped tubes.

In the bulk sensing materials, the humidity sensitivity can be more easily controlled because the porosity can be introduced up to the desired level, additionally increasing the overall surface contact area for the functioning active sites. The thick film technology (*e.g.*, screen-printing) offers easy and reliable manufacturing of sensing materials at a significantly low cost [30]. Finally, the thin film sensors are mainly used for micro humidity sensing. In these sensors,

water condensation is restricted due to the absence of capillary pores. Hence, electrolytic condensation becomes impossible to occur and consequently, the multi-layered physically adsorbed water layers contribute to lower humidity range sensing. Among the thin-film manufacturing techniques, physical vapour deposition (PVD) is one of the most known and used for the production of coatings with some micrometers thickness.

Magnetron sputtering is a well-established PVD technique. However, it is still difficult to control the stoichiometry of the produced films due to the large number of deposition parameters involved in the process. Nevertheless, homogeneous properties are obtained along the entire thickness of the films, which makes them reliable. Some authors mentioned that the thickness of the films affects humidity sensitivity [31], since the humidity response effect due to the thickness of the films gets reduced for high humidity levels. This happens because pore widening occurs to the extent that the entire structure is wetted with consequent loss of pore dielectric isolation among the pores. The barrier layer capacitance only governs the sensor capacitance. It is interesting to note that the capacitance is reduced in the low humidity range.

Faia *et al.* [32] showed that the sensitivity of thick titania films (with adequate volume of mesopores) fabricated by slow spinning process was strongly influenced by the surface reactivity with water and the porous microstructure. The humidity sensitivity measurements were performed using complex impedance spectroscopy, and the obtained Nyquist plots have clearly shown the sensitivity of the thick films towards changes in relative humidity. They concluded that the structural properties such as the morphology of the pore (pore volume, pore size, and shape), overall porosity, pore accessibility, and surface-active sites affected the sensor performance.

A uniform porosity throughout the sensor structure is critical for a good sensing response [33]. However, porous materials generally have irregular shapes and sizes, that negatively affects the humidity sensitivity. Faia *et al.* [34] reported that the pores at or near the mesoporous region are suitable for water condensation, with higher electrical response to the humidity level variations.

The shape of the pore also affects humidity sensitivity. Pores with spherical shapes do not contribute significantly toward humidity sensitivity [35]. In contrast, elongated columnar pores (i.e., long tubular shapes) in the direction of the applied field are vital in determining the sensor characteristics.

Banerjee *et al*. [36] proposed a probabilistic model for the pore size optimisation of humidity sensitivity in ceramics under simplified assumptions. This model suggests that the optimised pore size must be in nanometres (tubular pores are a reasonable approximation), and

the mean free path for the water molecules should be minimised so that the molecules can always move close to the potential field of the pore wall. Authors concluded that the water vapour adsorption for humidity sensitivity were found to be dependent on pore size and wall morphology.

2.4 Porous silicon

The formation of porous silicon (*p*-Si) was first observed in the late 1950s by Uhlir (1956) [37] and Turner (1958) [38] while performing electrolytic shaping of silicon and electropolishing of silicon in a hydrofluoric acid solution, respectively. It was not until the early 1980s that the importance of porous silicon was recognised. Since then, several research groups have explored the possibility of using porous silicon as core material for different applications. This has also increased the performance and functionality of silicon technology.

Bomchil *et al.* (1983) [39] studied the specific surface area, pore size distribution and total pore volume of porous silicon by adsorption isotherms. Porous silicon was fabricated using an anodic attack of single-crystal Si substrate in a 25% hydrofluoric acid solution. Mean pore radius was observed to be in the range of 20 to 100 Å.

Pickering *et al.* (1984) [40] produced porous silicon films in *p*-type degenerate and non-degenerate silicon. In degenerate semiconductors, the injection of electrons or holes is only possible from the Fermi energy level. In this case, a high level of doping can be observed, making the semiconductor act as a metal rather than a semiconductor. Contrarily, non-degenerate semiconductors can cause the formation of two types of contacts to organic material. The results revealed that the anodisation of a Si-wafer in aqueous solution of hydrofluoric acid with current densities below those used for electroplating resulted in the formation of the porous structure. The degenerate porous silicon layers showed good retention of the single crystal characteristics of the starting Si-wafer containing only crystalline silicon (*c*-Si) and voids, reflecting their nature to withstand any heat treatment. On the contrary, non-degenerate porous silicon had a much greater variability with more significant crystallinity loss. A substantial amount of oxygen incorporation was also observed resulting from partial oxidation occurring on or immediately after anodisation [41].

Beale *et al.* (1985) [42] reported a systematic study on the formation and properties of *p*-silicon produced by anodising Si under different conditions and dopant concentrations. The structural and morphological characteristics of the porous silicon were assessed by transmission electron microscopy. Authors proposed a theory for the formation of porous silicon, which describes the evolution of the microstructure to be dependent on the anodising conditions. The formation of porous gallium arsenide, similar to porous silicon, was reported in this article.

Canham *et al.* (1990) [43] performed the fabrication on *n*-type silicon with uniform deep trenches (large porous structures) ranging in different sizes for different component applications by a standard masking technique.

Canham *et al.* (1995) [44] fabricated a microporous silicon film through a nano etching technique that could act as an active biomaterial for invasive sensing, biosensing and other electronic prosthetic devices.

Canham *et al.* (1996) [45] reported photoluminescence properties of porous silicon at room temperature in the visible spectrum to the naked eye and in near-infrared waveguiding.

Various research articles were also published to describe the mechanisms behind the formation of porous silicon through various fabrication routes [46–49]. Hence within the research community, porous silicon was considered an esoteric material with substantial potential for various applications.

Kavalev *et al.* (2001) [50] discovered the strong explosive nature of hydrogenated porous silicon when interacting with liquid oxygen at cryogenic temperatures. The factors responsible for this long chain reaction were the large internal surface area (due to porous nature), atomic scale spacing between interacting Si atoms, surface bonded hydrogen, and oxygen adsorption.

Kochergin *et al.* (2006) [51] have shown the interaction of light propagating in the direction of pores in porous silicon. The results provided a lot of helpful information in the context of advanced optical engineering. They have also shown that porous silicon in various geometries and morphologies could be used as new optical elements with a combination of theoretical insights, such as suitable porous structure and better pre- and post-processing of silicon.

Ozdemir *et al.* (2007) [52] discussed the importance of the porous nature of silicon and how it has attracted researchers in the past for gas sensing applications. A large surface area and the relative ease in modifying its surface have evolved a variety of sensor configurations. Sensitivity and selectivity changes were observed as Au_xO, Pd, TiO_2, $TiO_{2-x}N_x$ and SnO_2 are placed on the porous silicon surface. Organic vapours, H_2O, CO_x, NO_x, NH_3, O_2, H_2, HCl, SO_2, H_2S and PH_3, have been detected/measured. The results showed that porous silicon can be used as a promising gas sensor if the porous silicon surface modification is better understood.

Since the 2000s, there has been an increase in the number of publications (including review articles, research articles, book chapters, conference abstracts, patents, short communications, etc.) dedicated to porous silicon, as shown in Fig. 9 (Web of Science).

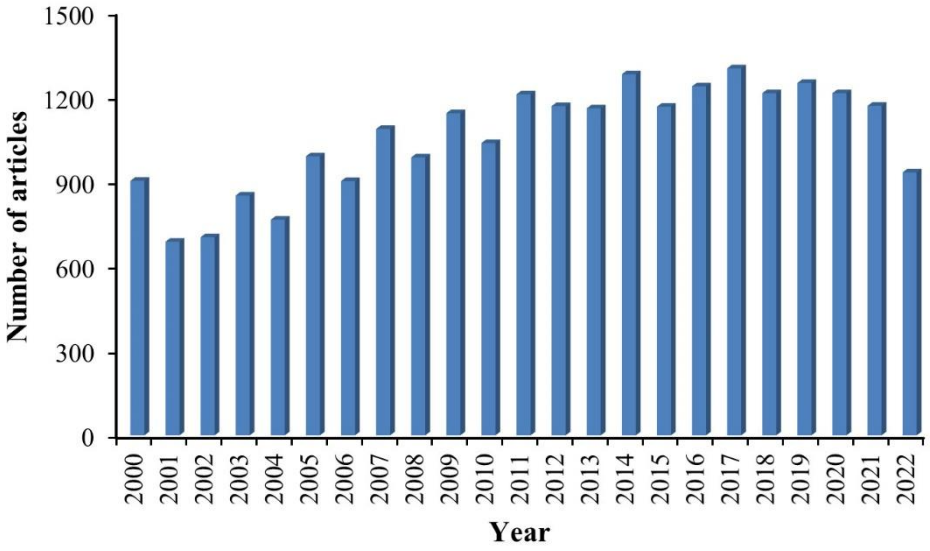

Figure 9. Number of publications concerning porous silicon from 2000 to 2022 (prepared using data collected from Web of Science).

The articles on porous silicon covered most research areas like materials science, physics, chemistry, science technology other topics, engineering, optics, electrochemistry, instruments instrumentation, energy fuels, metallurgical engineering, and others, as shown in Fig. 10 (Web of Science).

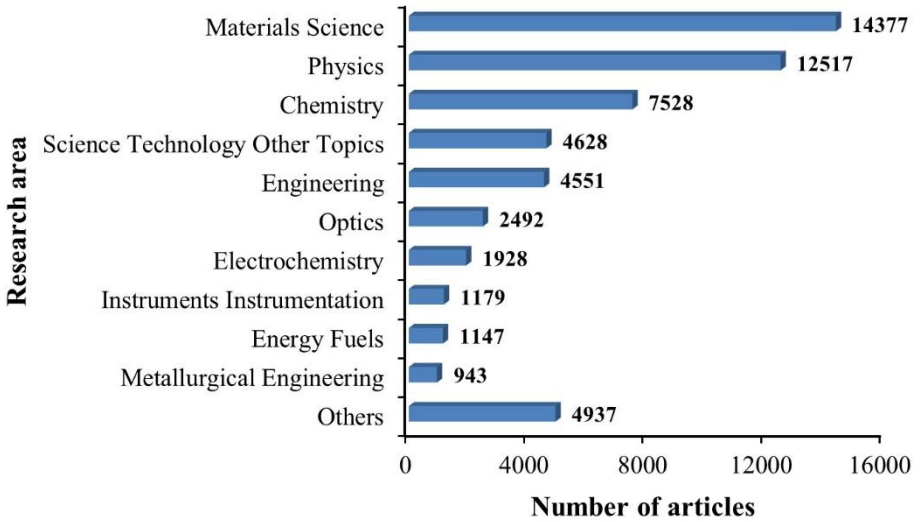

Figure 10. Number of articles on porous silicon published in various research areas (data collected from Web of Science).

The porosification of silicon at different levels (from micro- to nano-structure level) has been done through different fabrication routes, such as electrochemical etching, chemical strain etching, chemical vapour etching, laser-induced etching, reactive ion etching spray processing, chemical and physical vapour deposition, with a remarkable change in its overall properties. Porous silicon are used for the fabrication of parts for various fields like optoelectronics, photonics microelectronics, chemical sensing, medicine, and bioengineering [6,53–58].

Humidity sensing application of porous silicon dates to the early 1990s when Anderson *et al.* [59] studied the properties of porous silicon formed using an anodisation process for vapour sensing. The authors concluded that porosity in the silicon structure was responsible for an increase in the capacitance response of 440% in the humidity range from 0 to 100% RH at room temperature. By the end of that decade, Hubert (1999) [60] described various humidity sensors developed using silicon technology.

During the 2000s, with the increase in the requirement of controlled environmental conditions for sophisticated industrial and scientific applications, the role of precise humidity detection became even more crucial. Different fabrication routes and their mechanisms for the formation of porous silicon were studied in as much detail and depth as possible to understand and predict the more favourable and suitable properties for humidity sensing applications [61–64].

Connolly *et al.* (2002) [65] studied the suitability of porous polysilicon (*p*-type) and porous SiC as materials for humidity sensing. For porous polycrystalline silicon, the capacitance increased up to 2500%, with relative humidity variation from 10 to 90%. The sensor also showed good linearity from 30 to 90% RH. Additionally, the effect of temperature on humidity sensing for porous polysilicon was less when compared with porous single crystal Si.

Das *et al.* (2001) [66] studied the role of parasitic resistance and capacitances in determining the sensitivity of porous silicon humidity sensors. They observed that for both capacitive and conductive type sensors, the sensitivities increased with increasing the porosity from 60 to 85% but for higher values, the sensors became insensitive. Hence, they concluded the porosity should be around 80% for best sensing towards humidity. With regards to capacitive sensing, low-frequency ranges induced very low parasitic capacitance, and the measured capacitance truly represented the active capacitance of the sensor.

Islam *et al.* (2004) [67] investigated and described a comparative study on the performance of porous silicon and porous alumina sensors for the detection of moisture at ppm levels. The conclusions of that work pointed out to the lower sensitivity of the porous silicon

when compared to porous alumina for trace moisture levels (5-200 ppm_V). In contrast, the response and recovery time of porous silicon was much shorter than the porous alumina. Also, designing and fabricating of porous silicon sensors was much more straightforward, economical and IC compatible.

Guoguang *et al.* (2011) [68] proposed a porous silicon Fabry-Perot sensor for humidity measurement. The characteristic wavelength of the sensor showed a red shift when relative humidity was increased from 11% to 97%, with an increase in the refractive index. The authors proposed that the high sensitivity levels compared to that with more complex sensor structures were achieved due to larger surface area and the F-P cavity sensitive to any refractive index change. The ease of fabrication, small sensor size, and low-cost design make it very attractive for the sensor technology.

Jalkanen *et al.* (2012) [69] proposed a study on the production of 3D printed porous silicon. This was done by drop casting porous silicon particle solution on top of an integrated electrode configuration. The humidity sensing properties of the fabricated sensor were examined in the relative humidity range of 0 to 95%. The results showed that the sensor had good sensitivity and reproducibility throughout the entire relative humidity range. Moreover, response time, recovery time and hysteresis were also very small, making it very interesting for sensing applications

Jalkanen *et al.* (2015) [70] manufactured porous silicon using a roll-to-roll (R2R) fabrication process for real-time humidity monitoring. The sensing elements consisted of printed interdigitated silver electrodes and a spray-coated porous Si layer; these were fabricated on a coated paper substrate by a two-step process. The capacitive and the resistive response of the sensing elements were examined under different relative humidity concentrations from 0 to 90%. Relatively fast recovery without the need for any refreshing methods was observed with a change in RH. The humidity background signal and hysteresis arising from the paper substrate depended on the sensing porous Si layer's thickness. Hysteresis from a thick *p*-Si layer was still noticeable but was not detrimental anymore.

In a recent review article from Korotcenkov *et al.* (2019) [71] the advantages and disadvantages (limitations) of the use of porous silicon are described in detail. They concluded that while *p*-Si-based sensors have increased their sensitivity, selectivity, and stability. Yet, more work needs to be done in this area because current approaches do not provide the required stability of the characteristics and selectivity of their response.

2.5 Silicon-tin system

In the periodic table, silicon and tin are positioned in the same group (14) and periods 3 and 5, respectively. In the electronics industry, silicon is one of the most employed semi-conductors because of its wide range of properties and abundance in the earth's crust [72]. Tin, on the other hand, is one of the materials most used for sensing applications. Tin-oxides are used for the monitoring and controlling of several gases in the atmosphere [73].

The phase diagram of the silicon and tin system is shown in Fig. 11. Although silicon and α-tin phases have the same crystal structure and belong to the same periodic table group, the solubility of these two elements is almost negligible. Silicon and tin have atomic numbers of 14 and 50, respectively, and a significant atomic size difference (atomic radii of Si and Sn are 1.1 and 1.4 Å, respectively). The maximum solubility of tin in silicon at room temperature is ~ 0.1%, i.e. these elements are almost immiscible under thermodynamic equilibrium conditions [74]. This is in accordance with the solid solubility rules by Hume Ruthery, which state that the solid-state solubility between two elements can only be achieved if the size difference among their atoms does not exceed more than 15%.

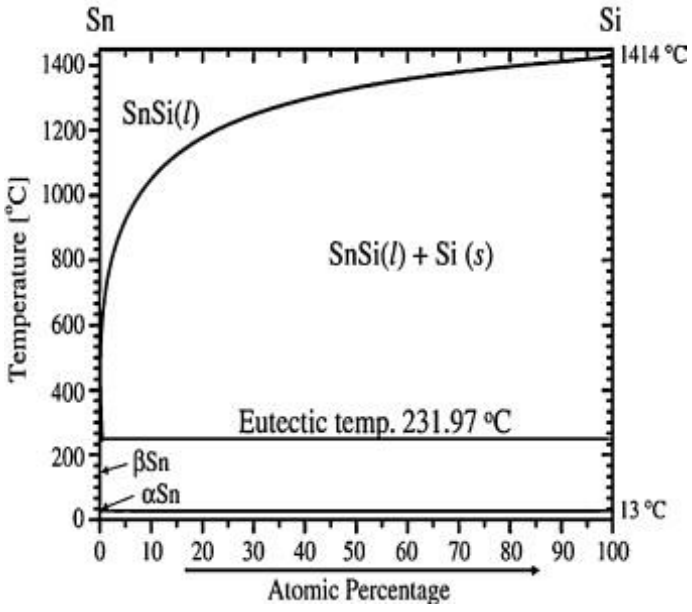

Figure 11. Silicon-tin system phase diagram [74].

Non-equilibrium (metastable) conditions are required to increase the solubility of tin in silicon. Several non-equilibrium processing technologies have been used in the past few decades to fabricate super-saturated Si-Sn systems, including rapid solidification, spray forming, mechanical alloying, ion mixing, physical vapour deposition, chemical vapour deposition, laser processing, and plasma processing. Out of the above-mentioned processing techniques, the most commonly used for the preparation of silicon-tin alloys are molecular-beam epitaxy [75–78],

vapour deposition [79–85], and mechanical alloying [10,86,87]. In the case of physical vapour deposition, the maximum solubility of tin in silicon can be increased up to 28-30%. Once this limit is crossed, tin precipitation occurs and small clusters of β-tin are formed in the amorphous silicon (*a*-Si) matrix [88,89].

The earliest paper on the amorphous silicon-tin system dates back to 1981 [90] when $Si_{1-x}Sn_x$ ($0 < x$ (at.%) < 0.12) alloys were prepared using a dc cathodic sputtering. The results revealed that both average and optical gaps decreased with the increase in tin content. The high sensibility of *a*-Si electronic structure to Sn substation was discussed there.

In the 1980s, Williamson *et al.* [84,91,92] and Vergnat *et al.* [85,93,94] performed some work on Si-Sn and Si-Sn:H systems using various manufacturing techniques. For low concentrations of tin (below 50 at. %), this element goes into tetragonal substitutional Si sites in a continuous random network whereas at high tin concentrations (above 50 at. %), tin fractions were observed in the form of crystalline β-tin. In another study, Mahan *et al.* (1984) [95] also observed an *n* to *p*-type conductivity transition with an increase in Sn content in the Si-Sn system. Changes in the optical band gap were also observed in the Si-Sn system with increasing tin content; the optical band gap decreased linearly with the increase in tin content. Adding hydrogen to the $Si_{1-x}Sn_x$ system promoted the formation of β-Sn precipitation. Other studies [96,97] were also conducted during this time, which also proposed results similar to the previously mentioned articles.

Shiryaev *et al.* (1995) [78] prepared $Si_{1-x}Sn_x$ ($0.001 < x < 0.052$) alloys on Si (001) substrates by molecular beam epitaxy at 220 and 280 °C. The as-grown alloys were strained and found to be pseudomorphic to Si with no indication of extended defects and tin precipitates. The compressive strain in those alloys corresponded to that deduced from Vegard's linear interpolation considering the lattice parameters of Si and β-Sn. The authors concluded that the alloys were thermally unstable at higher temperatures (1000 °C), with the formation of metallic β-tin particles and the appearing of 60 degrees misfit dislocations.

Maruyama *et al.* (1997) [88] prepared thin films of amorphous silicon-tin alloys ($a\text{-}Si_{1-x}Sn_x$, $0 < x < 0.456$) by RF magnetron sputtering using a silicon target and tin chips placed over it under argon atmosphere. Based on the results obtained by x-ray diffraction, the authors concluded that the films deposited with tin content lower than 28 at. % were fully amorphous, whereas those deposited with tin contents greater than or equal to 28 at. % showed weak peaks of crystalline β-Sn.

Ahn *et al.* (2005) [98] used RF-magnetron co-sputtering to prepare thin films from two silicon and tin targets under an argon gas atmosphere as potential anode material in Lithium-ion batteries. In order to obtain different compositions (atomic Si concentrations from 33 to 76 %), different powers were used on the silicon target, while the power applied to the tin target was kept constant. The authors concluded that the Li/Sn–Si cells fabricated with the Sn–Si nanocomposite electrodes showed excellent reversible capacity during the Li insertion and extraction processes. Therefore, using the Sn–Si nanocomposite electrodes is potentially crucial for high-performance Li rechargeable batteries.

Jeon *et al.* (2010) [76] studied the effect of annealing temperatures on Sn-induced crystallisation of hydrogenated amorphous Si (*a*-Si: H) thin films and showed that the films crystallised by annealing for 1 hour at 300°C.

Mohiddon *et al.* (2012) [99] produced nanocomposite films by thermal annealing bilayers of Sn and Si deposited on borosilicate glass substrates at various temperatures from 300 to 500 °C for 1 hour in air. They observed the formation of Sn-Si nanocomposites with a high refractive index, large band gap, and low optical absorption, suitable for many optical applications.

Wu *et al.* (2014) [10] discussed the use of silicon/graphite-tin powders prepared by high energy mechanical milling technique for anode materials in Li-ion batteries. The authors stated that tin with silicon and graphite forms a nano-structured interpenetrating phase which helps the powder to exhibit better cyclability and long life as an anode material.

One important reference work on the utilisation of mechanical alloying for the synthesis of silicon-tin alloys is by Wu *et al.* (2016) [86]. The authors took different amounts of silicon and tin powders and milled them for 1 to 25 hours at 300 rpm. By scanning electron microscopy and x-ray diffraction, they observed that the powders milled for 20 hours presented Si particles trapped in large Sn-entangled ribbons concluding that they behaved better in Li-ion batteries (better recyclability tests) when compared to the ones milled for different periods.

Yang et al. (2018) [87] prepared a composite material using Si/Sn with amorphous carbon-graphite in a high-energy ball milling followed by an annealing process. Cyclic voltammetry and electrochemical impedance spectroscopy results indicated that the Sn acted as an active matrix and could decrease the polarisation resistance. Besides, they found that the ductile Sn not only cushion the volumetric deformation of Si but also improves the dispersion of Si.

2.6 Alloying elements for Si-Sn system

Researchers have been using materials like metals, semiconductors, polymers, ceramics and 2D materials to improve the humidity sensing properties. Among these, transition metals like titanium, zinc, and copper are well known for this kind of applications. The incorporation of these metals into the Si-Sn system as dopant elements might increase the structural stability as well to help in the formation of pores with a geometry suitable for gas and vapour sensing applications [11–14,100,101].

Transition metal oxides such as ZnO, TiO_2, CuO, SnO_2, and Fe_2O_3 have also been used for humidity sensing applications due to their unique electrochemical and electronic properties coupled with high surface area, fast response and recovery times, ease of fabrication, low cost, stability, and repeatability factors.

Hind Ahmed *et al.* (2019) [101] published a review article and discussed the use of polymer-ceramic nanocomposites for potential applications as humidity sensors. The authors have also discussed about humidity sensors based on SnO_2, TiO_2, CuO and ZnO and cross-linked polymers, which were developed by various researchers in recent years.

Shaukat *et al.* (2021) [102] fabricated and studied the behaviour of a humidity sensor based on a 2D titanium disillicide ($TiSi_2$) material towards changes in relative humidity. The $TiSi_2$ powder was exfoliated into nanoflakes using the mechanical exfoliation method. The sensor showed a linear variation over the whole relative humidity range from 0 – 100 %, and a fast and stable response behaviour with impedance sensitivity of 63 kΩ/%RH at 1 kHz.

Strikha *et al.* (2000) [14] performed capacitive-voltage (C-V) and current-voltage (I-V) measurements on a multilayer material consisting of a Ti thin layer (20-30 nm) on a porous silicon one. They observed an increase of 5 to 10 % in conductivity and capacity values at frequencies greater than 10 kHz in response to the moisture change from 0 to 50 %.

Bai *et al.* (2014) [103] studied the physical, chemical, optical, photovoltaic and electrical properties of titanium dioxide (TiO_2) nanomaterials and their application in the sensor industry for detection of gases like H_2, O_2, CO, H_2O and volatile organic compounds (VOCs). The authors concluded that in order to develop efficient sensors with high accuracy, precision, reproducibility, low detection limits and long life. It is necessary to optimize the properties and microstructure of TiO_2 based materials.

Farzaneh *et al.* (2019) [104] performed humidity sensing studies of TiO_2 and Cu doped TiO_2. These sensors were fabricated by the sol-gel process. The authors concluded that the optical

band gap of TiO_2 films decreased with the increase in Cu content in the films. The Cu-doped sensor showed better sensitivity and high repeatability in the relative humidity range from 30 to 70 % when compared to the undoped one.

Au *et al.* (2011) [100] studied the performance of virgin Si and Si-Cu-based composite nanorods for anodes of Li-ion rechargeable batteries. Si nanorods resulted in a higher anodic capacity of 1500 $mAhg^{-1}$, but the capacity diminished after 50 cycles due to morphological changes and pulverisation resulting from the brittle nature of silicon. The addition of 70 % Cu to Si-nanorods demonstrated a capacity of 500 $mAhg^{-1}$ for 100 cycles, attributed to the flexibility and improved toughness of Si-Cu composite nanorods.

Ali *et al.* (2017) [12] studied the sensitivity of porous silicon and porous silicon with surfaces modified with Cu (acting as a catalyst). Pore structures in porous silicon with a very small amount of Cu improved the sensitivity of the pores towards NO_2 gas by more than 60,000 %. This sensor was tested at higher temperatures and had performed quite well up to 250 °C.

Horzum et al. (2011) [105] analysed ZnO-based fibers prepared by electrospinning for humidity sensing applications. The resistance of the ZnO-based fiber sensors decreased to about four orders of magnitude with increasing relative humidity from 10 % to 90 % RH. The sensor had fast recovery and response times of 0.5 and 1.5 seconds, respectively. These results also showed that the ZnO-based fibers are promising candidates for humidity sensing applications at room temperature. Different processing techniques such screen-printing, sol-gel process, and oxalate route have been used for the production of these sensors [106–108].

Based on the state of the art, we can conclude that porous silicon provides a wide range of properties and the incorporation of tin to *p*-Si helps in stabilising the system by the formation of interpenetrating microstructure. The use of the Si-Sn system as a potential material for humidity sensing applications is scarcely mentioned in the literature. The addition of different transition metals (Ti, Cu, and Zn) as dopant elements to the Si-Sn system provides better structural stability to Si along with the assistance to the formation of pores geometrically suitable for sensing-based mechanisms. Consequently, the aim of this research work was to fabricate the mesoporous Si-Sn and Si-Sn-X (X = Ti, Cu, and Zn) alloy systems using two distinct non-equilibrium manufacturing techniques of radio-frequency magnetron sputtering and mechanical alloying; and to investigate the correlation between the structure, morphology, chemical composition, and mechanical properties to the electrical response towards changes in relative humidity.

CHAPTER 3:

Experimental Details

This chapter describes the introductory notions and principles of the experimental and characterisation techniques employed in the thesis, as well as the main experimental parameters used in each of them. The first section of this chapter describes the two manufacturing techniques used in the thesis. The fabrication of the Si-Sn and Si-Sn-X (X = Ti, Cu, and Zn) alloys was performed under non-equilibrium conditions using: (a) RF-magnetron sputtering for co-deposition of thin films and (b) high energy mechanical alloying of powders followed by compaction and sintering. The second section of this chapter contains the theoretical and fundamental background of the structural, morphological, chemical, mechanical, and electrical characterisation techniques used in this work.

3.1 Alloy Preparation

As mentioned, the Si-Sn and Si-Sn-X (X = Ti, Cu, and Zn) alloy systems were synthesised using two different non-equilibrium processes: magnetron sputtering and high-energy mechanical alloying.

3.1.1 Magnetron sputtering

Sputter deposition is one of the most important physical vapour deposition (PVD) methods, along with thermal evaporation, arc vapour deposition, and ion plating. Generally, PVD processes are used for the production of thin monolithic or multilayer films [109].

Sputtering involves the physical vaporisation of atoms from the surface of the target (cathode) to the substrate holder (anode) in a vacuum or controlled environment. Atoms from the target are physically ejected by the momentum transfer resulting from the bombardment of energised atomic-sized particles. These particles are generally gaseous ions that get accelerated by plasma. Argon (Ar) is the commonly used inert gas for sputter deposition since it is heavier than Neon (Ne); it helps to increase the sputtering rates and is way cheaper than other heavier inert gases like Krypton (Kr) or Xenon (Xe). The target-to-substrate distance (TSD) is typically 50-150 mm [110,111].

Magnetron sputtering was developed to overcome some of the limitations of the sputtering process. Magnetron sputtering uses a magnetic field parallel to the target, to capture secondary electrons coming from the target during the bombardment of Ar^+ ions. This magnetic field helps keep these electrons in the vicinity of the target, increasing the plasma density closer to the target. Magnetron sputtering helps in increasing the sputtering rates and yields. There are some more advantages of magnetron sputtering, like less heating of the target, maintaining plasma at relatively low voltages and pressures, and better control of the growth and properties of the films [112].

However, when dealing with an insulating target for depositions, it may act as a capacitor for direct-current (DC) supply, resulting in the surface charge-up. Electrons cannot compensate for the charge of positive ions impinging on the non-conductive surface from the power supply.

Radio-frequency (RF) magnetron sputtering is a technique that involves an alternating electrical current in a vacuum at frequencies typically at around 13.56 MHz. Compared to DC magnetron sputtering, it avoids any charge building up, for certain types of sputtering target materials and removes the arcing as cleaning is done with each cycle. The plasma in an RF system

tends to diffuse throughout the entire chamber rather than concentrating around the target (cathode) [113].

In the present work, Si-Sn and Si-Sn-X (X = Ti, Cu, and Zn) alloys were deposited using an RF magnetron sputtering in an Edwards E306A equipment (Edwards vacuum, Burgess Hill, UK). The whole setup for this deposition equipment is mainly composed of a deposition chamber, three RF power sources, a vacuum system, a gas flow controller, and a control unit. Two RF power sources (ENI OEM 12-05 from ENI Power Systems, Inc., and Hüttinger PFG1000 from Hüttinger Elektronik GmbH+Co) with maximum powers output of 1250 W and 1000 W, respectively, were used. These were connected to two magnetrons through matching networks for the co-sputtering from the two cathode targets (Si and Sn). A third RF power source was used (ENI OEM 6AM from ENI Power Systems, Inc.), with a maximum power output of 750 W. This was connected to the substrate holder to sputter clean the substrates before each deposition. The three power sources were connected to the deposition chamber and operate at a radio frequency of 13.56 MHz. The deposition system is presented in Fig. 12.

The vacuum system comprised a combination of two vacuum pumps: a rotary pump and a turbomolecular pump. The rotary pump is used as a primary pump for roughing and backing, whereas a turbomolecular pump is a secondary pump for high vacuum. It was possible to achieve a base pressure of less than 2 $x10^{-3}$ Pa with this combination.

Figure 12. RF magnetron sputtering equipment used in this work.

The Si-Sn thin films were co-deposited from two polycrystalline single targets (Si with 99.999% purity and Sn with 99.99% purity) targets from Testbourne Ltd. The setup of Si and Sn targets within the deposition chamber is shown in Fig. 13 (a). The deposition of the Si-Sn-X (X

= Ti, Cu, and Zn) thin films was done by co-sputtering of the Si and Sn targets, with pellets (5 mm x 5 mm x 0.15 mm) of the dopant elements placed onto the erosion zone of the Si target as shown in Fig. 13 (b). The pellets of Ti (99.9% purity), Cu (99.9% purity), and Zn (99.95% purity) were acquired from Goodfellow. The number of pellets of each dopant element varied from 2 to 25 to obtain films with different chemical compositions.

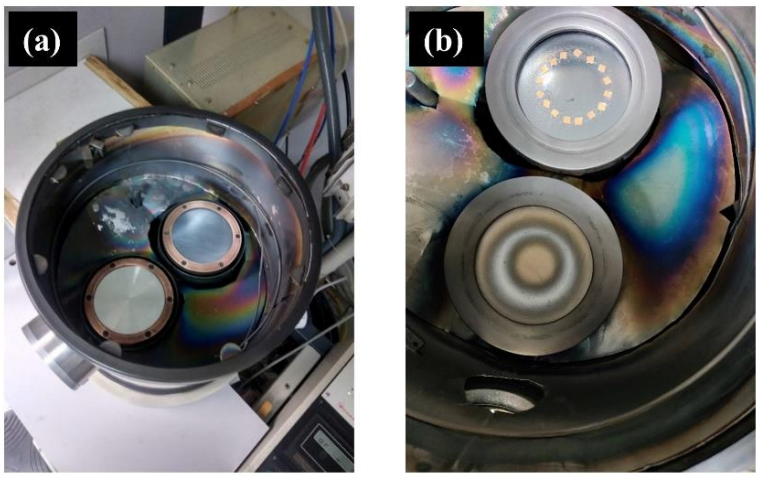

Figure 13. Top view images of the targets and pellets layout for the deposition of the (a) Si-Sn system, (b) Si-Sn-X (X = Ti, Cu, and Zn) system.

Prior to the depositions the chamber was evacuated up to a base pressure of less than 2 $x10^{-3}$ Pa. The depositions were carried out in an argon atmosphere, at two working pressures of 0.6 Pa or 0.7 Pa (low pressure) and 1 Pa (high pressure). The targets and substrates were sputter cleaned before the depositions for 20 and 10 minutes, respectively, to avoid contamination of the films. The deposition parameters along with powers applied to the Si and Sn targets and the number of dopant elements (Ti, Cu, and Zn) pellets are shown in Tables 3 to 6, respectively.

Table 3. Deposition parameters for the deposition of the Si-Sn thin films.

Sample name	**Target power (W)**		**Deposition pressure (Pa)**	**Deposition time (min.)**
	P_{Si}	**P_{Sn}**		
HP_25	400	25	1	60
HP_50	400	50	1	60
HP_75	400	75	1	60
HP_100	400	100	1	60
LP_25	400	25	0.6	60
LP_50	400	50	0.6	60
LP_75	400	75	0.6	60
LP_100	400	100	0.6	60

Table 4. Deposition parameters for the deposition of the Si-Sn-Ti thin films.

Sample name	Target power (W)		Number of Ti- pellets	Deposition pressure (Pa)	Deposition time (min.)
	P_{Si}	P_{Sn}			
S_4	400	50	4	1	60
S_6	400	50	6	1	60
S_8	400	50	8	1	60
S_15	400	40	15	1	60
S_25	400	40	25	1	60
S25-LP	400	40	25	0.7	60
A_8	500	40	8	1	60
A_15	500	40	15	1	60
A_25	500	40	25	1	60
A15-Sn	500	75	15	1	60

Table 5. Deposition parameters for the deposition of the Si-Sn-Cu thin films.

Sample name	Target power (W)		Number of Cu- pellets	Deposition pressure (Pa)	Deposition time (min.)
	P_{Si}	P_{Sn}			
HP_2	200	40	2	1	120
HP_4	200	35	4	1	120
HP_8	200	35	8	1	120
HP_16	200	30	16	1	120
LP_2	200	30	2	0.7	120
LP_4	200	35	4	0.7	120
LP_8	200	35	8	0.7	120
LP_16	200	30	16	0.7	120

Table 6. Deposition parameters for the deposition of the Si-Sn-Zn thin films.

Sample name	Target power (W)		Number of Zn-pellets	Deposition pressure (Pa)	Deposition time (min.)
	P_{Si}	P_{Sn}			
HP_2	200	35	2	1	120
HP_4	200	35	4	1	120
HP_8	200	35	8	1	120
HP_16	200	35	16	1	120
LP_2	200	35	2	0.7	120
LP_4	200	35	4	0.7	120
LP_8	200	35	8	0.7	120
LP_16	200	35	16	0.7	120

The applied silicon-to-tin power ratio was kept constant for all the studied systems. The substrate holder rotated at a speed of 30 rpm to attain films homogeneity. The distance between substrates and targets was set to 60 mm for all depositions. The thin films were deposited on various substrates for the different kind of analysis. Si-wafers with (100) and (111) orientations, and carbon-coated Cu grids. All the substrates were ultrasonically cleaned in acetone and ethanol for 10 minutes each before mounting them onto the substrate holder using a conductive silver paint (SPI # 05002-AB).

3.1.2 High energy mechanical alloying

High energy mechanical alloying (HEMA) or just mechanical alloying (MA) is a solid-state powder processing technique that was developed in the 1960s by John S. Benjamin *et al.* [114], at one of the research labs from International Nickel Company (INCO). In the early 1980s, mechanical alloying was recognised as a technique with high potential for producing metastable alloys (supersaturated solid solutions, intermediate and amorphous phases) [115,116].

MA requires individual elemental powders to be alloyed in specific quantities and proportions. This mixture is then milled in a planetary mill at pre-defined milling parameters like the powder to ball weight ratio, speed of rotation (rpm), number of cycles, time of pause between cycles and time of milling. The milling parameters in the MA process play an essential role in defining the final properties of the milled powders [117–119]. The obtained mechanically alloyed powders are usually further compacted by hot or cold consolidation routes with the help of moulds to achieve a bulk shape. In the last process, the formed bulk sample is known as green sample or pellet, which is subsequently sintered to reduce porosity and to acquire specific microstructure and properties. MA has some advantages over other alloying techniques; one of them is that the

powder's dispersion is homogeneous throughout the mixture. Figures 14 (a) and (b) shows the primary MA mechanism and planetary motion of the mill, respectively.

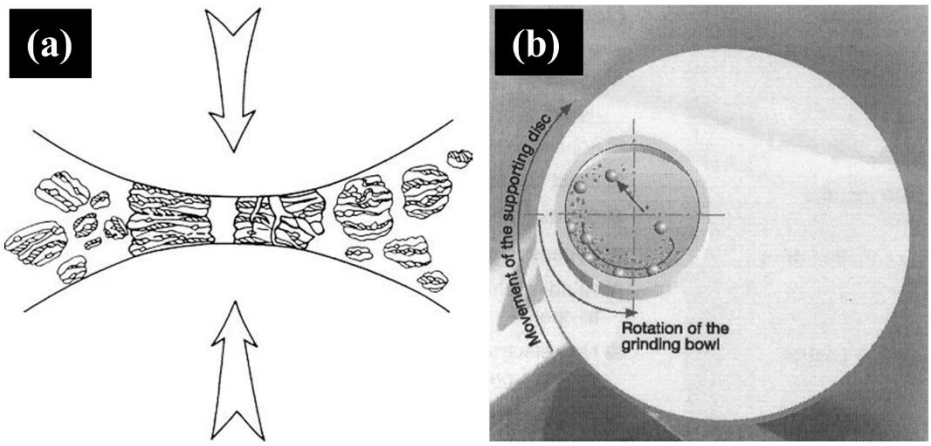

Figure 14. (a) The fracture and welding processes and (b) planetary motion of the mill with powder and ball movements [115,116].

The mechanism of mechanical alloying involves continuous and repeated deformation, fracture, and cold-welding of powder particles. Fracture and welding processes can be controlled for desirable properties and powder particle size requirements during mechanical alloying. This is usually done using process control agents (PCA). In recent years, PCAs (typically in a 1-3 wt.% amount) have been used for the milling of ductile metals where long milling times previously resulted in problems like powder sticking to the vial walls, powder aggregation, and less powder yield [120]. These problems are encountered due to the welding parameter dominating the fracturing one. PCAs act as surface-active agents and are adsorbed on the surface of the particles, which results in the reduction of the welding process. However, they might affect the rate of alloying and therefore, their amount must be carefully selected. There are many PCAs available in the market, out of which some are listed here: stearic acid, hexane, oxalic acid, methanol, ethanol, acetone, heptanes, Nopcowax-22DSP, Toluene, etc.

Elemental powders of Si (99.999% purity), and Sn (99.9% purity) from Testbourne Ltd. and stearic acid (99% purity) from Labospirit Lda were used in this work. HEMA of the powders was performed at room temperature using a Pulverisette 7 planetary micro mill system from Fritsch (Fig. 15 (a)). Cr-tempered steel vials with a capacity of 80 ml, and 2-sets of grinding balls of the same material with 10 mm (10 units) and 5 mm (20 units) of diameter were used. For each run, 5g of the powder mixture and 2 wt.% of stearic acid (0.1g) were placed inside the vial, corresponding to a ball-to-powder ratio of 10:1. Figure 15 (b) shows the top view of the vial with the powders and balls. The rotation speed was 300 rpm. A break of 5 minutes was taken after every 15 minutes of MA to avoid any excessive increase of temperature. For additional safety (to

ensure the temperature check), the vails were opened for 2 hours, after each 4 hours of continuous MA.

Figure 15. (a) Mechanical equipment used for milling (b) top view of the vial with the powder and balls.

For the Si-Sn system, two sets of samples with 4 and 12 hours of milling time at different compositions were milled The milled powders were compacted by using two procedures: (i) cold uniaxial pressing (P = 50 MPa) followed by sintering at 220°C for 3 hours in an electric furnace in an Ar + 5%H_2 atmosphere, and (ii) hot pressing with P = 26 MPa at a temperature of 240°C, for 0.5 hours. Table 7 shows the parameters for the preparation of Si-Sn system using high energy mechanical alloying route.

Table 7. Parameters to produce Si-Sn system using mechanical alloying route.

Sample name	**Content (at. %)**		**Milling time (h)**	**Consolidation process 1**	**Consolidation process 2**
	Si	**Sn**			
$Si_{85}Sn_{15}$- 4 MA	85	15	4	Cold uniaxial compaction (50 MPa), followed by sintering (220°C for 3 hours).	Uniaxial hot pressing (26 MPa, 240°C for 0.5 hours).
$Si_{70}Sn_{30}$- 4 MA	70	30	4		
$Si_{60}Sn_{40}$- 4 MA	60	40	4		
$Si_{85}Sn_{15}$- 12 MA	85	15	12		
$Si_{70}Sn_{30}$- 12 MA	70	30	12		
$Si_{60}Sn_{40}$- 12 MA	60	40	12		

3.2 Characterization of the alloys

The characterisation techniques used in this work and the properties provided by each technique are listed in Table 8.

Table 8. Characterisation techniques used for the evaluation of various properties of the produced materials.

Characterisation technique	**Property**
X-ray diffraction (XRD)	Structure and phase investigation
Scanning electron microscopy (SEM)	Top and cross-sectional morphology
Energy-dispersive spectroscopy (EDS)	Chemical composition
Transmission electron microscopy (TEM)	Morphology, structure, and phase analysis
Atomic force microscopy (AFM)	Surface topography
Mössbauer spectroscopy (MS)	Chemical and structural analysis
Hardness (nano-indentation)	Mechanical
Mercury intrusion porosimetry (MIP)	Pore size distribution
Laser diffraction (LD)	Particle size distribution
Complex impedance spectroscopy (CIS)	Electrical

3.2.1 X-ray diffraction

X-ray diffraction (XRD) is a non-destructive analytical method to identify the nature (crystalline or amorphous structure) and phases of a material that correspond to a specific unit cell dimension and atomic spacing. XRD peaks are produced by constructive interference of a monochromatic x-ray beam scattered from each set of the lattice planes in a sample at specific angles. Conventional XRD equipment is composed of an x-ray source unit, a wavelength-dispersive spectrometer and measuring electronics. The spectrometer and its components are geometrically arranged based on the Bragg-Brentano configuration [121,122].

X-ray diffraction operation is based on x-rays (generated in a cathodic ray tube, which is then filtered and collimated to produce monochromatic concentrated radiation) that interact with the sample in a range of 2θ angle, which is being diffracted and collected by a detector. Bragg's Law defines the diffraction of x-rays:

$$n\lambda = 2d\,sin\theta \quad (5)$$

Where λ is the wavelength of the x-rays, n is an integer and serves as an order of the reflection, d is the distance perpendicularly measured between pairs of adjacent planes, and θ is

the incidence angle, also known as Bragg angle. Figure 16 shows a schematic for the scattering phenomenon for monochromatic x-rays at an angle of 2θ [123].

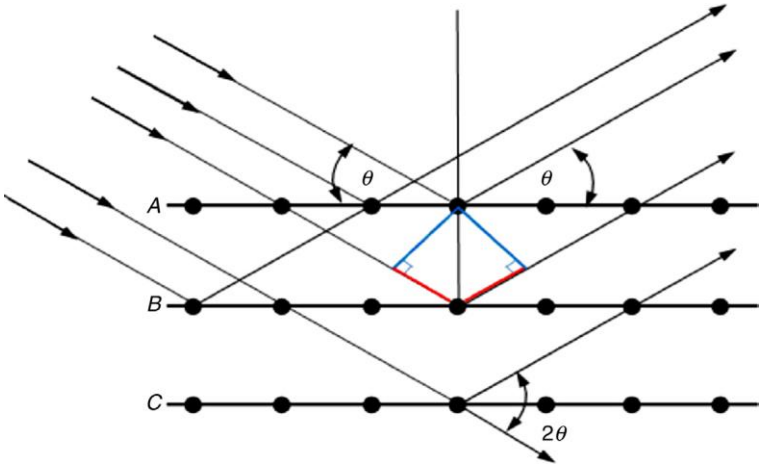

Figure 16. Schematic representation for the deduction of Bragg's law [124].

Each material has a unique atomic structure. Interaction with x-rays causes a constructive and destructive interference of the scattered x-ray beam: this gives origin to a discreet diffraction pattern containing peaks, known as Bragg diffraction peaks. In crystalline materials, the diffraction peaks are well-defined at specific scattering angles. In contrast, in the case of amorphous materials, the diffraction peaks are absent, or, in some cases, the maximum intensity peak extends over several degrees of 2θ. XRD patterns for amorphous and crystalline materials are exhibited in Figs. 17 (a) and (b), respectively.

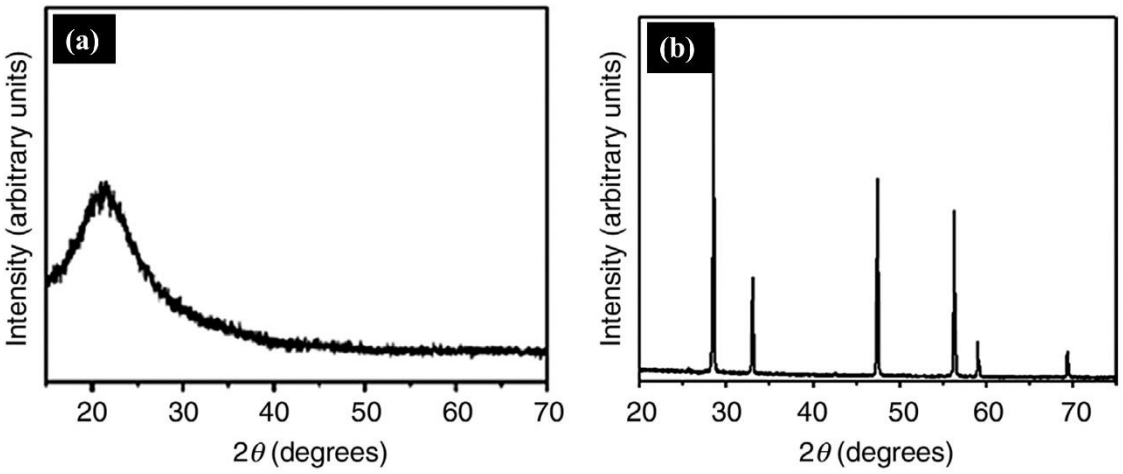

Figure 17. X-ray diffraction patterns of (a) an amorphous and (b) a crystalline material [124].

The position and intensity of the peaks are unique for the crystalline structure of the analysed material. The peak broadening and peak position information from the XRD patterns also allow to determine the crystallite size, degree of crystallinity, micro strain, dislocation density, d-spacing (Å), and lattice parameters.

Williamson-Hall (W-H) method

The imperfection in the crystallinity leads to the broadening of the diffraction peaks. Hence, the broadening of the peak (peak width, β) brings essential information about both the crystallite size (a measure of the size of coherently diffracting domains) and lattice strain (a measure of the distribution of lattice constants arising from crystal imperfections such as dislocations, point defects, grain boundaries, grain boundary triple junctions, or stacking faults) [125,126]. The Williamson-Hall method is an essential method that considers these factors while calculating the crystallite size (D). Consequently, the data of crystallite size obtained from this method is more accurate and reliable [127]. The total peak broadening β_T is given by:

$$\beta_T = \beta_D + \beta_\epsilon \tag{6}$$

where β_D – is the peak broadening due to crystallite size and β_ϵ – is the peak broadening due to micro-strain.

Peak broadening due to crystallite size (β_D) is represented as:

$$\beta_D = \frac{k\lambda}{D\ \cos\theta} \tag{7}$$

Where β_D is the full width at half maximum (FWHM), k = 0.9 (shape factor), λ is the wavelength of the x-ray source, D is the crystallite size, and θ is the peak position in radians.

β_ϵ is given by:

$$\beta_\epsilon = 4\,\epsilon \tan\theta \tag{8}$$

where ϵ is the strain and θ is the again peak position in radians.

Substituting values from equations (7) and (8) to equation (6) results in

$$\beta_T = \frac{k\lambda}{D\ cos\,\theta} + 4\,\epsilon\, tan\,\theta \tag{9}$$

Here, multiplying both the sides of equation (9) by cos θ the following equation is obtained:

$$\beta_T \cos\theta = \frac{k\lambda}{D} + 4\,\epsilon \sin\theta \tag{10}$$

or,

$$\beta_T \cos\theta = \epsilon\,(4\sin\theta) + \frac{k\lambda}{D} \tag{11}$$

Here, equation (11) can be compared with first degree linear form (y = mx + c), where y = $\beta_T \cos\theta$, x = 4 $\sin\theta$, m is the slope equal to ϵ, and c is the intercept = $\frac{k\lambda}{D}$.

Micro strain (ϵ) and crystallite size (D) are calculated by plotting the graph known as Williamson-Hall (W-H) plot. Figure 18 shows the W-H plots from two samples as a reference for the calculations.

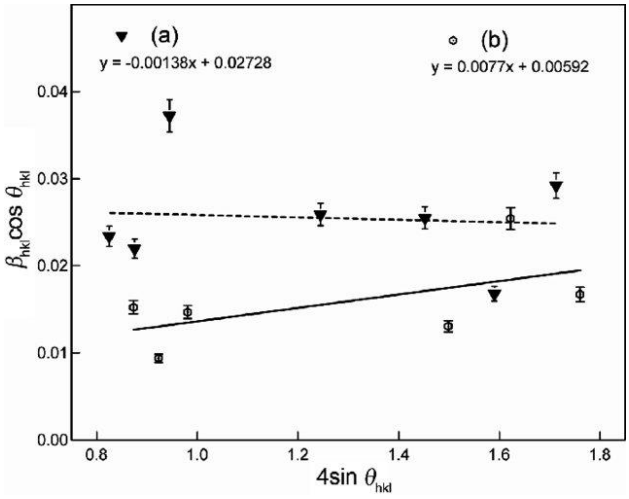

Figure 18. Graphical representation of W-H plots from two samples (a) and (b) [128].

X-ray peak profile analysis method

X-ray peak profile analysis (XPPA) method calculates the degree of crystallinity (χ_c) from XRD data. The peak's intensity is related to the degree of crystallinity on the x-ray diffractograms. Generally, when the degree of crystallinity is low, there are no crystalline peaks and vice-versa [129].

Based on this principle, χ_c is defined and calculated using the area under the crystalline peaks of diffraction, A_c, and the area of amorphous peaks of diffraction, A_a [129]. The equation for the determination of the degree of crystallinity is:

$$\chi_c = \left(\frac{A_c}{A_c + A_a}\right) 100 \qquad (12)$$

The x-ray diffraction (XRD) analysis was performed by means of a PANalytical X'Pert PRO MPD (Fig. 19) using Cu Kα radiation (λ = 0.15406 nm) in both the conventional θ-2θ and grazing (2θ) modes. The x-ray tube voltage and current were fixed at 45 kV and 40 mA, respectively. The acquisitions were performed in the 2θ range from 20 to 90°, with a step size of 0.025° and a time per step of 6 seconds.

Figure 19. XRD equipment used for structural analysis of the samples.

The XRD patterns were analysed with a HighScore X'Pert software, and patterns were confirmed by the ICDD (International Centre for Diffraction Data) standards. Origin software was used to calculate the full-width half maximum values, β (FWHM) of the diffraction peaks, needed for the estimation of crystallite size (D) and the degree of crystallinity (χ_c), by the Williamson-Hall (W-H) plot, and x-ray peak profile analysis (XPPA) methods, respectively.

3.2.2 Scanning Electron Microscopy

Scanning electron microscopy (SEM) is performed by a focused, high-energy beam of electrons in the raster pattern, allowing for scanning of the samples. The SEM technique helps understand the surface morphology, the topography of the features [130].

SEM was invented by Manfred von Ardenne in 1937 (Germany). The high energy electrons interact with the surface features in different ways, producing various signals that contain information about the surface. These are secondary electron (SE) signals, back-scattered electrons (BSE), characteristic x-rays, light (CL, cathodoluminescence) and transmitted electrons. Figure 20 shows the different electron interactions with surface features and produced signals.

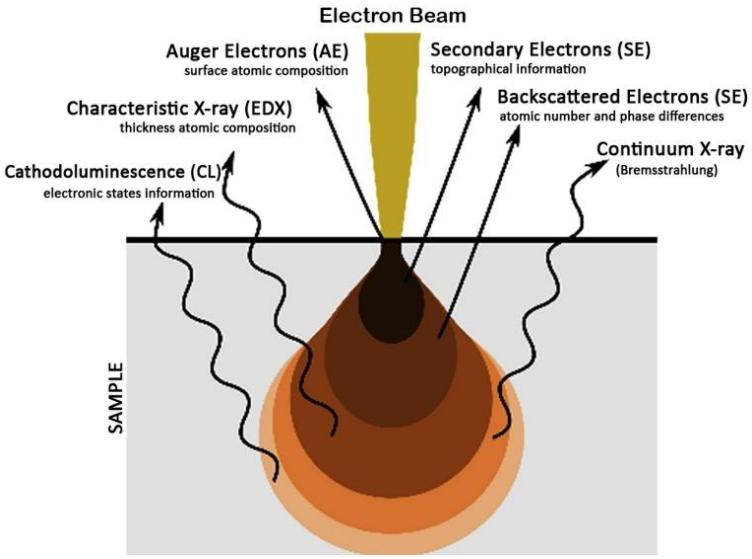

Figure 20. Electron-beam interaction resulting in various signals [131].

To identify and understand the morphology, specific detectors are used. SEM returns a magnified image, also known as an SEM micrograph. In a standard SEM microscope, secondary electrons (SE) are used for producing a magnified image (resolution up to 10 nm).

Energy-dispersive X-ray spectroscopy

Energy-dispersive X-ray spectroscopy (EDS or EDX) is a chemical analytical technique that is usually attached to SEM equipment and allows to determine the chemical composition of a sample. EDS is based on the interaction of a high beam of electrons with the sample surface for emission of characteristic x-rays, which are later compared with emission peaks standards to identify the chemical composition [132]. Figure 21 shows a scanning electron microscope equipped with an EDX detector.

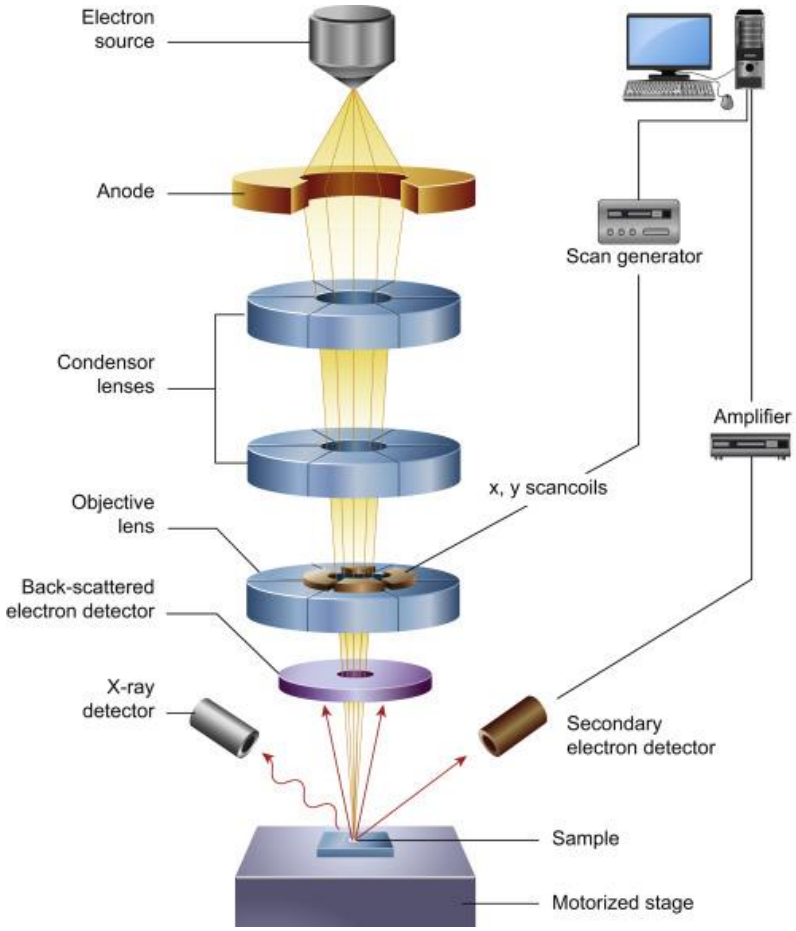

Figure 21. Schematic of a scanning electron microscope with an EDS detector [133].

The morphological characterisation and the measurement of the thickness of the samples (thin films, powders, and pellets) were done using a scanning electron microscope (SEM) from Zeiss Merlin (Gemini 2). The chemical composition of the samples was assessed using an EDS equipment) from Oxford X-Max^N 20 attached to the SEM instrument. To analyse the chemical composition of the thin films, a low beam voltage (6 kV) was used to avoid the substrate's influence. The data was analysed using AZtec software from Oxford Instruments. EDS elemental mapping was also performed for some samples. Figure 22 shows the setup of SEM-EDS used in this work.

Figure 22. SEM-EDS setup used in this work.

3.2.3 Transmission Electron Microscopy

Transmission electron microscopy (TEM) is a technique in which an electron beam passes through an ultra-thin specimen, giving origin to the formation of an image resulting from the interaction of the electrons and the sample. The image is then magnified and focussed. The obtained TEM images can be structurally analysed and observed at an atomic level. The transmission electron microscope was invented in 1931 (Germany) by Max Knoll and Ernst Ruska, which was awarded the Nobel Prize in Physics in 1986. Based on the interaction between the electrons and the sample, TEM can have multiple operating modes: imaging, scanning, diffraction, spectroscopy or even a combination of the previous modes [134].

High-resolution transmission electron microscopy (HR-TEM) is a powerful imaging mode of TEM that enables the visualisation of crystallographic structure and the individual atoms of a sample. HR-TEM is usually employed to study the nanoparticle's shape, size, and crystallographic structure and nanocrystalline features in amorphous or quasi-amorphous films, in nanofibers and other porous materials. Selected area electron diffraction (SAED) mode allows us to understand the crystallographic structure of nanoparticles. SAED patterns consisting of broad rings mean amorphous nature. In contrast, SAED pattern consisting of diffraction spots and rings, correspond to crystalline structure. Figure 23 shows the schematic of a TEM with its components.

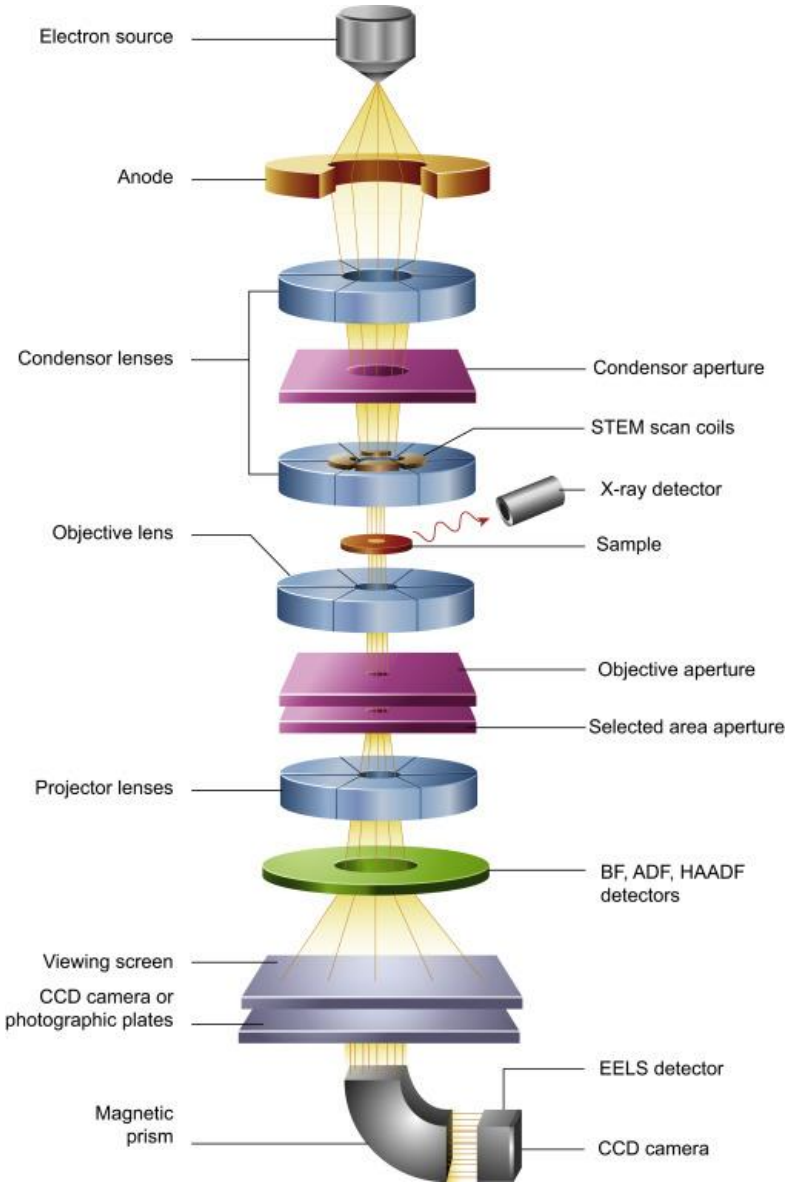

Figure 23. Schematic of a transmission electron microscope [133].

High-resolution transmission electron microscopy (HRTEM) was performed using a JEOL JEM-2100 200 kV equipment (Fig. 24) with a lanthanum hexaboride (LaB_6) filament as electrons source. The thin films for TEM analysis had 30-50 nm of thickness and were deposited on Cu-coated carbon grids for 2-3 min. High resolution (HRTEM) imaging mode and selected area electron diffraction (SAED) modes were used to generate high-resolution images and crystallographic patterns, respectively. The SAED patterns were analysed with the use of the ICDD standards.

Figure 24. Transmission electron microscope used in this work.

3.2.4 Mössbauer spectroscopy

Mössbauer spectroscopy (MS) is a nuclear spectroscopy technique based on the Mössbauer effect, discovered by Rudolf Mössbauer in 1957. It consists of recoil-free, resonant adsorption and emission of gamma rays (γ-rays) in solids: therefore, sometimes, this technique is also referred to as Gamma rays resonance spectroscopy. Most of the Mössbauer spectra are taken in transmission mode. In Mössbauer spectroscopy, a source of gamma rays moves over a range of velocities using a linear motor to observe the Doppler effect [135]. Simultaneously, the radiations transmitted from the absorber (sample) are recorded as a function of the source velocity. The resulting spectrum is plotted as gamma-ray intensity vs function of the source velocity. At velocities that correspond to the resonant energy levels of the sample, a fraction of the gamma rays are absorbed, and a sudden drop in the intensity is observed in the spectrum, in the form of a dip (peaks). In general, nuclear interactions can be of three types: (1) isomer shift (δ), (2) quadrupole splitting (Δ) and (3) magnetic or hyperfine splitting which is also referred to as Zeeman Effect [136]. Different ^{57}Fe Mossbauer spectra are shown in Fig. 25.

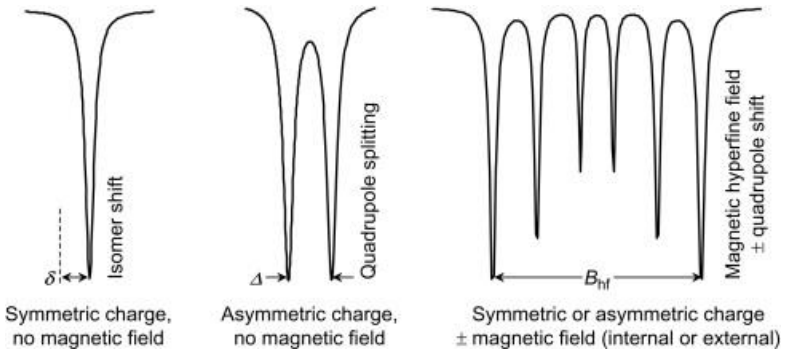

Figure 25. Different ^{57}Fe Mossbauer spectra [136].

Isomer shift corresponds to a shift in the nuclear energy level of the source velocity at which the adsorption is maximum. The shift in the spectra is usually relative to the source or some standard material. Quadrupole splitting occurs only under specific conditions: for instance, when the nuclei of a non-radially symmetric shape (the spin quantum number is greater than 1/2) are immersed in an external field gradient. In Mössbauer spectroscopy, splitting of a state into two is known as a quadrupole-split doublet. Zeeman splitting or hyperfine splitting occurs when the nucleus interacts with any surrounding magnetic field.

The limitation of this method is that the recoilless fraction should be large enough to exhibit measurable Mössbauer effects. Hence, only a few nuclei exhibit the Mössbauer effect, for example, ^{57}Fe, ^{61}Ni, ^{119}Sn, ^{121}Sb, ^{151}Eu and ^{197}Au [137]. The schematic of a Mössbauer spectroscope is shown in Fig. 26.

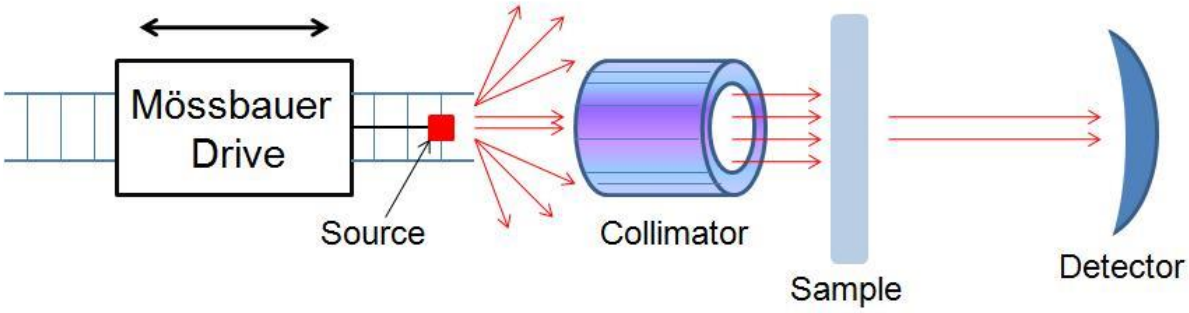

Figure 26. Schematic of Mössbauer spectroscopy.

The Mössbauer spectroscope (standard transmission geometry spectrometer) was equipped with a Janis Cryostat. $Ba^{119m}SnO_3$ (10mCi) that was used as a source and reference for the isomer shift. The velocity scale was calibrated with a 57CoRh source (25mCi) and a metallic iron foil, both at room temperature. The Mössbauer spectroscopy was performed at 77 K because of the lower recoil-free fraction of β-Sn at room temperature.

3.2.5 Atomic force microscopy

Atomic force microscopy (AFM) is a powerful technique that allows quantitative high-resolution imaging to characterise the surface structure with unprecedented accuracy. AFM microscope uses a scanning probe, in which a topographical image with 3D visualisation of the sample surface is produced as a result of its interaction with the tip (probe), and magnifications can go up to 10^7 X (sub-nanometer scale, which is 1000 times better than the optical diffraction limit). AFM is slightly different from conventional imaging microscopes (optical or electron microscopes), where images are formed by focusing light or electrons onto the sample's surface. For AFM measurements, the sharp tip of the probe physically interacts with the sample surface under the influence of atomic forces. It builds an image, considering the height of the features on the sample's surface. This also provides AFM with the exceptional capability to produce high-quality images even for non-conductive surfaces. Besides, and in opposition with other imaging techniques, AFM does not require vacuum to be established. AFM has various spectroscopic imaging modes that can be used depending on the properties of the sample [138].

AFM system is composed of a microscale cantilever with a sharp tip (probe) used to scan the sample surface, a piezoelectric scanner, a laser, and a 4-quadrant photodiode. Typically, the AFM setup is supported on a vibration isolation platform to reduce the noise from the environment and enhance the resolution of the AFM images. Figure 27 shows an atomic force microscope and its components.

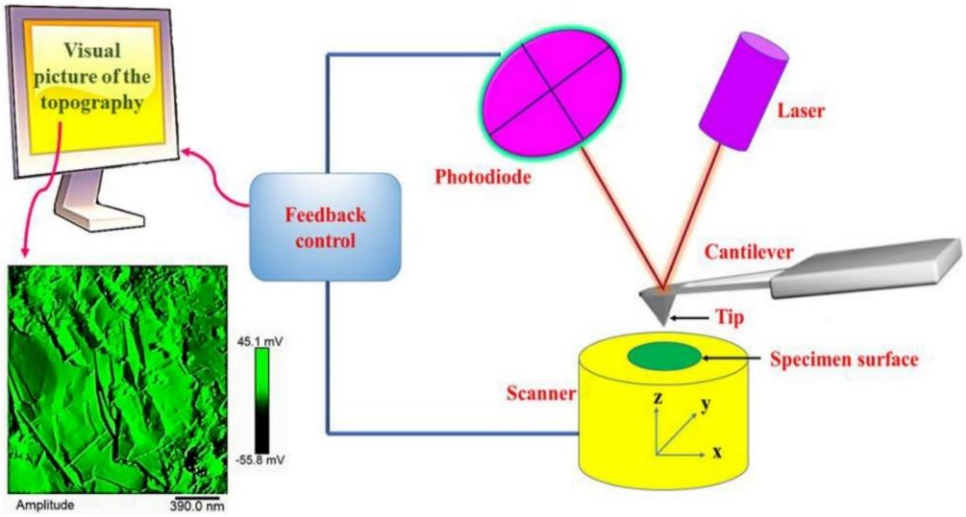

Figure 27. Schematic of an AFM and its components [139].

The cantilever is usually made up of silicon or silicon nitride, the tip radius of curvature is in the order of nanometres. When the cantilever tip comes very close to the surface, the interaction results in attractive and repulsive forces, which may cause a negative or positive bending of the cantilever. This bending is detected with the help of a laser beam. The cantilever

can be thought of as a spring. The quantity of the generated force between the tip and the surface depends on the cantilever's spring constant (stiffness) and the distance between the tip and the surface. This force can be identified using Hooke's Law. As the tip travels across the surface, it moves up and down according to the features of the surface. These displacements are analysed, and a topographical 3D representation (image) of the surface features is obtained.

Depending upon the specific application, AFM can operate in different modes for imaging the surface (i.e., determining the roughness and topography of the sample surface at the nanoscale level). Generally, these modes are classified into three main categories: contact, non-contact, and intermittent contact mode [140]. Figure 28 shows the force regimes during these modes.

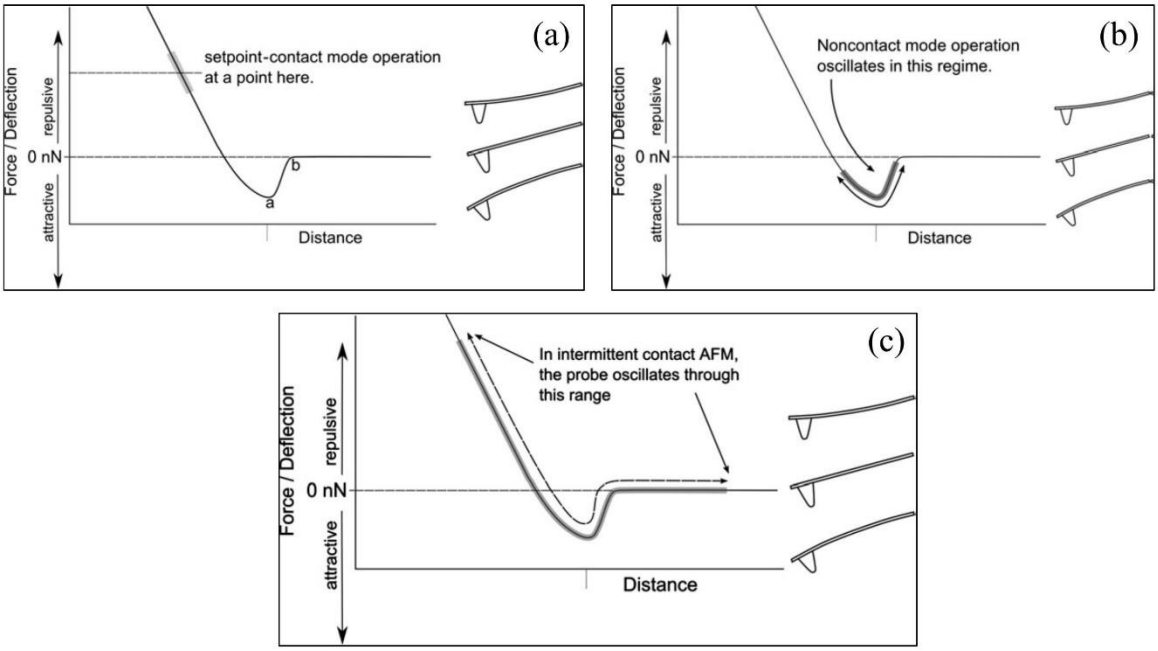

Figure 28. Operating regimes of forces for AFM (a) contact mode: repulsive regime, (b) non-contact mode: attractive regime, and (c) intermittent contact mode: repulsive to attractive regime [141].

In contact mode, the tip of the cantilever is in direct contact (touch) with the surface. Hence, it operates in the repulsive regime of the atomic forces. The resulting force between the tip and the surface is maintained constant during scanning using a feedback control system that maintains a constant deflection. However, continuous contact between the tip and the surface can damage either of the two, which will affect the measurements.

In non-contact mode, the tip of the cantilever does not get in contact with the surface: it simply oscillates at a resonant frequency above the surface during the scan. The oscillation amplitude of the probe is small. Here, AFM operates in the attractive regime of atomic forces.

When the oscillating probe approaches the surface, there is a change in the oscillation frequency due to the interaction between the surface and the probe, resulting in the damping of the cantilever oscillation, which reduces the frequency amplitude of the oscillation. A force transducer monitors the changes in the oscillation, while a scanner determines the height, which forms a feedback loop to maintain the probe-sample surface interaction constant. Non-contact mode is generally used for soft materials.

In intermittent contact mode, AFM operates similarly to the non-contact mode, the only difference being the oscillation speed of the probe. In this mode, a large oscillation amplitude results in the interaction between the tip and the surface in-between the zero-force regime, the attractive regime, and the repulsive regime. Once it involves larger forces, the tip or the sample surface can be more easily damaged, but it is easier to implement, making it more attractive than other AFM modes. This mode is more commonly designated as 'tapping mode'. It presents some advantages over the contact and non-contact modes, like the elimination of lateral forces (contact mode) and capillary forces (non-contact mode). Hence, the Intermittent contact mode is more popular and relevant for AFM measurements.

Quantitative analysis from AFM images is done using roughness parameters [142]. The most used statistical parameters for describing the roughness are arithmetic roughness (R_a) and root-mean-squared roughness (R_q or R_{rms}). These parameters define the roughness magnitude, i.e., larger values represent rougher surfaces. They can be determined by employing equations (13) and (14):

$$R_a = \frac{1}{n}\sum_{i=1}^{n} |\gamma_i| \tag{13}$$

$$R_q \; or \; R_{rms} = \sqrt{\frac{1}{n}\sum_{i=1}^{n} (\gamma_i)^2} \tag{14}$$

Where γ_i is the height of the surface feature at each point i, and n is the number of points of the square array.

Topography analysis of the sample surface was performed in a Bruker Innova AFM equipment (Veeco diInnova), using a silicon probe with less than 10 nm of tip radius in the intermittent contact mode. AFM measurements were performed under a controlled atmosphere at room temperature. A vibration isolation platform supports the AFM stage in order to obtain stable images. Figure 29 shows the setup of the AFM used in this work.

Figure 29. AFM equipment used in this work.

The configuration and selection of the operation mode were made using the NanoDrive software of the AFM equipment. The AFM results were analysed and processed using the Gwyddion software. The plane levelling (level data by mean plane subtraction) was performed as the first processing step for all measurements, correcting any misalignment between the sample and the scanner. Polynomial fitting (align rows using various methods) was also performed horizontally to remove the background and obtain a flattened image [142]. After these processing stages, a three-dimensional view of the data is graphed to interpret the surface height features better. For comparison purposes, the function 'shift minimum data value to zero' was used to compare the maximum height of the features between the samples. Statistical roughness for topographical variations on the surface was performed using mean roughness (R_a) and root-mean-square roughness (R_{rms}) as roughness parameters.

3.2.6 Hardness

Hardness is a measure of the resistance of a material to localised plastic deformation. The behaviour of a material under forces (or loads) is very complex; hence, various hardness measurements can be used for different types of materials namely. These measurements are scratch hardness, indentation hardness and rebound hardness. The hardness measurements are also sometimes classified based on the technique used for hardness measurement: macro-, micro-, and nano-scale hardness [143]. The hardness measurements of the thin films are generally performed using depth indentation technique or nanoindentation. In this case, usually the indentation depth does not exceed 50 nm. To obtain such low indentation depths, the applied loads on the indentor are also inside a small range, usually between 0.1 and 100 mN. The principle of this technique is to press a hard tip onto the material surface with a predefined load for some time and then calculate the hardness using penetration depth. The analysis of load vs displacement

curves, following the method from Oliver and Pharr, is used for the calculations of the nanoindentation [144]. A graphical representation of nanoindentation result analysis is shown in Fig. 30.

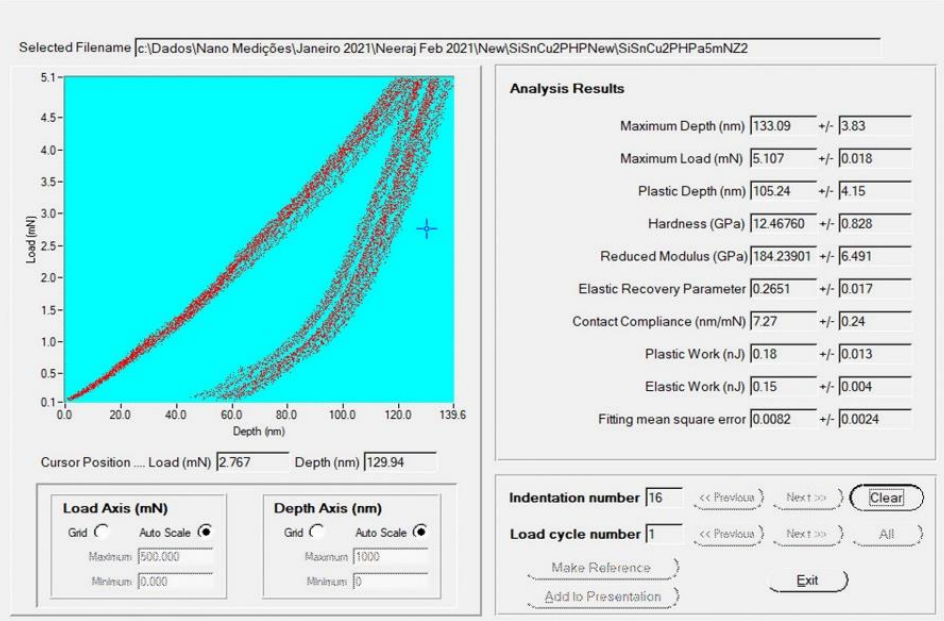

Figure 30. A graphical representation of nanoindentation.

The hardness of the thin films was determined using a MicroMaterialsNano Tester apparatus with a Berkovich diamond indenter using a load-controlled mode and loads of 3 and 5mN. Figure 31 shows the nano hardness tester used in this study.

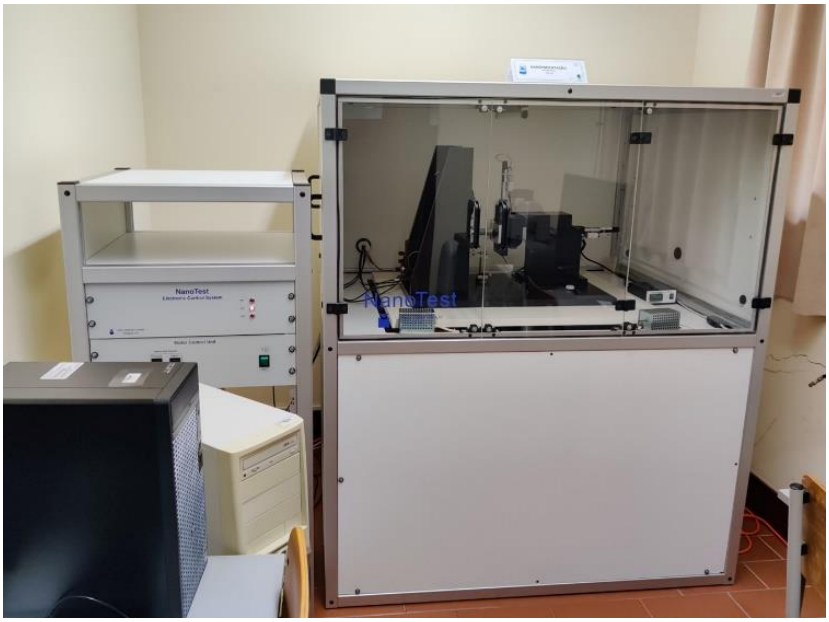

Figure 31. Nano hardness tester used in this work.

The indentation depth was ensured to be less than 10% of the thin film thickness. For statistical analysis, a total of 32 indentations in two different areas (16 tests per area) of the surface

were performed on each sample. The average hardness values were calculated using all measures performed for each thin film sample.

3.2.7 Mercury intrusion porosimetry

Mercury intrusion porosimetry (MIP) is a widely used and well-established technique, allowing characterising a material in terms of its porosity, pore size distribution and volume. The principle of MIP dates back to 1921 when Edward W. Washburn [145] proposed a method to determine the distribution of pore sizes in a porous material by forcing mercury (a non-wetting liquid) to penetrate the capillary pores. The pore size distributions are determined from the volume being intruded by mercury as a function of increasing applied pressure. The relationship between the applied pressure and capillary radius is given by Washburn relationship, equation (15):

$$P = -\frac{4\gamma cos\theta}{d} \tag{15}$$

where P is the applied pressure, γ is the surface tension of the liquid, θ stands for the contact angle, and d represents the diameter of the capillary pore.

MIP is based on the principle that a non-wetting liquid (having a contact angle greater than 90°), generally mercury due to its high surface tension, which does not spontaneously penetrate pores by capillary action, will only intrude the sample pores under external pressure (also known as capillary depression phenomenon). Figure 32 shows the comparison between a wetting and a non-wetting liquid. The required pressure is inversely proportional to the size of the pores, i.e., for the mercury to intrude tiny pores, more considerable pressures are required. Therefore, the volume of mercury that enters the sample surface with each pressure change can be easily calculated, and the volume of pores in the corresponding size class is determined. The instrument used for MIP is a porosimeter that employs a pressurised chamber to force the mercury to intrude into the pores or voids in the sample. As the pressure is applied, mercury starts by filling the larger pores first: then, as the pressure increases, the mercury fills the smaller ones [146,147].

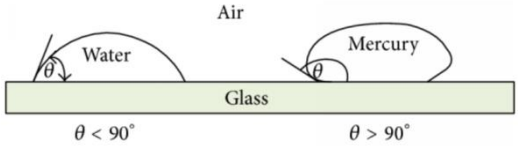

Figure 32. Contact angles for wetting (water) and non-wetting (mercury) liquids.

The volume of mercury intruded into the sample is continuously monitored by a capacitance change sensor located in a metal-clad capillary analytical cell, also known as a penetrometer. Using the pressure versus intrusion data, the instrument generates volume and pore

size distribution curves using the Washburn equation. Hence, accurate measurement of applied pressure is essential for MIP. MIP covers an extensive range of pore sizes, including macro and mesopore ranges. It is possible to characterise capillary pores in the range of 0.005- 10 μm. The total porosity is determined by the total volume intruded by mercury [148]. Schematic of MIP is shown in Fig. 33.

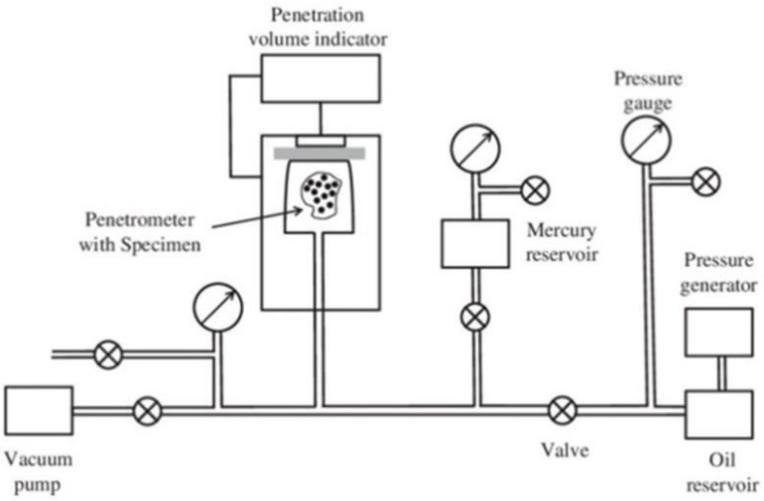

Figure 33. Schematic of mercury intrusion porosimeter [149].

Although the MIP is a widely used technique, it possesses some limitations. For instance, it does not give any information about the geometry of the pores. The whole principle of MIP is based on the fact that the pores are capillaries in nature (i.e., cylindrical). Hence, the technique suffers from the hysteresis phenomenon, i.e., the intrusion and extrusions curves do not fully overlap each other. The latter generally occurs due to the existence of ink-bottle pores: consequently, mercury is not subjected to pore wall interactions during the intrusion; on the contrary, it gets partly or wholly held in pores upon mercury extrusion.

Porosity measurements were performed in an AutoPore IV, model 9500, Microelectronics apparatus. Figure 34 shows the Mercury porosimeter apparatus used in this work.

Figure 34. Mercury intrusion porosimeter used in this work.

The samples were placed inside a penetrometer and degasified to remove gases such as water vapour or contaminants present over the surface or inside the pores. After and under vacuum, the entire chamber is filled with mercury, which is then pushed inside the chamber and forced inside the sample pores under controlled pressure. The pressures applied varied in the range starting from 0.5 to 31000 absolute pressure (psai) in two different ports: low- and high-pressure ports. Mercury contact angle was set to 140°, while mercury surface tension was adjusted to 480.0 dynes/cm. These values were considered for the calculations of pore size and respective distributions, using AutoPore IV 9500 V1.09 software, where the ultimate output generates a graphical distribution of the pore size diameter (μm) versus Log Differential Intrusion (mL/g) curve. Figure 35 shows a MIP curve from one sample as a reference.

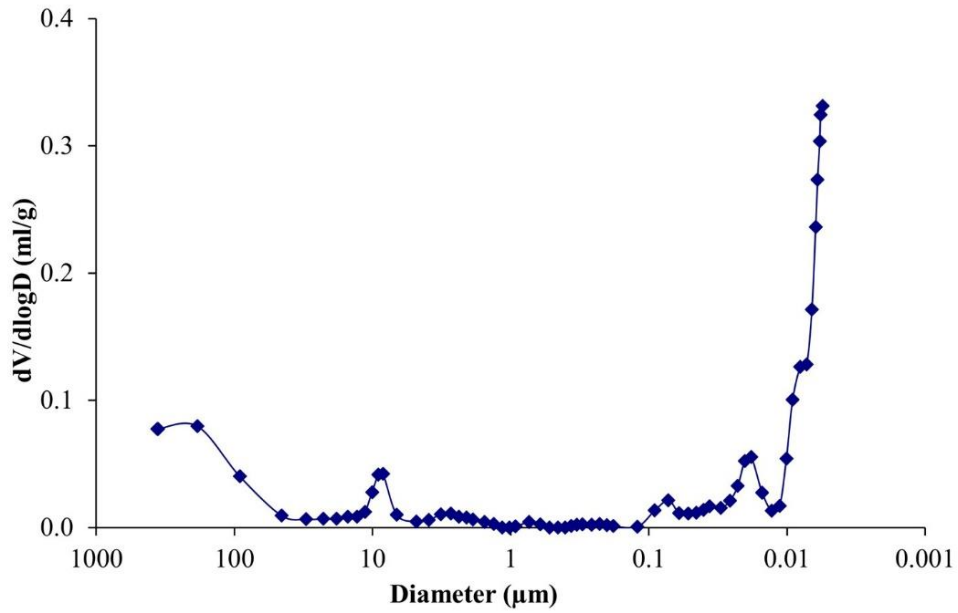

Figure 35. Graphical representation of MIP result as volume versus pore size distribution curve.

3.2.8 Particle size distribution

Particle size distribution (PSD) is a significant property to monitor in the case of powders and granular materials. There are currently various types of equipment available for the determination of PSD. PSD can be done using several methods, out of which sieve analysis and laser diffraction are the most common ones. A sieve shaker consists of a series of sieves in decreasing mesh sizes. The weighted powder is placed on the top sieve, and the whole set-up is agitated in the vertical direction using a mechanical shaker. PSD is calculated using the amounts of powder on each sieve. The laser diffraction (LD) scattering method is used for the determination of particles size and particles size distribution in the range from 20 nm – 2000 µm [150,151]. Laser diffraction analysis is based on the Fraunhofer diffraction theory, which states that the intensity of scattered light by a particle is directly proportional to the size of the particle. Hence, the smaller particles scatter the laser beam at large angles, whereas the larger particles scatter at small angles. The laser diffraction method assumes all the particles to be circular, which is a drawback for this technique. Fig. 36 shows the schematic of the laser diffraction technique for particle size distribution.

Droplet size distribution, volume median diameter (d_{50}) and the span values were evaluated from numerical laser diffraction results. The volume median diameter (d_{50}) value indicates the median particle size i.e., 50 % of the total particles are smaller than this size. Whereas the span quantifies the spread of the droplet size [152].

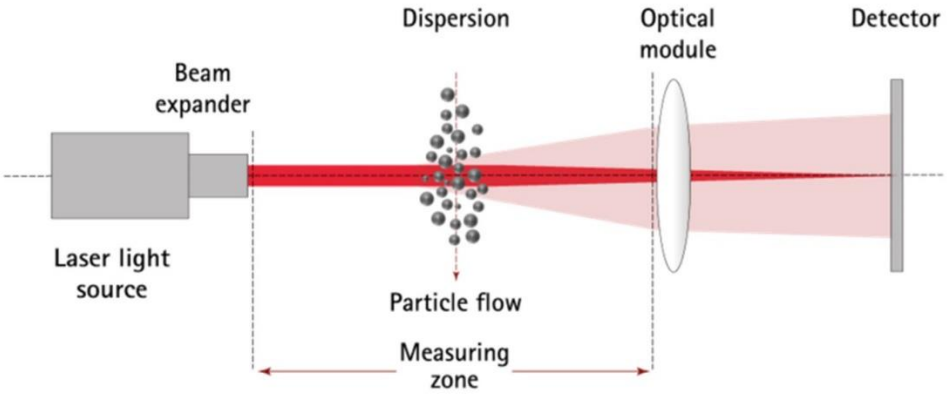

Figure 36. Schematic of laser diffraction for particle size distribution.

The particle size distribution of powder samples (before and after milling) was determined using a Mastersizer 3000 equipment from Malvern (Fig. 37). The operation principle is based on the laser diffraction scattering method. Particle sizes in the range of 0.01 – 3500 μm can be measured using this equipment. This equipment comes with a software tool also developed by Malvern to analyse diffraction data and obtain relevant information concerning particle size distribution like median-diameter (d_{50}) and span (degree of consistency). These parameters are generally used for comparison purposes regarding powders characteristics before and after milling.

Figure 37. Mastersizer 3000 used in this work.

3.2.9 Complex impedance spectroscopy

In an ideal resistor system (where Ohm's law is valid for all current and voltage levels), the electrical resistance is defined as the ability of a circuit element to oppose itself to the electrical

current flow. According to Ohm's law, resistance is defined as the ratio between voltage (V) and current (I):

$$R = \frac{V}{I} \tag{16}$$

However, in real systems, circuit elements exhibit much more complex behaviour and instead of resistance a new element, named Impedance, is used to express circuit performance. Electrochemical impedance is measured by applying an AC sinusoidal current shaped signal to the under-evaluation impedance, using a test cell and by measuring the obtained response, which is in the form of an AC voltage signal containing its excitation frequency and harmonics. Electrochemical Impedance operates typically using a small excitation signal to assure that the cell's response is pseudo-linear. In a linear or pseudo-linear system, the AC response to a sinusoidal current signal will present the same frequency but will be phase-shifted. Figure 38 represents sinusoidal of voltage and current for a linear system with a phase shift of ø.

$$Z(\omega) = \frac{V(\omega)}{I(\omega)} \tag{17}$$

where Z is the impedance, V is the measure voltage, I is the applied current, and ω stands for the angular frequency. (All variables are a function of the applied signal frequency).

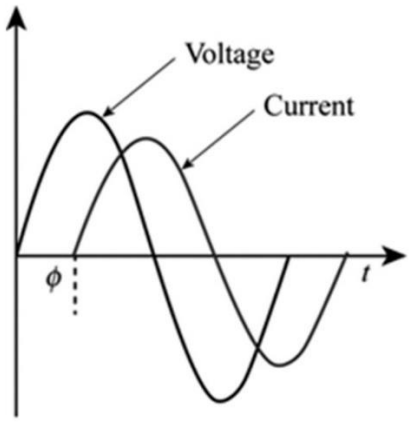

Figure 38. The sinusoidal for applied voltage and response current in a linear system.

The impedance (Z) changes with the applied signal frequency, therefore, it is measured as a function of the frequency being both resistance and reactance of the sample evaluated. Consequently, frequency sweeps are done, and the corresponding impedance is measured at each frequency. This technique is called AC impedance spectroscopy or complex impedance spectroscopy (CIS) [153].

AC impedance is typically measured using a small excitation signal as a function of time:

$$V(t) = V_0 \exp(i\omega t) \quad (18)$$

$$I(t) = I_0 \exp(i\omega t - i\phi) \quad (19)$$

Therefore, from Ohm's law,

$$Z = \frac{V(t)}{I(t)} = \frac{V_0 \exp(i\omega t)}{I_0 \exp(i\omega t - i\phi)} = Z_\circ \exp(i\phi) \quad (20)$$

Using Euler's relationship ($e^{i\phi}$ = cosϕ + i sinϕ),

$$Z = Z_\circ \cos(\phi) + i\{Z_\circ \sin(\phi)\} \quad (21)$$

$$Z = Z' + Z'' \quad (22)$$

where, Z' is equal to $Z_\circ \cos(\phi)$ (Real part of Z), and Z´´ is equal to $i\{Z_\circ sin(\phi)\}$ (Imaginary part of Z).

The complex impedance spectroscopy (CIS) data representation can be done in many ways. The most preferred ones are Nyquist and Bode plots. Figures 39 (a) and (b) shows the typical representation of Nyquist and bode plots, respectively. Sometimes, Nyquist plots are also referred to as Cole-Cole plots [154].

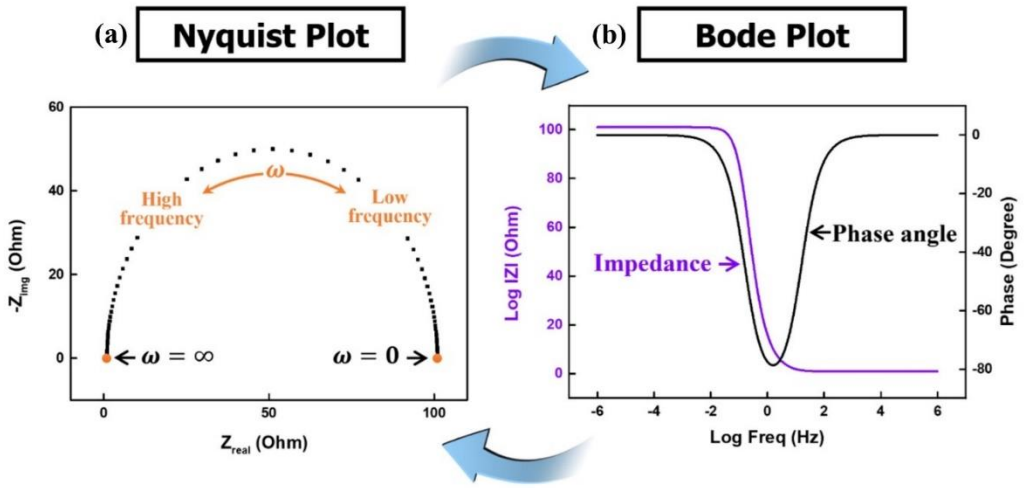

Figure 39. Complex impedance spectroscopy (CIS) representation by (a) Nyquist plot and (b) Bode plot [155].

Nyquist plots were devised by Harry Nyquist. It is defined as a parametric plot of a frequency response of a feedback system, i.e., a complex graphical plot, where the real part of the impedance is plotted in the X-axis and its respective imaginary part on the Y-axis. Bode plots were introduced by Hendrik Wade Bode. In bode plots the response of the system is exhibited as

logarithmic plots of both modulus of impedance, |Z|, and corresponding phase angle, Ø (from 0 to 90), as a function of the frequency. In Nyquist plots, most of the points are located at both ends of the spectrum, whereas in a bode plot, the points are evenly distributed throughout the spectrum.

Nyquist plots are used to design equivalent circuit diagrams with the circuit elements involved in a particular circuit. These equivalent circuits provide essential information about understanding the phenomena's occurring inside the system. Therefore, the significance of complex impedance spectroscopy increases, considering the amount of information it could reveal. Figure 40 depicts some of the Nyquist plots and their equivalent circuit diagrams. Validation of the complex impedance data is also one of the crucial factors before interpretation and modelling for the equivalent circuit. For this purpose, Karmer-Krönig transformations are used.

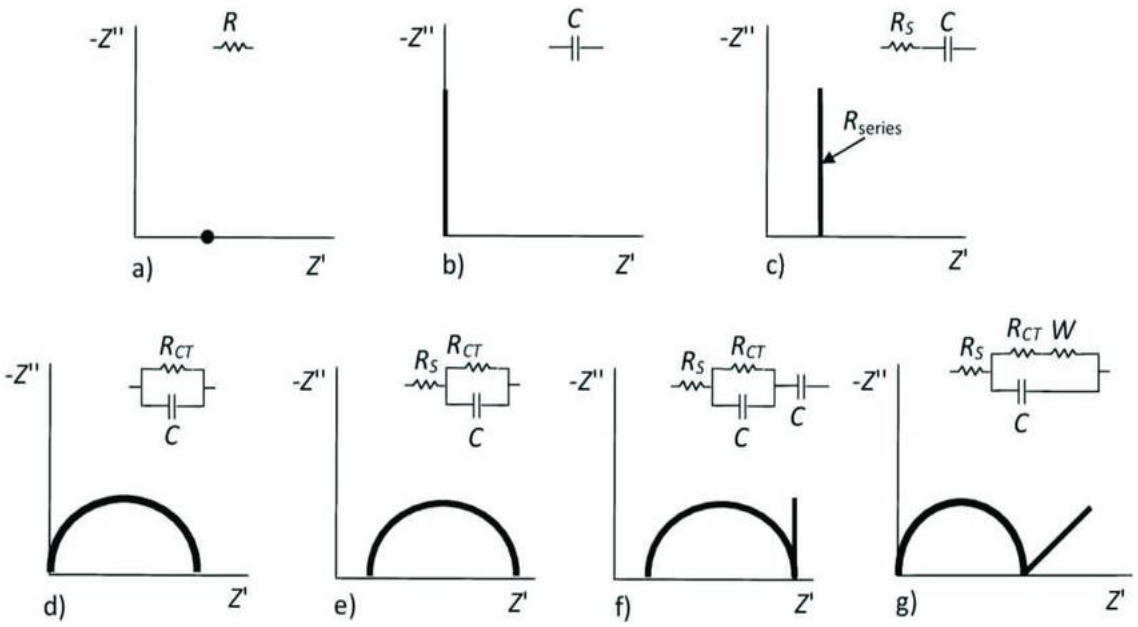

Figure 40. Nyquist plots for some electrochemical systems together with their respective equivalent circuit diagrams [156].

Complex impedance spectroscopy (CIS) was performed on a Precision Impedance Analyser Agilent 4294A from Keysight Technologies. CIS measurements were carried out in the frequency range from 400 Hz to 40 MHz to evaluate the electrical response of the samples towards relative humidity (RH) changes. The measurements were performed inside a closed chamber by varying the relative humidity using synthetic dry air (0% RH) to fully humidified air (100%) with increments of 10% humidity. The different relative humidity values were obtained by mixing water-saturated air, obtained by bubbling synthetic air through the water bubbler and dry synthetic air. Two independent mass flow controllers (MFC) were used to control the volumetric flow of dry and wet air and maintain the ratios for specific RH values. MFCs together with their power

supply used during this work were model 400 from Hastings Instruments. Dry and wet air are mixed inside a mixer before passing tangentially over the sample surface. The schematic of the whole setup for humidity measurements is shown in Fig. 41.

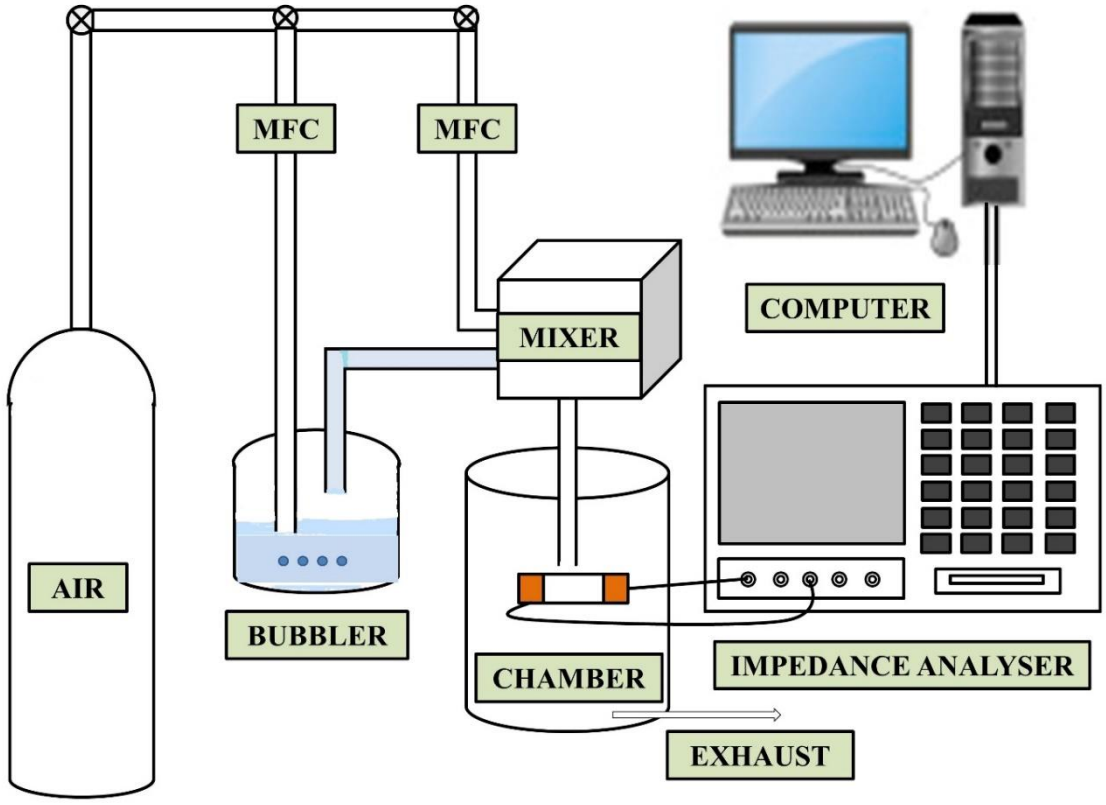

Figure 41. Schematic of setup for RH measurements.

The temperature inside the chamber was controlled to room temperature (25 ± 1ºC) using a Gefran 1000 temperature controller. The volume of the closed chamber was 6.5 litre. Hence, with the 5 litre/hour flow rate of mixed air, each RH value inside the chamber was maintained for 90 minutes before recording the impedance measurements. For impedance measurements, a pair of gold electrodes were printed through a mask onto the surface extremities of each sample, using gold ink from Gwent Group (Gold Polymer Electrode Paste C2041206P2) and heat-treated at 80ºC for 60 min. The complex impedance data validation was ensured by the Agilent equipment since it has inbuilt Kramer-Krönig transformations. All the compositions were studied under humidity tests for Si-Sn and Si-Sn-X (X = Ti, Cu, and Zn) systems. These humidity measurements were also performed 1 and 6 months after the first run to evaluate the stability of humidity sensitivity with respect to time. Two specimens were tested for each sensor, and three measuring runs were performed for each one. Therefore, the values presented correspond to the average of six tests for each sample.

CHAPTER 4: Results and Discussion

4.1. Si-Sn system

This section focuses on the fabrication and characterisation of the Si-Sn alloys prepared using two different manufacturing techniques (a) radio frequency magnetron sputtering and (b) mechanical alloying. The characterisation of each system was done one by one using structural, morphological, chemical, mechanical, and electrical techniques. The electrical response of these samples towards changes in relative humidity (RH) was performed using complex impedance spectroscopy.

The work developed in this chapter resulted in 3 research articles:

- N. Kumar, P. Sanguino, S. Diliberto, P. Faia & B. Trindade, *Tailoring thin mesoporous silicon-tin films by radio-frequency magnetron sputtering*, Thin Solid Films, 704 (2020) 137989, https://doi.org/10.1016/j.tsf.2020.137989. Impact factor: 2.358.

- N. Kumar, M. Evaristo, B. Trindade & P.Faia, *Humidity sensing properties of thin silicon-tin films prepared by magnetron sputtering*, Sensors and Actuators B: Chemical, 321 (2020) 128554, https://doi.org/10.1016/j.snb.2020.128554. Impact factor: 9.221.

- N. Kumar, P. Sanguino, P. Faia & B. Trindade, *Porous Si-Sn alloys produced by mechanical alloying and subsequent consolidation by sintering and hot-pressing*, Materials and Manufacturing Processes, 37 (2) (2022) 169-176, https://doi.org/10.1080/10426914.2021.1967979. Impact factor: 4.783.

4.1.1 Thin Silicon-tin (Si-Sn) films produced by radio frequency magnetron sputtering

(Based on papers "Tailoring thin mesoporous silicon-tin films by radio-frequency magnetron sputtering, Thin Solid Films, 704 (2020) 137989, https://doi.org/10.1016/j.tsf.2020.137989" and "Humidity sensing properties of thin silicon-tin films prepared by magnetron sputtering, Sensors and Actuators B: Chemical, 321 (2020) 128554, https://doi.org/10.1016/j.snb.2020.128554".)

Abstract

Thin $Si_{100-x}Sn_x$ films with $0 < x < 51$ (at.%) have been deposited from Si and Sn targets by radio-frequency magnetron sputtering at vacuum pressures of 1 and 0.6 Pa. The different contents of Sn incorporation were achieved by varying the power applied to the Sn target (25, 50, 75 and 100 W) while maintaining a constant power of 400 W on the silicon target. The results showed that the films deposited at 1 Pa were more porous, in the mesoporous region than the films deposited at 0.6 Pa. For the Sn concentrations lower than 28 %, the films were amorphous. For higher Sn concentrations, the films were formed by a β-Sn nanocrystalline structure embedded in an amorphous matrix. The hardness values decreased with the increase in the Sn content in the films. The electrical response to changes in the relative humidity of the films was evaluated at room temperature by means of complex impedance spectroscopy in the frequency range of 400 Hz - 40 MHz. The results showed that the surface morphology, the level of porosity in the mesoporous region, and the chemical composition of the thin films contributed to the sensor's sensitivity to water vapour. The thin films deposited at a vacuum pressure of 1 Pa presented better sensitivity towards humidity variations than the films deposited at 0.6 Pa. In particular, the thin $Si_{72}Sn_{28}$ film, the best suited for humidity detection, displayed p-type conduction with an almost linear variation of the impedance modulus with the increase in the relative humidity content. Moreover, humidity tests performed 1 and 6 months after the first run revealed that the electrical response of this sensor is quite stable over time.

Deposition parameters for Si-Sn thin films

The RF-magnetron sputtering parameters for the co-deposition of Si-Sn thin films using Si (99.999%) and Sn (99.99%) targets in the Edwards equipment are illustrated in Table 9. Films with the prefix HP on sample names refer to the high-pressure (1 Pa) depositions whereas depositions with LP prefix are low-pressure (0.6 Pa) depositions.

Table 9. Deposition parameters for the formation of Si-Sn thin films.

Sample name	**Target power (W)**		**Deposition pressure (Pa)**	**Deposition time (min.)**
	P_{Si}	P_{Sn}		
HP_25	400	25	1	60
HP_50	400	50	1	60
HP_75	400	75	1	60
HP_100	400	100	1	60
LP_25	400	25	0.6	60
LP_50	400	50	0.6	60
LP_75	400	75	0.6	60
LP_100	400	100	0.6	60

Chemical composition, thickness, and deposition rates

The chemical composition, thickness, and deposition rates for the thin Si-Sn films are shown in Table 10. The thickness of the films was determined by cross-sectional SEM images whereas the chemical composition was obtained by EDS analysis.

Table 10. Chemical composition, thickness, and deposition rates of Si-Sn thin films.

Sample name	**Chemical comp. (at. %)**		**Thickness (µm)**	**Deposition rate (nm/min)**
	Si	**Sn**		
HP_25	92.7	7.3	1.4	22.7
HP_50	72.1	27.9	1.5	20.3
HP_75	60.7	39.3	1.9	31.3
HP_100	48.7	51.3	2.5	41.8
LP_25	85.1	14.9	0.8	13.8
LP_50	70.5	29.5	1.3	21.3
LP_75	57.5	42.5	1.6	27
LP_100	55.0	45.0	1.6	27

Figure 42 shows Si/Sn atomic ratio versus power applied on the tin target for the two deposition pressures. As can be observed, the higher the power applied to the Sn target, the lower is the Si/Sn ratio. This is because a large number of Sn atoms are ejected from the targets at higher powers onto tin targets which eventually increases the density of tin in the thin films as can also be observed from the increase of deposition rates in Table 10. However, the Si/Sn ratios for depositions at 25 W are different for the depositions at HP and LP. This is because Sn is highly prone to contamination by oxygen, also at high pressure, there are more no. of Ar molecules in the deposition chamber hence the energy of Ar^+ ions arriving at the Sn target is lower. This results in the ejection of lower no. of tin atoms from the target as they have higher at. mass of 118.7 a.m.u. (while for Si atomic mass is 28 a.m.u.). The large no. of collisions also decreases the mean free path, and the resultant thin film is having lower Sn content.

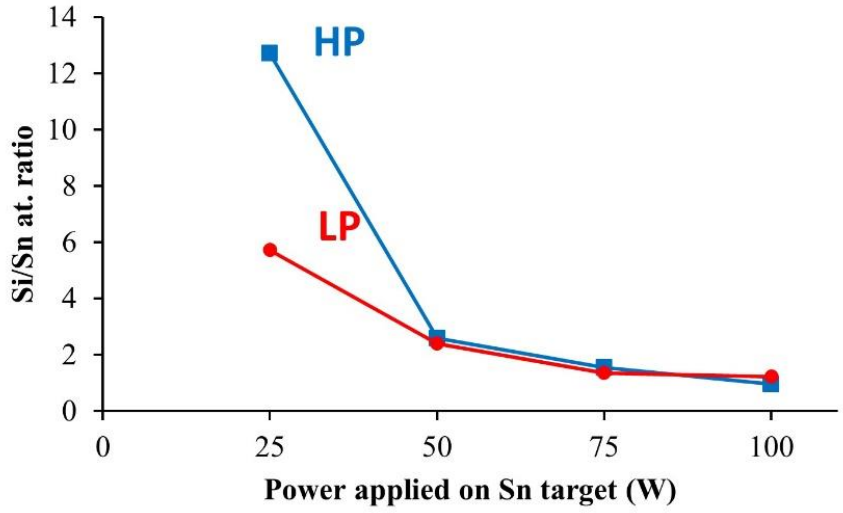

Figure 42. Si/Sn atomic ratio of the high and low pressure deposited thin films as a function of power applied at the Sn target (W).

Figure 43 shows the relationship between the thickness of the films to the power applied on the tin target at different deposition pressures. As expected, the thickness increases with the power applied onto the Sn target for both deposition pressures [157]. However, the thickness of films deposited at HP was always higher than the LP films deposited under the same conditions. Since the deposition pressure affects the sputtering rate in the following two ways: at low pressures, the density of ion current increases as the pressure increases, which leads to the rise of deposition rate. Whereas, at high pressures, the quantity of argon gas molecules is significantly higher, leading to a higher no. of collisions between sputtered atoms and gas molecules. The latter phenomenon reduces the energy of the sputtered atoms and consequently decreases the deposition rate. Here, in these depositions, the increase in the current density of ions dominated over the impact of collisions between ejected atoms and gas molecules [158].

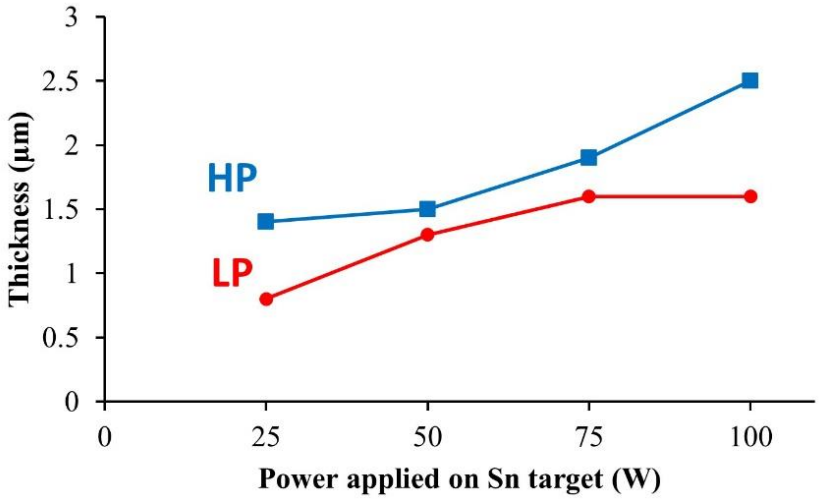

Figure 43. Thickness of the thin films as a function of power applied on the Sn target (W).

Structural, morphological, porosity and mechanical characterisation

Figure 44 shows high magnification images of the surfaces and cross-sections of the Si-Sn thin films obtained by scanning electron microscopy (SEM). The surface morphology images reveal uniform globular features for all the Si-Sn thin films; contrarily, the cross-sectional images show a difference between HP and LP deposited films. The films deposited at HP show a columnar growth of the films with a more porous structure than the thin films deposited at LP, which appear to be more compact. Since the deposition pressure impacts the development of thin films, thereby increasing the deposition pressure, the kinetic energy of Si and Sn atoms (or mean free path) reduces due to the large no. of collisions with argon atoms. Hence, the adatom mobility and the nucleation processes decrease, leading to less dense films with more pores and intergranular voids. To validate these results, the pore size distribution of two samples one from each deposition rate was performed using mercury intrusion porosimetry. Figures 45 and 46 shows the plots of logarithmic differential curves versus pore size distribution for samples HP_50 and LP_50. The mercury intrusion porosimetry analysis shows a higher number of pores, especially in the mesoporous region for sample HP_50 (Fig. 46). The porosity of the films promotes the absorption mechanisms (chemisorption, physisorption and capillary condensation) of water vapour during humidity sensing. The humidity sensitivity response is more reliable with the maximum porosity in the mesoporous region (2 to 50 nm) [159]. The amount of porosity in the mesoporous region was calculated using the Washburn equation [160], which was 3.3 and 1.0 % for the HP_50 and LP_50 films, respectively.

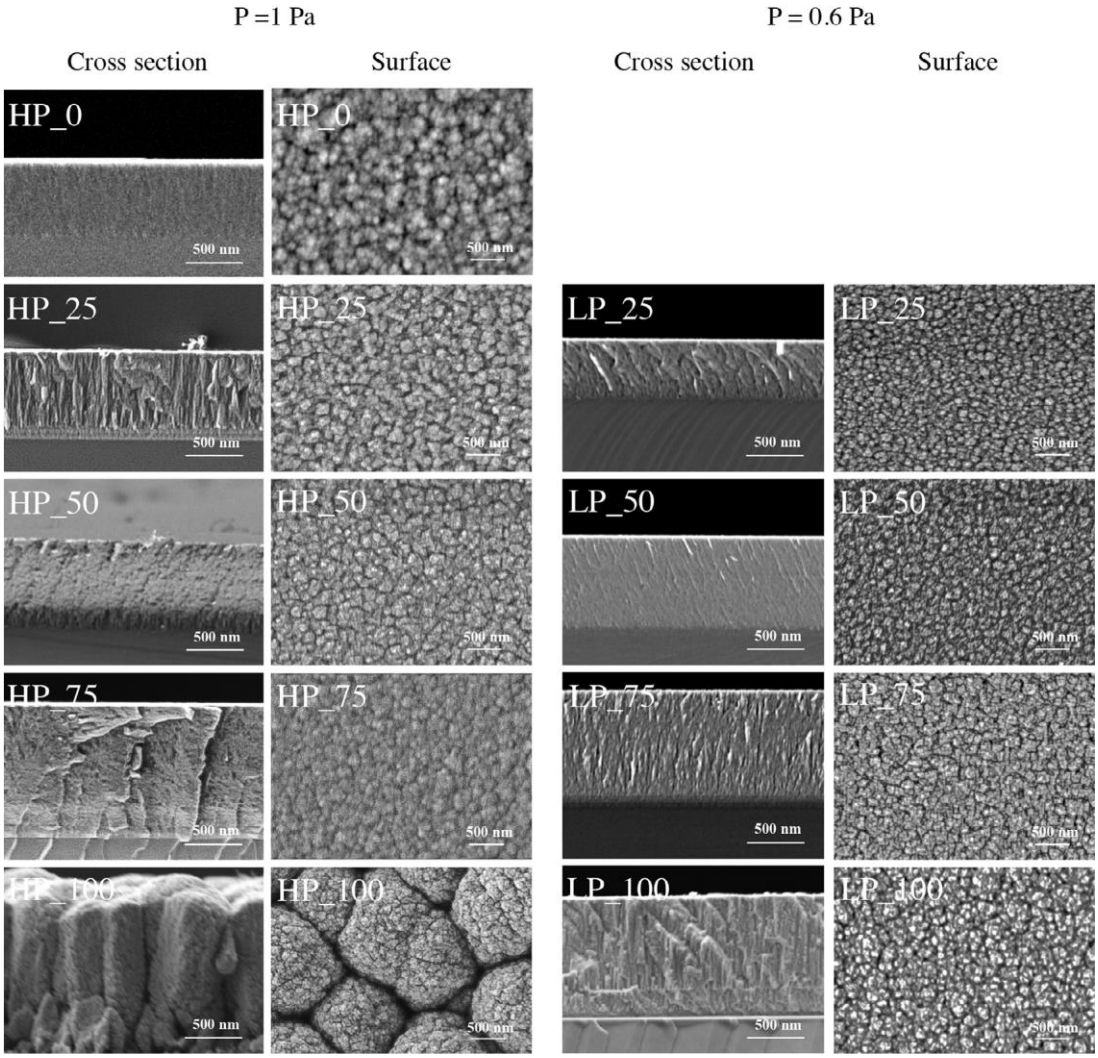

Figure 44. SEM images for surface and a cross-sectional view for Si-Sn thin films deposited at HP and LP.

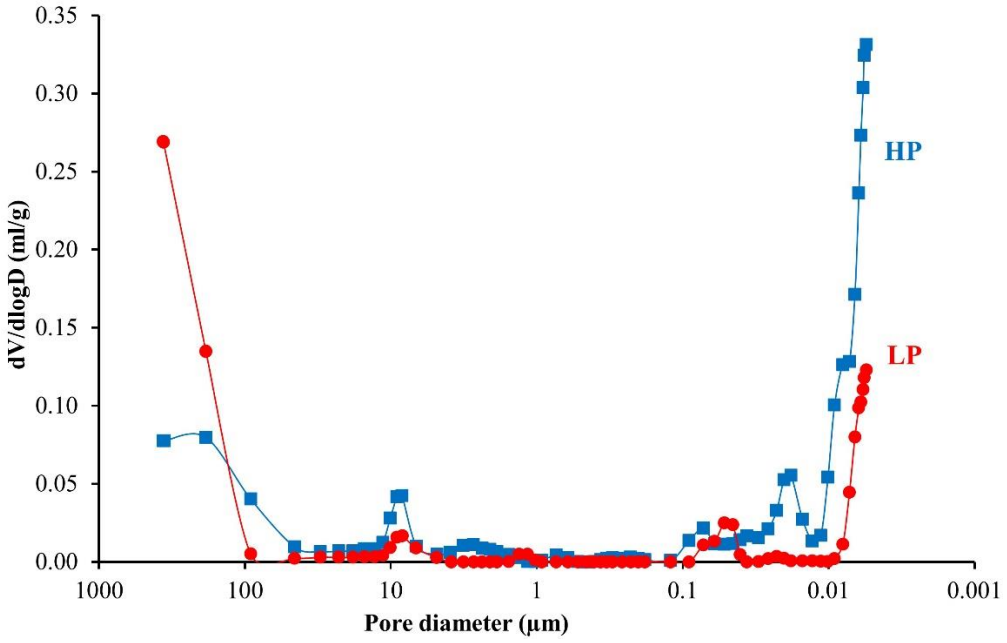

Figure 45. Pore volume versus pore diameter for samples HP_50 and LP_50.

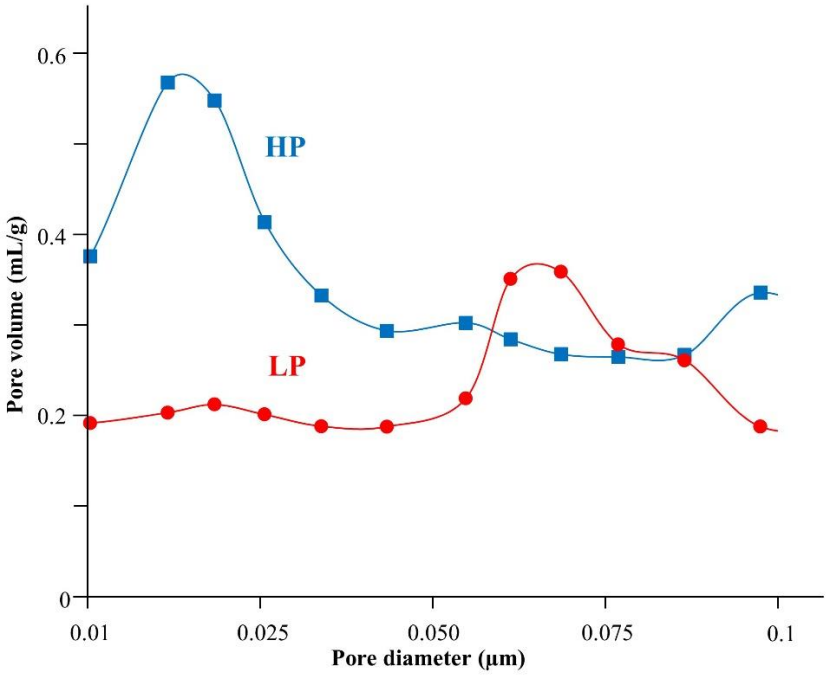

Figure 46. Pore volume versus pore diameter for samples HP_50 and LP_50 in the mesoporous region.

Figure 47 shows the AFM topographical as well as 3D images to understand the roughness of the thin films. Figures 47 (a) and (b) are topographical images from samples HP_50 and LP_50, respectively. The root mean square roughness (R_{rms}) values are 5.4 nm and 2.8 nm respectively, these values indicate the higher roughness for samples deposited at high pressure. Figures. 47 (c) and (d) shows the 3D images of the features from samples HP_50 and LP_50, respectively. These 3D features are bigger for sample HP_50 (up to 44 nm) when compared with LP_50 (up to 25 nm). High roughness also promotes better sensitivity towards response to the change in humidity.

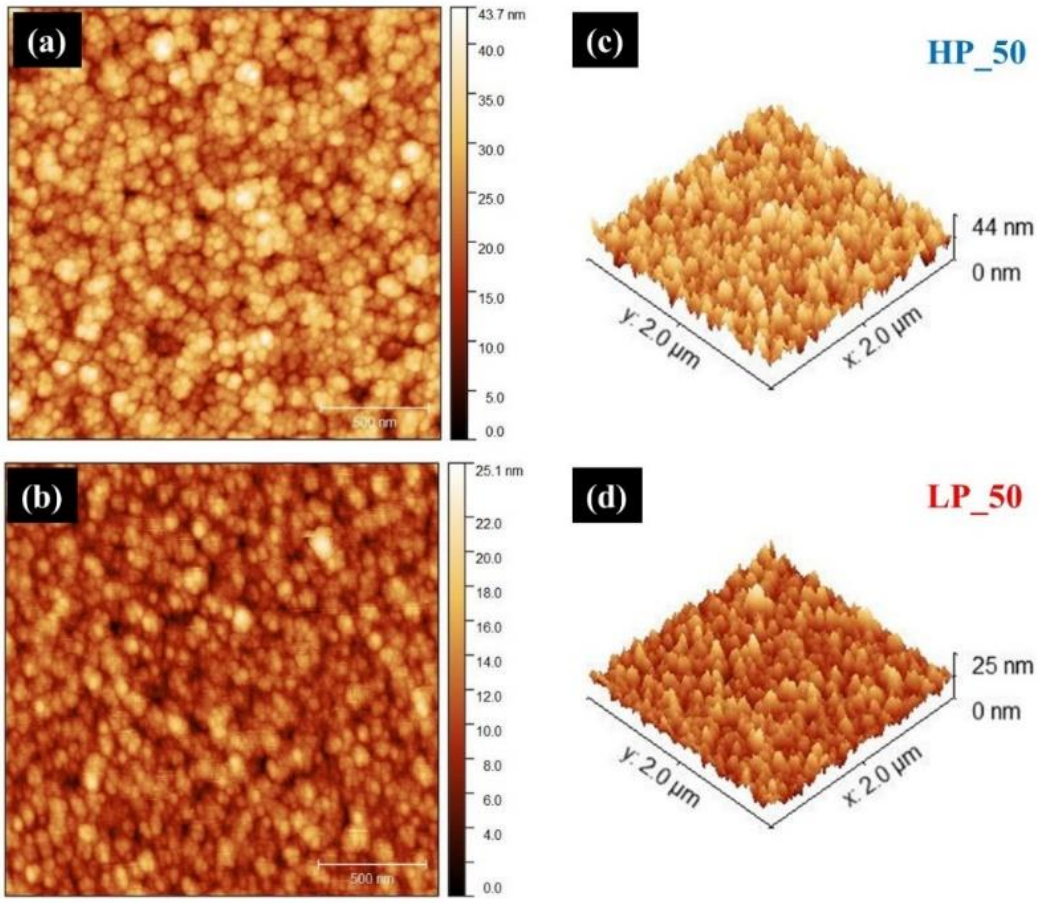

Figure 47. Topographical and 3D images for samples HP_50 ((a) and (c)), and LP_50 ((b) and (d)).

Figures 48 (a) and (b) show the XRD patterns of the Si-Sn thin films deposited at both high and low vacuum pressures: 1 Pa and 0.6 Pa, respectively. The films deposited with lower Sn contents (HP_25 and LP_25) are fully amorphous. In a previous study L.Y. Beaulieu et al. [83], on $Si_{66}Sn_{34}$ coating prepared by magnetron sputtering, stated an amorphous structure with a short-range ordered diamond structure and a lattice parameter of 5.6 Å. Since this value is slightly higher than one of the ICDD card value (5.43 Å) for the crystalline Si phase [98] the authors suggest that this increase is probably a result of the larger Sn atoms incorporated by substitution into the amorphous phase. The films deposited during our study also confirm this incorporation of tin in the Si phase by sputtering. Thin films HP_50 and LP_50 are quasi-amorphous with low intensity of Sn peak on XRD patterns, whereas films with even higher tin contents (HP_75, HP_100, LP_75 and LP_100) form broad XRD peaks corresponding to metallic tin (β-Sn). These peaks are detected at diffraction angles (2θ) = 30.6°, 32.0°, 43.9° and 44.9° corresponding to (200), (101), (220) and (211) planes of beta-tin, respectively (ICDD card no. 00-086-2265).

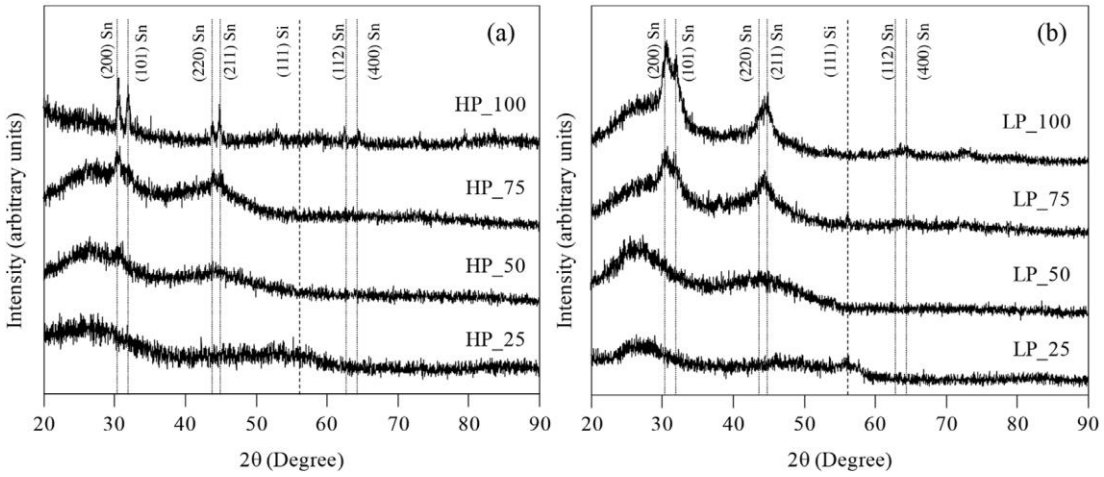

Figure 48. XRD patterns for Si-Sn thin films deposited at (a) HP, and (b) LP.

Figures 49 (a) and (b) show the HRTEM and SAED pattern of pure silicon thin film. The observation of this film using high-resolution transmission electron microscopy did not reveal any lattice fringes. And the selected area electron diffraction pattern shows two broad and diffuse SAED rings at 0.32 and 0.192 nm corresponding to (111) and (220) planes of fcc-Si-phase, confirming the amorphous nature of Si film.

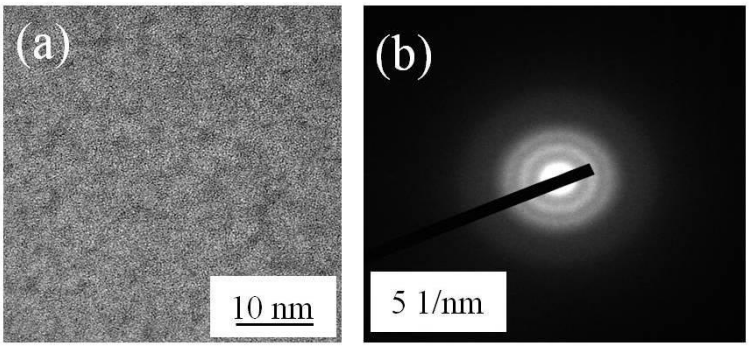

Figure 49. (a) HRTEM image, and (b) SAED patterns of samples from pure Si film.

Figures 50 (a) and (b) show the HRTEM at different magnifications to observe the lattice fringes from sample HP_50. Figure 50 (a) shows the nanoparticles with an average diameter of 5 nm embedded in an amorphous structure. Figure 50 (b) shows one nanoparticle at higher resolution with an atomic lattice fringe of 0.291 nm, corresponding to the lattice parameter of the β-Sn (200) crystal plane. This is also the most intense plane of β-Sn (ICDD card no. 00-086-2265). The SAED pattern from this sample is shown in Fig. 50 (c). The SAED pattern presents the diffuse rings from the matrix of amorphous Si, in addition to that SAED pattern also contains Sn nano-dots at d = 0.292, 0.279, 0.206, 0.202, 0.166, 0.146 and 0.129 nm corresponding to (200), (101), (220), (211), (301), (400), (411) planes of β-Sn phase (ICDD card no. 00-086-2265).

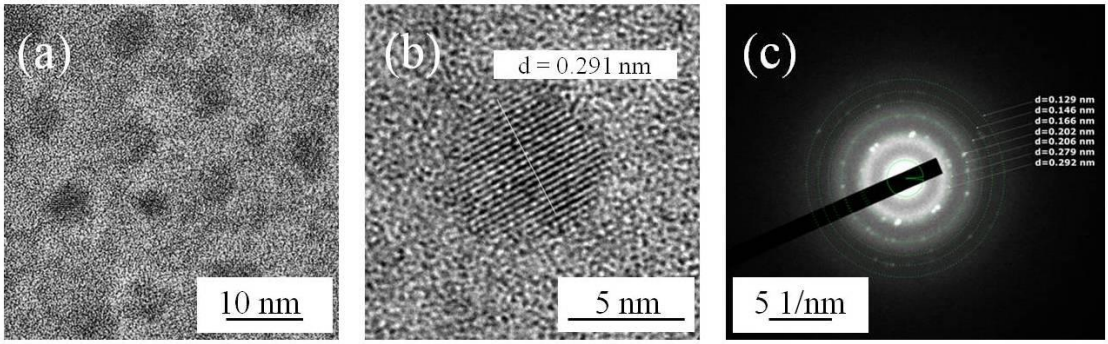

Figure 50. (a) and (b) HRTEM images, and (c) SAED patterns of sample HP_50.

Figure 51 shows the Mössbauer spectrum obtained from the thin-film HP_50 sample, revealing a very large singlet slightly asymmetric. This was chosen to fit the spectrum using a singlet peak distribution (and compared with the literature isomer shift values for α, β, and amorphous Sn). A slight shift of the optimum from 2.4 mm/s (attributed to the crystalline β-Sn located in the particle's core) to 2.0 mm/s can be ascribed due to different atomic environments due to the presence of nanometric domains rich in Sn. These Sn atoms have Si atoms as first or second neighbours, implying a decrease in electron density. Consequently, this induces a slight shift of the Isomer centre, and hence, a large signal. This behaviour was also observed by Vergant et. al [85] during their study on Si-Sn thin films.

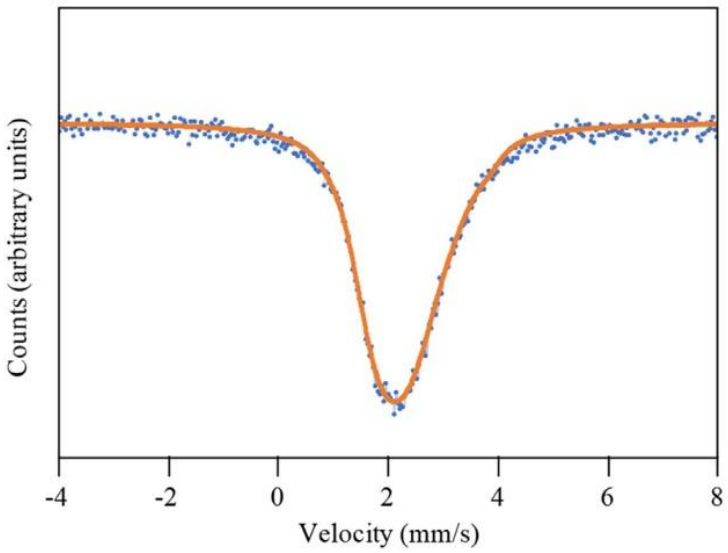

Figure 51. Mössbauer spectrum of sample HP_50.

Figure 52 shows the relationship between the hardness values of all Si-Sn thin films versus the power applied onto the tin target. The hardness of the thin films is also affected by the Sn target applied power and the deposition pressure. The hardness values decrease with an increase in the Sn content within the films. The pattern for the decrease in hardness values was also expected as tin is relatively softer than silicon. The hardness for pure silicon was reported as

5 GPa [161], whereas for pure tin it is 0.4 GPa [162]. There is a difference in hardness values for the films deposited at both pressures, especially at low Sn contents. This is probably because the low-pressure films are more compact with lower porosity and roughness values. Also, the film HP_25 and LP_25 have a large difference in the tin content which might have also influenced the final hardness values.

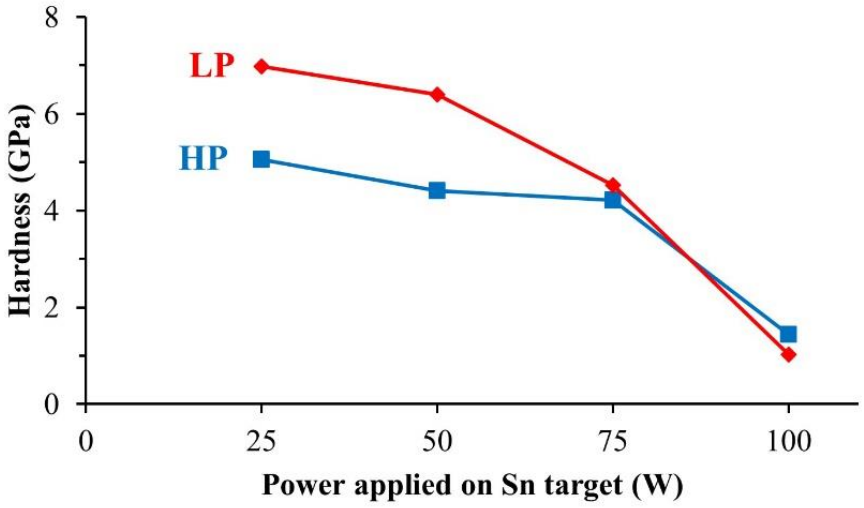

Figure 52. Hardness as a function of power applied onto the Sn target.

Humidity sensing response of Si-Sn thin films:

Influence of deposition pressure on the humidity response:

Figure 53 shows the Nyquist and impedance modulus plots for two sensors with similar chemical compositions (HP_50 and LP_50) prepared at different deposition pressures of 1 Pa and 0.6 Pa. The comparative study on the structural, morphology, porosity and roughness of these sensors are discussed in detail in previous sections and Figs. 44, 45, 46, and 47, respectively. Sensor HP_50 was observed to have a columnar surface with a porous structure when compared with the LP_50 sample surface which was more compact and less porous (Fig. 44). Mercury intrusion porosimetry results also confirmed the porous behaviour of sample HP_50, especially in the mesoporous region which is responsible for humidity sensing mechanisms (Fig. 46). The AFM topography and R_{rms} roughness values obtained for these samples, indicate sample HP_50 to have better roughness on the surface than sample LP_50 (Fig. 47). Higher roughness on the surface also promotes better humidity sensing behaviour. Hence, we can conclude that the sensor HP_50 has better properties for being a potential candidate for humidity sensing than sensor LP_50.

The Nyquist plots of sensors HP_50 (Fig. 53 (a)) and LP_50 (Fig. 53 (b)) show quite different responses towards changes to relative humidity. The area under the impedance spectra for sample HP_50 is continuously increasing with respect to relative humidity whereas the change in impedance spectra area for sample LP_50 is almost insignificant. These changes in impedance area for sample HP_50 are due to the changes in the conductivity with an increase in relative humidity from 10 to 100%. Sensor HP_50 shows a *p*-type conduction behaviour which refers to the decrease in the conductivity with an increase in relative humidity. This is confirmed by its impedance modulus variation at 1 kHz as a function of relative humidity from 10 to 100% (Fig. 53 (c)). On the other hand, for sample LP_50, the impedance modulus versus relative humidity plot at 1 kHz is almost constant or in other words insignificant (Fig. 53 (d)).

The Nyquist plot of sensor HP_50 (Fig. 53 (a)) is typically composed of semicircles which arise from the interaction of the water molecules with the grains and grain boundaries (diffusion mechanism are also present in very small quantities as there are no straight lines after or around the semicircle). The conductivity variation is smaller at low humidity levels whereas the conductivity variation is high when extreme humidity levels are reached. This behaviour of the sensor could be explained by the two adsorption stages (chemisorption and physisorption) which dominate at different levels of humidity. Typically, at lower humidity levels the layers of water molecules are chemisorbed due to the formation of a chemical bond between a polar water molecule and an oppositely charged ion on the sensor surface. The process is known as ‘proton hopping’. The second stage starts at high humidity levels after the completion of the chemisorbed layer, when protonic conductivity sets in. When, water molecules are continuously adsorbed on the surface and layers of water are added one by one, the pores having dimensions below the Kelvin radii start to fill [23] and protons can then hop between adjacent water molecules through Grotthuss chain reaction [32]. Sensor LP_50 (Fig. 53 (b)) is composed of a semicircle (due to the interaction between water molecules with grains and grain boundaries) followed by a straight line which is typical of diffusion mechanisms which could be attributed to several factors such as the one originated by the geometry of pores that fill with water and another originating from the interaction between the electrodes and the water molecules [159].

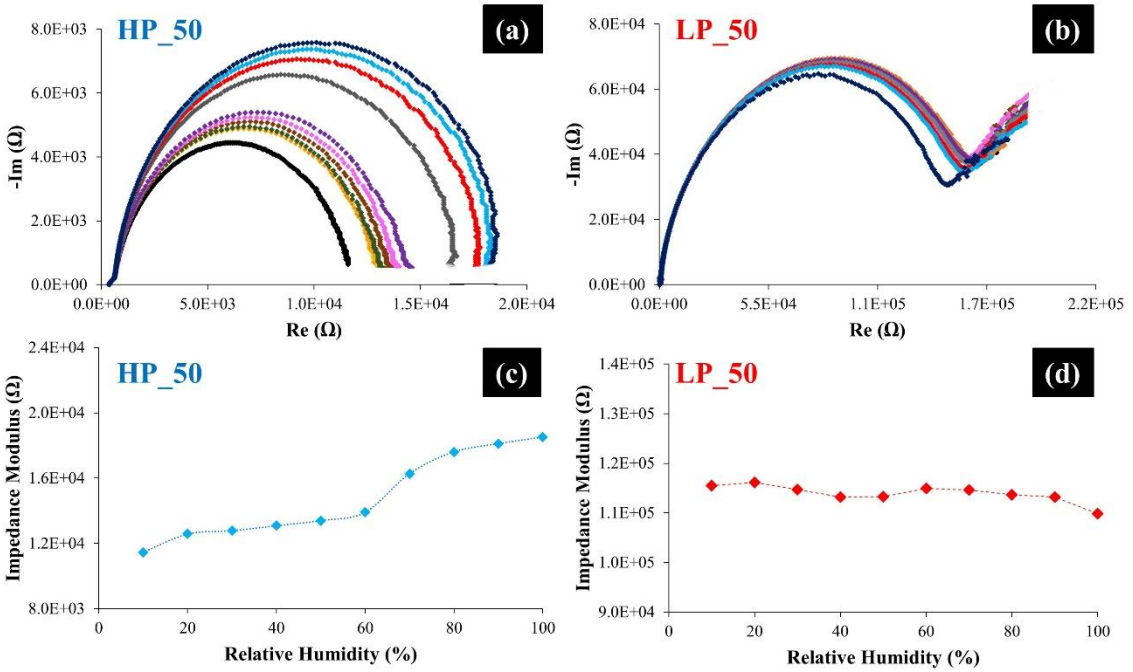

Figure 53. Impedance spectra and modulus plots for sample HP_50 ((a) and (c)), and LP_50 ((b) and (d)) (for different relative humidity contents colours black, orange, dark green, brown, rose, purple, grey, red, light blue and dark blue stands for 10, 20, 30, 40, 50, 60, 70, 80, 90 and 100 % RH, respectively).

Influence of chemical composition on the humidity response:

In this section, the influence of chemical composition on the response of sensors exhibiting higher sensitivity (HP_25, HP_50, HP_75 and HP_100) towards changes in relative humidity are discussed. As discussed earlier the advantages of incorporation of tin into porous silicon matrix in terms of microstructural stability by the formation of interpenetration structure. In Fig. 48, the XRD patterns show how the amorphous nature of the thin films changes to quasi-amorphous and crystalline with an increase in tin content.

Figure 54 and 55 shows impedance spectra and impedance modulus of thin films deposited at high pressure. Sensor HP_25 which is almost amorphous in nature with 7 at. % of tin does show some impedance changes with a change in relative humidity (Fig. 54 (a)) but the impedance modulus does not vary uniformly with relative humidity from 10 % to 100 % as shown in Fig. 55 (a). With an increase in relative humidity from 10 to 20 % the impedance area under the Nyquist plot increases whereas from 20 to 100 % there is a decrease in the impedance area (Fig. 54 (a)). The impedance modulus variation at 1 kHz decreases as a function of relative humidity and this sensor also shows a *p*- to *n*-type conduction transition with a level-type behaviour (Fig. 55 (a)). Since for *a*-Si, the conduction behaviour is *n*-type and the introduction of tin which predominantly exhibits *p*-type behaviour the *n*-to *p*-type conduction mechanism is

observed here, this is also explained by Mahan et. al [95]. Moreover, the change in sensors conduction behaviour occurs in the low impedance coverage range, thus the transition must be electronic in nature. The concentration of the dominant charge carriers, the electrons, increases, due to the presence of small quantities of tin and thus the band bending decreases due to variations in the surface work function because of increased exposure to RH.

With the increase in tin contents, sensors HP_50 (28 at. %) and HP_75 (39 at. %) show a better and uniform increase in impedance modulus values towards the increase in relative humidity. The higher incorporation of tin in the form of β-Sn nanocrystalline structure embedded in the amorphous Si-Sn matrix makes it more stable and more responsive to the changes in relative humidity. The activation energy and pre-exponential factor values for the diffusion of Sn in Si are 4.9 eV and 5×10^3 cm^2/s, respectively [163]. In consequence, if a sensor is working below 100 °C, the maximum diffusion coefficient for Sn in Si is quite low around 2.46×10^{-54} cm^2/s. Hence, the metastable amorphous Si-Sn phase of these sensors would be structurally and thermodynamically stable for a long period of time. Both the sensors exhibit a *p*-type condition behaviour along the entire relative humidity range from 10 to 100 % (Figs. 54 (b) and (c)) i.e., these sensors exhibit an increase in the impedance area under the Nyquist plot with the increase in relative humidity. Although the variation of sensor HP_50 is higher by almost 1 order of magnitude this could be explained in terms of the amount and phases of tin in these sensors. This is also confirmed by the increase in impedance modulus variation of these sensors at 1 kHz as a function of relative humidity (Figs. 55 (b) and (c)). The impedance moduli of these sensors can be fitted with straight lines. Sensor HP_50 shows a higher slope, which confirms its higher sensitivity towards relative humidity changes.

At very high tin contents, sensor HP_100 (51 at. %) still shows a variation to changes in relative humidity. With an increase in relative humidity from 10 to 30 % the impedance area under the Nyquist plot decreases whereas from 30 to 40 %, there is an increase in the impedance area and again from 40 to 100 %, there is a decrease in the impedance area (Fig. 54 (d)). This behaviour could also be observed with the impedance modulus variation at 1 kHz as a function of relative humidity (Fig. 55 (d)). HP_100 sample is highly crystalline in nature (Fig. 48 (a)) and also has a high density of defect states, created by Sn dangling bonds [97]. The large amounts of macro-crystallites of metallic tin (β-Sn) in the HP_100 sample help in increasing the overall conductivity of the sensor [93]. This increase in conductivity influences the behaviour of the sensor and results in an *n*-type semiconductor dominating behaviour. The humidity sensing mechanism is based on capillary condensation and the adsorption of water on the surface. The adsorption mechanism is divided into two stages: chemisorption and physisorption. With the increase in relative humidity at around 20 to 30 % RH the adsorption mechanism changes from chemisorption to physisorption

[32], this change could have played a role in the slight change in conductivity behaviour from *n* to *p*-type at 30 % RH for sensor HP_100.

In conclusion, based on the Nyquist and impedance modulus plots from samples HP_25, HP_50, HP_75, and HP_100 deposited at a pressure of 1 Pa showed an overall good response towards humidity sensing. The chemical composition played one of the critical roles in the response of sensors to changes in relative humidity from 10 to 100 %, and the sensor HP_50 was best suited for humidity sensing applications.

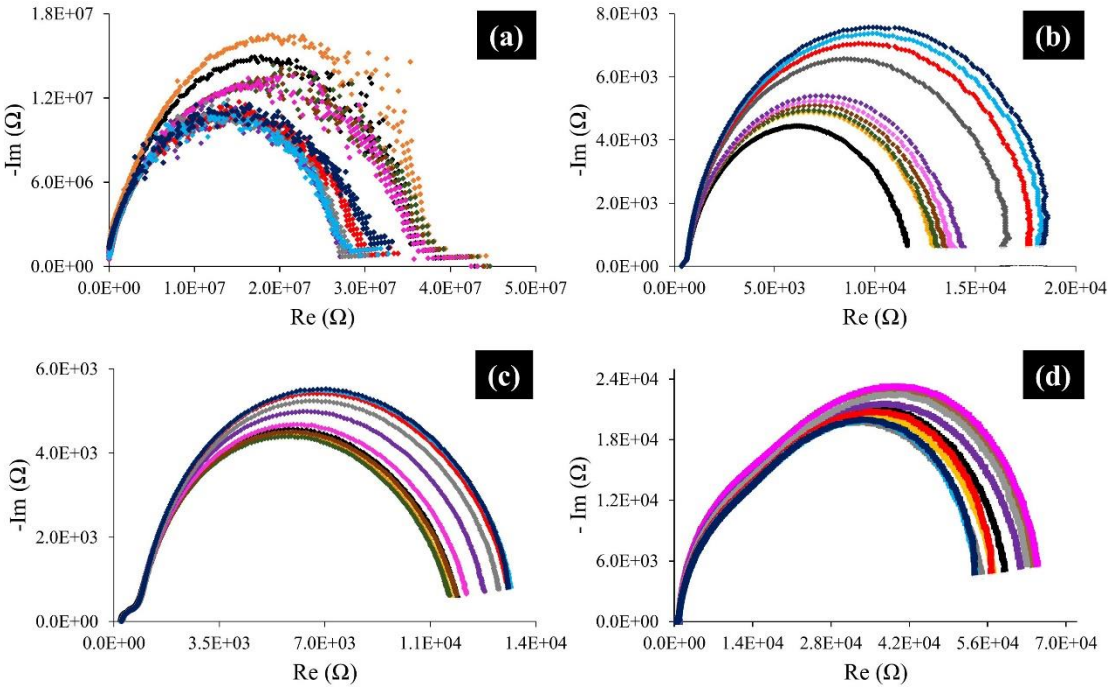

Figure 54. Nyquist plots for thin films deposited at high pressure: (a) HP_25, (b) HP_50, (c) HP_75, and (d) HP_100 (for different relative humidity contents colours black, orange, dark green, brown, rose, purple, grey, red, light blue and dark blue stands for 10, 20, 30, 40, 50, 60, 70, 80, 90 and 100 % RH, respectively).

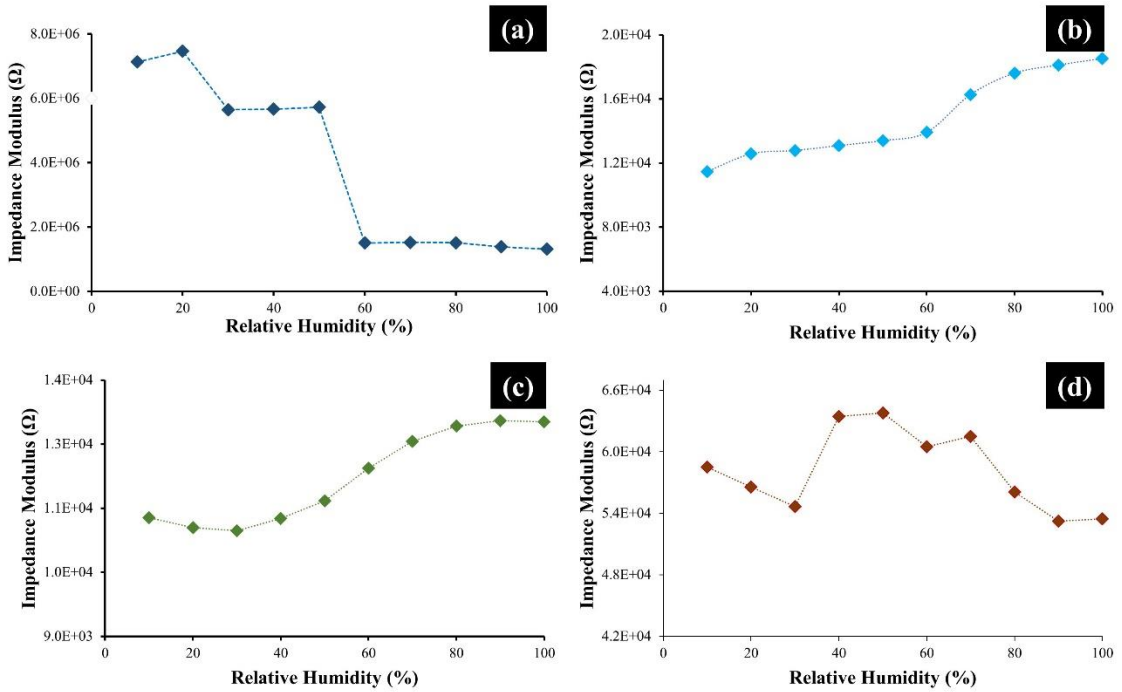

Figure 55. Impedance modulus plots (at 1 kHz) as a function of relative humidity for thin films deposited at high pressure: (a) HP_25, (b) HP_50, (c) HP_75, and (d) HP_100.

Time stability humidity response of sensor HP_50:

For time stability humidity response, sample HP_50 was analysed 3 times at different timings: first analysis (at t = 0), second (at t = 1 month, after the first analysis) and third (at t = 6 months, after the first analysis). The Nyquist plots for all three analyses are shown in Figs. 56 (a), (b), and (c), respectively. These plots for all three measurements are similar apart from slightly higher impedance modulus values for 1 - and 6 - month measures when compared with the first measure. Although, the sensor's humidity response suffers from an ageing effect which is more clearly visible for the measurement taken after 6 months from the initial measure (Fig. 56 (c)), then also the humidity sensitivity was not affected. Impedance modulus variations at 1 kHz with increase in relative humidity from 10 to 100 %, for t = 0 month, t = 1 month, and t = 6 months are presented in Figs. 56 (d), (e), and (f), respectively. All three measurements display almost linear variations of the impedance modulus values as a function of RH contents. The corresponding slopes of the straight trendlines are also quite similar: 84 Ω/RH(%) for the first measure (Fig. 56 (d)), 83 Ω/RH(%) for the second measure performed 1 month after the first measure (Fig. 56 (e)), and 84 Ω/RH(%) for the third measure performed 6 months after the first measure(Fig. 56 (f)), confirming the good stability of sensor's response towards relative humidity over time.

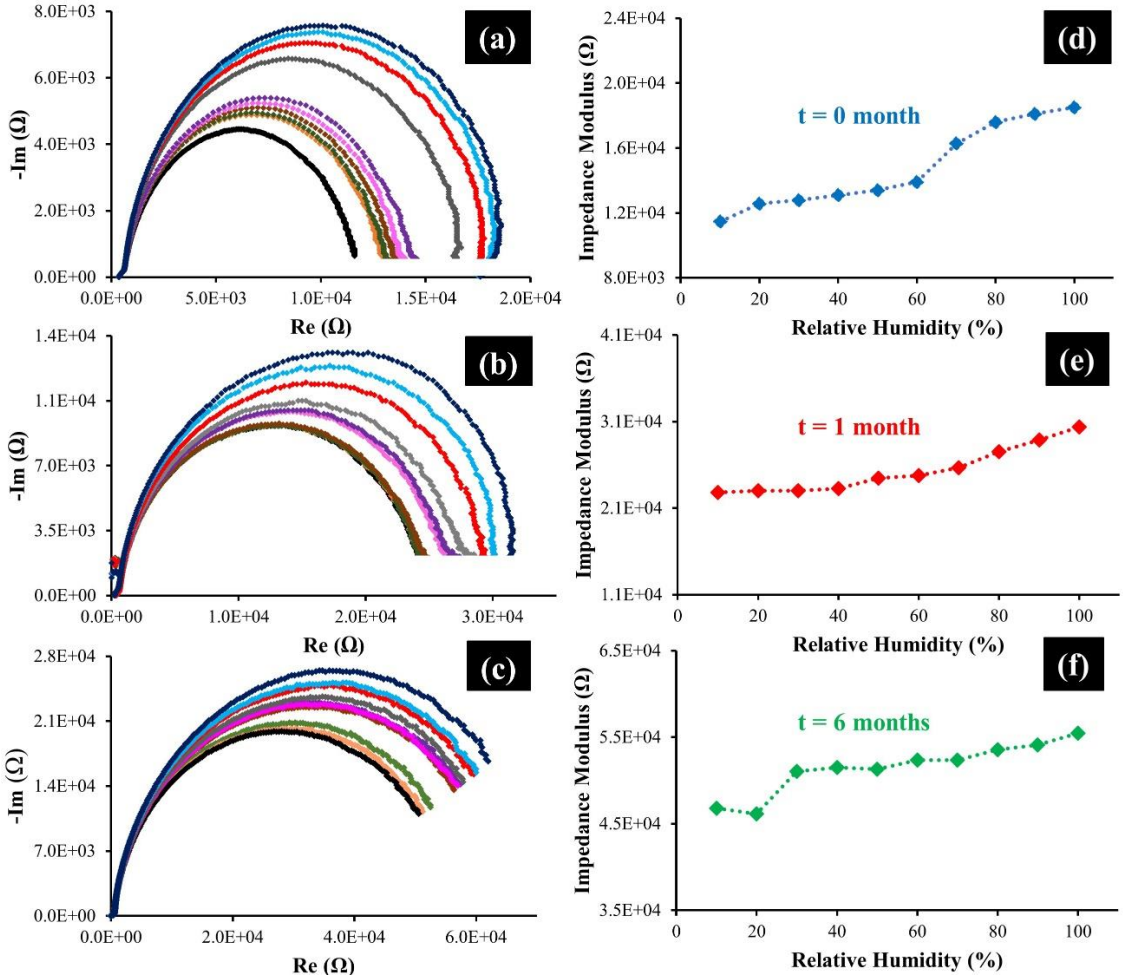

Figure 56. Impedance spectra ((a), (b), and (c)) and impedance modulus at 1 kHz ((d), (e), and (f)) for HP_50 sample at t = 0, t = 1 month and t = 6 months (for different relative humidity contents colours black, orange, dark green, brown, rose, purple, grey, red, light blue and dark blue stands for 10, 20, 30, 40, 50, 60, 70, 80, 90 and 100 % RH, respectively).

Conclusions

Si-Sn thin films were prepared by RF-magnetron sputtering with different concentrations of tin from 0 to 51 at.% at two vacuum pressures. The structure of the films was dependent on the chemical composition. At low concentrations of tin, films were fully amorphous. Whereas at 28 at. % of Sn, the formation of nano-crystalline β-tin phase was observed; this marks the change in the structure of films from amorphous to quasi-amorphous. At even higher concentrations of tin, the structure becomes more and more crystalline. The surface morphology for high- and low-pressure films appears to be globular. The cross-section images show high-pressure films (1 Pa) to be more porous, whereas low-pressure (0.6 Pa) films seem to be more compact and denser. These results were confirmed by mercury intrusion porosimetry, where sample HP_50 (deposited at high pressure) shows a higher pore volume than sample LP_50. The porosity in and close to the mesoporous region promotes adsorption mechanisms for humidity sensing. Here, the amount of porosity in the mesoporous region was 3.3 and 1 % for HP_50 and LP_50 films, respectively. The hardness of the thin films was dependent on the chemical composition. The hardness values were inversely proportional to the concentration of tin in the films. For humidity sensing detection, the sample HP_50 was shown to be best suited, displaying good response, repeatability, and reproducibility. The sensor demonstrated a *p*-type conduction behaviour with a linear variation of the impedance modulus with the increase in the relative humidity content from 10 to 100 %. Humidity tests were also performed 1 and 6 months after the first run to study the electrical response of the sensor with respect to time. The sensitivity behaviour of this sample was relatively stable with time as the slopes obtained for the impedance variation with an increase in relative humidity were quite similar. The factors responsible for superior sensor's response to changes in relative humidity are the high content of tin, surface morphology, roughness, and porosity level in the mesoporous region.

4.1.2 Silicon-tin alloys produced by mechanical alloying and ensuing consolidation using sintering and hot pressing

(Based on paper "Porous Si-Sn alloys produced by mechanical alloying and subsequent consolidation by sintering and hot-pressing, Materials and Manufacturing Processes, 37 (2) (2022) 169-176, https://doi.org/10.1080/10426914.2021.1967979.)

Abstract

$Si_{100-x}Sn_x$ alloy pellets with 0 < x < 40 (at. %) have been produced from Si and Sn elemental powders by mechanical alloying for 4 and 12 hours of milling times. After milling the alloyed powders were consolidated using two different routes. First, cold uniaxial pressing followed by sintering at 220 °C; second, hot pressing at 240 °C. The structure of all the samples was composed of Si, Sn and SnO phases, confirmed by TEM. A few samples prepared using former process showed Sn-whisker growth on the surface with an increase in the tin content in the alloys. Most of the samples presented porosity close to 0.1 µm. However, the porosity of the sample $Si_{70}Sn_{30}$ milled for 12 hours and synthesised using cold pressing and sintering at 220 °C for 3 hours was mainly in the mesoporous region. Apart from porosity, the compacted samples produced using cold pressing had quite high roughness values in terms of R_{rms} parameter. Even though the porosity and roughness values for these alloys are quite high, the humidity sensing electrical response towards changes to relative humidity are not very promising. This could be explained by the fact that the pores having a radius greater than kelvin radii do not show a good response towards humidity. The roughness values of the samples are also high, favouring for response to changes in relative humidity. These factors have affected the interaction of water molecules with the alloy surfaces resulting in non-uniform impedance characteristics.

Alloy formation parameters and consolidation processes

Mechanical alloying (MA) of silicon (99.999% purity) and tin (99.9% purity) elemental powders, in the presence of stearic acid (2 wt.%) was performed at different chemical compositions and milling times. The MA process was carried out for 4 and 12 hours and a rotation speed of 300 revolutions per minute (rpm) was used for all millings. This was followed by two different consolidation routes. The first being compaction and sintering, whereas the second route was hot pressing. Sample names with the suffix '4 MA' refer to the powders mechanically alloyed for 4 hours whereas the suffix '12 MA' refers to powders mechanically alloyed for 12 hours. Sample preparation parameters for both processes are shown in Table 11.

Table 11. Sample names, milling parameters and consolidation processes used to produce Si-Sn samples.

Sample name	**Content (at. %)**		**Milling time (hours)**	**Consolidation process 1**	**Consolidation process 2**
	Si	**Sn**			
$Si_{85}Sn_{15}$- 4 MA	85	15	4	Cold uniaxial compaction (50 MPa), followed by sintering (220 °C for 3 hours).	Uniaxial hot pressing (26 MPa, 240 °C for 0.5 hours).
$Si_{70}Sn_{30}$- 4 MA	70	30	4		
$Si_{60}Sn_{40}$- 4 MA	60	40	4		
$Si_{85}Sn_{15}$- 12 MA	85	15	12		
$Si_{70}Sn_{30}$- 12 MA	70	30	12		
$Si_{60}Sn_{40}$- 12 MA	60	40	12		

Raw material characterisation

The SEM image of Si (Fig. 57 (a)) shows an agglomeration of particles with different sizes (nanometric to micrometric dimensions). On the other hand, the Sn particles (Fig. 57 (b)) have an elliptical shape, and no agglomeration was observed. Concerning the particles size distribution (Fig. 58), Si particles present a bimodal distribution around 1 and 10 µm, with a median-diameter d_{50} = 7.31 µm and width-of-particle size distribution, span = 2.26, whilst the Sn particles are characterised by a unimodal distribution, with d_{50} = 6.01 µm and span = 2.33.

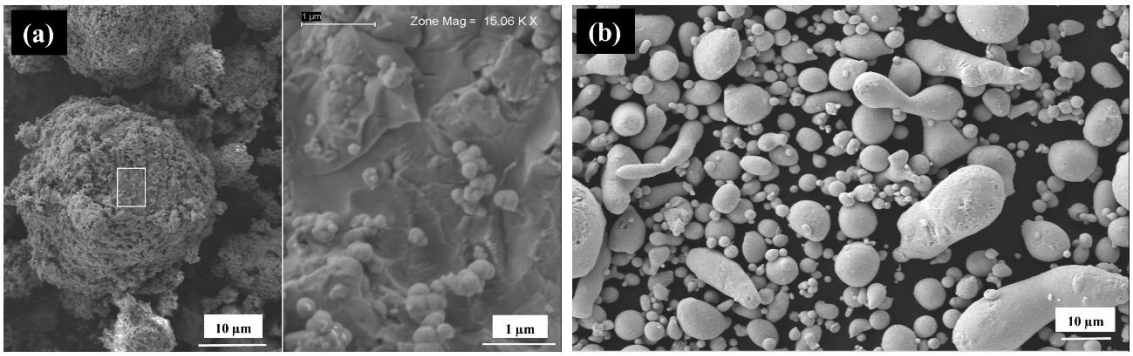

Figure 57. SEM images shows the particles of (a) Si, and (b) Sn elemental powders.

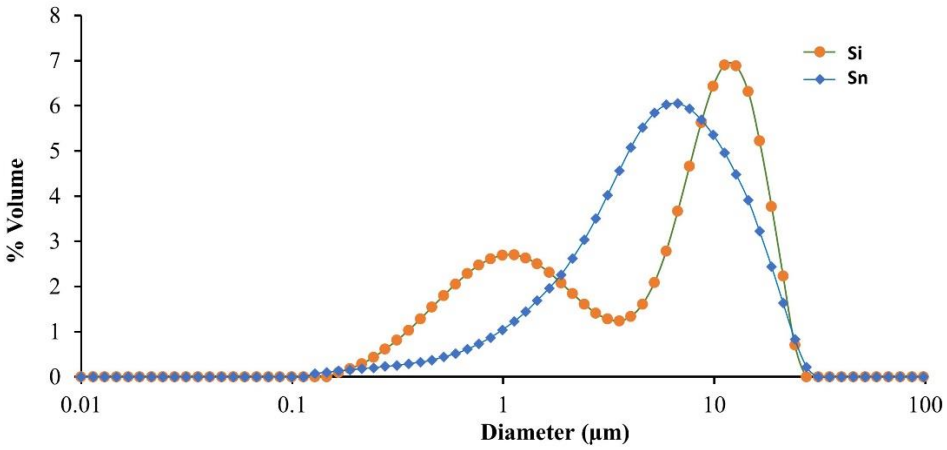

Figure 58. Particle size distribution of Si and Sn elemental powders.

The XRD patterns of the raw materials are presented in Fig. 59. The Si powders are partially crystalline, characterized by an Fd-3m (cubic) structure (ICDD card No. 01-075-0589) and an amorphous phase with two broad peaks centred at 2θ angles of 28.4º and 47.3º. The Sn powders are fully crystalline and are characterised by a tetragonal phase structure of β-Sn (ICDD card No. 01-086–2265).

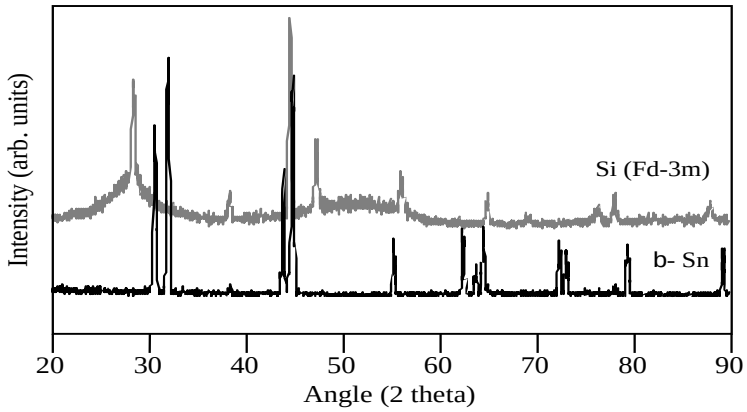

Figure 59. XRD patterns of the Si and Sn raw materials.

Characterisation of Mechanically alloyed powders

Figures 60 (a) and (b) shows the XRD results of the $Si_{85}Sn_{15}$, $Si_{70}Sn_{30}$ and $Si_{60}Sn_{40}$ samples after 4 and 12 hours of mechanical alloying, respectively. The XRD peaks correspond to metallic tin (β-Sn) and Si phase matching with ICDD cards of 01-086-2265 and 01-075-0589, respectively. Although, the intensity of these phases is not constant i.e., either increases or decreases with the respective amounts of Sn and Si present in the samples, there is no shift of the diffraction planes for two milling times. There is no formation of new phases for either of the two milling times. This means that no solid solutions were formed during mechanical alloying.

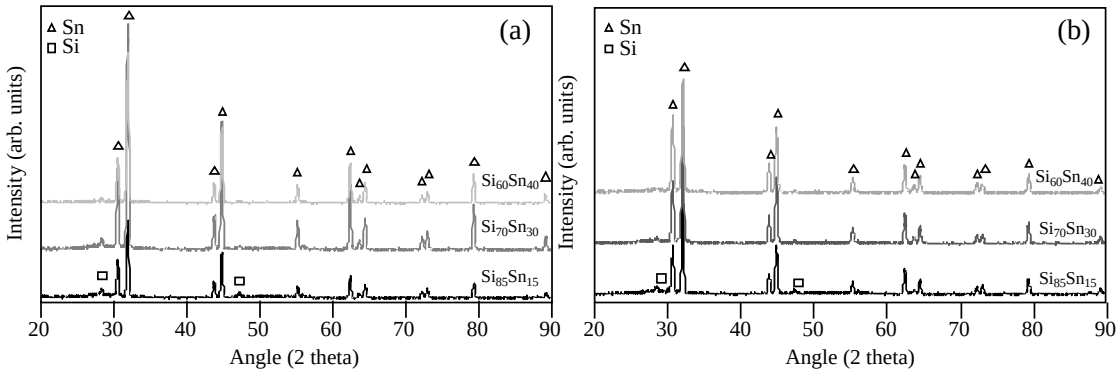

Figure 60. XRD patterns of the $Si_{85}Sn_{15}$, $Si_{70}Sn_{30}$, and $Si_{60}Sn_{40}$ mixtures mechanically alloyed for (a) 4 and (b) 12 hours.

Under equilibrium conditions, the maximum solubility of tin in silicon is quite low, limited to ~ 0.1 at. % [74]. In order to increase the solubility, metastable or non-equilibrium processing conditions are required. Mechanical alloying is a non-equilibrium technique allowing the fabrication of metastable supersaturated solid solutions for specific compositional ranges. This signifies that the energy involved in the MA process during this work was not enough to produce supersaturated structures.

The evolution of the crystallite size (D) and the degree of crystallinity (χ_c) of the β-Sn phase as a function of the MA time are plotted in Figs. 61 (a) and (b), respectively. The crystallite size was calculated using X-ray peak profile analysis (XPPA) by the Williamson-Hall plot method (W-H method) [125] whereas the degree of crystallinity was measured using area analysis [129].

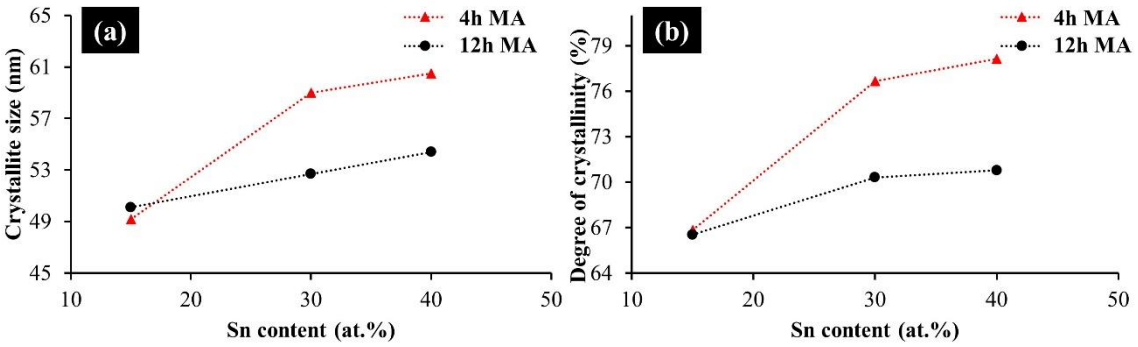

Figure 61. (a) Crystallite size, and (b) degree of crystallinity of the β-Sn phase for the $Si_{85}Sn_{15}$, $Si_{70}Sn_{30}$, and $Si_{60}Sn_{40}$ mixtures mechanically alloyed for 4 and 12 hours.

The crystallite size (D) and degree of crystallinity (χ_c) for the β-tin phase of the initial powders was 87 nm and 89 %, respectively. Mechanical alloying has caused a decrease in both these parameters. With the increase in tin content, there is an increase in crystallite size and crystallinity which was expected due to the metallic nature on tin. Longer milling hours (from 4 to 12 hours) affect both crystallite size and crystallinity, for sample $Si_{70}Sn_{30}$ crystallite size and crystallinity values were 59 nm and 77 % for 4 hours and 52 nm and 70 % for 12 hours of mechanical alloying, respectively. MA of an equilibrium crystalline phase increases the crystal's free energy and therefore the crystalline-to-amorphous transition is favoured.

The morphology and the Si and Sn elemental maps of the mechanically alloyed $Si_{85}Sn_{15}$, $Si_{70}Sn_{30}$ and $Si_{60}Sn_{40}$ mixtures for 4 and 12 hours of MA are presented in Figs. 62 and 63, respectively.

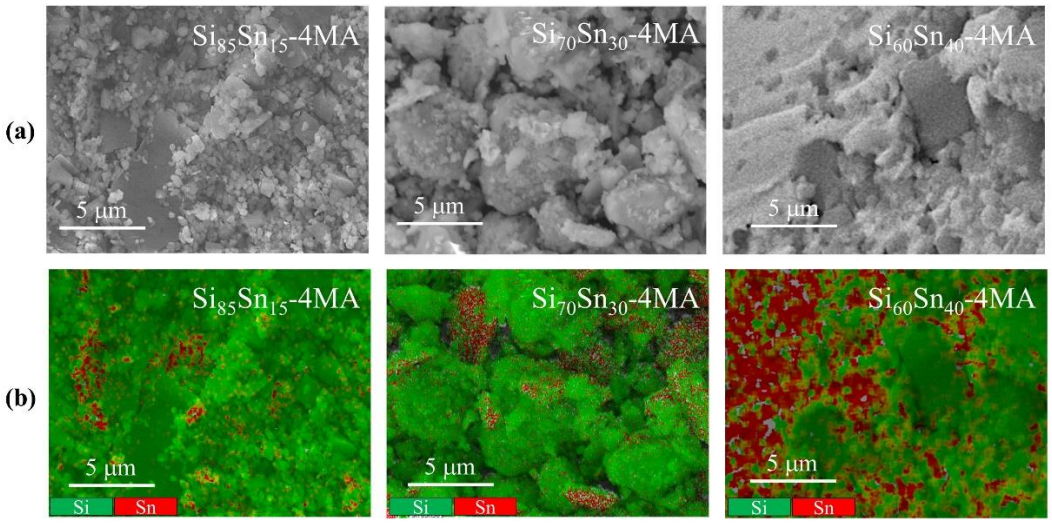

Figure 62. (a) Morphology, and (b) Si and Sn elemental maps, of the $Si_{85}Sn_{15}$, $Si_{70}Sn_{30}$ and $Si_{60}Sn_{40}$ mixtures mechanically alloyed for 4 hours.

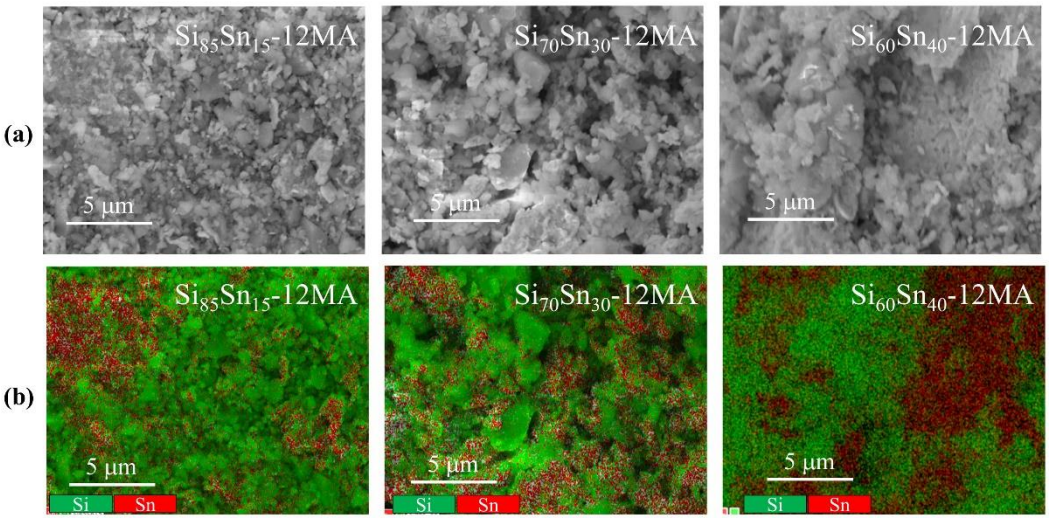

Figure 63. (a) Morphology, and (b) Si and Sn elemental maps, of the $Si_{85}Sn_{15}$, $Si_{70}Sn_{30}$ and $Si_{60}Sn_{40}$ mixtures mechanically alloyed for 12 hours.

The SEM results show quite homogeneous distribution of the Si and Sn powders in the microstructure. However, the samples with a composition of $Si_{60}Sn_{40}$ (at both milling times of 4 and 12 hours) have certain Sn-rich regions. The size of these regions is around 5 µm. This is because of the greater number of tin particles in this mixture, which may have enhanced the welding process between them, due to their high ductility.

The particle size distributions of the $Si_{85}Sn_{15}$, $Si_{70}Sn_{30}$ and $Si_{60}Sn_{40}$ powders after 4 and 12 hours of mechanical millings are shown in Figs. 64 (a) and (b), respectively.

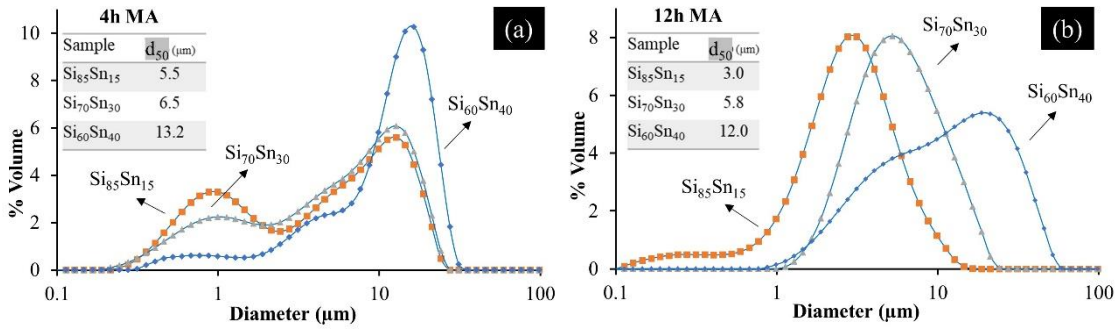

Figure 64. Particle size distributions of the $Si_{85}Sn_{15}$, $Si_{70}Sn_{30}$ and $Si_{60}Sn_{40}$ mixtures mechanically alloyed for (a) 4 and, (b) 12 hours.

After 4 hours of mechanical milling (Fig. 64 (a)), the samples $Si_{85}Sn_{15}$ and $Sn_{70}Si_{30}$ have quite similar particle size distribution curves. The amount of the smaller particles is the only apparent variation (around 1 µm size), where sample $Si_{85}Sn_{15}$ has a higher volume than sample $Sn_{70}Si_{30}$. This is because of the increase in the amount of tin powder content for which the d_{50} was 7.3 µm (Fig. 57). The d_{50} values for these two mechanically alloyed samples increase from 5.5 to 6.5 µm, for the $Si_{85}Sn_{15}$ and $Sn_{70}Si_{30}$ mixtures, respectively. Since, both these values are slightly

lower than the ones of the raw Si and Sn powders (7.31 and 6.01 µm, respectively). This suggests that the fracture process (for both Si and Sn powders) during mechanical milling has been a dominating factor for these samples prepared after 4 hours of milling. However, for the sample $Si_{60}Sn_{40}$, the particle size distribution curve is different from the other 4 hours milled samples. This sample has less existence of smaller particles, but the volume percentage for bigger particles is significantly higher. This result can be supported by the higher number of tin particles for this sample and the high ductility nature of Sn particles dominating the welding process during mechanical alloying hence the higher no. of particles are formed by agglomeration. As a consequence, the d_{50} value of this mixture is reported to be 13.2 µm.

After 12 hours of mechanical milling (Fig. 64 (b)), the samples $Si_{85}Sn_{15}$, $Si_{70}Sn_{30}$ and $Si_{60}Sn_{40}$ have a right-shift for particle size distribution curves with the increase in the levels of tin contents. However, the d_{50} values for the three distributions are 3.0, 5.8 and 12.0 µm for samples $Si_{85}Sn_{15}$, $Si_{70}Sn_{30}$ and $Si_{60}Sn_{40}$ milled for 12 hours. These d_{50} values are lower than the corresponding ones for 4h of MA. This suggests that a continuous fracture process occurred between 4 and 12 hours of MA.

J. Wu et al. [86], in their work with mechanical alloying of Si and Sn powders observed entangled ribbon structure, but these structures were not observed in the present work even after 12 hours of milling at 300 rpm. This can be explained by the lower percentage of tin in our samples and the use of a process control agent, stearic acid (2 at. %) in the MA process which helps in countering the cold-welding process of ductile phases (β-Sn) during mechanical alloying.

Consolidation process 1 (Compaction and sintering)

The mechanically alloyed $Si_{85}Sn_{15}$, $Si_{70}Sn_{30}$ and $Si_{60}Sn_{40}$ samples for 4 and 12 hours were compacted using uniaxial cold pressing at 50 MPa followed by sintering for 3 hours at 220 ºC. Figures 65 (a) and (b) show the XRD patterns for 4- and 12-hours MA samples after sintering. The XRD patterns are similar to those observed before sintering (Fig. 60) and the only difference was the formation of tin-oxide. Although sintering was performed at a controlled Ar (±5% H_2) atmosphere, yet all the samples had small peaks corresponding to the SnO phase (ICDD card no. 01-085-0423). These results were also verified by TEM analysis on sample $Si_{70}Sn_{30}$-12MA (Fig. 66). The HR-TEM (Fig. 66) revealed the lattice fringes corresponding to the (101) plane of the SnO phase. Besides the formation of SnO phase, sintering did not induce any other phase transformations.

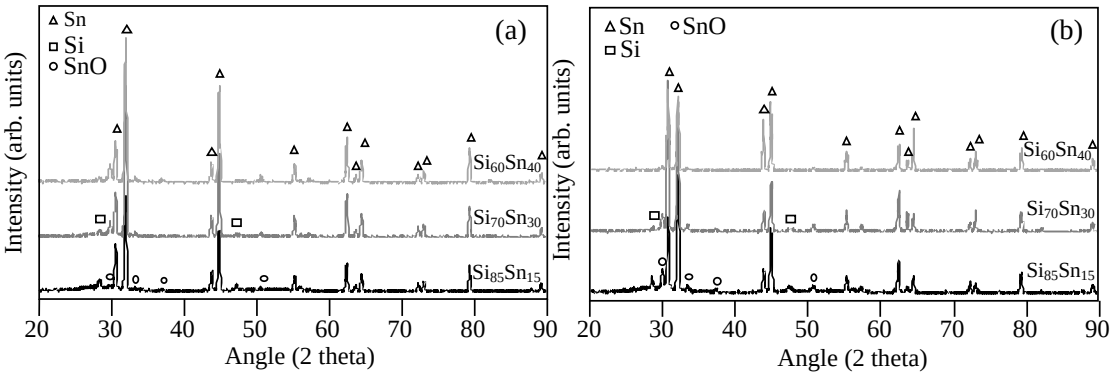

Figure 65. XRD patterns of the sintered $Si_{85}Sn_{15}$, $Si_{70}Sn_{30}$ and $Si_{60}Sn_{40}$ samples mechanically alloyed for (a) 4 and (b) 12 hours of MA.

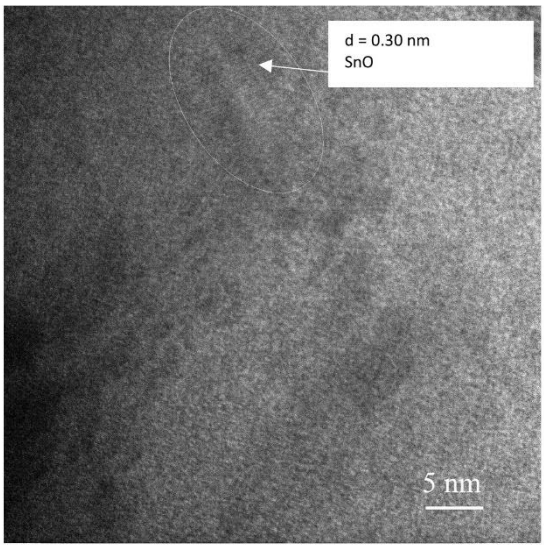

Figure 66. TEM image for the sintered $Si_{70}Sn_{30}$-12MA sample.

There is a high possibility for the oxygen to be incorporated into the powders during the mechanical alloying process from PCAs, in this case from stearic acid. Tin has two oxidation states: +2 (stannous) and +4 (stannic) and the formation of tin oxide for these samples during annealing for 3 hours at 220 ºC is in accordance with the literature. Nikiforov et al. [164], in their study, explained the formation of tin oxides (SnO and SnO_2 phases) during the annealing of $SnO_{(x)}$ films obtained by molecular beam epitaxy. They concluded that during annealing, Stannous tin oxide (SnO) is the first tin oxide to be formed at 200 °C (PDF no. 000-55-0837), whereas the phase transition to stannic tin oxide (SnO_2) only occurs at higher temperatures of above 500 °C (PDF no. 010-75-9495).

According to XRD patterns (Figs. 65 (a) and (b)), the intensity of the diffraction peaks of SnO in the samples mechanically alloyed for 4 hours increases as the tin content increases,

contrary to this, an opposite trend is observed for the sintered samples mechanically alloyed for 12 hours.

SEM images and EDS analysis of $Si_{85}Sn_{15}$, $Si_{70}Sn_{30}$ and $Si_{60}Sn_{40}$ samples mechanically alloyed for 4 and 12 hours presented in Figs. 67 (a) and (b), respectively, provide an explanation for this behaviour.

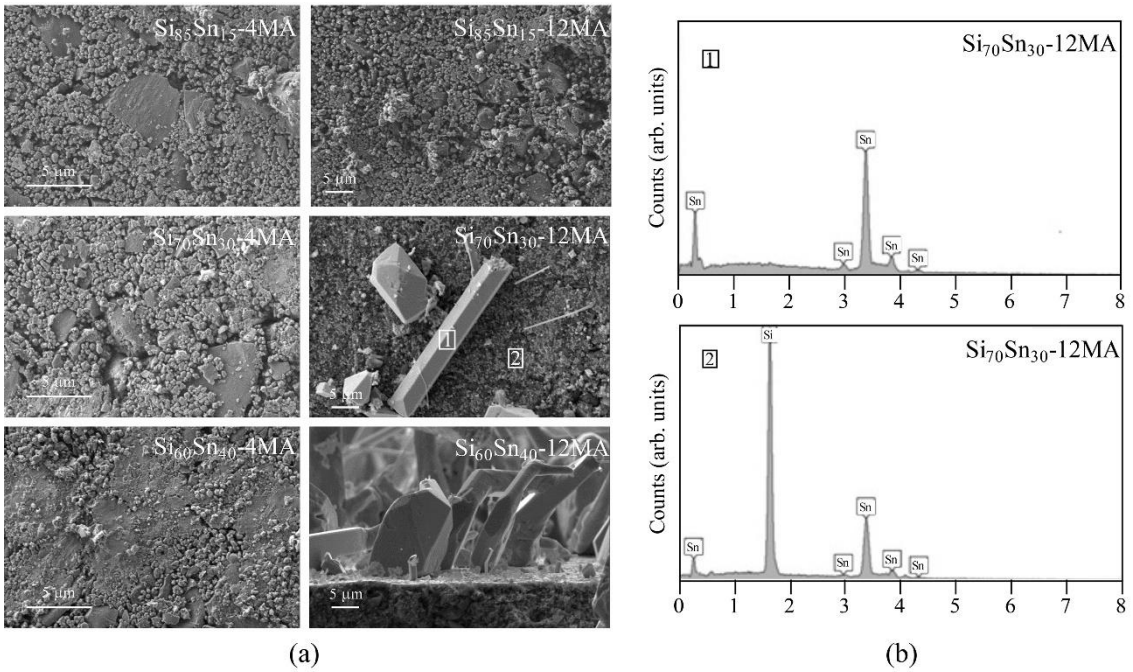

Figure 67. (a) SEM images of the sintered $Si_{85}Sn_{15}$, $Si_{70}Sn_{30}$ and $Si_{60}Sn_{40}$ samples, mechanically alloyed for 4 and 12 hours, and (b) EDS analysis of the $Si_{70}Sn_{30}$-12MA sintered sample.

Figure 67 (a), the samples after 4 hours of milling followed by sintering, show homogeneous distribution of phases (Si, Sn and SnO) throughout the surface. Whereas for 12 hours milled and sintered samples have different surface features. The sample $Si_{85}Sn_{15}$-12MA, has homogenous surface features as those observed with 4h milled samples. But with higher tin content samples $Si_{70}Sn_{30}$-12MA and $Si_{60}Sn_{40}$-12MA, present several crystals on the surface, with well-defined dimensions. These crystals are classified as metallic whiskers. A metallic whisker is a single crystal filamentary eruption from the surface. The EDS analysis of sample $Si_{70}Sn_{30}$-12MA shows that these crystals are tin whiskers (Fig. 67 (b)). Therefore, the XRD patterns from the surface of these samples mainly show the presence of pure β-tin phase. This is particularly true for the sample with higher tin contents, in which the diffracted peaks of the Si and SnO phases have very low intensity.

The phenomenon of whiskering for different metals is highly distinctive and is based on a large no. of parameters that affect the nucleation and growth processes for the whisker

formation. There are two very common whisker growth models: the first, Vianco and Rejent's whisker model [165] proposes the dynamic recrystallization to be responsible for whisker growth, and the second, Smetana's model [166] states that the atoms around the grain boundaries at the base of the whisker, are at lower energy levels (compressive stress levels) than grain areas. This assists the movement of tin atoms without requiring them to go to a higher energy state. According to this model, vacancies at the base of the whisker grain boundary allow the Sn atoms to diffuse during recrystallization and form whiskers at obliquely angled grains at the surface.

The formation of Sn oxides also plays a significant role in the formation of these crystals because their growth can be non-uniform and heterogenous [167]. As a result, the presence of holes and defects within the oxide layer favours the diffusion of tin through these regions. According to another hypothesis proposed by Wu et.al. [168], excess tin present in a system under any kind of compressive stresses moves along the unpinned grain boundaries, such as those close to the tin-oxide breaches. These areas act as nucleation sites for the tin atoms to condense and erupt on the surface in the form of a whisker.

It should be noted that no whisker formation was detected before sintering, but only just after sintering. This sintering process was performed at 220 ºC, just a few degrees Celsius below the melting temperature of tin (231.9 ºC), which corresponds to a high diffusivity process. Therefore, we can conclude that the key factor contributing to the formation of whiskers in the current investigation was the segregation of tin from the compressive layers below the surface caused by the elevated temperatures used during the sintering operation.

Figures 68 (a) and (b) show the pore size distribution in the range of 0.01 to 10 µm and the level of porosity of the sintered Si-Sn samples mechanically alloyed for 4 and 12 hours, respectively.

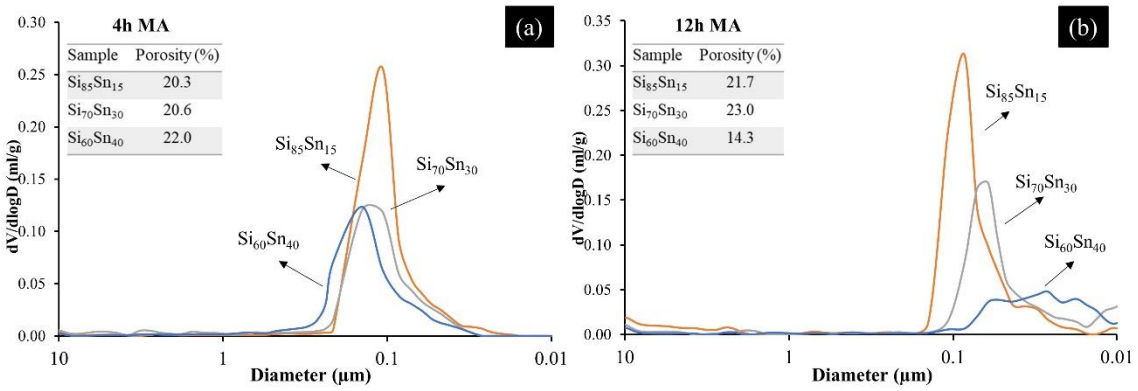

Figure 68. Pore size distribution and porosity levels of the sintered $Si_{85}Sn_{15}$, $Si_{70}Sn_{30}$ and $Si_{60}Sn_{40}$ samples mechanically alloyed for (a) 4 and (b) 12 hours of MA.

The pores distribution for all the samples was centred around 0.1 µm with the exception of sample $Si_{60}Sn_{40}$–12MA. The sample $Si_{60}Sn_{40}$-12MA presents a flatter pore size distribution with a maximum value at around 0.6 µm. This sample also presents a porosity level of 14 %, which is also quite low from all the other samples (where porosity is around 20 – 23 %). The porosity of these samples appears to be independent of the chemical composition and the mechanical alloying process. In actuality, the two sintered samples richer in tin ($Si_{60}Sn_{40}$) have completely different levels of porosity (22.0 and 14.3 % for 4 and 12 hours of MA, respectively). Additionally, the MA powders for these two samples had higher values of d_{50} after milling (13.2 and 12 µm for 4 and 12 hours of MA, respectively), which was anticipated to yield superior final porosities after sintering. Sample $Si_{60}Sn_{40}$–12MA, contains a great number of dense Sn crystals (whiskers) at the surface which might explain the lowest value of porosity.

Table 12 represents the root-mean-square (R_{rms}) values (obtained from AFM images) to provide an understanding towards the roughness of the sintered $Si_{85}Sn_{15}$, $Si_{70}Sn_{30}$ and $Si_{60}Sn_{40}$ samples, mechanically alloyed for 4 and 12 hours. The samples $Si_{70}Sn_{30}$-12MA and $Si_{60}Sn_{40}$-12MA, have higher roughness values, in which Sn whiskers were present at the surface. These tin whiskers are responsible for the significant roughness change especially for $Si_{60}Sn_{40}$-12MA sample where the R_{rms} value is 650 nm.

Table 12. Roughness values (R_{rms}) of the sintered $Si_{85}Sn_{15}$, $Si_{70}Sn_{30}$ and $Si_{60}Sn_{40}$ samples, mechanically alloyed for 4 and 12 hours.

Sample name	Milling time (hours)	Root-mean-square (R_{rms}) (nm)
$Si_{85}Sn_{15}$- 4 MA	4	132
$Si_{70}Sn_{30}$- 4 MA	4	109
$Si_{60}Sn_{40}$- 4 MA	4	84
$Si_{85}Sn_{15}$- 12 MA	12	100
$Si_{70}Sn_{30}$- 12 MA	12	169
$Si_{60}Sn_{40}$- 12 MA	12	650

The humidity sensing response is enhanced by an increase in the contact area, which is driven by an increase in the pore volume, particularly near the mesoporous region (2 - 50 nm), and surface roughness [22]. In fact, the humidity sensing mechanisms are related to electrical conduction through water vapour adsorption and capillary condensation phenomena on the material surface, which are enhanced by a high surface contact area [169]. Although the samples produced by this consolidation process (compaction and sintering) have pore size distribution (along with porosity levels) with optimum concentration close to the mesoporous region (2 - 50

nm) coupled with their quite high roughness values, which may enable them to have an adequate level of sensitivity towards changes in relative humidity.

Consolidation process 2 (Hot pressing)

For this consolidation process of hot pressing the powders after 4 and 12 hours of mechanical alloying were compacted using uniaxial hot pressing at P = 26 MPa and T = 240 ºC for t = 0.5 hour (where P is pressure applied, T is temperature, and t is time). The samples obtained from this process had a silicon oxide layer (discussed in the later sections) on the surface which could potentially affect the surface characteristics of the samples hence for the sake of simplicity and clarity one sample $Si_{70}Sn_{30}$-12MA was chosen for comparative study of not polished and polished surfaces.

Figure 69 shows the XRD patterns of the hot-pressed $Si_{70}Sn_{30}$-12MA sample, before and after surface polishing. The XRD pattern peak intensities from before polishing the surface correspond to the SiO_2, Si, β-Sn and SnO phases. The intensity of SiO_2 peak at 2θ angle = 26.19° (ICDD card 01-075-1555) is quite high which suggests oxidation of silicon along with Sn had occurred during hot pressing. The formation of SiO_2 at such low temperatures was observed in all the other hot-pressed samples. Several investigations in the past have also demonstrated the formation of this native silicon oxide around these temperatures [170]. Conversely, the formation of silicon oxide did not occur during the pressure-less sintered samples i.e., in consolidation process 1, which suggests pressure plays a very crucial role. Kurosawa et al. [75] in their study have also observed that there is a correlation between the oxide thickness and the applied pressure. By increasing the pressure, a faster oxidation rate exists, and thicker oxidized layers are formed. After surface polishing (Fig. 69), the XRD pattern peak intensities correspond to Si, β-Sn and SnO phases and SiO_2 layers were no longer detected. The tin oxide (SnO phase) was also detected in the case of compacted and sintered samples at 220 ºC (consolidation process 1). The tin oxide formed during hot pressing corresponds to the tetragonal stannous tin oxide (SnO) phase (ICDD card no. 01-085-0423).

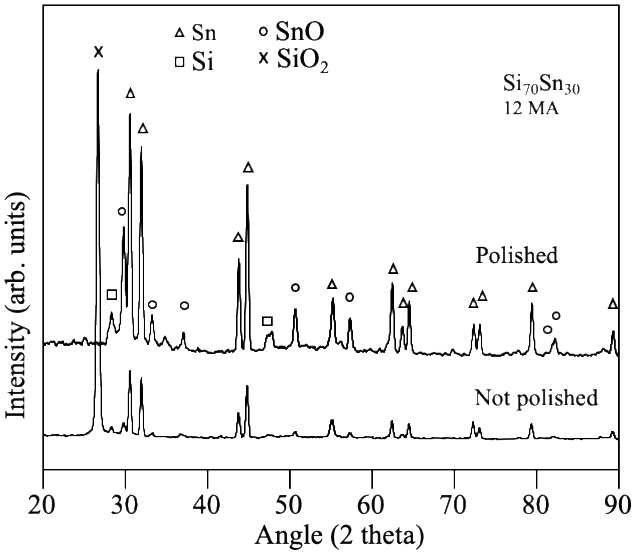

Figure 69. XRD pattern of the hot pressed $Si_{70}Sn_{30}$-12MA sample, before and after surface polishing, as a typical example of all the other samples.

TEM analysis on sample $Si_{70}Sn_{30}$-12MA (Fig. 70) at separate zones i.e., surface (not polished) and bulk (polished) were performed to confirm and validate the XRD results. The HR-TEM image (Fig. 70 (a)) on the surface confirmed crystalline zones ascribed to the (101) lattice fringe of the SiO_2 phase (d = 0.34 nm). The HR-TEM image (Fig 70 (b)) from the bulk present the lattice fringes corresponding to (002) (d = 0.24 nm) and (101) (d = 0.27 nm) of SnO and β-tin phases, respectively (ICDD card no. 01-085-0423 for SnO and 01-086-2265 for β-Sn phases, respectively).

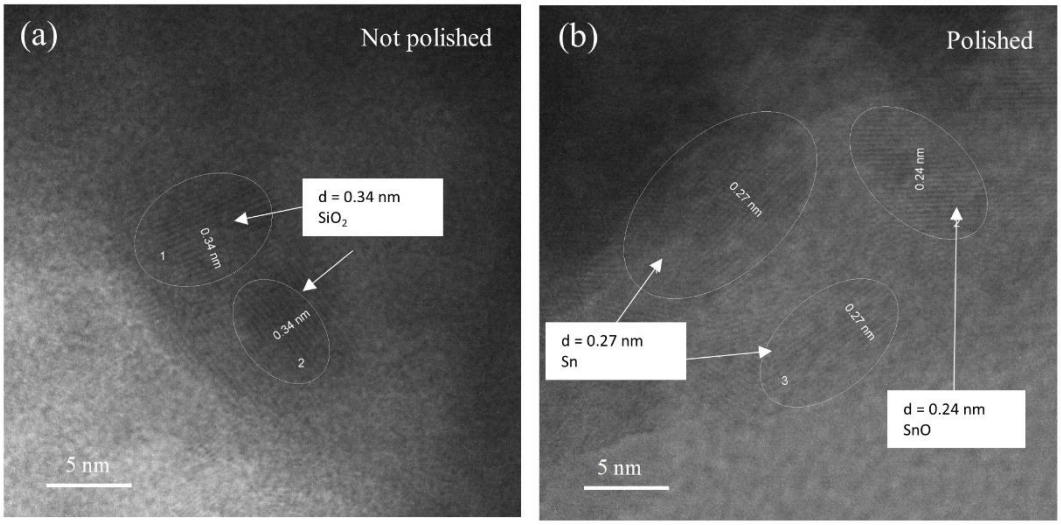

Figure 70. TEM images of (a) not polished, and (b) polished surface of the $Si_{70}Sn_{30}$-12MA sample.

Figures 71 (a) and (b) shows the SEM image and EDS analysis (elemental mapping), respectively, of the hot-pressed $Si_{70}Sn_{30}$-12MA sample after polishing. The surface morphology reveals a rather uniform homogeneous microstructure, formed of well-defined silicon grains (dark regions) having an average size close to 1 µm and Sn in the form of β-tin phase (bright regions) which are embedded into a Si matrix. A small amount of tin was observed in the silicon grains and vice-versa, which is an indication of the low solubility of these elements towards one another.

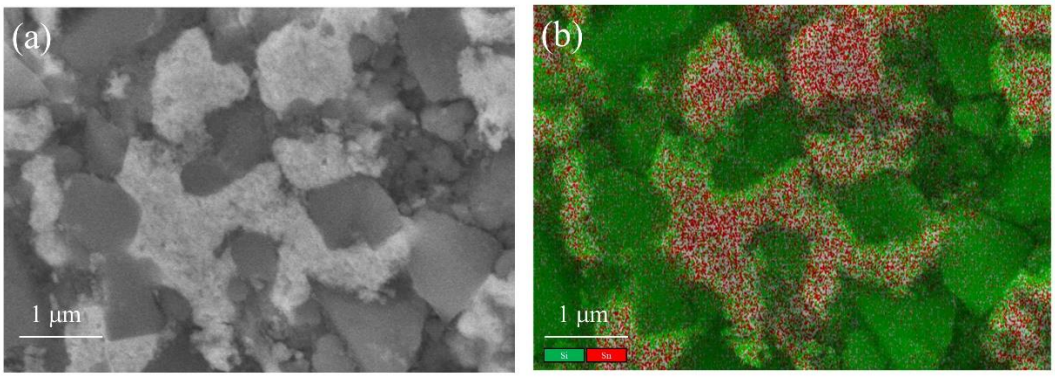

Figure 71. (a) SEM image, and (b) EDS Si and Sn elemental maps of the hot-pressed $Si_{70}Sn_{30}$ - 12MA sample, after polishing.

Figures 72 (a) and (b) shows the pore size distribution and porosity levels of the 4 and 12 hours MA and hot-pressed (consolidation process 2) samples in the range of 0.01 to 10 µm. The pores distribution of the hot-pressed Si-Sn samples are localised at higher values (between 0.1 and 0.20 µm) as compared to the sintered Si-Sn samples (consolidation process 1). Furthermore, the levels of porosity achieved are higher for most of the samples. This behaviour may be explained by the formation of the SiO_2 layer on the surface of these samples. The silicon oxide layer acts as a thermal insulator and could have lowered the temperatures inside the samples during the ongoing hot-pressing process. As a consequence, this potentially can lead to a lower diffusivity and a higher level of porosity for samples prepared by consolidation process 2.

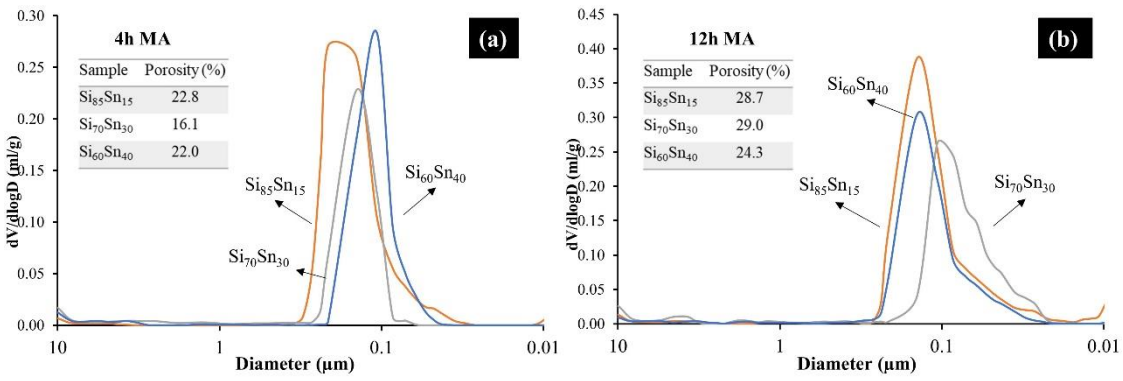

Figure 72. Pore size distribution of the hot-pressed $Si_{85}Sn_{15}$, $Si_{70}Sn_{30}$ and $Si_{60}Sn_{40}$ samples, mechanically alloyed for (a) 4 and (b) 12 hours.

Electrical response of Si-Sn alloys towards relative humidity

The electrical response towards changes in relative humidity for the Si-Sn alloys prepared by consolidation processes 1 and 2 was investigated using complex impedance spectroscopy.

Figure 73 represents Nyquist plots and impedance modulus versus relative humidity graphs for samples $Si_{85}Sn_{15}$-4 MA and $Si_{85}Sn_{15}$-12 MA prepared by consolidation process 1 (cold compaction and sintering). The Nyquist plots for both the samples (Figs. 73 (a) and (b), respectively) exhibit impedance measurements with large amounts of dispersion, especially at higher frequencies. For sample $Si_{85}Sn_{15}$-4 MA (Fig. 73 (a)), the trendline with second order on the polynomial function represents a semi-circular curve derived from the interaction of grains and grain boundaries response behaviour with humidity. The impedance modulus versus relative humidity graph at 1 kHz (Fig. 73 (c)) does not show any variation with relative humidity changes. Fig. 73 (b) shows the Nyquist plot for sample $Si_{85}Sn_{15}$-12 MA; the response was better than the previous sample but still inadequate to yield any significant electrical response towards changes in humidity. These results are confirmed by the impedance modulus versus relative humidity variation curve (Fig. 73 (d)), which shows a small *p*-type variation with relative humidity (%). However, these variations are still inconsequential to be considered for humidity-based applications.

These electrical results could be explained in terms of XRD patterns, SEM images, and pore size distributions (Figs. 65, 67, and 68) mentioned in the previous sections. The XRD results for both samples show some formation of SnO phases, which negatively impacts the electrical properties for humidity sensing (the SnO_2 phase favours sensing behaviour instead) [171]. SEM images for 4 hours milled, cold compacted, and sintered samples reveal big particles with non-structural homogeneity, whereas contrasting results were obtained after 12 hours milled samples where particle size was significantly reduced, resulting in a distinctive homogeneous structure. Porosity results for samples $Si_{85}Sn_{15}$-4 MA and $Si_{85}Sn_{15}$-12 MA reveal higher porosity values among all the samples prepared using consolidation process 1. However, the volume of the pores in the mesoporous range is almost inexistent. Still sample $Si_{85}Sn_{15}$-12 MA has slightly better porosity close to the mesoporous region. Hence, the $Si_{85}Sn_{15}$-12 MA sample's behaviour was comparatively better than sample $Si_{85}Sn_{15}$-4 MA; yet not enough to respond to humidity sensing mechanisms.

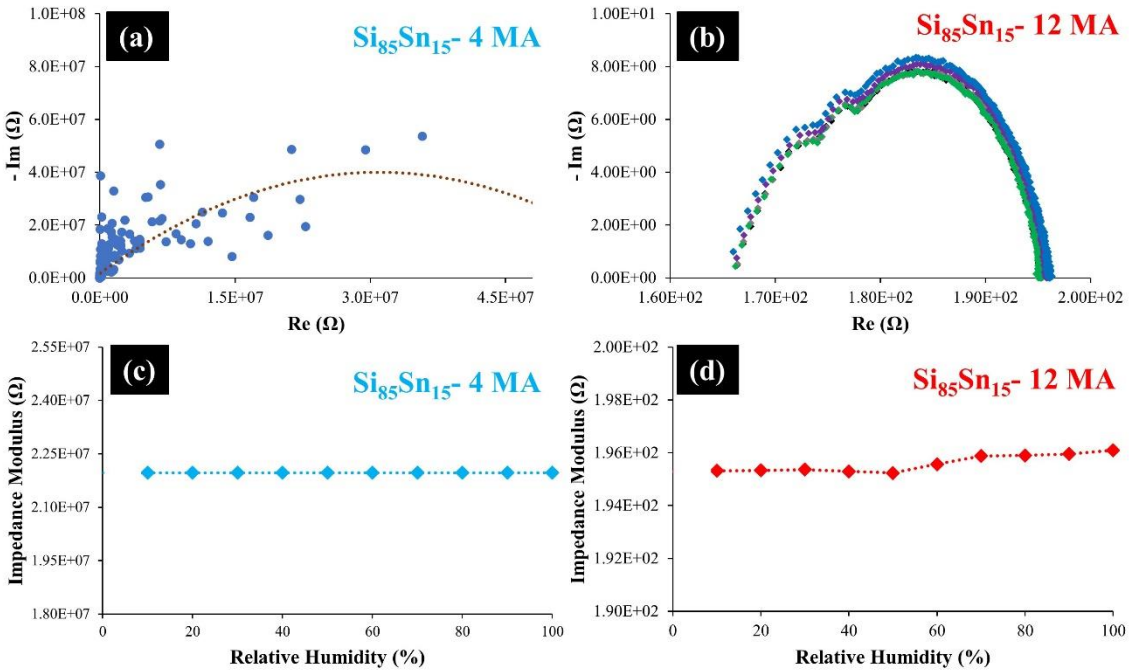

Figure 73. Nyquist, and impedance modulus plots for samples $Si_{85}Sn_{15}$-4MA ((a) and (c)), and $Si_{85}Sn_{15}$-12MA ((b) and (d)) prepared by consolidation process 1.

Figure 74 shows the Nyquist and impedance modulus graphs of samples $Si_{85}Sn_{15}$-4 MA and $Si_{85}Sn_{15}$-12 MA prepared by consolidation process 2 (hot pressing). The Nyquist plots for both the samples (Figs. 74 (a) and (b), respectively) exhibit impedance measurements with a lot of dispersion around the obtained trendline values. And in this case, it was only after considering a trendline of second order on the polynomial function that predicted the trend's shape due to the interaction between surface features and water molecules. The high values of the impedance spectra observed drive us to conclude about the domination of a "capacitive type" behaviour for these samples (i.e., the potential barriers are too high for the charge carriers to cross, and so they display a behaviour similar to capacitors with a dielectric in between plates, with high relative permittivity making it harder for the conduction paths to get established). The impedance modulus versus relative humidity (%) curves at 1 kHz (Figs. 74 (c) and (d), respectively) are constant i.e., there is no change in the conduction behaviour to relative humidity changes.

These electrical results could be addressed in terms of pore size distribution curves (Fig. 72) which show significant amounts of porosities but not in the mesoporous regions. The size of the pores here is bigger than the kelvin radius, which does not participate in the humidity sensing mechanisms [172].

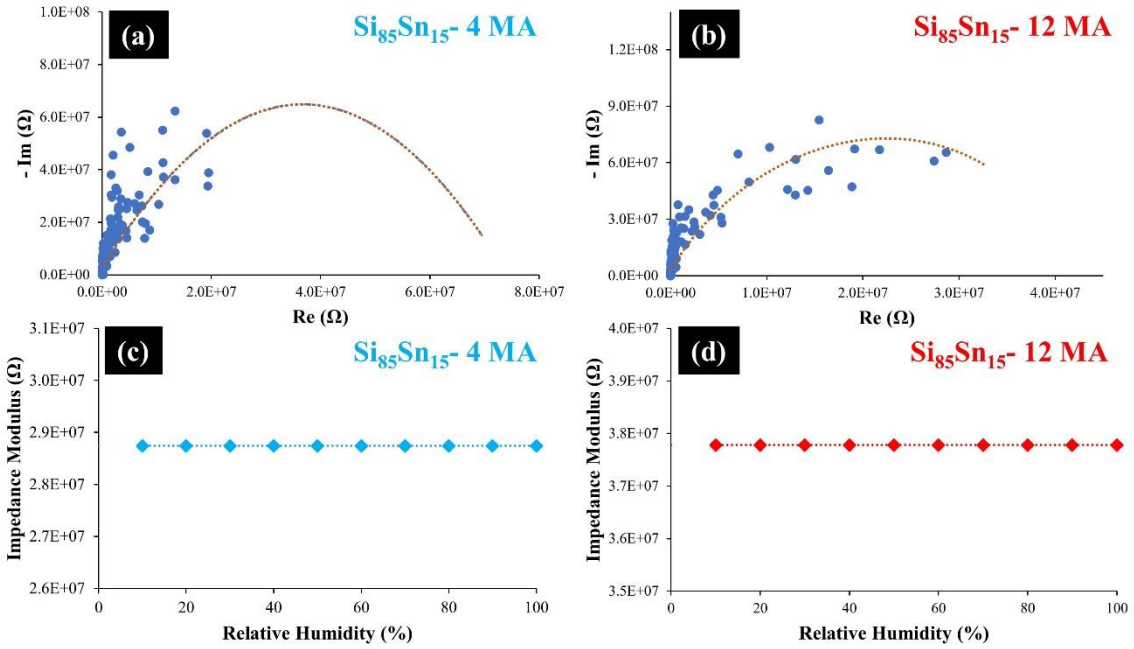

Figure 74. Nyquist and impedance modulus plots for samples $Si_{85}Sn_{15}$-4MA ((a) and (c)) and $Si_{85}Sn_{15}$-12MA ((b) and (d)) prepared by consolidation process 2.

It should be noted here that all the samples with similar consolidation routes (processes 1 and 2) had identical electrical behaviour; hence only a few were considered for the results and discussion section.

Several factors, like chemical composition, morphology, roughness, and porosity are together responsible for better humidity detection. And this was not the case with Si-Sn samples prepared from mechanical alloying followed by consolidation, which yielded only a portion of these factors hence these samples were unsuitable for humidity detection.

Conclusion

Si-Sn alloys with different chemical compositions ($Si_{85}Sn_{15}$, $Si_{70}Sn_{30}$ and $Si_{60}Sn_{40}$) were produced from Si and Sn elemental powders using mechanical alloying for two different milling times of 4 and 12 hours. After 4 and 12 hours of milling, the structural study does not reveal any shift in the diffraction planes of the Si and Sn phases. This indicates that no new phases are formed during either milling time. The crystallite size for the β-tin phase decreased from 87 nm (Sn elemental powder) to 59 nm, and 52 nm for sample $Si_{70}Sn_{30}$ milled for 4h and 12h, respectively. The degree of crystallinity also decreased from 89 % (for initial powder) to 77 % and 70 % for sample $Si_{70}Sn_{30}$ milled for 4 and 12 hours, respectively. The morphology of milled powders shows a relatively homogeneous distribution of the Si and Sn powders at different compositions. However, for samples, $Si_{60}Sn_{40}$ milled for both 4 and 12 hours, the microstructure shows some Sn-rich regions. This is due to the high tin presence in these samples, which causes tin clustering during milling as the welding parameter predominates. This is also confirmed by particle size distribution measurements where d_{50} values are significantly higher for $Si_{60}Sn_{40}$ milled for both 4 and 12 hours.

Once milled, the alloyed powders were consolidated by two different compaction routes. First, cold uniaxial pressing followed by sintering at 220 °C for 3 hours. Structural observations resulted in the formation of a new SnO phase in addition to the former Si and Sn phases. This was due to the high possibility of oxygen incorporation into the powders during the mechanical alloying process from stearic acid (acting as a process control agent), which at high temperature reacts with Sn to form the SnO phase (formation of SnO phase is favoured over the SnO_2 phase at these temperatures). The surface morphology for most of the samples was not much different from the powder analysis after milling. The samples $Si_{70}Sn_{30}$ and $Si_{60}Sn_{40}$ milled for 12 hours unveiled the formation of Sn crystals (whiskers) which dominated the surface. This could be due to dynamic recrystallization and compressive stress levels around the grain boundaries. The porosity and roughness values for these samples were quite high. The pore size distribution for samples milled for 4 hours was relatively uniform and also had similar porosity values. Contrary, pore size distribution and porosity varied a lot for samples milled for 12 hours. The second consolidation process is the hot pressing of powders at 240 °C. The structural study revealed diffraction peaks corresponding to Si, Sn and SnO phases. These results were also confirmed at high magnification using a transmission electron microscope. The microstructure for these samples was relatively homogeneous, with the β-tin phase embedded in the well-defined Si grains. When compared with sintered samples, the pore size distribution of hot-pressed samples is concentrated at higher values (0.1 – 0.2 µm). The levels of porosity were also higher for hot-

pressed samples. This was because of the formation of the SiO_2 layer on the surface. Which acted as thermal insular and resulted in lower diffusivity for the samples below this layer.

The electrical response towards changes in relative humidity for Si-Sn alloys prepared by MA and followed by both consolidation routes 1 and 2 were investigated using complex impedance spectroscopy. The humidity-sensing response of these alloys were not promising. This could be explained by the higher concentration of large-sized pores for these samples, which have a radius greater than kelvin radii that do not show a good response toward relative humidity change. The extremely high roughness values obtained for these alloys also affect the interaction of water molecules with the alloy surfaces resulting in non-uniform impedance characteristics and no response toward change in relative humidity.

4.2. Si-Sn-X (Ti, Cu, and Zn) systems

The production and characterisation of the Si-Sn-X (Ti, Cu, and Zn) alloy systems, synthesised using radio frequency magnetron sputtering, are the main objectives of this section. The thin films fabricated from each alloy system are individually characterised using structural, morphological, chemical, mechanical, and electrical techniques. Complex impedance spectroscopy was the electrical technique used to study the thin film's response to the changes in relative humidity (RH).

4.2.1 Silicon-tin-titanium (Si-Sn-Ti) thin films produced by RF-magnetron sputtering

Abstract

Thin Si-Sn-Ti films were deposited from Si, Sn targets and Ti- pellets by radio frequency magnetron sputtering. The two sets of samples were produced using 400 and 500 W power on the Si target while power on the Sn-target was kept constant at around 40 - 50 W. Different concentrations of titanium were incorporated into the films by varying the no. of Ti-pellets during each deposition. All the depositions were carried out at a vacuum pressure of 1 Pa (only one deposition was performed at 0.7 Pa for comparison purposes). During these depositions, Ti content varied from 3.1 to 13.6 % (at.). Most of the films were amorphous and quasi-amorphous except for a film where the tin content was above 28 % (at.). Thin films had uniform globular surface morphology with the cross-section suggesting compact in conjunction with a slight columnar structure. The roughness values were also similar for all the thin films. Samples S_8 and A_8 (deposited at similar conditions with 400 and 500 W of power on the Si target, respectively) had distinct pore size distributions and porosity values. This change also affected the electrical response of these films towards changes in relative humidity. A_8 film prepared at 500 W on the Si-target presented a better electrical response in the humidity range of 10 – 90 % RH. This film showed a p-type conduction behaviour. This film's electrical responses 1 and 6 months after were also analysed and showed quite stable responses till 70 % RH, after which they suffered from ageing effects.

Deposition parameters for Si-Sn-Ti thin films

The Si-Sn-Ti thin films were co-deposited using Si (99.999%), Sn (99.99%) targets and Ti-pellets (99.8% purity, and 5 mm x 5 mm x 0.15 mm) placed onto the erosion zone of the Si target. The depositions were carried out in Edwards equipment using RF-magnetron sputtering and the parameters for the deposition are listed in Table 13. Two series of depositions were made namely S and A series. The prefix 'S' on the sample name refers to the depositions performed at constant power on Si target of 400 W, whereas prefix 'A' represents depositions at constant Si target power of 500 W. The suffix in the sample's name represents the number of Ti pellets used during the depositions. All the depositions were performed at 1 Pa pressure with the exception of thin film 'S25-LP' where deposition pressure was 0.7 Pa.

Table 13. Deposition parameters for the formation of Si-Sn-Ti thin films.

Sample name	Target power (W)		Number of Ti-pellets	Deposition pressure (Pa)	Deposition time (min.)
	P_{Si}	P_{Sn}			
S_4	400	50	4	1	60
S_6	400	50	6	1	60
S_8	400	50	8	1	60
S_15	400	40	15	1	60
S_25	400	40	25	1	60
S25-LP	400	40	25	0.7	60
A_8	500	40	8	1	60
A_15	500	40	15	1	60
A_25	500	40	25	1	60
A15-Sn	500	75	15	1	60

Chemical composition, thickness, and deposition rates

Table 14 shows the chemical composition, thickness, and deposition rate of the deposited Si-Sn-Ti thin films. Energy dispersive spectroscopy (EDS) analysis was performed on each film to determine the chemical composition of these films. Scanning electron microscopy (SEM) cross-sectional images were used to determine the thickness of the films. Deposition rates were determined using the thickness of the films deposited per unit of time (minute).

Table 14. Chemical composition, thickness and deposition rates of Si-Sn-Ti thin films.

Sample name	Chemical composition (at. %)			Thickness (µm)	Deposition rate (nm/min)
	Si	Sn	Ti		
S_4	73	23.8	3.1	1.3	21.7
S_6	72.4	23.6	4	1.2	20
S_8	70.1	24.5	5.8	1.2	20
S_15	68.3	20.5	11.1	1.1	18.3
S_25	63.3	23.9	13.6	1.0	16.7
S25-LP	63.7	23.9	12.4	1.0	16.7
A_8	71.4	22.5	6.1	1.4	23.3
A_15	70.7	21.3	8.1	1.5	25
A_25	65.6	21.1	13.3	1.2	20
A15-Sn	59.9	31.8	8.3	1.4	23.3

For both S and A- series films, Figures 75 (a) and (b) illustrate the amount of titanium in terms of at. % and thickness of the films, respectively, as a function of the number of Ti pellets employed during the depositions.

Figure 75 (a) shows an increase in the Ti content with an increasing no. of Ti pellets used in the films. Although, it doesn't follow a linear trend, both S and A- sample series follow similar Ti composition patterns. The three depositions with 15 Ti-pellets (S_15, A_15 and A15-Sn) have reported different amounts of Ti contents (11.1, 8.1 and 8.3 at. %, respectively). The depositions A_15 and A15-Sn were performed at high power on the Si and Sn targets and hence, involved a larger number of Si and Sn atoms during depositions. This impacts the final composition of the thin films.

In Fig. 75 (b) for the S-series depositions, the thickness of the films continuously decreases, suggesting the films are becoming more and more compact with the increase in titanium content. However, this variation was not followed for A-series films. Here the thickness first increases with an increase in the number of Ti pellets from 8 to 15, but abruptly decreases with a further increase of pellets to 25. In general, the thickness values are higher for A-series films than S-series films. A-series films are deposited at higher power on the Si target (although power on the tin target was reduced from 50 to 40 W), resulting in more Si atoms being involved in the deposition process. This would result in thicker films or indicates A-series films to be slightly more porous than S-series films.

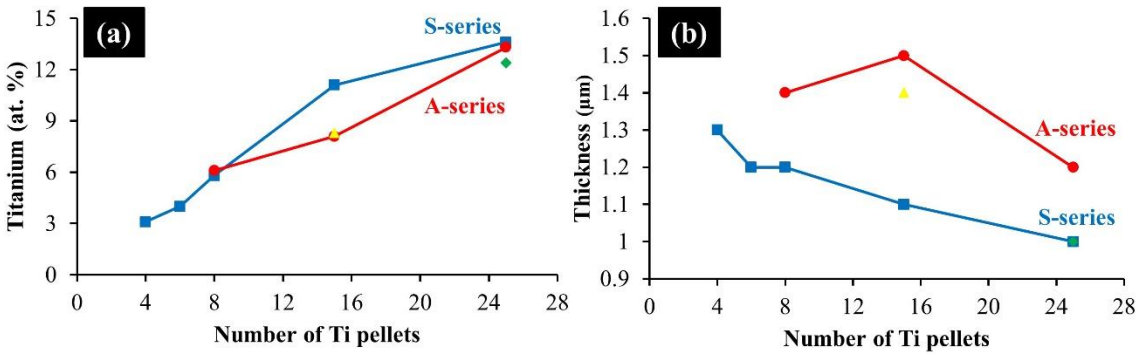

Figure 75. (a) Atomic percentage (at. %) of Titanium, and (b) thickness of the films as a function of number of Ti pellets.

Structural, morphological, porosity, and mechanical characterisation

Figures 76 (a) and (b) show the X-ray diffractogram patterns of Si-Sn-Ti thin films for both S- and A-series, respectively. From the previous study on the Si-Sn system, it was discovered that the films with tin contents lower than 28 % were amorphous in nature. This behaviour was also reflected in Si-Sn-Ti thin films, where lower contents of tin and titanium also stemmed the amorphous nature of films, and no XRD peaks were observed. The increase in titanium and tin contents (totalling close to 28 at. %) represented very small intensities of broad XRD peaks associated with short-range structures. With higher titanium contents in S_25 film, new additional peaks are detected at 2θ values of 38.5°, 55.5°, and 69.6°, attributed to (110), (200) and (211) planes of β-Ti phase (cubic), respectively (ICDD card no. 00-044-1288). Deposition with tin content higher than 28%, the A15-Sn film with 31.4% of tin content had additional peaks of β-Sn phase (tetragonal) at 2θ values of 30.6°, 32.0°, 43.9° and 44.9° that correspond to (200), (101), (220) and (211) planes, respectively (ICDD card no. 00-086-2265).

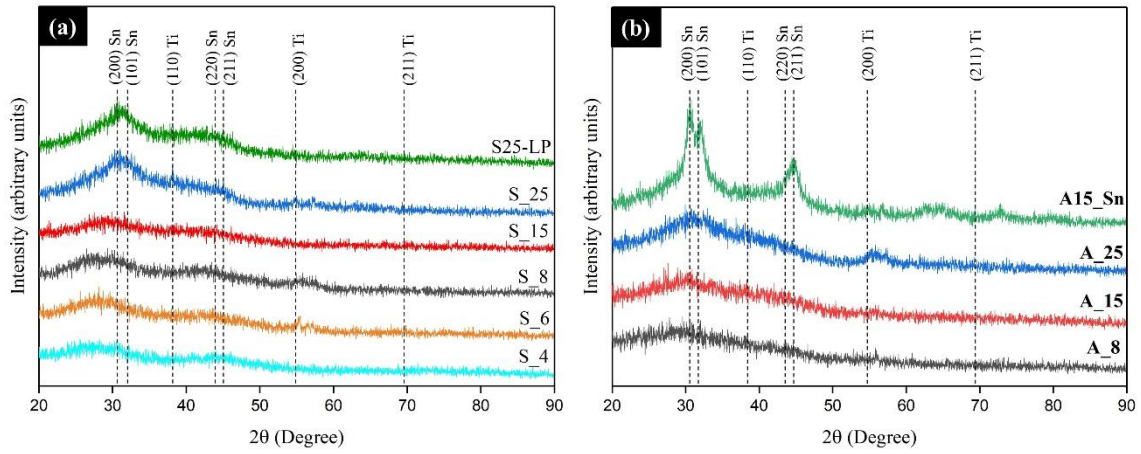

Figure 76. XRD patterns of Si-Sn-Ti thin films: (a) S-series, and (b) A-series

Figure 77 shows the results from TEM and Mössbauer spectroscopy analysis performed on samples S_15 and S_8 respectively.

High-resolution transmission electron microscopy, HRTEM image (Fig. 77 (a)) and selected area electron diffraction, SAED pattern (Fig. 77 (b)) from sample S_15 ($Si_{68}Sn_{21}Ti_{11}$) represents a typical amorphous structure with two broad and diffusion SAED rings. These amorphous rings correspond to the *a*-Si phase. The absence of any crystalline phases validates the XRD results, giving us an understanding that even 11.1 at. % of Ti in the a-Si matrix is not adequate for fabricating Si-Sn-Ti films with crystalline Ti.

Mössbauer spectrum (Fig. 77 (c)) from sample S_8 exhibits only one large asymmetric singlet peak with an isomer shift of 2.1 mm/s. Although the optimal isomer shift for crystalline β-tin is 2.4 mm/s, there is a small change in isomer shift this could be because tin atoms here have been embedded in an amorphous Si matrix, which results in a decrease in the electron density and consequently lowers the isomer shift value. This is a usual phenomenon for the systems-dominated phases other than tin. This behaviour was also explained in the previous study on the Si-Sn system [85,173]. This behaviour also explains why there was no Sn crystalline phase detected during TEM analysis. Mössbauer spectrum also confirms that there is no phase formation between tin and titanium, although the S_8 thin film contains around 5.8 and 24.5 at. % of Ti and Sn, respectively.

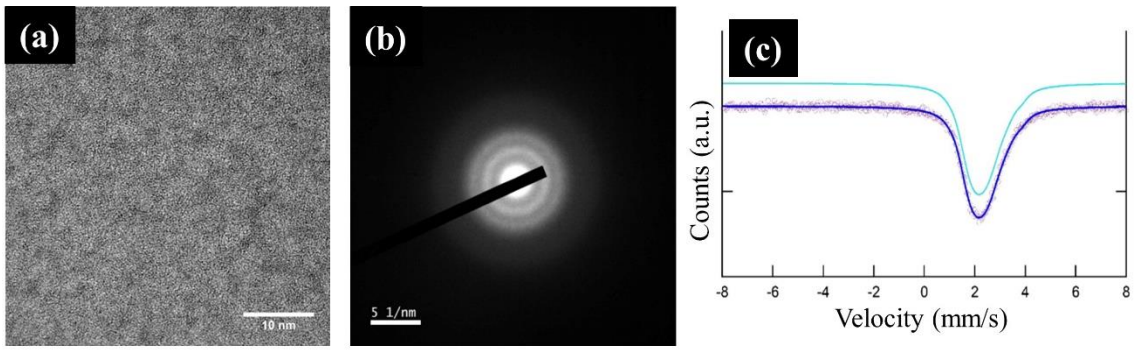

Figure 77. (a) HRTEM image, (b) SAED pattern of sample S_15 and (c) Mössbauer spectrum of S_8.

Figures 78 and 79 show the SEM (surface and cross-section) and AFM (topography and 3D feature) images to study surface morphology and roughness, respectively, of the deposited Si-Sn-Ti thin films.

Figure 78 (a) to (f) shows the SEM surface and cross-section images of the deposited S-series thin films. The surface morphology of these films is comprised of uniform globular features. The cross-section images reveal columnar and slightly denser or compact thin films. Thin film S25-LP (Fig. 78 (f)) appears to be more compact than other films, this could be explained as the thin film was deposited at lower pressure (0.7 Pa). Figure 78 (g) to (j) presents

SEM images of A-series Si-Sn-Ti thin films. The surface morphology of these films show uniform globular surface features. The cross-sectional images exhibit the films to have a columnar growth with a more porous structure when compared with S-series films. The surface morphology of the film A15-Sn (Fig. 78 (j)) with a tin content of 31.4 % has a slightly different morphology which is referred to as cauliflower-type morphology and the cross-section appears to be like S-series samples i.e., compact.

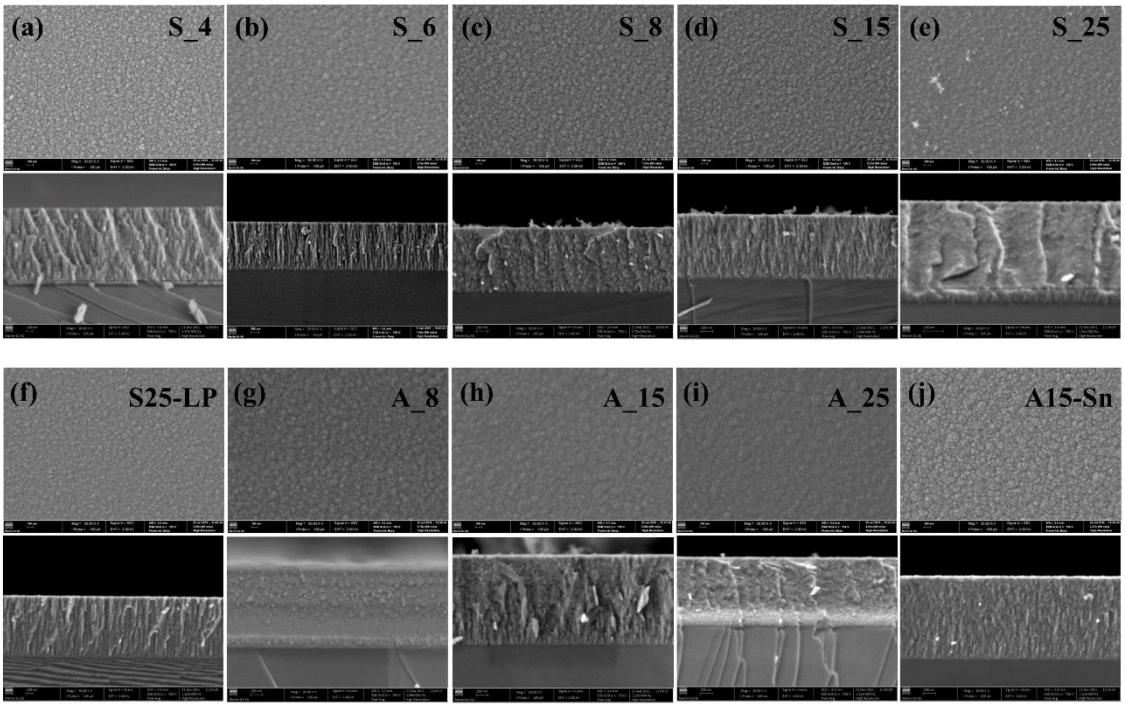

Figure 78. (a) to (j), SEM images showing the surface and cross-section of the Si-Sn-Ti thin films.

Figure 79 shows the AFM images of both S-series ((a) to (f)) and A-series ((g) to (j)) samples. The A-series samples appear to have larger topographical features than the S-series samples. Table 15 shows the roughness (R_a and R_{rms}) values of the thin film samples calculated from AFM images using Gwyddion software. The S-series of thin films does not have any significant variation in roughness values. The mean roughness (R_a) values vary from 3.7 to 4.0 nm. The sample S25-LP deposited at the low vapour pressure of 0.7 Pa, had a R_a value of 3.6 nm, which was slightly lower than the roughness of other S-series films. The roughness values of A-series thin films do not follow a uniform pattern. They have a large variation in the roughness values varying from 3.6 to 4.6 nm (sample A15-Sn had a R_a value of 4.9 nm). Overall, we can conclude the A-series samples possess higher roughness than the S-series samples.

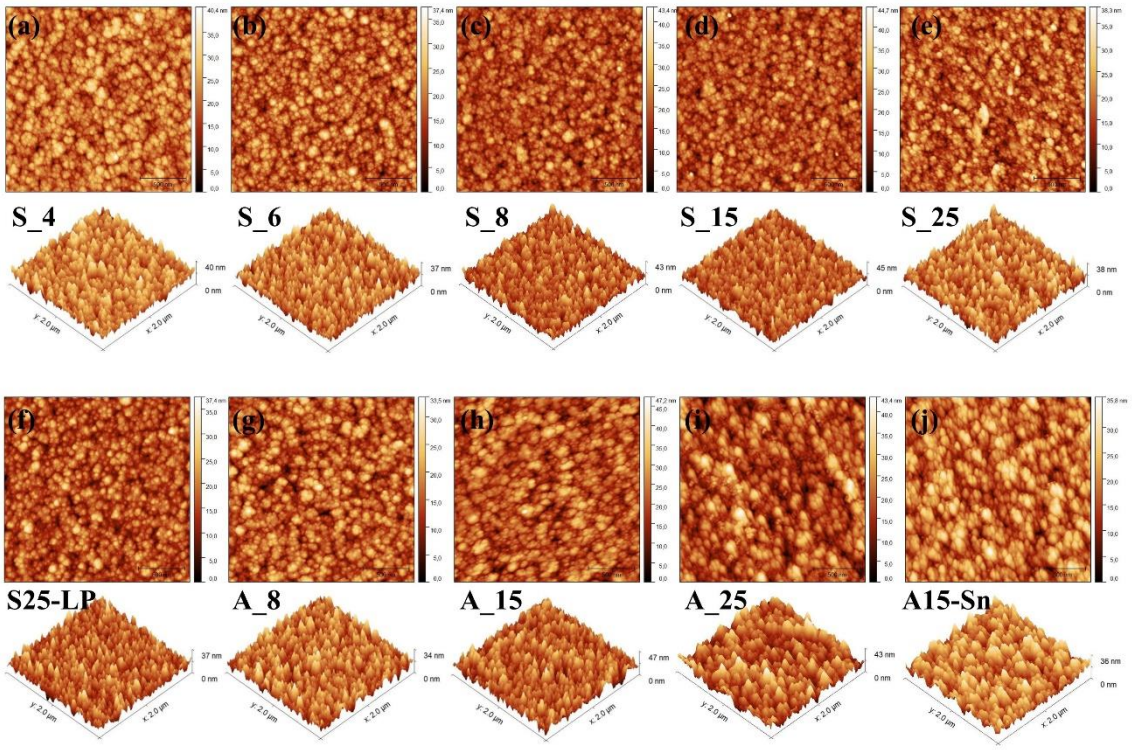

Figure 79. (a) to (j), AFM topography and 3D images for Si-Sn-Ti thin films.

Table 15. Roughness parameters for Si-Sn-Ti deposited thin films.

Roughness parameter	Sample name									
	S_4	S_6	S_8	S_15	S_25	S25-LP	A_8	A_15	A_25	A15-Sn
R_a (nm)	4.0	3.7	3.8	3.9	4.0	3.6	3.6	4.6	4.1	4.9
R_{rms} (nm)	5.0	4.7	4.8	4.9	5.1	4.5	4.5	5.8	5.1	6.2

Figure 80 shows the graphs of logarithmic differential curves versus pore size distribution for samples A_8 and S_8. The plots show a higher no. of mesopores for sample A_8 with the majority of the pores around 5 to 100 nm whereas sample S_8 has lower porosity in the mesoporous region. According to the Washburn equation [160], the total amount of porosity levels were 17.2 and 12.1 % for samples A_8 and S_8, respectively. Higher porosity in the mesoporous region favours the water vapour adsorption mechanisms and capillary condensation for good sensitivity and response towards humidity sensing applications. Hence, we can conclude that sample A_8 has a better ability to respond towards change in relative humidity. However, it should be noted that pore sizes greater than 1 micron don't have any effect on the humidity sensitivity as they serve as a passage for the water vapour.

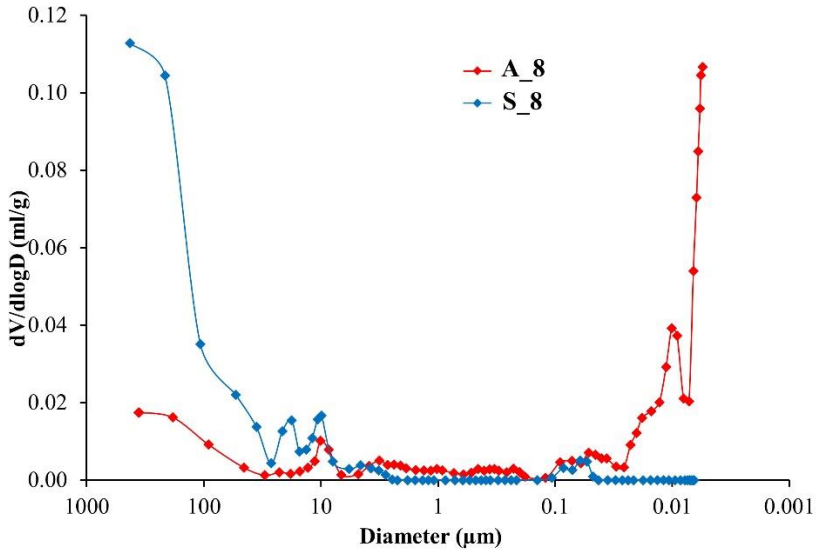

Figure 80. Pore size distribution of thin films A_8 and S_8.

The hardness values obtained from the thin films are presented in Figure 81. For the S-series, the hardness curve follows an increasing trend except for both samples with 25 pellets (S_25 and S25-LP). However, S25-LP has a slightly higher hardness value since the film was deposited at low pressure and was slightly more compact than the S_25 film with the same number of pellets deposited at high pressure. For the A-series, the hardness curve shows a constant decrease in the hardness values, which cannot be properly explained as there is an increase in the no. of Ti pellets from thin films A_8 to A_25. The A15-Sn film with the highest amount of tin content shows a significantly low hardness value. This was expected as Sn is a much softer metal among Sn, Si and Ti with a hardness value of 0.4 GPa. (Hardness of Si and Ti are 5 GPa and 1.1 GPa, respectively [161,174])

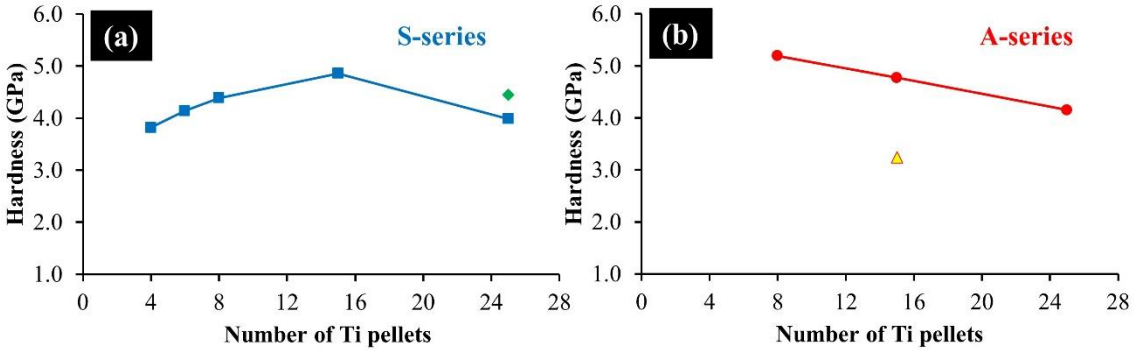

Figure 81. Hardness curves of (a) S-series, and (b)A-series of Si-Sn-Ti thin films.

Humidity response of Si-Sn-Ti thin films:

Figure 82 shows the Nyquist and impedance modulus plots for two samples, A_8 and S_8, prepared at similar deposition conditions except for the power on the Si target, which was 500 and 400 W, respectively. Although, SEM and AFM images (Figs. 78 and 79, respectively) reveal morphology and surface roughness characteristics, respectively which slightly favour sample over S_8 sample. The mercury intrusion porosimetry exhibits completely different levels of porosities (Fig. 80), especially in the desired mesoporous region. Sample A_8 has an overall 17.2 % porosity, whereas it is 12.1 % for the S_8 sample. These porosity levels could be due to higher adatom mobility for depositions at higher Si target power (500 W), which results in slightly porous films than thin films deposited at Si target power of 400 W (S_8). These results concluded that sample A_8 could be potentially better for humidity sensing applications.

The Nyquist plots of sensors A_8 and S_8 (Figs. 82 (a) and (c), respectively) are entirely different from each other. They are typically composed of semicircles arising from the interaction of the water molecules with the grains and grain boundaries. The variation in the Nyquist plots, i.e., the area under the impedance spectra, is continuously increasing for sample A_8 concerning increase in relative humidity. In contrast, the change in area under the impedance spectra for sample S_8 is almost insignificant. The changes in impedance spectra area for sample A_8 is due to the changes in the electrical conductivity and polarisation phenomenon that occur with an increase in relative humidity. The electrical response of a sensor to relative humidity changes depends on the water molecule adsorption through chemisorption and physisorption phenomena. At lower humidity levels, water molecules are chemisorbed using proton hopping, whereas at high humidity levels, the physisorption process is dominant, and Grotthuss chain mechanisms occur.

The impedance modulus at 1 kHz with respect to changes in relative humidity for samples A_8 and S_8 is plotted in Figs. 82 (b) and (d), respectively. The impedance modulus of sensor A_8 at 1 kHz (Fig. 82 (b)) increases (decrease in conductivity because of the decrease in free electrons which participate in conduction) with the increase in relative humidity from 10 to 90 %, this type of response is commonly referred to as a *p*-type semiconductor behaviour. However, in this case, the trend possesses a moderate slope. Conversely, for the sensor S_8, impedance modulus (at 1 kHz) variation is almost constant throughout the entire relative humidity range (Fig. 82 (d)).

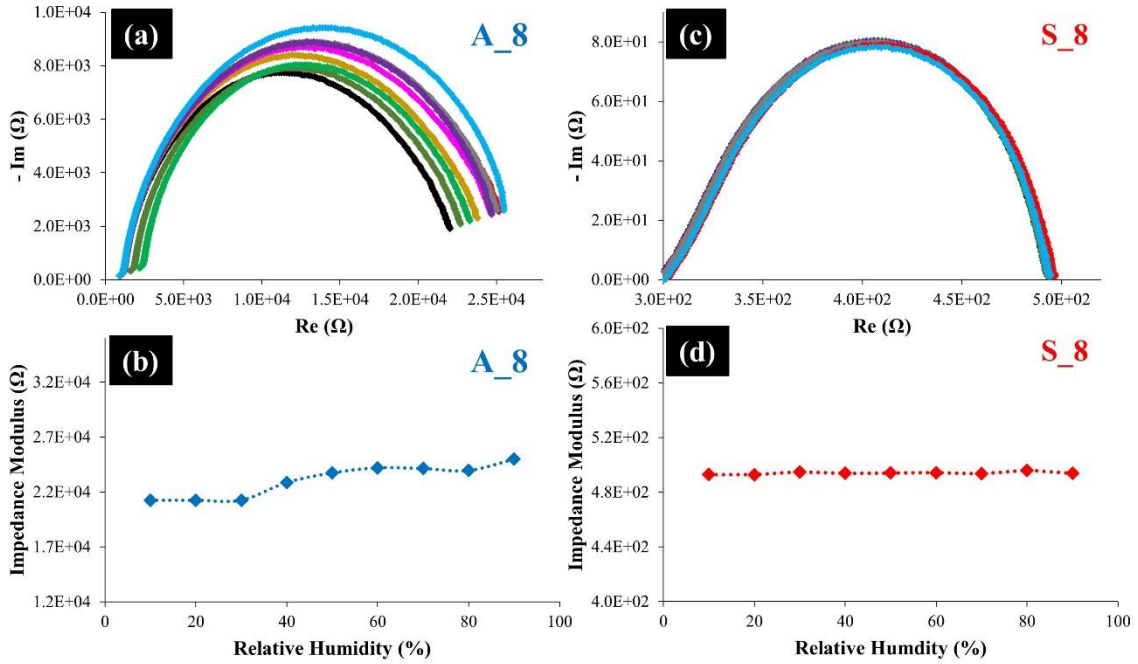

Figure 82. (a) and (c) represent Impedance spectra plots of samples A_8 and S_8, respectively (For different relative humidity contents (black, orange, dark green, brown, rose, purple, grey, red, and light blue stands for 10, 20, 30, 40, 50, 60, 70, 80, and 90 % RH, respectively)). And (b) and (d) represent Impedance modulus versus relative humidity plots for samples A_8 and S_8, respectively.

Additionally other samples from S- and A-series, yielded similar electrical response towards changes to relative humidity and therefore were not considered for the citation. The electrical results from sample S_8 refers to S-series deposited samples whereas A_8 serves as a reference for A-series deposited samples.

Time stability humidity response of sensor A_8

The time stability electrical response for sample A_8 towards change in relative humidity was also recorded 1 and 6 months after the first analysis (i.e., at t = 0 (first run), at t = 1 month (second run) and t = 6 months (third run)). Figures. 83 (a), (b), and (c) represent the impedance spectra in the form of Nyquist plots for all three analyses. Looking at these Nyquist plots, the first thing that can be observed is the sample's humidity response which is similar for all three analyses, but they suffer from an ageing effect which is more significantly visible for measurements taken after 6 months from the first analyses. The Nyquist plot at t = 0 (Fig. 83 (a)) shows a constant increase in the area under the impedance spectra indicating a continuous *p*-type behaviour throughout the humidity range (10 - 90 %). Whereas after 1 month, the Nyquist plot (Fig. 83 (b)) shows a constant *p*-type behaviour from 10 to 70 % RH and then a sudden change in conduction behaviour from a *p*- to *n*-type transition. This *n*-type behaviour is observed from 70

to 90 % RH. Similar observations were carried out for the measurement at t = 6 months and results are illustrated in Fig. 83 (c).

The impedance modulus plots with variation to relative humidity from 10 to 90% at two different frequencies of 1 and 10 kHz for sample A_8, at t = 0 (first run), at t = 1 month (second run) and t = 6 months (third run) are shown in Figs. 83 (d), (e), and (f). The *p*-type electrical conduction behaviour is more accurately visible for the first run (but the trend displays a very small slope). While a *p*-type conduction behaviour along with a conduction transition from *p*- to *n*-type, at 70 % RH, start to be visible for the second and third runs. The corresponding slopes of the straight trendlines for the RH ranges where *p*-type behaviour is observed at 1 kHz are 41, 76 and 16 Ω/RH(%) for the first, second and third runs, respectively. The slopes computed for 10 kHz were 17, 19, and 12 Ω/RH(%) for the first, second and third runs, respectively. These slopes validate the observations made during the previous section about the performance of these sensors suffering from the ageing effect.

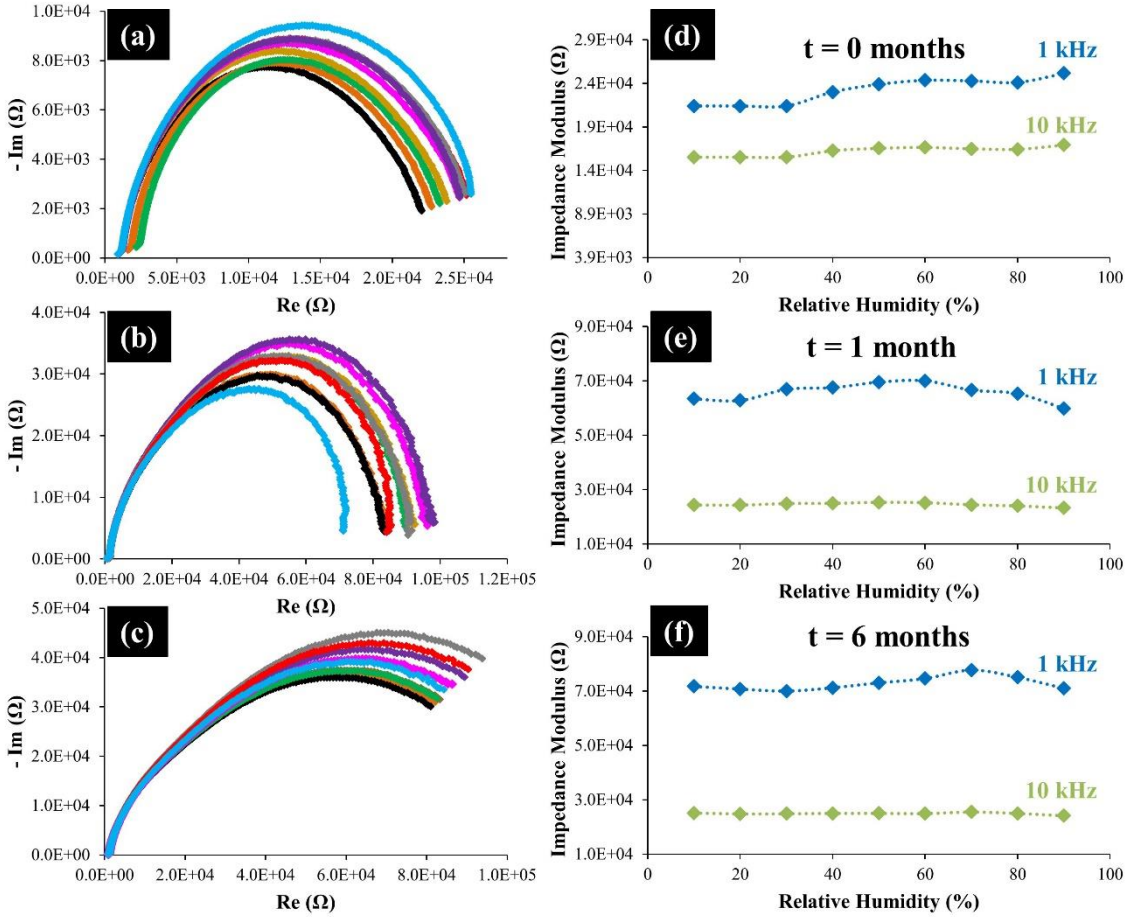

Figure 83. Nyquist plots and Impedance modulus for sample A_8 ($Si_{500}Ti_8Sn_{40}$): (a), (d) initial; (b), (e) after 1 month; and (c), (f) after 6 months. (For different relative humidity contents (black, orange, dark green, brown, rose, purple, grey, red, and light blue stands for 10, 20, 30, 40, 50, 60, 70, 80 and 90 % RH, respectively)).

Conclusion

Silicon-tin-titanium thin films with different concentrations were produced using RF-magnetron sputtering. The two sets of samples were produced at 400 W (S-series) and 500 W (A-series) of power on the Si target, while power on the Sn-target was constant and number of Ti pellets also varied. Most of the depositions were carried out at a vacuum pressure of 1 Pa, with exception of 1 deposition carried out at 0.7 Pa. The atomic Ti concentration varies from 3.1 to 13.6 %, whereas thickness varied from 1.0 to 1.5 μm. In general, the A-series films had a higher thickness value when compared with S-series films. The XRD analysis shows most of the films to be either amorphous or quasi-amorphous. The films with cumulative tin and titanium contents exceeding 28 % showed some weak peaks corresponding to β-Ti and β-Sn phases. These XRD results were also validated using TEM and Mössbauer spectroscopy analysis. The morphological analysis of the films reveals the A-series films to be more columnar and porous than S-series films, particularly when comparing samples, A_8 and S_8 from A- and S- series, respectively. The roughness (R_{rms}) values for A_8 and S_8 samples were very similar (4.5 and 4.8 nm, respectively). The pore size distribution shows a higher no. of mesopores for sample A_8 than S_8. The total porosity is also higher for sample A_8. The humidity response of these samples with respect to changes in relative humidity were analysed using complex impedance spectroscopy. This revealed that sample A_8 is a better sensor for humidity sensing applications with a *p*-type behaviour in comparison to sample S_8. The time stability humidity response of sensor A_8 was also observed at three different times (t = 0, 1, and 6 months). The Nyquist and Impedance modulus plots obtained here revealed the sample's humidity response suffering from ageing.

4.2.2 Silicon-tin-copper (Si-Sn-Cu) thin films produced by RF-magnetron sputtering

Abstract

Si-Sn-Cu thin films were deposited from Si, Sn targets and Cu pellets by radio frequency magnetron sputtering. The two sets of samples were produced at vacuum pressures of 1 and 0.7 Pa. The different concentrations of Cu were incorporated into the films by varying the number of Cu pellets. Thin films were named with a prefix referring to the vacuum pressure they were deposited at (HP for high pressure and, LP for low pressure), whereas the suffix represented the number of Cu pellets used for the depositions (2, 4, 8, and 16). For these depositions, the Cu content varied from 7 to 42.4 at. % and was present in the form of amorphous to quasi-amorphous structure. Some of the films had quasi-amorphous or crystalline nature but it was primarily due to a higher concentration of tin. Morphological analysis of the surface revealed uniform globular features with compact and columnar thin films. The exception to this were samples HP_4 and LP_16 which on further analysis revealed filamentary eruption of tin whiskers on the sample's surfaces. The roughness values are higher for thin films deposited at 1 Pa in comparison with low-pressure deposited films (with of course exception of films HP_4 and LP_16, due to tin whiskering). For most of the samples, the pore size distribution curves do not reveal any significant porosity in the desired mesoporous region. The hardness values are higher for thin films deposited at low pressure, implying the low-pressure films are even more compact and less porous than high-pressure deposited films. The electrical response towards humidity variations for these thin films was measured using complex impedance spectroscopy. The Nyquist plots for samples HP_8 and LP_8 do show the formation of semi-circle curves due to the interaction between grain and grain boundaries with water molecules. But the variation in relative humidity does not reveal any significant changes to the Cole-Cole plots. This behaviour is also confirmed by impedance modulus plots at 1 kHz, which do not reveal sufficient changes in impedance modulus values with changes to relative humidity from 10 to 100 % (the corresponding slopes are almost 0 Ω/RH (%)). Hence, Si-Sn-Cu thin films prepared here are not suitable for humidity-sensing applications.

Deposition parameters for the Si-Sn-Cu thin films

Si (99.999% purity), Sn (99.99% purity) targets, and Cu (99.9% purity, 5 mm x 5 mm x 0.15 mm) pellets were used for the deposition of Si-Sn-Cu thin films. The co-sputtering was performed using RF power sources on Si and Sn targets, while the Cu pellets were placed onto the erosion zone of the Si target. A summary of the deposition parameters is shown in Table 16. Two sets of depositions were carried out under an Argon gas atmosphere at high pressure of 1 Pa, and at low pressure of 0.7 Pa. Thin films with the prefix HP in their sample names were deposited at high pressure (1 Pa) and in contrast, with LP prefix were low-pressure (0.7 Pa) depositions. The number of Cu pellets (2, 4, 8, and 16) employed during the depositions is indicated by the suffix in the sample names.

Table 16. Deposition parameters for the formation of Si-Sn-Cu thin films.

Sample name	**Target power (W)**		**No. of Cu-pellets**	**Deposition pressure (Pa)**	**Deposition time (min.)**
	P_{Si}	P_{Sn}			
HP_2	200	40	2	1	120
HP_4	200	35	4	1	120
HP_8	200	35	8	1	120
HP_16	200	30	16	1	120
LP_2	200	30	2	0.7	120
LP_4	200	35	4	0.7	120
LP_8	200	35	8	0.7	120
LP_16	200	30	16	0.7	120

Chemical composition, thickness, and deposition rates

The Si-Sn-Cu thin film's chemical composition in at. %, thickness (μm), and deposition rates (nm) are presented in Table 17. The chemical composition of the films was determined through energy dispersive spectroscopy (EDS) analysis at the surface. The chemical composition was determined by measuring the intensities of silicon Kα, tin Lα and copper Kα lines. The thickness of the films was measured from cross-sectional scanning electron microscopy images. Deposition rates are defined as the increase in the film thickness (nm) per unit time (minute) and are mathematically calculated.

Table 17. Chemical composition, thickness, and deposition rates of Si-Sn-Cu thin films.

Sample name	Chemical comp. (at. %)			Thickness (µm)	Deposition rates (nm/min)
	Si	Sn	Cu		
HP_2	45.1	47.9	7	1.4	11.7
HP_4	53.1	33.5	13.4	1.0	8.3
HP_8	52.3	25.5	22.2	0.9	7.5
HP_16	39.6	18	42.4	0.9	7.5
LP_2	53.5	38.7	7.8	0.9	7.5
LP_4	55.1	31.1	13.8	0.8	6.7
LP_8	49.7	24.8	25.5	0.9	7.5
LP_16	37.4	30.3	32.3	1.0	8.3

Figures 84 (a) and (b) plots the amount of Cu in terms of at. % and thickness of the films, respectively, against the number of Cu pellets used during the depositions for both sets of samples.

Figure 84 (a) shows a graph describing a constant increase in the at. % of Cu within the films with increasing number of Cu pellets from 2 to 16 for both sets of depositions. This is because the large number of Cu atoms are ejected from increasing the number of Cu pellets, which increases the concentration of Cu within the thin films. However, both sets of depositions do not follow a linear trend, and the slopes for both depositions (high and low pressure) are distinct. The difference in the at. % of Cu was more noticeable for HP_16 and LP_16 samples, where the Cu concentration was 42.4 and 32.3 at. %, respectively. This phenomenon can be explained as at low pressure, the concentration of Ar atoms is lower, which results in the lower number of collisions for all the species present during the depositions, and the densities for all the atoms within the film, including Si, Sn, and Cu should increase. Since the same cannot be said for samples deposited at high pressure where the no. of collisions is higher due to higher number of Ar atoms, also the larger Sn-sized atoms with an atomic mass of 118.7 a.m.u. (atomic mass of Si and Cu is 28 and 63.5 a.m.u., respectively) could lose significant energy during collisions resulting in a decrease in the no. of Sn atoms arriving at the film deposition. Sn concentration for sample HP_16 was 18 at. %, whereas it was 30.3 at. % for LP_16, confirming the hypothesis [158].

Figure 84 (b) illustrates a correlation between the film's thickness and the number of Cu pellets used for the two sets of depositions. The thickness of the films was higher for films deposited at higher pressures than those deposited at low pressure. However, the exception to this were films HP_16 and LP_16, where the observed thickness values were 0.9 and 1 µm, respectively. The factor responsible for this peculiar behaviour was the increase in the atomic

density of the species involved in the lower pressure depositions (explained in the previous section), causing an increase in the deposition rate for sample LP_16 (in comparison with sample HP_16), hence, resulting in the higher thickness value for the sample LP_16. The thickness of the sample HP_2 was also higher (1.4 µm), but this could account for the factor that we used slightly higher power (40 W) on the tin target for this deposition.

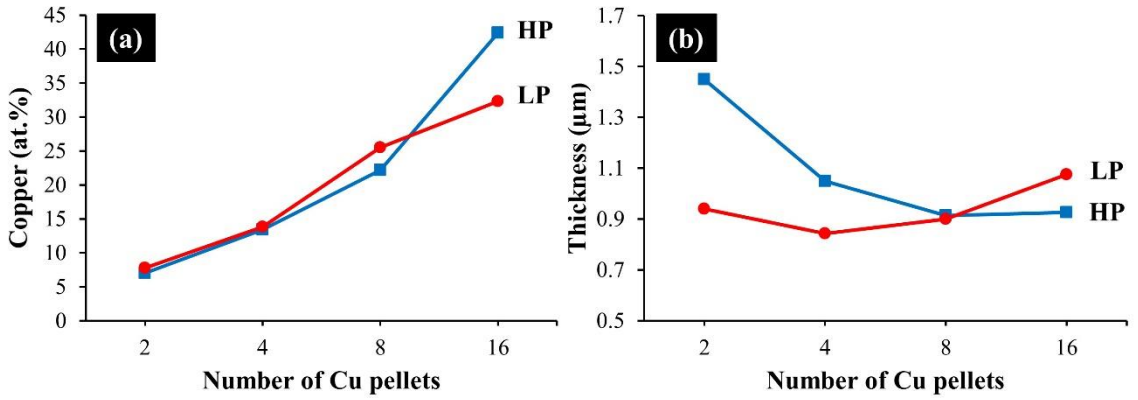

Figure 84. (a) Atomic % of Cu in the films, and (b) thickness of the films as a function of number of Cu pellets.

Structural, morphological, porosity, and mechanical characterisation

The XRD patterns for thin Si-Sn-Cu films deposited at 1 and 0.7 Pa are represented in Figures 85 (a) and (b), respectively. The Si-Sn films with tin (crystalline counterpart) concentrations lower than 28 % were found to have an amorphous structure during earlier investigations. Consequently, the structure of the Si-Sn-Cu films deposited was amorphous/ quasi-amorphous. Some compositions (with higher tin contents, specifically HP_2, HP_4, and LP_16) illustrated XRD diffraction peaks of the β-Sn phase acquired at 2θ values of 30.6°, 32.0°, 43.9°, and 44.9° that correspond to (200), (101), (220), and (211) planes, respectively (JCPDS card no. 00-086-2265). Similarly, films with higher no. of Cu pellets during depositions, the Cu concentration increases, and the crystalline XRD peaks for Cu (cubic) are visible, though have very low intensity at 2θ angles of 43.5°, 50.7°, and 74.7°, corresponding to (111), (200), and (220) planes, respectively (JCPDS card no. 00-001-1242). This happens because Si, which is present in the amorphous form and all the other alloying elements (Sn and Cu) get embedded by substitution into this amorphous matrix produced by the *a*-Si phase. Hence, with the increase in crystalline alloying elements, the nature of the films changes from being fully amorphous (for pure Si film) to quasi-amorphous with the addition of certain amounts of Sn and Cu [83,98,175]. Here, it is worth noting that there are no other crystalline peaks that might correspond to any intermetallic phases between these elements. It should be noted that a peak at 2θ angle = 69.3° corresponds to the substrate Si-wafer with (100) orientation crystalline facet.

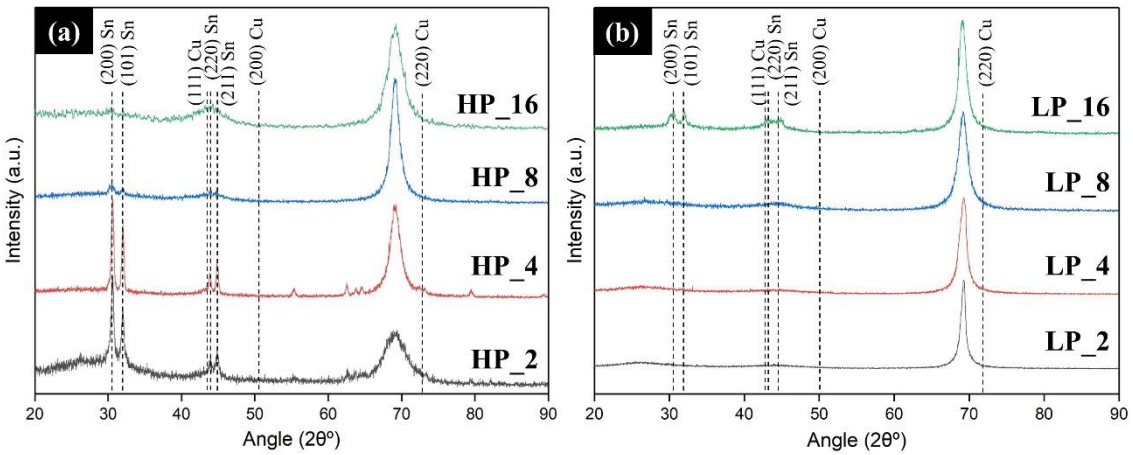

Figure 85. XRD patterns for Si-Sn-Cu thin films deposited at (a) HP and, (b) LP.

Figures 86 (a) shows the HRTEM image to observe the lattice fringes from sample HP_4. The nanoparticles with diameters from 5 to 10 nm embedded in an amorphous matrix were observed. Figure 86 (a) shows two nanoparticles at higher resolution with an atomic lattice fringe of 0.292 and 0.280 nm, corresponding to the (200) and (101) crystal planes of β-Sn phase. The sample HP_4 contains around 33 at. % of Sn and 13 at. % of Cu, then too, there are no lattice fringes corresponding to the Cu crystal phase. Figure 86 (b) shows the SAED pattern from the same sample. This presents the diffuse rings corresponding to the amorphous Si phase and Sn nano-dots at d = 0.292, 0.280, 0.208, 0.202, 0.168, 0.145, and 0.130 nm corresponding to (200), (101), (220), (211), (301), (400), and (411) planes of β-Sn phase (JCPDS card no. 00-086-2265). This confirms that most of the copper is present in the form of an amorphous structure.

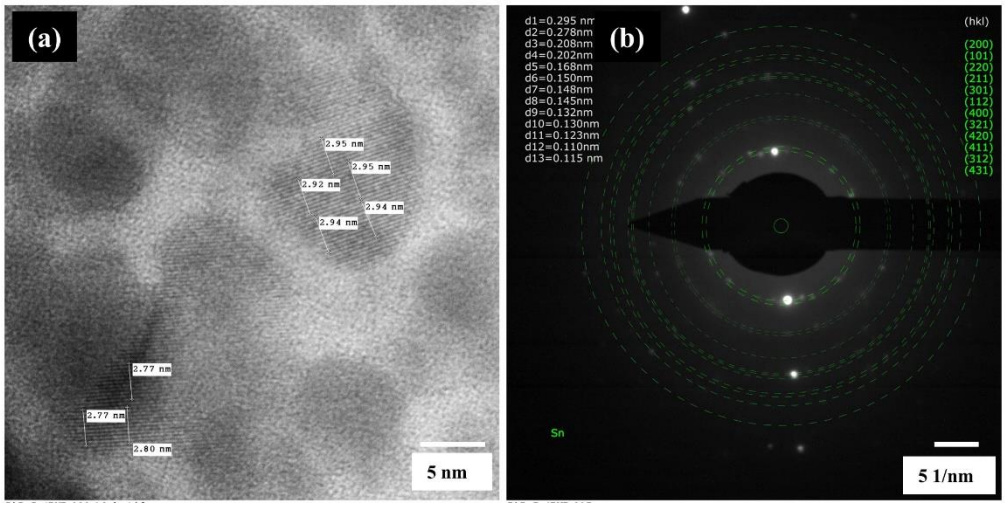

Figure 86. (a) HR-TEM image, and (b) SAED pattern from sample HP_4.

Figure 87 (a) to (p) shows the SEM images at both surface and cross-sections for Si-Sn-Cu thin films. The surface morphology images reveal regular and uniform globular features for all the Si-Sn-Cu thin films and the cross-section images describe the columnar and denser (or

compact) nature of the films. In the previous studies on Si-Sn and Si-Sn-Ti systems, the samples deposited at high vapour pressure resulted in more columnar, porous, and less dense films, and these films were potentially ideal for sensing-based applications. But Si-Sn-Cu-based thin films do not have similar film structures when deposited at high vapour pressures. These differences in the results could be due to the powers used on the Si and Sn targets during depositions; during Si-Sn and Si-Sn-Ti, the target powers used were 400 W (and 500 W) and 25 - 100 W for Si and Sn-targets, respectively. Whereas for Si-Sn-Cu depositions, although the target powers were maintained in the Si/Sn ratios but did not yield similar results (the powers of 200 W and 30 - 40 W on Si and Sn targets were used). Since during depositions, not only deposition pressures but powers on targets also play a significant role in the development of the thin films, thereby decreasing the target powers could have potentially reduced the kinetic energy of the Si, Sn and Cu atoms, affecting the nucleation and growth mechanisms for the development of the thin films.

An exception to the above discussed were samples HP_4 and LP_16. These samples showed the presence of some surface features, which are better revealed at higher magnified images and are discussed in the following section.

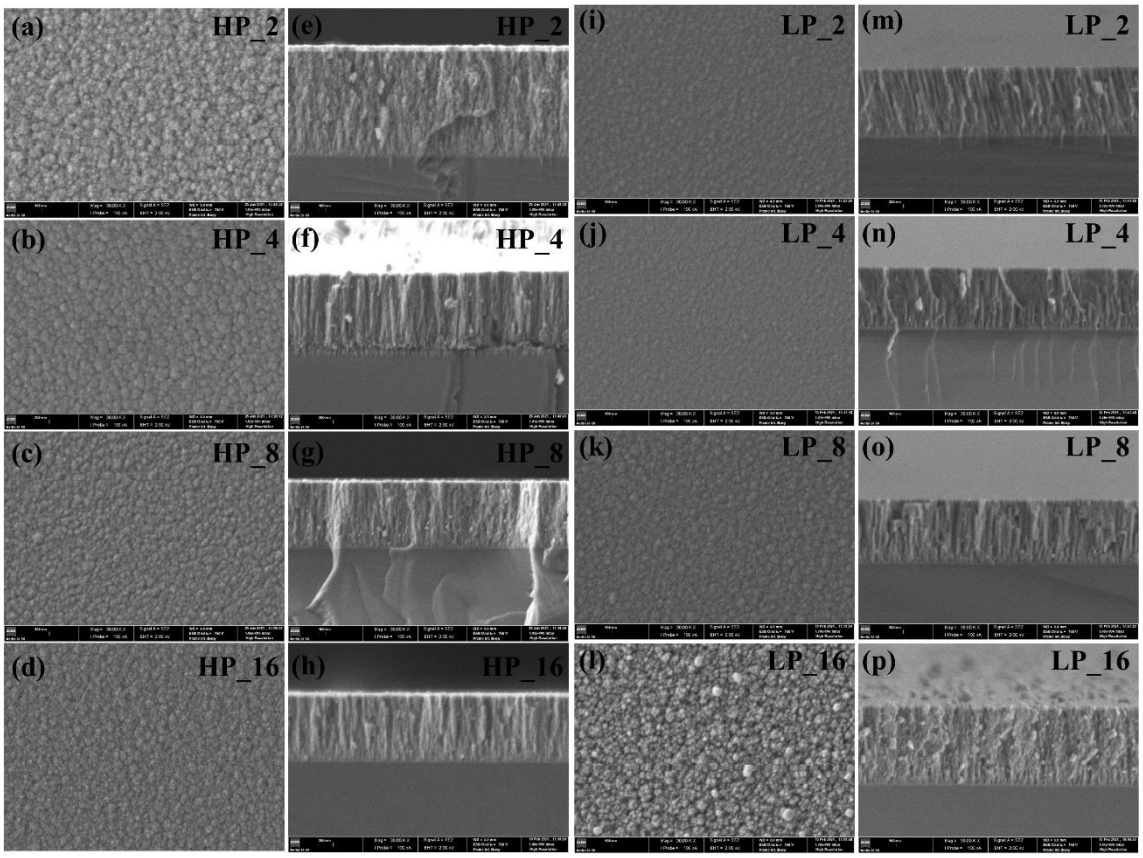

Figure 87. SEM images ((a) to (p)), for surface and a cross-sectional view for Si-Sn-Cu thin films deposited at HP and LP.

Figure 88 (a), (b), and (c) shows SEM images of the surface morphology and cross-section for sample HP_4, revealing the presence of some metallic whiskers. These whiskers were analysed using EDS for chemical composition (Figs. 88 (e) and (f)). These crystalline whiskers have high concentrations of tin. It confirms them to be metallic tin whiskers. This phenomenon of Sn whiskering was also observed during our previous study of Si-Sn alloys prepared by cold compaction and sintering process. There we have discussed the mechanisms responsible for Sn whiskering. Although the mechanism here will also be the same (dynamic recrystallisation), another additional factor is responsible for Si-Sn-Cu thin films. This factor is the presence of copper. Several articles believe copper promotes the Sn whiskering phenomenon by increasing the internal or compressive stresses within the films [176]. Hence, this assists the movement of tin atoms to erupt in the form of crystals to achieve a state of minimum energy level.

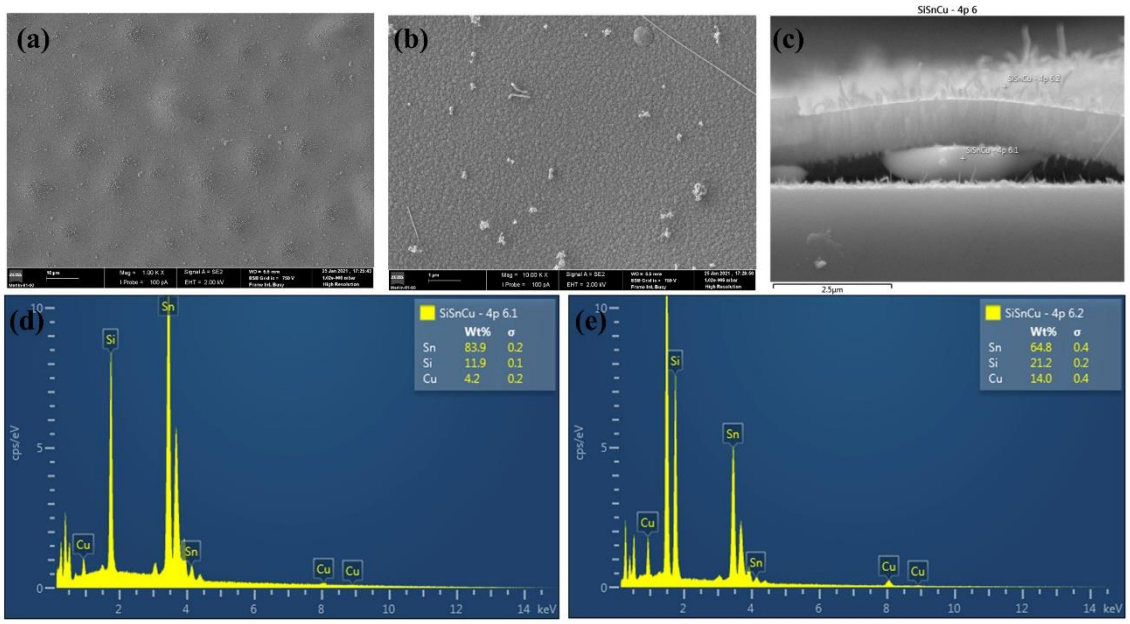

Figure 88. SEM ((a) to (c)), and EDS ((d) and (e)) analysis for sample HP_4.

Figure 89 (a) to (p) shows the AFM topographical and 3D images of the surface features to understand the roughness of the Si-Sn-Cu thin films. Samples HP_4 and LP_16 indicate the presence of tin whiskers on the surface. Table 18 shows the roughness (R_a and R_{rms}) values of the films calculated from AFM images using Gwyddion software. The roughness values are generally higher for high-pressure deposited samples than for low-pressure deposited samples. An exception is only sample LP_16 (Figs. 89 (l) and 89 (p)) which suffers from tin whiskering and accounts for very high or un-reasonable roughness values during calculations.

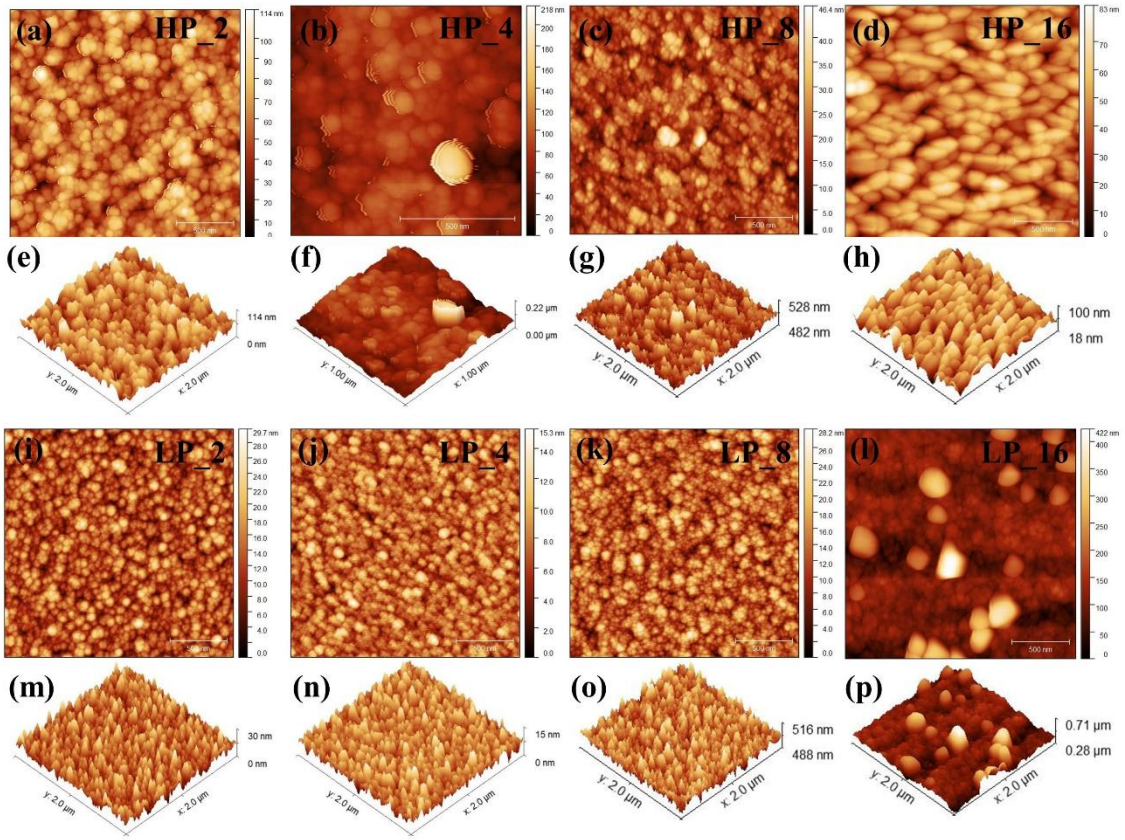

Figure 89. (a) to (p), AFM topography and 3D images of HP and LP samples respectively.

Table 18. Roughness parameters for Si-Sn-Cu thin films.

Roughness parameter	Sample name							
	HP_2	HP_4	HP_8	HP_16	LP_2	LP_4	LP_8	LP_16
R_a (nm)	12.1	16.2	4.6	9.7	3.3	1.5	3.1	37
R_{rms} (nm)	14.9	22.7	5.8	12.2	4.1	1.9	3.9	56

Figures 90 and 91 shows pore size distribution curves obtained by mercury intrusion porosimetry for samples deposited at high and low pressures, respectively. Porosity values show a minimal porosity in the expected range of 2 - 100 nm (considered a mesoporous to near-mesoporous region). However, these porosity levels are insufficient for the sample's response towards complex water vapour adsorption and capillary condensation mechanisms. The Si-Sn thin film system describes a specific number of parameters (chemical composition, surface morphology, surface roughness) along with porosity needed for better humidity sensing. Moreover, it should be emphasised here that pores larger than 1 micron do not concern with humidity sensitivity as these simply serve as a passage for the water vapours.

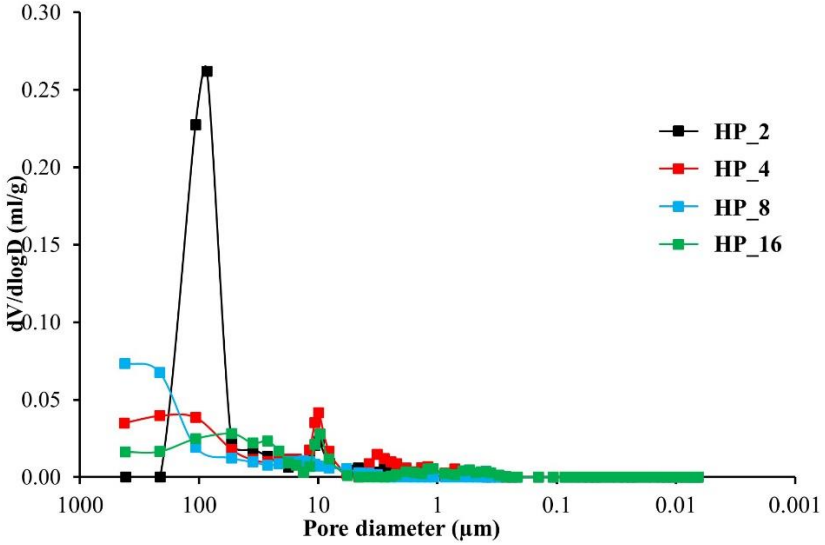

Figure 90. Pore size distribution curves for Si-Sn-Cu thin films deposited at high-pressure (HP).

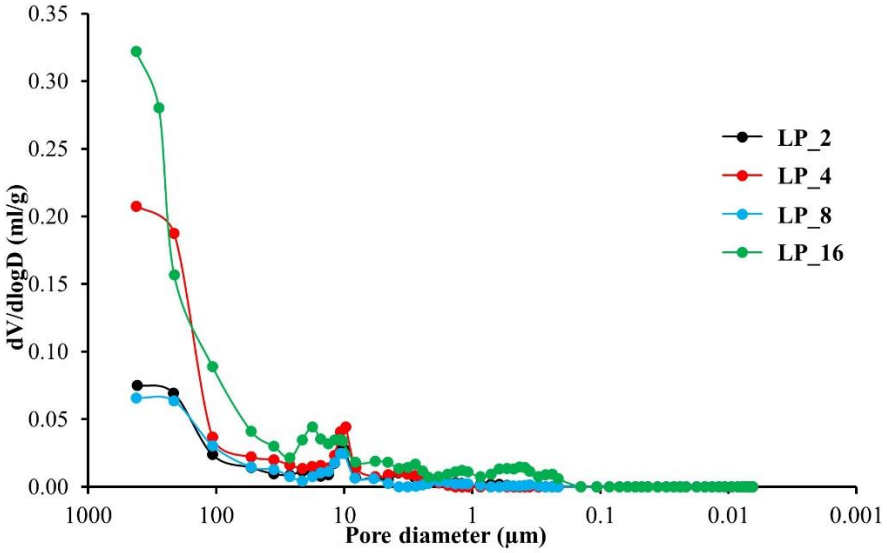

Figure 91. Pore size distribution curves for Si-Sn-Cu thin films deposited at low-pressure (LP).

Figure 92 shows the relationship between the hardness versus number of pellets used during the deposition of thin Si-Sn-Cu films. The hardness values for high-pressure deposited films decrease very slightly with an increase in the number of Cu pellets, although this decrease in the hardness is not very significant. Here, the hardness value for sample HP_4 was not determined due to the higher amounts of tin whiskers present on the surface. Whereas, for low-pressure deposited thin films the hardness values initially increase for LP_4 but then followed a continuous decrease flow thereafter. This behaviour of sample LP_4 could be related to the slightly dense film, which was also backup by low thickness, low roughness value and very small globular structure under scanning electron microscopy. Overall, the low-pressure deposition films have higher hardness values than high-pressure deposited thin films. The exception to this is sample LP_16, where the hardness value is 2.4 GPa, this could be explained by higher tin content

(30.3 at. %) in this film than its similar composition deposited at high-pressure sample HP_16 where hardness was 3.01 GPa and tin content was 18 at. %.

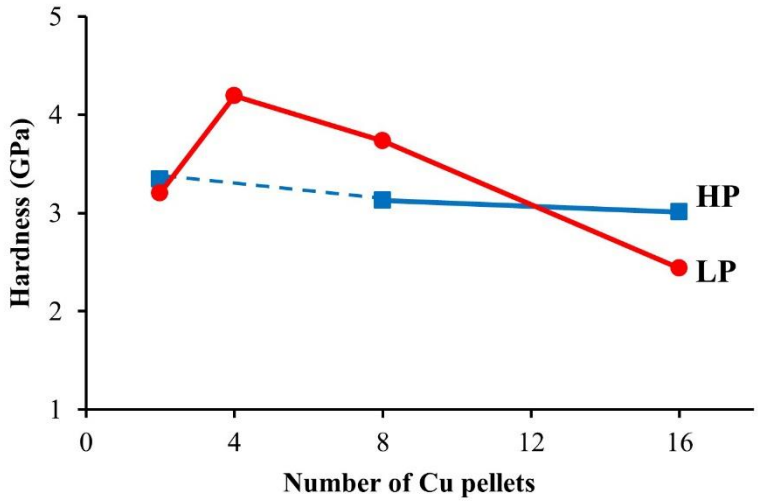

Figure 92. The hardness of Si-Sn-Cu thin films.

Humidity response of Si-Sn-Cu thin films:

The electrical response of two samples with similar chemical compositions prepared at different deposition pressures (1 and 0.7 Pa) was investigated using complex impedance spectroscopy. Figure 93 represents the Nyquist and impedance modulus plots of HP_8 and LP_8 sensors. The Nyquist plots of samples HP_8 (Fig. 93 (a)) and LP_8 (Fig. 93 (b)) show semi-circle curve variations to changes in relative humidity. These semi-circles emerge due to the interaction between water molecules with grain and grain boundaries. But this conductivity variation towards changes to relative humidity (10 to 100 % RH) is not sufficient (or favourable enough) to be considered for humidity sensing applications.

These results were also confirmed by Impedance modulus curves of samples HP_8 (Fig. 93 (c)) and LP_8 (Fig. 93 (d)) at 1 kHz, where the impedance modulus variation with respect to an increase in relative humidity values from 10 to 100 % RH (increment by 10 % RH during each measure) do not reveal sufficient changes (the corresponding slopes are almost 0 Ω/RH(%)).

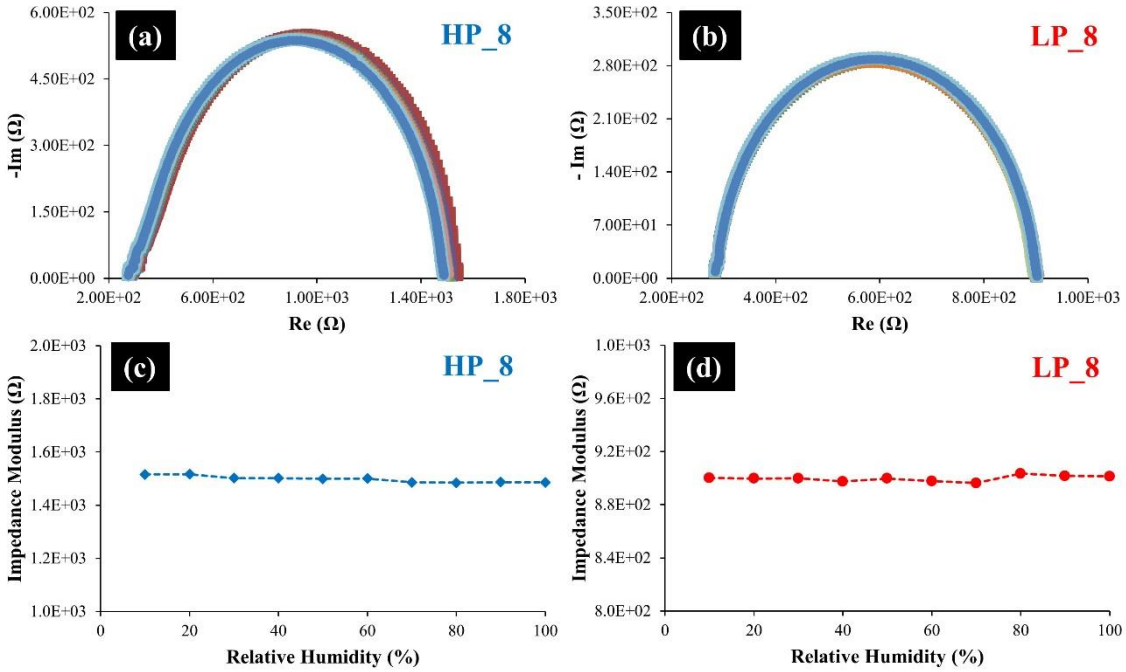

Figure 93. Impedance spectra and impedance modulus plots for samples HP_8 ((a) and (c)), and LP_8 ((b) and (d)).

Several potential factors are responsible for the better response to humidity detection (chemical composition, morphology, roughness, and porosity): however, Si-Sn-Cu thin films were slightly compact with small surface features (also indicated by roughness values) and had minimal porosity in the mesoporous region. Since these factors do not contribute favourably, they are responsible for Si-Sn-Cu films being unsuitable for humidity-sensing applications.

Additionally, other samples of Si-Sn-Cu thin film depositions also had similar electrical characterisation results to those described initially and hence were not considered for the citation here. Sample HP_8 serves as a reference to the samples deposited at high pressure, whereas LP_8 is for low-pressure deposited samples.

Conclusion

Silicon-tin-copper thin films with different concentrations were produced using RF-magnetron sputtering. The two sets of samples were produced at different vacuum pressures of 1 and 0.7 Pa. The concentration of copper was varied by using different number of pellets. The amount of Cu within the films increased by increasing the number of Cu pellets during deposition, although the variation for the thickness of the films which does not follow a uniform pattern with an increase in the number of pellets. The Cu content varied from 7 to 42.4 at. % in the films, but there were merely any XRD peaks relating to the Cu phase. Most of the Cu was present in the amorphous form, although there were very weak XRD peaks at 2θ angles of 43.5°, 50.7°, and 74.7° corresponding to the Cu cubic phase. Films having quasi-amorphous or crystalline structure was primarily due to higher concentrations of tin phase. Morphological and topographical analysis of the surface revealed uniform globular features with dense-columnar thin films. The exception to this were samples HP_4 and LP_16 which on further analysis revealed filamentary eruption of tin whiskers on the surfaces. The tin whisker growth is triggered due to the presence of compressive stresses within the films and even the presence of Cu prompts the tin whisker formations. The root-mean-square (R_{rms}) roughness values are higher for thin films deposited at 1Pa, with the exception of films HP_4 and LP_16. The pore size distribution curves do not reveal any significant porosity in the desired mesoporous to near-mesoporous region. The hardness values are higher for thin films deposited at low pressure. The electrical response for humidity sensing for these thin films was determined through CIS. The Nyquist plots for samples HP_8 and LP_8, show semi-circular variation occurring due to the interaction of water molecules with grain and grain boundaries. Although this interaction does not change with changes in relative humidity. To confirm this behaviour, impedance modulus versus relative humidity plots at 1 kHz were prepared for both samples. The slopes corresponding to these plots were almost 0 Ω/RH, i.e., the trendline is parallel to the relative humidity axis. The humidity response to all the other samples was similar to HP_8 and LP_8 samples depending on whether they were prepared at high and low pressures respectively. Therefore, Si-Sn-Cu thin films prepared here were not suitable for humidity sensing applications.

4.2.3 Silicon-Tin-Zinc (Si-Sn-Zn) thin films produced by RF-magnetron sputtering

Abstract

Si-Sn-Zn thin films were deposited from Si, Sn targets and Zn pellets by radio frequency magnetron sputtering. The different concentrations of Zn were incorporated into the films by varying the number of Zn-pellets. The films were produced at high and low vacuum pressures of 1 and 0.7 Pa, respectively. These thin films were named with a prefix referring to the deposition vacuum pressure (HP or LP), whereas the suffix represented the number of Zn pellets used for the depositions (2, 4, 8, and 16). For these depositions, the Zn content varied from 1.9 to 18.5 at. %. The XRD patterns reveal the films to be amorphous to quasi-amorphous in nature. SEM analysis shows uniform globular surface features, and the cross-sectional images display the films to be slightly compact and have columnar growth The root-mean-square roughness values for all thin films were in the range of 3.5 to 10.2 nm. The only exception was sample HP_16 where large surface features were observed. The pore size distribution curves from samples HP_8 and LP_8 do not reveal any significant porosity in the mesoporous to near-mesoporous region. The hardness values are higher for thin films deposited at low pressure in comparison to high-pressure deposited films, this suggests that the low-pressure films are more compact and denser. The electrical response for Si-Sn-Zn thin films to relative humidity variations was investigated by electrical impedance spectroscopy. Sample HP_8 has a uniform (p-type conduction behaviour) but a weak variation, whereas sample LP_8 do not show any changes in the conduction behaviour to increase in relative humidity (RH). These behaviours were also confirmed by impedance modulus versus relative humidity variation (10 – 100 %) curves for these samples at 1 kHz. Sample HP_8 has some variation in conduction behaviour with an increase in relative humidity. However, these variations are not sufficiently strong enough to be considered for applications related to humidity detection.

Deposition parameters for Si-Sn-Zn thin films

The Si-Sn-Zn thin films were deposited in an Edwards equipment using Si (99.999%), Sn (99.99%) targets and Zn (99.95% purity, 5 mm x 5 mm x 0.15 mm) pellets. The deposition parameters for Si-Sn-Zn thin films are represented in Table 19. All the depositions were performed for 2 hours each. The two sets of depositions were prepared under an Ar gas atmosphere at high pressure of 1 Pa and at low pressure of 0.7 Pa. Films with the prefix HP on sample names refer to the high pressure (1 Pa) depositions, whereas depositions with LP prefix are low pressure (0.7 Pa) depositions. The suffix in the sample's name represents the number Cu of pellets used during the depositions.

Table 19. Deposition parameters for the formation of Si-Sn-Zn thin films.

Sample name	**Target power (W)**		**No. of Zn-pellets**	**Deposition pressure (Pa)**	**Deposition time (min.)**
	P_{Si}	P_{Sn}			
HP_2	200	35	2	1	120
HP_4	200	35	4	1	120
HP_8	200	35	8	1	120
HP_16	200	35	16	1	120
LP_2	200	35	2	0.7	120
LP_4	200	35	4	0.7	120
LP_8	200	35	8	0.7	120
LP_16	200	35	16	0.7	120

Chemical composition, thickness, and deposition rates

Table 20 represents the chemical composition, thickness, and deposition rates of the Si-Sn-Zn thin films. Energy dispersive spectroscopy analysis using Si Kα, Sn Lα and Zn Kα lines on the surface was performed to determine the chemical composition of the thin films. The thin film thickness is determined from the cross-sectional images obtained through scanning electron microscopy. Deposition rates are calculated mathematically as the increase in film thickness in nanometres per unit time in minutes.

Table 20. Chemical composition, thickness, and deposition rates of Si-Sn-Zn thin films.

Sample name	Chem. comp. (at. %)			Thickness (µm)	Deposition rate (nm/min.)
	Si	Sn	Zn		
HP_2	50.4	47.7	1.9	1.0	8.3
HP_4	57.5	36.0	6.5	0.8	6.7
HP_8	48.4	43.8	7.8	1.1	9.2
HP_16	43.1	38.4	18.5	1.3	10.8
LP_2	43.1	53.6	3.3	1.1	9.2
LP_4	54.4	41.3	4.3	0.9	7.5
LP_8	52.2	41.0	6.8	1.0	8.3
LP_16	46.5	40.1	13.4	1.3	10.8

The amount of atomic % of Zn and the thickness of the films are plotted versus the number of Zn pellets used for both sets of depositions and are illustrated in Figs. 94 (a) and (b), respectively.

The amount of Zn (at. %) increases with an increase in the number of Zn pellets during both sets (high and low pressure) of depositions (Fig. 94 (a)). This is a general phenomenon and was also observed for other Si-Sn and Si-Sn-X (X= Ti/Cu) systems during the course of this thesis. However, the trendlines (slopes) for both sets of depositions are distinct. The films HP_16 (18.5 at. %) and LP_16 (13.4 at. %) had the most significant difference in Zn concentrations among all similar compositions. At low-pressure depositions, the lower no. of collisions among the atoms of species involved (Si, Sn and Zn) result in an evenly increase of mean free path for all species. However, this is not the case at high pressure and the higher no. of collisions decreases the mean free path for the species in a non-uniform manner hence, the concentration difference arises among the species involved.

The thickness of the films versus the number of Zn pellets used for both sets of depositions are shown in Fig. 94 (b). The thickness of the films increases with the number of Zn pellets increasing from 2 to 16, although this variation had a slight decrease in thickness values for both depositions with 4 zinc pellets (HP_4 and LP_4). The thickness values for the first two films deposited at high pressure (HP_2 and HP_4) are lower than their counterparts deposited at low pressure (LP_2 and LP_4). An inverse relationship was observed for samples HP_8 and HP_16 with their counterparts (LP_8 and LP_16), although the difference was not very significant. This difference could be due to the potential for the formation of porous films at high pressure.

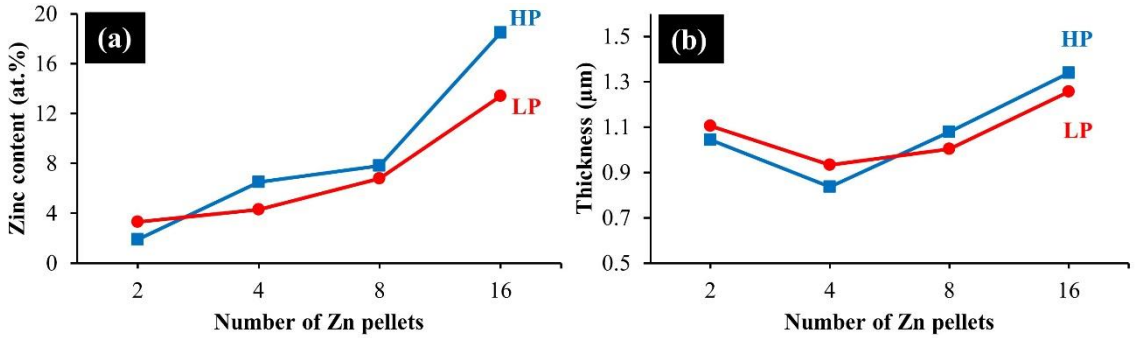

Figure 94. (a) Atomic % of Zn content in the films, and (b) thickness of the films as a function of number of Zn pellets.

Structural, morphological, porosity, and mechanical characterisation

The XRD patterns for Si-Sn-Zn thin films deposited at high and low pressure are shown in Figs. 95 (a) and (b), respectively. Here most of the XRD patterns are amorphous, only HP_16 and LP_16 thin films had small crystalline peaks. This is due to the amorphous nature of Si, which dominates the thin film matrix (Sn and Zn atoms occupy substitutional positions) during the deposition. Compared with Si-Sn-X (X= Ti and Cu) thin films, the Si-Sn-Zn thin films had significantly lower amounts of Zn (alloying element) present with similar compositions, which affected the overall crystalline nature of the films. No significant XRD peaks for the Zn phase were observed till the highest no. of Zn pellets (16) were used for the depositions. The low-intensity crystalline peaks for Zn (hexagonal) are visible at 2θ angles of 36.3°, 39.0°, 43.2°, and 54.3° attributed to the (002), (100), (101), and (102) planes, respectively (JCPDS card no. 01-08-0713). The XRD peaks for the β-Sn (tetragonal) phase were also present at 2θ values of 30.6°, 32.0°, 43.9°, and 44.9° that correspond to (200), (101), (220), and (211) planes, respectively (JCPDS card no. 01-086-2264). An XRD peak at 2θ = 69.3° corresponds to the substrate Si-wafer with (100) orientation crystalline facet.

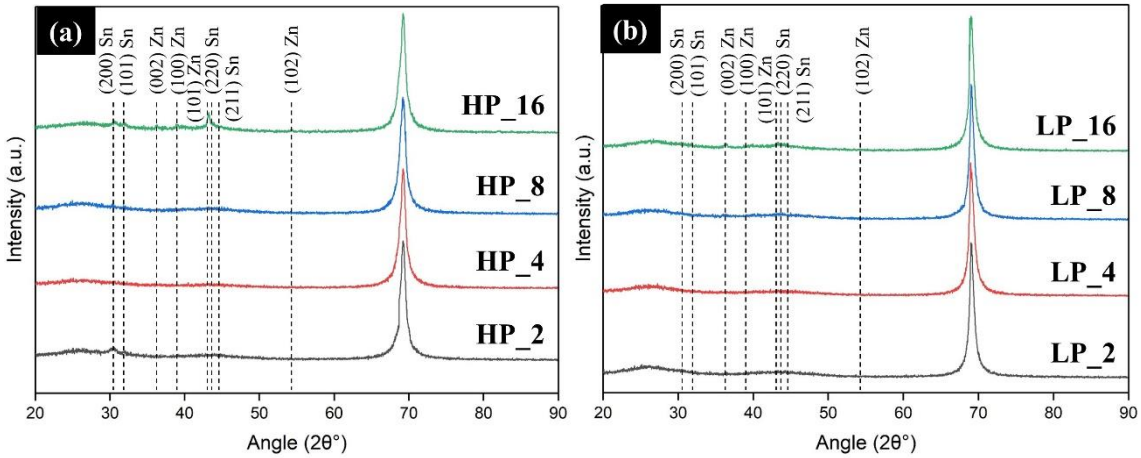

Figure 95. XRD patterns for Si-Sn-Zn thin films deposited at (a) HP, and (b) LP.

Figure 96 (a) to (p) shows the SEM images of the deposited Si-Sn-Zn thin films. The surface of the films is composed of uniform globular features. Although, the cross-sectional images reveal columnar and denser (or compact) Si-Sn-Zn films for all compositions. However, there was a difference in the size of the globular features (grain size), and the cross-sectional images still reveal large columnar structures for samples (HP_16 and LP_16). The study on the Si-Sn system (in the previous section), also reveals large grain size at higher tin contents; hence this could be rather related to the high contents of tin in the films.

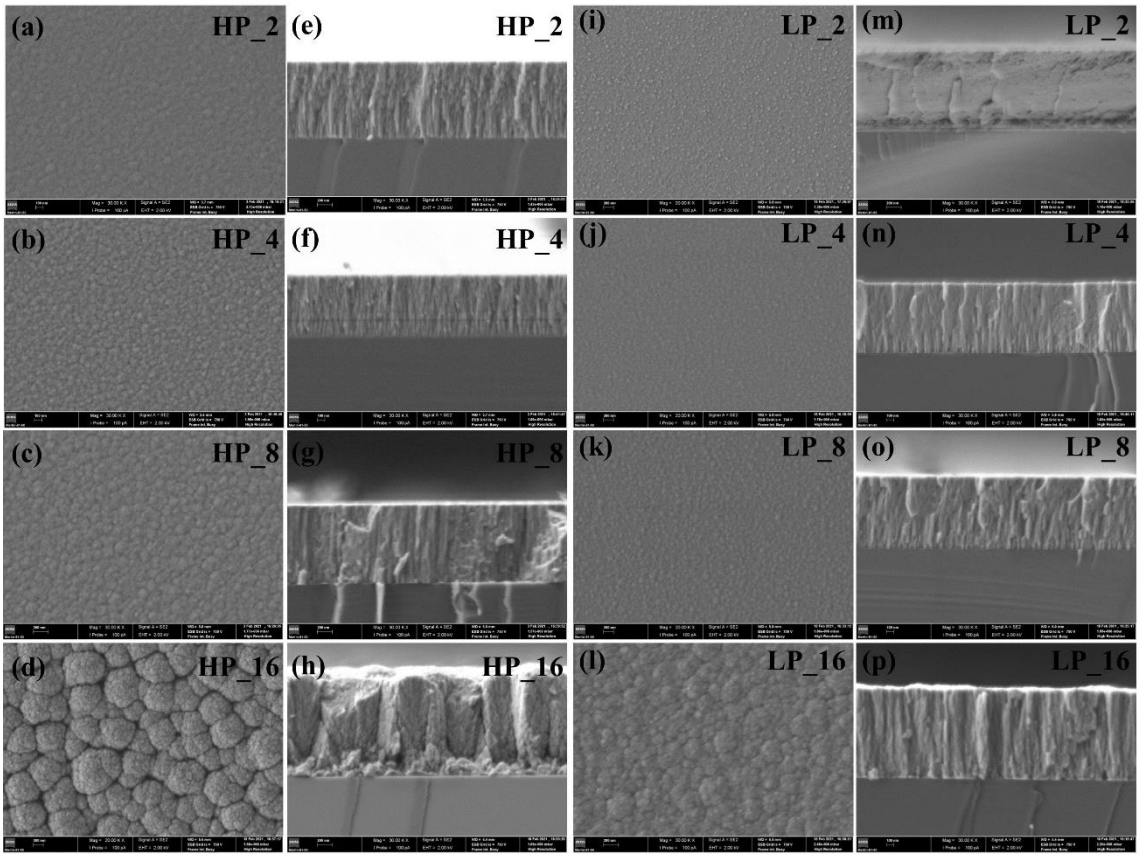

Figure 96. SEM images ((a) to (p)) for surface and a cross-sectional view for Si-Sn-Zn films.

Figure 97 (a) to (p) shows the AFM topographical and 3D images of the features present on the surface to get an understanding of the roughness of the Si-Sn-Zn thin films. Most of the samples have uniform surface features, and the roughness values (R_a and R_{rms}) displayed in Table 21, calculated from these images, also do not show any significant difference. However, sample HP_16 has very high roughness values resulting from large globular surface features discussed in the previous section.

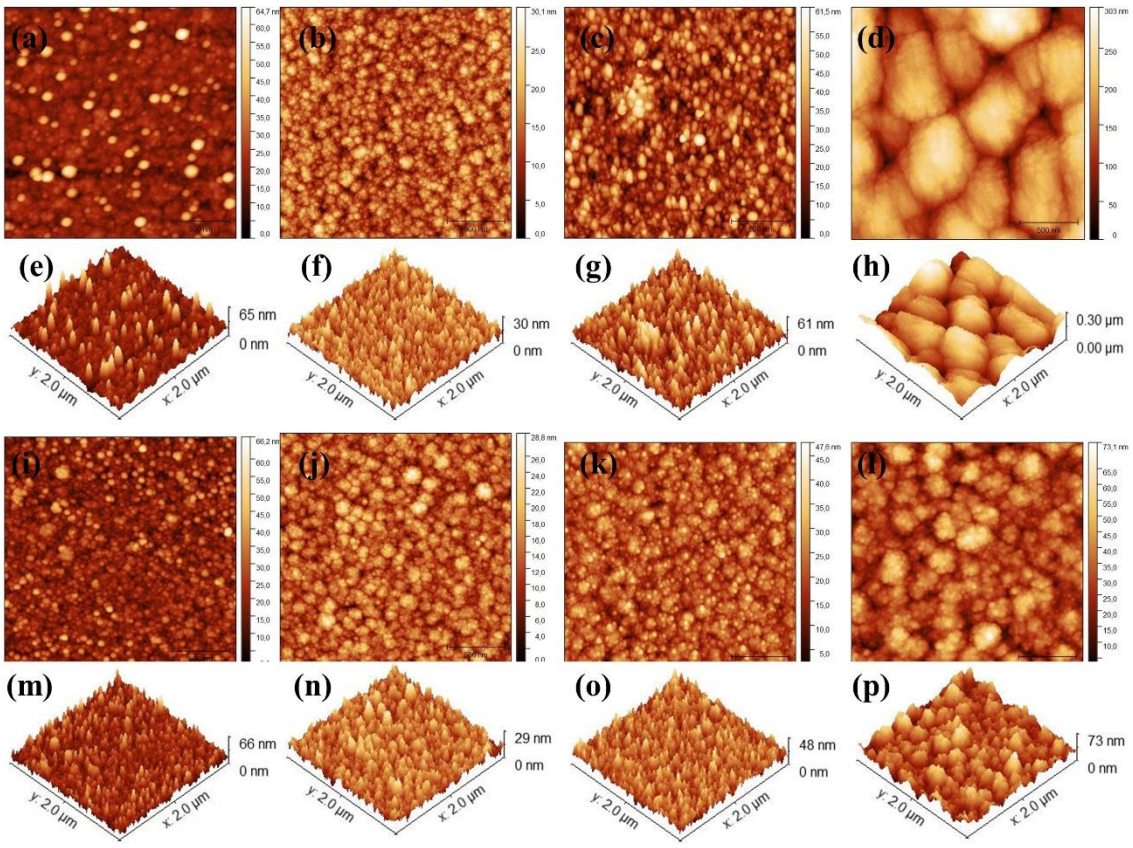

Figure 97. AFM topography and 3D images ((a) to (p)) for HP and LP samples.

Table 21. The average roughness and R_{rms} values for the thin films.

Roughness parameters	Sample name							
	HP_2	HP_4	HP_8	HP_16	LP_2	LP_4	LP_8	LP_16
R_a (nm)	4.6	3.0	8.0	41.0	5.3	2.8	4.2	7.1
R_{rms} (nm)	6.9	3.8	10.2	50.4	6.9	3.5	5.3	8.9

Figure 98 shows the plots of logarithmic differential curves versus pore size distribution for samples HP_8 and LP_8. The porosity curves for both samples display no significant porosity in the mesoporous region (2 - 50 nm). The porosity in the mesoporous or near-mesoporous region promotes water vapour adsorption and capillary condensation mechanisms for humidity sensing applications. The desired pore size for humidity sensing is also expressed in terms of kelvin radius, which states that the minimum size of the pore to promote humidity sensing characteristics should be greater than the kelvin radius [177]. Therefore, the pores larger than 1 micron in diameter just serve as a passage for the water vapours and do not concern with humidity sensing mechanisms.

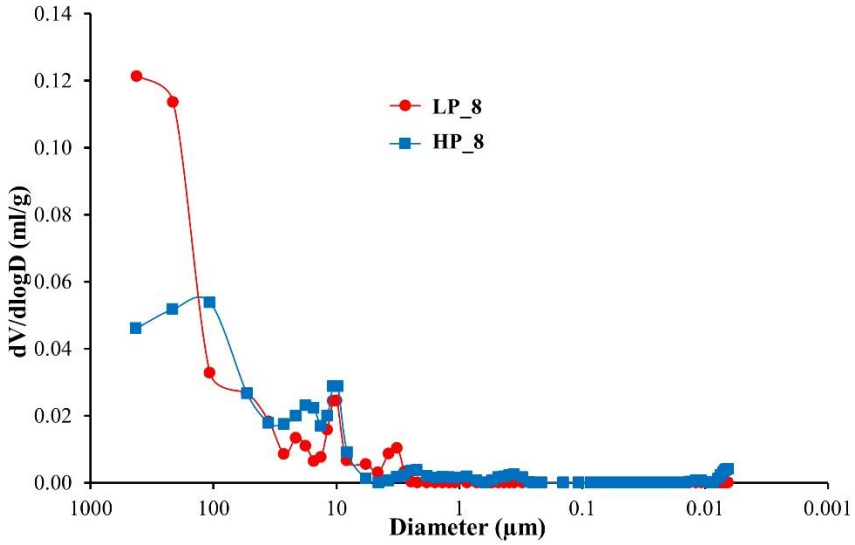

Figure 98. Pore size distribution for samples HP_8 and LP_8.

Figure 99 shows the graph between the hardness versus number of Zn pellets used during the deposition of thin Si-Sn-Zn films. The hardness of the films is affected by the number of Zn pellets and the vacuum pressure applied. There is a difference in hardness values for the films deposited at both high and low pressures, especially at high Zn contents. This is because of the variation in the adatom mobility and nucleation process of the film, as at lower pressure, the atoms have higher energy during the formation of the film and hence end up forming more compact, denser and less porous films, which in turn result in higher hardness values. At both deposition pressures, there is an increase in the hardness value from 2 to 4 pellets, and then there is a decrease in the hardness values with the incorporation of higher Zn contents. This is due to the fact that the samples HP_4 and LP_4 have lower roughness values and could be more compact than other films.

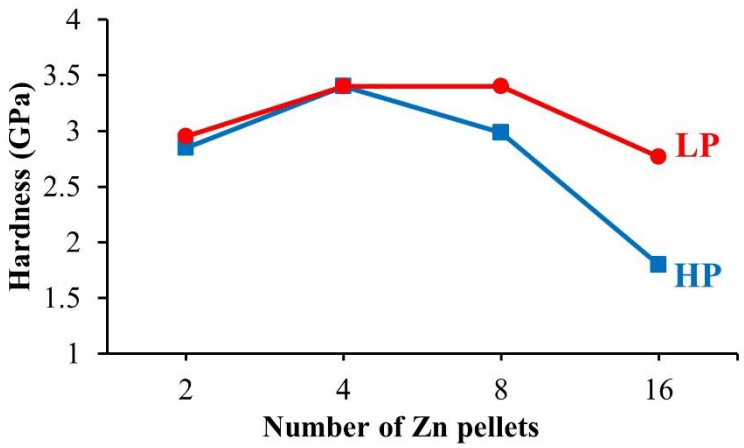

Figure 99. Hardness values as a function of number of Zn pellets for both high- and low-pressure thin films.

Humidity response of Si-Sn-Zn thin films

The electrical response for Si-Sn-Zn thin films to relative humidity variations was investigated by electrical impedance spectroscopy. The samples electrical response to humidity depends on the concentration of water molecules adsorbed along the porous structure of the surface. At low humidity concentrations, water molecules are adsorbed by the chemisorption (chemical adsorption) phenomenon, whereas at high humidity concentrations, the physisorption (physical adsorption) phenomenon is dominant.

Figure 100 shows the Nyquist and impedance modulus graphs of samples HP_8 and LP_8. These two samples were deposited at similar deposition parameters except deposition pressure (where sample HP_8 was at 1 Pa and 0.7 Pa for LP_8). The Nyquist plots of samples HP_8 (Fig. 100 (a)) and LP_8 (Fig. 100 (b)) show semi-circle curve variations to changes in relative humidity. These semi-circles are formed due to the interaction of grain and grain boundaries with the water molecules. Sample HP_8 (Fig. 100 (a)) has a weak but uniform increase in the area under the impedance spectra curve, which corresponds to a *p*-type conduction behaviour with an increase in relative humidity (RH) from 10 to 100 %. On the other hand, the change in impedance spectra area for sample LP_8 (Fig. 100 (b)) is insignificant, i.e., do not show any changes in the conduction behaviour with increasing relative humidity. These behaviours were also confirmed by impedance modulus versus relative humidity variation curves for these samples at 1 kHz, where sample HP_8 (Fig. 100 (c)) shows the alight variation of impedance modulus values to changes in relative humidity from 10 to 100 % RH (with 10 % RH increase between each measurement) but sample LP_8 (Fig. 100 (d)) does not show any change in impedance modulus values.

As already mentioned, several factors are responsible for the enhanced response of a sensor towards humidity sensing: chemical composition, structure, morphology, roughness, and porosity are the most common ones. Samples HP_8 and LP_8 contain large amounts of silicon and tin in the matrix, whereas Zn contents were 7.8 and 6.8 at. %, respectively. SEM images (Fig. 96) reveal bigger surface features for the HP_8 sample compared to sample LP_8. This was confirmed by AFM images (Fig. 97) and roughness (R_{rms}) values of 10.2 and 5.3 nm, for samples HP_8 and LP_8, respectively. The porosity results did not yield any porosity in the desired mesoporous region. Overall, the majority of factors favouring RH sensitivity were absent even in sample HP_8, which was the one that showed more changes in the electrical response with RH variations. However, these variations are not sufficiently strong enough to be considered for humidity-sensing applications.

Other samples from Si-Sn-Zn thin film depositions also had comparable results to those previously described and therefore were not considered here for the citation. Sample HP_8 refers to the samples deposited at high pressure (1 Pa), whereas sample LP_8 serves as a reference for low-pressure (0.7 Pa) deposited samples.

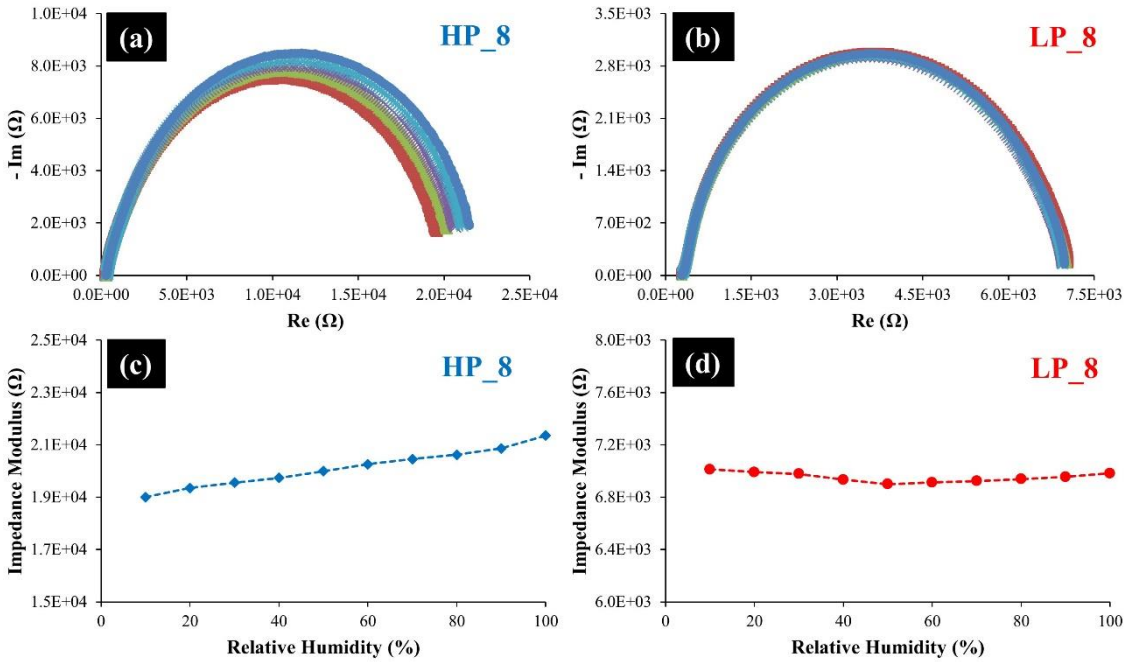

Figure 100. Nyquist and impedance modulus plots for samples HP_8 ((a) and (c)), and LP_8 ((b) and (d)) (for different relative humidity contents colours brown, orange, light green, dark green, rose, purple, grey, red, light blue and dark blue stands for 10, 20, 30, 40, 50, 60, 70, 80, 90 and 100 % RH, respectively).

Conclusions

Silicon-tin-zinc thin films with different concentrations were produced using RF-magnetron sputtering. The two sets of samples were produced at different vacuum pressures of 1 Pa (HP) and 0.7 Pa (LP). The concentration of zinc varied from 1.9 to 18.5 at. % by using different no. of pellets (2, 4, 8 and 16). The thickness of the films increases with an increase in the Zn pellets with the films. Although the maximum concentration of Zn was 18.5 % within the films, the XRD results showed very weak peaks at 2θ angles of 36.3°, 39.0°, 43.2°, and 54.3°, corresponding to the Zn phase. Most of the films were amorphous to quasi-amorphous in nature. Morphological and topographical analysis of the surface revealed uniform globular features with dense-columnar thin films. A slight exception to this was sample LP_16 which revealed very big globular surface features. The pore size distribution curves do not reveal any significant porosity in the desired region of meso-porosity (2 - 50 nm). The hardness values are higher for thin films deposited at low pressure, suggesting the low-pressure films to be even more compact. The humidity sensing response for samples HP_8 and LP_8 was evaluated using complex impedance spectroscopy. These samples serve as reference to all other samples prepared at high and low pressures respectively. Sample HP_8 has a small uniform p-type conduction behaviour but sample LP_8 do not show any conduction behaviour to an increase in relative humidity from 10 to 100 %. These behaviours were also confirmed by impedance modulus versus increase in relative humidity at 1 kHz, where the slope of impedance modulus versus relative humidity (%) increases for sample HP_8 and observes no changes to slope for sample LP_8. Interestingly, sample HP_8 exhibits some change in conduction behaviour as the relative humidity rises, but those variations are not significant enough to be taken into account for humidity sensing applications.

CHAPTER 5: Conclusions and future work

This chapter summarises the main conclusions of the research work performed during this thesis. It also indicates some open windows for future improvement in some systems coupled with better physical properties (structural, chemical, and morphological) towards response to humidity sensing.

Conclusions

In this research work, the Si-Sn and Si-Sn-X (Ti, Cu, and Zn) alloy systems were produced by two non-equilibrium routes (RF-magnetron sputtering and high-energy mechanical alloying). Their structure, morphology, porosity, roughness, hardness, and electrical response as a function of the relative humidity were evaluated by several characterisation techniques. The two main objectives of this work were to study the ability of these processing techniques on the production of humidity sensors based on porous silicon and the influence of Sn, Ti, Cu, and Zn on the electrical response of the Si-based system.

The production of the Si-Sn system was carried out by the two different manufacturing techniques mentioned. $Si_{100-x}Sn_x$ thin films with $0 < x < 51$ (at. %) were co-sputtered by RF-magnetron sputtering using Si and Sn targets at two vacuum pressures (1 Pa and 0.6 Pa). The chemical composition results showed that different levels of Sn incorporation could be achieved by varying the power applied to the Sn target (25, 50, 75, and 100 W) while maintaining a constant power of 400 W on the silicon target. The surface of all the films presented a globular morphology. The SEM cross-section images showed a higher porosity for films deposited at higher pressure (1 Pa). These results were confirmed by mercury intrusion porosimetry, where the sample $Si_{72}Sn_{28}$ (referred by sample name: HP_50 in chapter 4) deposited at 1 Pa, showed a higher pore volume (especially in the mesoporous region) than the sample $Si_{70}Sn_{30}$ (referred by sample name: LP_50 in chapter 4) deposited at 0.6 Pa. The amount of porosity in the mesoporous region was 3.3 and 1 % for $Si_{72}Sn_{28}$ and $Si_{70}Sn_{30}$ films, respectively. The roughness (R_{rms}) value was also higher for the sample $Si_{72}Sn_{28}$ (5.4 nm) when compared with $Si_{70}Sn_{30}$ (2.8 nm). The crystalline structure of the films was dependent on the chemical composition. The films with low concentrations of tin were fully amorphous. For higher tin concentrations (above 28 at. %), the films were formed by a nano-crystalline β-tin phase embedded in the amorphous silicon matrix. The hardness values obtained were inversely proportional to the concentration of tin in the films. Moreover, the samples deposited at high pressure showed better response to humidity changes from 10 to 100 % RH, in comparison to low-pressure deposited films. The sample $Si_{72}Sn_{28}$ presented the best sensing ability (good response, repeatability, and reproducibility) and showed a *p*-type conduction behaviour with a linear variation of the impedance modulus with the increase for relative humidity contents from 10 to 100 %. The electrical response of the sensor with respect to time measured after 1 and 6 months after the first measurement allowed us to conclude that its sensitivity behaviour was relatively stable with time.

Concerning the production of the Si-Sn system by high-energy mechanical alloying, $Si_{100-x}Sn_x$ alloys with x = 15, 30, and 40 at. % were synthesised from elemental Si and Sn powders for

two different milling times (4 and 12 hours). Stearic acid (2 wt. %) was used as process control agent for all the millings. The alloyed powders were then compacted by two different compaction processes: (1) cold pressing followed by sintering, and (2) hot pressing. The porosity results demonstrated that the samples produced from the former process had major porosity close to 0.1 μm size. The roughness (R_{rms}) values for these samples were also quite high. For the Si-Sn hot-pressed samples the porosity values were concentrated at higher levels (between 0.1 to 0.2 μm). The structure of all the final samples was composed of Si, Sn and SnO phases. The samples prepared from the hot-pressed process presented more homogeneous morphology when characterised using scanning electron microscopy. Based on the above-mentioned results, it was expected that the samples prepared by the former process would better respond to relative humidity changes. However, none of the samples fabricated by high-energy mechanical alloying (independently of the compaction process used) performed well to the humidity changes. This was explained by the fact that these samples presented a high concentration of large-sized pores, with a radius greater than the kelvin radii. The extremely high roughness values obtained for these alloys also affected the interaction of water molecules with the alloy surfaces resulting in non-uniform impedance characteristics and no response toward change in relative humidity.

Therefore, we may say that compared to the HEMA technique, the RF magnetron sputtering process provided more suitable conditions to produce Si-Sn samples with better surface properties for humidity sensing applications.

Based on the results obtained for the Si-Sn system, the Si-Sn-X (X = Ti, Cu, and Zn) alloy systems were only prepared by RF- magnetron sputtering. Two sets of Si-Sn-Ti (3.1 < Ti < 13.6 (at. %)) samples were produced with 400 and 500 W of applied power on the Si target, while different applied powers on the Sn target and a different number of Ti pellets (4, 6, 8, 16, and 25) were used. Most depositions were carried out at a vacuum pressure of 1 Pa. The 500 W Si target films had higher thicknesses values when compared with the 400 W films. The XRD patterns showed the thin films to be either amorphous or quasi-amorphous in structure. The films with cumulative tin and titanium contents exceeding 28 at. % showed weak XRD peaks corresponding to β-Ti and β-Sn phases. The film's morphological analysis revealed that the 500 W deposited films were more columnar and porous than the 400 W series films. The pore size distribution and the amount of porosity in the mesoporous region, were higher for the thin film deposited with an applied power on the Si target of 500 W and with 8 Ti pellets, $Si_{71}Sn_{23}Ti_6$ (referred by sample name: A_8 in chapter 4) than for the sample deposited with 400 W with the same number of Ti pellets $Si_{70}Sn_{24}Ti_6$ (referred by sample name: S_8 in chapter 4) The humidity response of sample $Si_{71}Sn_{23}Ti_6$ revealed the better humidity sensing detection with a *p*-type behaviour in the humidity range of 10 to 90 % RH. The time stability humidity response of this sample was also observed

at three different times (t = 0, 1, and 6 months). However, the Nyquist and impedance modulus plots revealed that the sample's humidity response suffered from ageing behaviour.

Concerning the Si-Sn-Cu system, thin films with different Cu concentrations (7.0 < Cu < 42.4 (at. %)) were produced by RF-magnetron sputtering. Two sets of samples were produced at different vacuum pressures of 1 and 0.7 Pa, and different number of Cu pellets (2, 4, 8, and 16). The amount of Cu within the films increased by increasing in the number of Cu pellets. Most of the Cu was present in the amorphous form, although there were very weak XRD peaks corresponding to cubic copper phase. The thin films having quasi-amorphous or crystalline nature were primarily due to higher concentrations of tin phase. Morphological and topographical analysis revealed uniform globular features of the surface with dense-columnar morphology. The exception to this were samples $Si_{53}Sn_{34}Cu_{13}$ and $Si_{38}Sn_{30}Cu_{32}$ (referred by sample names: HP_4 and LP_16 in chapter 4), which revealed filamentary eruption of tin whiskers on the surfaces. The tin whisker growth was triggered due to the presence of compressive stresses within the films, and the presence of Cu. The roughness (R_{rms}) values were high for films deposited at 1 Pa. The pore size distribution curves did not reveal any significant porosity in the desired region of 2 - 100 nm. The electrical response for humidity sensing for samples $Si_{52}Sn_{26}Cu_{22}$ and $Si_{50}Sn_{25}Cu_{25}$ (referred by sample names: HP_8 and LP_8 in chapter 4) prepared at similar deposition parameters except for deposition pressure, of 1 and 0.7 Pa, respectively, showed semi-circular variation due to the interaction of water molecules with grain and grain boundaries. However, this interaction did not change with changes in relative humidity. Therefore, samples from Si-Sn-Cu films were considered unsuitable for humidity-sensing applications.

Concerning the Si-Sn-Zn system, films with different concentrations were produced using RF-magnetron sputtering. Two sets of samples were produced at different vacuum pressures of 1 Pa (high pressure) and 0.7 Pa (low pressure). The concentration of zinc varied from 1.9 to 18.5 at. % by using different no. of pellets (2, 4, 8 and 16). Most of the films were amorphous to quasi-amorphous in nature. Morphological analysis of the surface revealed uniform globular features with dense-columnar morphology. A slight exception to this was sample $Si_{47}Sn_{40}Zn_{13}$ (referred by sample name: HP_16 in chapter 4) which revealed very big globular surface features. The pore size distribution curves did not reveal any significant porosity in the mesoporosity region. The hardness values were higher for thin films deposited at low pressure, suggesting the low pressure deposited thin films to have more compact morphology. The humidity sensing response characterised by Nyquist plots of sample $Si_{48}Sn_{44}Zn_8$ (referred by sample name: HP_8 in chapter 4) prepared at high pressure with 8 Zn pellets displays a small uniform *p*-type conduction behaviour, whereas sample $Si_{52}Sn_{41}Zn_7$ (referred by sample name: LP_8 in chapter 4) prepared at low pressure with 8 Zn pellets did not show any conduction behaviour to increase in relative

humidity from 10 to 100 %. This was confirmed by the impedance modulus versus the relative humidity at 1 kHz. Interestingly, sample $Si_{48}Sn_{44}Zn_8$ prepared at high pressure exhibited some change in conduction behaviour as the relative humidity raised, but those variations were not significant enough for these films to be considered suitable for humidity sensing applications.

Overall, the research work performed on the Si-Sn and Si-Sn-X (Ti, Cu, and Zn) alloy systems showed that the best humidity sensing properties depend upon several factors including chemical composition, morphology, surface roughness, structure, and mesoporosity. Among all the systems synthesised during the work on this thesis, Si-Sn and Si-Sn-Ti systems produced by RF-magnetron sputtering showed the most promising response towards relative humidity variations. A sensor produced by Si-Sn thin-film with composition $Si_{72}Sn_{28}$ (at. %) deposited at 1 Pa presented a *p*-type conduction behaviour in a relative humidity range from 10 to 100 %. The impedance modulus values obtained at 1 kHz for this sample showed a stable and linear variation of the impedance modulus as a function of relative humidity content with a trendline slope of 83 Ω/RH(%). Moreover, the humidity tests performed 1 and 6 months after the first run revealed that the electrical response of this sensor is quite stable over time. On the other hand, a sensor from the Si-Sn-Ti system with chemical composition $Si_{71}Sn_{23}Ti_6$ deposited at 1 Pa showed a *p*-type humidity sensing behaviour in a relative humidity range from 10 to 90 %. However, this sample suffered from the ageing effect after 1 and 6 months from the first measurement. (A sensor from the Si-Sn-Zn system with the chemical composition $Si_{48}Sn_{44}Zn_8$ displayed a small *p*-type conduction behaviour to increase relative humidity from 10 to 100 %. However, these variations were not significantly enough to be considered for humidity sensing behaviour. Si-Sn alloy systems produced by mechanical alloying and Si-Sn-Cu thin films were not able to display any promising results towards humidity sensing mechanisms).

Future work

The production of Si-Sn-X (X = Cu and Zn) thin films with higher Si contents might increase mesoporosity as was obtained by Si-Sn and Si-Sn-Ti thin films. This might potentially improve the response of these systems towards humidity sensing detection. Hence, the synthesis and characterisation of these systems could be performed in future to obtain the desired properties to support humidity sensing mechanisms.

The response of the best humidity sensors obtained in this thesis can be studied in the future as a function of temperature till 100°C. Moreover, other gases can be used to evaluate their response to gas detection.

A calibration circuit can be implemented in the future to get a better understanding of the changes in the base impedance moduli variations observed for samples and also to have an understanding on the effect of ageing on samples with good sensing responses (Fig. 101). An additional set-up in future can be introduced to study the sample's response and recovery time to changes in relative humidity.

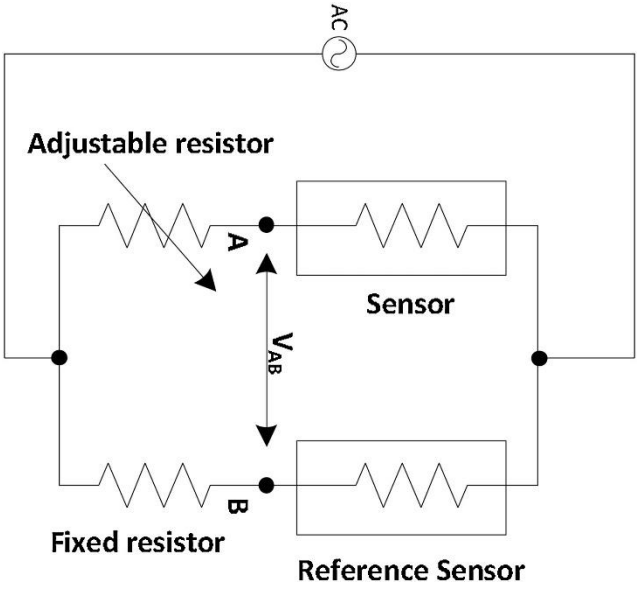

Figure 101. Sensors ageing drift compensation assembly [178].

References

[1] Electrical and electronic measurements - General terms relating to measurements, IEV ref 311-05-01, International Electrotechnical Commission, www.electropedia.org/iev/iev.nsf/display?openform&ievref=311-05-01. Accessed 25 May 2022, (2001).

[2] T. Grandke, W.H. Ko, W. Göpel, J. Hesse, J. Zemel, Sensors: A comprehensive survey, Fundamentals and General Aspects, Vol. 1, 1989. https://doi.org/10.1002/9783527620128.

[3] T.A. Blank, L.P. Eksperiandova, K.N. Belikov, Recent trends of ceramic humidity sensors development: A review, Sensors Actuators, B Chem. 228 (2016) 416–442. https://doi.org/10.1016/j.snb.2016.01.015.

[4] G. Korotcenkov, Handbook of Humidity Measurement: Methods, Materials and Technologies, Vol. 1: Spectroscopic Methods of Humidity Measurement, CRC Press, Boca Raton, USA, 2018.

[5] N. Baran, S. Renka, M. Raić, D. Ristić, M. Ivanda, Effects of Thermal Oxidation on Sensing Properties of Porous Silicon, Chemosensors. 10 (2022). https://doi.org/10.3390/chemosensors10090349.

[6] L. Sujatha, C.R. Chaudhuri, E. Bhattacharya, Application of Porous Silicon in MEMS and Sensors Technology, Mater. Fail. MEMS NEMS. (2015) 121–172. https://doi.org/10.1002/9781119083887.ch4.

[7] G. Barillaro, A. Diligenti, A. Nannini, L.M. Strambini, E. Comini, G. Sberveglieri, Low-concentration NO_2 detection with an adsorption porous silicon FET, IEEE Sens. J. 6 (2006) 19–23. https://doi.org/10.1109/JSEN.2005.859360.

[8] J.L. Gole, S.E. Lewis, Chapter 4 - Porous Silicon – Sensors and future applications , in: NanoSilicon - N. Kumar (Ed.), Nanosilicon, Elsevier, Amsterdam, 2008: pp. 149–175. https://doi.org/10.1016/B978-008044528-1.50005-1.

[9] E. Comini, G. Faglia, G. Sberveglieri, CO and NO_2 response of tin oxide silicon doped thin films, Sensors Actuators, B Chem. 76 (2001) 270–274. https://doi.org/10.1016/S0925-4005(01)00581-0.

[10] J. Wu, Z. Zhu, H. Zhang, H. Fu, H. Li, A. Wang, H. Zhang, Z. Hu, A novel nano-structured interpenetrating phase composite of silicon/graphite-tin for lithium-ion rechargeable batteries anode materials, J. Alloys Compd. 596 (2014) 86–91. https://doi.org/10.1016/j.jallcom.2014.01.187.

[11] K. Nnakwo, I. Okeke, E. Nnuka, Effect of Zinc Content on the Structure and Mechanical Properties of Silicon Bronze, 3 (2017) 179–183.

[12] I. Ali, M. Kaood, Improving NO_2 Sensitivity of porous silicon by functionalization its surface with copper as catalyst, 2017.

[13] A.A. Istratov, E.R. Weber, Physics of Copper in Silicon, J. Electrochem. Soc. 149 (2002) G21. https://doi.org/10.1149/1.1421348.

[14] V. Strikha, V. Skryshevsky, V. Polishchuk, E. Souteyrand, J.R. Martin, A Study of Moisture Effects on Ti/Porous Silicon/Silicon Schottky Barrier, J. Porous Mater. 7 (2000) 111–114. https://doi.org/10.1023/A:1009634720436.

[15] Z. Chen, C. Lu, Humidity sensors: A review of materials and mechanisms, Sens. Lett. 3 (2005) 274–295. https://doi.org/10.1166/sl.2005.045.

[16] D. Camuffo, Chapter 2A - Theoretical Grounds for Humidity, in: Microclimate for Cultural Heritage (Second E. Camuffo (Ed.), Elsevier, Boston, 2014: pp. 49–76. https://doi.org/10.1016/B978-0-444-63296-8.00002-0.

[17] D.A. Yadav, Classification and Applications of Humidity Sensors: A Review, Int. J. Res. Appl. Sci. Eng. Technol. 6 (2018) 3686–3699. https://doi.org/10.22214/ijraset.2018.4616.

[18] N. Yamazoe, Y. Shimizu, Humidity sensors: Principles and applications, Sensors and Actuators. 10 (1986) 379–398. https://doi.org/10.1016/0250-6874(86)80055-5.

[19] E. Traversa, Ceramic sensors for humidity detection: the state-of-the-art and future developments, Sensors Actuators B Chem. 23 (1995) 135–156. https://doi.org/10.1016/0925-4005(94)01268-M.

[20] E.S. Araújo, J. Libardi, P.M. Faia, H.P. de Oliveira, Characterization and Electrical Response to Humidity of Sintered Polymeric Electrospun Fibers of Vanadium Oxide-(TiO_2/WO_3), J. Electron. Mater. 47 (2018) 2710–2717. https://doi.org/10.1007/s11664-018-6112-1.

[21] B.M. Kulwicki, Humidity Sensors, J. Am. Ceram. Soc. 74 (1991) 697–708. https://doi.org/10.1111/j.1151-2916.1991.tb06911.x.

[22] P.M. Faia, J. Libardi, Response to humidity of TiO_2:WO_3 sensors doped with V_2O_5: Influence of fabrication route, Sensors Actuators, B Chem. 236 (2016) 682–700. https://doi.org/10.1016/j.snb.2016.05.109.

[23] T.A. Blank, L.P. Eksperiandova, K.N. Belikov, Recent trends of ceramic humidity sensors development: A review, Sensors Actuators B Chem. 228 (2016) 416–442. https://doi.org/10.1016/J.SNB.2016.01.015.

[24] E. McCafferty, V. Pravdic, A.C. Zettlemoyer, Dielectric behaviour of adsorbed water films on the α-Fe_2O_3 surface, Trans. Faraday Soc. 66 (1970) 1720–1731. https://doi.org/10.1039/TF9706601720.

[25] M. Pandey, K. Sharma, S. Islam, Wide Range RH Detection with Digital Readout: Niche Superiority in Terms of Its Exceptional Performance and Inexpensive Technology, Adv. Mater. Phys. Chem. 09 (2019) 11–24. https://doi.org/10.4236/ampc.2019.92002.

[26] N. Agmon, The Grotthuss mechanism, Chem. Phys. Lett. 244 (1995) 456–462. https://doi.org/10.1016/0009-2614(95)00905-J.

[27] X. Chen, L. Rieth, M.S. Miller, F. Solzbacher, High temperature humidity sensors based on sputtered Y-doped $BaZrO_3$ thin films, Sensors Actuators B Chem. 137 (2009) 578–585. https://doi.org/10.1016/j.snb.2009.01.024.

[28] K.-S. Chou, T.-K. Lee, F.-J. Liu, Sensing mechanism of a porous ceramic as

humidity sensor, Sensors Actuators B Chem. 56 (1999) 106–111. https://doi.org/10.1016/S0925-4005(99)00187-2.

[29] J.K. Kwan, J.C. Sit, High sensitivity Love-wave humidity sensors using glancing angle deposited thin films, Sensors Actuators B Chem. 173 (2012) 164–168. https://doi.org/10.1016/j.snb.2012.06.069.

[30] A. Lorenz, M. Linse, H. Frintrup, M. Jeitler, A. Mette, M. Lehner, R. Greutmann, H. Brocker, M. Konig, D. Erath, F. Clement, Screen Printed Thick Film Metallization of Silicon Solar Cells - Recent Developments and Future Perspectives, Conference: 35th EUPVSEC, 2018. https://doi.org/10.4229/35thEUPVSEC20182018-2DV.3.65.

[31] Y. Zhu, H. Yuan, J. Xu, P. Xu, Q. Pan, Highly stable and sensitive humidity sensors based on quartz crystal microbalance coated with hexagonal lamelliform monodisperse mesoporous silica SBA-15 thin film, Sensors Actuators B Chem. 144 (2010) 164–169. https://doi.org/10.1016/j.snb.2009.10.053.

[32] P.M. Faia, C.S. Furtado, A.J. Ferreira, Humidity sensing properties of a thick-film titania prepared by a slow spinning process, Sensors Actuators, B Chem. 101 (2004) 183–190. https://doi.org/10.1016/j.snb.2004.02.050.

[33] K. Sen Chou, T.K. Lee, F.J. Liu, Sensing mechanism of a porous ceramic as humidity sensor, Sensors Actuators, B Chem. (1999). https://doi.org/10.1016/S0925-4005(99)00187-2.

[34] P.M. Faia, J. Libardi, Response to humidity of TiO_2:WO_3 sensors doped with V_2O_5: Influence of fabrication route, Sensors Actuators, B Chem. 236 (2016) 682–700. https://doi.org/10.1016/j.snb.2016.05.109.

[35] R.K. Nahar, V.K. Khanna, Ionic doping and inversion of the characteristic of thin film porous Al_2O_3 humidity sensor, Sensors Actuators B Chem. 46 (1998) 35–41. https://doi.org/10.1016/S0925-4005(97)00323-7.

[36] G. Banerjee, K. Sengupta, Pore size optimisation of humidity sensor—a probabilistic approach, Sensors Actuators B Chem. 86 (2002) 34–41. https://doi.org/10.1016/S0925-4005(02)00142-9.

[37] A. Uhlir Jr., Electrolytic Shaping of Germanium and Silicon, Bell Syst. Tech. J. 35 (1956) 333–347. https://doi.org/10.1002/j.1538-7305.1956.tb02385.x.

[38] D.R. Turner, Electropolishing Silicon in Hydrofluoric Acid Solutions, J. Electrochem. Soc. 105 (1958) 402. https://doi.org/10.1149/1.2428873.

[39] G. Bomchil, R. Herino, K. Barla, J.C. Pfister, Pore Size Distribution in Porous Silicon Studied by Adsorption Isotherms, J. Electrochem. Soc. 130 (1983) 1611–1614. https://doi.org/10.1149/1.2120044.

[40] C. Pickering, M.I.J. Beale, D.J. Robbins, P.J. Pearson, R. Greef, Optical studies of the structure of porous silicon films formed in p-type degenerate and non-degenerate silicon, J. Phys. C Solid State Phys. 17 (1984) 6535–6552. https://doi.org/10.1088/0022-3719/17/35/020.

[41] V. Lehmann, H. Föll, Formation Mechanism and Properties of Electrochemically Etched Trenches in n-Type Silicon, J. Electrochem. Soc. 137 (1990) 653–659. https://doi.org/10.1149/1.2086525.

[42] M.I.J. Beale, J.D. Benjamin, M.J. Uren, N.G. Chew, A.G. Cullis, An experimental and theoretical study of the formation and microstructure of porous silicon, J. Cryst. Growth. 73 (1985) 622–636. https://doi.org/10.1016/0022-0248(85)90029-6.

[43] L.T. Canham, Silicon quantum wire array fabrication by electrochemical and chemical dissolution of wafers, Appl. Phys. Lett. 57 (1990) 1046–1048. https://doi.org/10.1063/1.103561.

[44] L.T. Canham, Bioactive silicon structure fabrication through nanoetching techniques, Adv. Mater. 7 (1995) 1033–1037. https://doi.org/10.1002/adma.19950071215.

[45] L.T. Canham, T.I. Cox, A. Loni, A.J. Simons, Progress towards silicon optoelectronics using porous silicon technology, Appl. Surf. Sci. 102 (1996) 436–441. https://doi.org/10.1016/0169-4332(96)00094-3.

[46] R.L. Smith, S.D. Collins, Porous silicon formation mechanisms, J. Appl. Phys. 71 (1992) R1–R22. https://doi.org/10.1063/1.350839.

[47] V. Lehmann, The Physics of Macropore Formation in Low Doped n-Type Silicon, J. Electrochem. Soc. 140 (1993) 2836–2843. https://doi.org/10.1149/1.2220919.

[48] V. Lehmann, Developments in porous silicon research, Mater. Lett. 28 (1996) 245–249. https://doi.org/10.1016/0167-577X(96)00102-4.

[49] M.K. Lee, C.H. Chu, Y.C. Tseng, Mechanism of porous silicon formation, Mater. Chem. Phys. 53 (1998) 231–234. https://doi.org/10.1016/S0254-0584(97)02069-5.

[50] D. Kovalev, V.Y. Timoshenko, N. Künzner, E. Gross, F. Koch, Strong Explosive Interaction of Hydrogenated Porous Silicon with Oxygen at Cryogenic Temperatures, Phys. Rev. Lett. 87 (2001) 68301. https://doi.org/10.1103/PhysRevLett.87.068301.

[51] V. Kochergin, H. Foell, Novel optical elements made from porous Si, Mater. Sci. Eng. R Reports. 52 (2006) 93–140. https://doi.org/10.1016/j.mser.2006.05.002.

[52] S. Ozdemir, J.L. Gole, The potential of porous silicon gas sensors, Curr. Opin. Solid State Mater. Sci. 11 (2007) 92–100. https://doi.org/10.1016/j.cossms.2008.06.003.

[53] H. Föll, M. Christophersen, J. Carstensen, G. Hasse, Formation and application of porous silicon, Mater. Sci. Eng. R Reports. 39 (2002) 93–141. https://doi.org/10.1016/S0927-796X(02)00090-6.

[54] M.K. Sahoo, P. Kale, Restructured porous silicon for solar photovoltaic: A review, Microporous Mesoporous Mater. 289 (2019) 109619. https://doi.org/10.1016/j.micromeso.2019.109619.

[55] R. Vercauteren, G. Scheen, J.-P. Raskin, L.A. Francis, Porous silicon membranes and their applications: Recent advances, Sensors Actuators A Phys. 318 (2021) 112486. https://doi.org/10.1016/j.sna.2020.112486.

[56] N. Khinevich, H. Bandarenka, S. Zavatski, K. Girel, A. Tamulevičienė, T.

Tamulevičius, S. Tamulevičius, Porous silicon - A versatile platform for mass-production of ultrasensitive SERS-active substrates, Microporous Mesoporous Mater. 323 (2021) 111204. https://doi.org/10.1016/j.micromeso.2021.111204.

[57] G. Marsh, Porous silicon a useful imperfection, Mater. Today. 5 (2002) 36–41. https://doi.org/10.1016/S1369-7021(02)05141-6.

[58] Y. Jung, Y. Huh, D. Kim, Recent advances in surface engineering of porous silicon nanomaterials for biomedical applications, Microporous Mesoporous Mater. 310 (2021) 110673. https://doi.org/10.1016/j.micromeso.2020.110673.

[59] R.C. Anderson, R.S. Muller, C.W. Tobias, Investigations of porous silicon for vapor sensing, Sensors Actuators A Phys. 23 (1990) 835–839. https://doi.org/10.1016/0924-4247(90)87042-H.

[60] T. Hübert, Humidity-Sensing Materials, MRS Bull. 24 (1999) 49–54. https://doi.org/10.1557/S0883769400052519.

[61] P. Fürjes, A. Kovács, C. Dücso, M. Ádám, B. Müller, U. Mescheder, Porous silicon-based humidity sensor with interdigital electrodes and internal heaters, Sensors Actuators B Chem. 95 (2003) 140–144. https://doi.org/10.1016/S0925-4005(03)00423-4.

[62] G. Di Francia, A. Castaldo, E. Massera, I. Nasti, L. Quercia, I. Rea, A very sensitive porous silicon based humidity sensor, Sensors Actuators B Chem. 111–112 (2005) 135–139. https://doi.org/10.1016/j.snb.2005.06.048.

[63] M. Björkqvist, J. Salonen, J. Paski, E. Laine, Characterization of thermally carbonized porous silicon humidity sensor, Sensors Actuators A Phys. 112 (2004) 244–247. https://doi.org/10.1016/j.sna.2004.01.002.

[64] T. Islam, H. Saha, Study of long-term drift of a porous silicon humidity sensor and its compensation using ANN technique, Sensors Actuators A Phys. 133 (2007) 472–479. https://doi.org/10.1016/j.sna.2006.03.019.

[65] E.J. Connolly, G.M. O'Halloran, H.T.M. Pham, P.M. Sarro, P.J. French, Comparison of porous silicon, porous polysilicon and porous silicon carbide as materials for humidity sensing applications, Sensors Actuators A Phys. 99 (2002) 25–30. https://doi.org/10.1016/S0924-4247(01)00885-8.

[66] J. Das, S.M. Hossain, S. Chakraborty, H. Saha, Role of parasitics in humidity sensing by porous silicon, Sensors Actuators A Phys. 94 (2001) 44–52. https://doi.org/10.1016/S0924-4247(01)00684-7.

[67] T. Islam, K. Mistry, K. Sengupta, H. Saha, Measurement of gas moisture in the PPM range using porous silicon and porous alumina sensors, Sensors Mater. 16 (2004) 345–356. ISSN 0914 4935.

[68] G. Rong, S. Pan, C. Wu, X. Li, M. Yang, Porous silicon-based optical fiber Fabry-Perot sensor for relative humidity determination, in: Proc.SPIE, 2011. https://doi.org/10.1117/12.884851.

[69] T. Jalkanen, E. Mäkilä, A. Määttänen, J. Tuura, M. Kaasalainen, V.-P. Lehto, P. Ihalainen, J. Peltonen, J. Salonen, Porous silicon micro- and nanoparticles for printed humidity sensors, Appl. Phys. Lett. 101 (2012) 263110. https://doi.org/10.1063/1.4773361.

[70] T. Jalkanen, A. Määttänen, E. Mäkilä, J. Tuura, M. Kaasalainen, V.-P. Lehto, P. Ihalainen, J. Peltonen, J. Salonen, Fabrication of Porous Silicon Based Humidity Sensing Elements on Paper, J. Sensors. 2015 (2015) 927396. https://doi.org/10.1155/2015/927396.

[71] G. Korotcenkov, E. Rusu, How to Improve the Performance of Porous Silicon-Based Gas and Vapor Sensors? Approaches and Achievements, Phys. Status Solidi. 216 (2019) 1900348. https://doi.org/10.1002/pssa.201900348.

[72] S. Ozdemir, J.L. Gole, The potential of porous silicon gas sensors, Curr. Opin. Solid State Mater. Sci. 11 (2007) 92–100. https://doi.org/10.1016/j.cossms.2008.06.003.

[73] E. Comini, G. Faglia, G. Sberveglieri, CO and NO_2 response of tin oxide silicon doped thin films, Sensors Actuators, B Chem. 76 (2001) 270–274. https://doi.org/10.1016/S0925-4005(01)00581-0.

[74] R.W. Olesinski, G.J. Abbaschian, The Si-Sn (Silicon-Tin) system, Bull. Alloy Phase Diagrams. 5 (1984) 273–276. https://doi.org/10.1007/BF02868552.

[75] M. Kurosawa, M. Kato, T. Yamaha, N. Taoka, O. Nakatsuka, S. Zaima, Low temperature growth of SiSn polycrystals with high Sn contents on insulating layers, in: 2014 7th Int. Silicon-Germanium Technol. Device Meet. ISTDM 2014, 2014: pp. 83–84. https://doi.org/10.1109/ISTDM.2014.6874680.

[76] M. Jeon, C. Jeong, K. Kamisako, Tin induced crystallisation of hydrogenated amorphous silicon thin films, Mater. Sci. Technol. 26 (2010) 875–878. https://doi.org/10.1179/026708309X12454008169500.

[77] A. Tonkikh, A. Klavsyuk, N. Zakharov, A. Saletsky, P. Werner, SnSi nanocrystals of zinc-blende structure in a Si matrix, Nano Res. 8 (2015) 3905–3911. https://doi.org/10.1007/s12274-015-0890-z.

[78] S.Y. Shiryaev, J. Lundsgaard Hansen, P. Kringhoj, A. Nylandsted Larsen, Pseudomorphic $Si_{1-x}Sn_x$ alloy films grown by molecular beam epitaxy on Si, Appl. Phys. Lett. 67 (1995) 2287. https://doi.org/10.1063/1.115128.

[79] V. Neimash, V. Poroshin, P. Shepeliavyi, V. Yukhymchuk, V. Melnyk, A. Kuzmich, V. Makara, A.O. Goushcha, Tin induced a-Si crystallization in thin films of Si-Sn alloys, J. Appl. Phys. 114 (2013). https://doi.org/10.1063/1.4837661.

[80] S. Huang, Y. Chen, H. Xiao, F. Lu, Characterization of Sn and Si nanocrystals embedded in SiO_2 matrix fabricated by magnetron co-sputtering, Surf. Coatings Technol. 205 (2010) 2247–2250. https://doi.org/10.1016/j.surfcoat.2010.08.142.

[81] A.H. Mahan, D.L. Williamson, A. Madan, Properties of amorphous silicon tin alloys produced using the radio frequency glow discharge technique, Appl. Phys. Lett. 44 (1984) 220–222. https://doi.org/10.1063/1.94716.

[82] G.N. Parsons, J.W. Cook, G. Lucovsky, S.Y. Lir, M.J. Mantini, Deposition of a-Si, Sn: H alloy films by reactive magnetron sputtering from separate Si and Sn targets, J. Vac. Sci. Technol. A Vacuum, Surfaces Film. 4 (1986) 470–474. https://doi.org/10.1116/1.573910.

[83] L.Y. Beaulieu, K.C. Hewitt, R.L. Turner, A. Bonakdarpour, A.A. Abdo, L.

Christensen, K.W. Eberman, L.J. Krause, J.R. Dahn, The electrochemical reaction of Li with amorphous Si-Sn alloys, J. Electrochem. Soc. 150 (2003). https://doi.org/10.1149/1.1530151.

[84] D.L. Williamson, S.K. Deb, Mössbauer spectroscopy of amorphous silicon-tin-hydrogen alloys, J. Appl. Phys. 54 (1983) 2588–2592. https://doi.org/10.1063/1.332329.

[85] M. Vergnat, M. Piecuch, G. Marchal, M. Gerl, Structure and short-range order of vapour-deposited $Si_{1-x}Sn_x$ amorphous alloys, Philos. Mag. B. 51 (1985) 327–336. https://doi.org/10.1080/13642818508240578.

[86] J. Wu, Z. Zhu, H. Zhang, H. Fu, H. Li, A. Wang, H. Zhang, A novel Si/Sn composite with entangled ribbon structure as anode materials for lithium ion battery, Sci. Rep. 6 (2016). https://doi.org/10.1038/srep29356.

[87] D. Yang, J. Shi, J. Shi, H. Yang, Simple synthesis of Si/Sn@C-G anodes with enhanced electrochemical properties for Li-ion batteries, Electrochim. Acta. 259 (2018) 1081–1088. https://doi.org/10.1016/j.electacta.2017.10.117.

[88] T. Maruyama, H. Akagi, Thin Films of Amorphous Silicon-Tin Alloy Prepared by Radio-Frequency Magnetron Sputtering, J. Electrochem. Soc. . 144 (1997) 4350–4353. https://doi.org/10.1149/1.1838191.

[89] E. Evshchik, D. Novikov, A. Levchenko, S. Nefedkin, A.V. Shikhovtseva, O.V. Bushkova, Y.A. Dobrovolsky, Magnetron sputtering silicon thin film electrodes for lithium-ion batteries, Int. J. Electrochem. Sci. 13 (2018) 2860–2874. https://doi.org/10.20964/2018.03.05.

[90] C. Vérié, J.F. Rochette, J.P. Rebouillat, New Amorphous Alloy semiconductors : a-$Si_{1-x}Sn_x$, J. Phys. Colloques 42 (1981) C4-667 - C4-669. http://doi.org/10.1051/jphyscol:19814147.

[91] D.L. Williamson, R.C. Kerns, S.K. Deb, Properties of amorphous hydrogenated silicon-tin alloys prepared by radio frequency sputtering, J. Appl. Phys. 55 (1984) 2816–2824. https://doi.org/10.1063/1.333320.

[92] K.M. Jones, D.L. Williamson, B.G. Yacobi, Microstructural observations of sputtered silicon-tin-hydrogen alloys, J. Appl. Phys. 56 (1984) 1220–1223. https://doi.org/10.1063/1.334053.

[93] M. Vergnat, G. Marchal, M. Piecuch, M. Gerl, Structure and d.c. conductivity of amorphous $Si_{1-x}Sn_x$ alloys, Solid State Commun. 50 (1984) 237–242. https://doi.org/10.1016/0038-1098(84)90803-2.

[94] A. Mohamedi, M.L. Thèye, M. Vergnat, G. Marchal, M. Piecuch, Optical studies of bonding in coevaporated amorphous silicon-tin alloys, Phys. Rev. B. 39 (1989) 3711–3719. https://doi.org/10.1103/PhysRevB.39.3711.

[95] A.H. Mahan, D.L. Williamson, A. Madan, Properties of amorphous silicon tin alloys produced using the radio frequency glow discharge technique, Appl. Phys. Lett. 44 (1984) 220–222. https://doi.org/10.1063/1.94716.

[96] C. Guang-hua, Z. Fang-qing, Z. Nan-ping, H. De-yan, Study on the structural properties of a-$Si_{1-x}Sn_x$: H films prepared by rf sputtering, Sol. Energy Mater. 12 (1985) 471–478. https://doi.org/10.1016/0165-1633(85)90040-1.

[97] D. Girginoudi, N. Georgoulas, A. Thanailakis, Optical and electronic properties of sputtered hydrogenated amorphous silicon-tin alloys, J. Appl. Phys. 66 (1989) 354–357. https://doi.org/10.1063/1.343881.

[98] H.-J. Ahn, Y.-S. Kim, K.-W. Park, T.-Y. Seong, Use of Sn-Si nanocomposite electrodes for Li rechargeable batteries, Chem. Commun. (2005) 43–45. https://doi.org/10.1039/b407264b.

[99] M.A. Mohiddon, M.G. Krishna, Growth and optical properties of Sn–Si nanocomposite thin films, J. Mater. Sci. 47 (2012) 6972–6978. https://doi.org/10.1007/s10853-012-6647-0.

[100] M. Au, Y. He, Y. Zhao, H. Ghassemi, R.S. Yassar, B. Garcia-Diaz, T. Adams, Silicon and silicon–copper composite nanorods for anodes of Li-ion rechargeable batteries, J. Power Sources. 196 (2011) 9640–9647. https://doi.org/10.1016/j.jpowsour.2011.07.022.

[101] I.J. Biosci, A.A. Hashim, I.J. Biosci, Biopolymer- Ceramics Nanocomposites for Humidity Sensors : A Review University of Babylon , College of Education for Pure Sciences , Department of Physics , Iraq, 6655 (2019) 276–281.

[102] R.A. Shaukat, M.U. Khan, Q.M. Saqib, M.Y. Chougale, J. Kim, J. Bae, All range highly linear and sensitive humidity sensor based on 2D material $TiSi_2$ for real-time monitoring, Sensors Actuators B Chem. 345 (2021) 130371. https://doi.org/10.1016/j.snb.2021.130371.

[103] J. Bai, B. Zhou, Titanium dioxide nanomaterials for sensor applications, Chem. Rev. 114 (2014) 10131–10176. https://doi.org/10.1021/cr400625j.

[104] A. Farzaneh, A. Mohammadzadeh, M.D. Esrafili, O. Mermer, Experimental and theoretical study of TiO_2 based nanostructured semiconducting humidity sensor, Ceram. Int. 45 (2019) 8362–8369. https://doi.org/10.1016/j.ceramint.2019.01.144.

[105] N. Horzum, D. Taşçıoglu, S. Okur, M.M. Demir, Humidity sensing properties of ZnO-based fibers by electrospinning, Talanta. 85 (2011) 1105–1111. https://doi.org/10.1016/j.talanta.2011.05.031.

[106] Q. Qi, T. Zhang, Q. Yu, R. Wang, Z. Yi, li Liu, H. Yang, Properties of humidity sensing ZnO nanorods-base sensor fabricated by screen-printing, Sensors Actuators B Chem. 133 (2008) 638–643. https://doi.org/10.1016/j.snb.2008.03.035.

[107] A. Erol, S. Okur, B. Comba, O. Mermer, M. Arikan, Humidity sensing properties of ZnO nanoparticles synthesized by sol–gel process, Sensors Actuators B-Chem. 145 (2010) 174–180. https://doi.org/10.1016/j.snb.2009.11.051.

[108] B. Yadav, R. Srivastava, C.D. Dwivedi, P. Pramanik, Moisture sensor based on ZnO nanomaterial synthesized through oxalate route, Sensors Actuators B Chem. 131 (2007) 216–222. https://doi.org/10.1016/j.snb.2007.11.013.

[109] D.M. Mattox, Introduction, in: D.M.B.T.-H. of P.V.D. (PVD) P. (Second E. Mattox (Ed.), Handb. Phys. Vap. Depos. Process., Elsevier, Boston, 2010: pp. 1–24. https://doi.org/10.1016/B978-0-8155-2037-5.00001-0.

[110] P.J. Kelly, R.D. Arnell, Magnetron sputtering: a review of recent developments

and applications, Vacuum. 56 (2000) 159–172. https://doi.org/10.1016/S0042-207X(99)00189-X.

[111] G. Bräuer, Magnetron Sputtering, in: S. Hashmi, G.F. Batalha, C.J. Van Tyne, B.B.T.-C.M.P. Yilbas (Eds.), Compr. Mater. Process., Elsevier, Oxford, 2014: pp. 57–73. https://doi.org/10.1016/B978-0-08-096532-1.00403-9.

[112] J.T. Gudmundsson, D. Lundin, 1 - Introduction to magnetron sputtering, in: D. Lundin, T. Minea, J.T.B.T.-H.P.I.M.S. Gudmundsson (Eds.), Elsevier, 2020: pp. 1–48. https://doi.org/10.1016/B978-0-12-812454-3.00006-1.

[113] D.K. Maurya, A. Sardarinejad, K. Alameh, Recent Developments in R.F. Magnetron Sputtered Thin Films for pH Sensing Applications—An Overview, Coatings . 4 (2014). https://doi.org/10.3390/coatings4040756.

[114] J.S. Benjamin, Mechanical Alloying, Sci. Am. 234 (1976) 40–49. http://www.jstor.org/stable/24950349.

[115] C. Suryanarayana, Mechanical alloying and milling, 46 (2001).

[116] C. Suryanarayana, Chapter 4 Mechanical Alloying, (1998).

[117] M. Toozandehjani, K.A. Matori, F. Ostovan, S.A. Aziz, Effect of milling time on the microstructure, Physical and Mechanical Properties of Al-Al_2O_3 nanocomposite synthesized by Ball milling and Powder metallurgy, Materials 10(11) (2017) 1232. https://doi.org/10.3390/ma10111232.

[118] C. Suryanarayana, Mechanical Alloying: A Novel Technique to Synthesize Advanced Materials, Research. (2019) 4219812. https://doi.org/10.34133/2019/4219812.

[119] M.J. Burek, A. Suriadi, Z. Jahed, N. Tamura, M. Kunz, S. Jin, S. Min, J. Han, G. Lee, C. Zamecnik, T.Y. Tsui, Fabrication , microstructure , and mechanical properties of tin nanostructures, Mater. Sci. Eng. A. 528 (2011) 5822–5832. https://doi.org/10.1016/j.msea.2011.04.019.

[120] I.N. Company, N. Al, Mechanical Alloying, (1989) 1–5.

[121] B.D. Cullity, Elements of X-Ray Diffraction, Am. J. Phys. 25 (1957) 394–395. https://doi.org/10.1119/1.1934486.

[122] Principles of X-ray Diffraction, Thin Film Anal. by X-Ray Scatt. (2005) 1–40. https://doi.org/10.1002/3527607595.ch1.

[123] M. Kaliva, M. Vamvakaki, Chapter 17 - Nanomaterials characterization, in: R.B.T.-P.S. and N. Narain (Ed.), Elsevier, 2020: pp. 401–433. https://doi.org/10.1016/B978-0-12-816806-6.00017-0.

[124] D.G. Lamas, M. de Oliveira Neto, G. Kellermann, A.F. Craievich, 5 - X-Ray Diffraction and Scattering by Nanomaterials, in: A.L. Da Róz, M. Ferreira, F. de Lima Leite, O.N.B.T.-N.T. Oliveira (Eds.), Micro Nano Technol., William Andrew Publishing, 2017: pp. 111–182. https://doi.org/10.1016/B978-0-323-49778-7.00005-9.

[125] T. Ashokkumar, A. Rajadurai, Gouthama, Mechanism of Reduction in Grain and Particle Sizes of Ni_xFe_{100-x} Nanopowder by Mechanical Alloying, Mater. Manuf. Process. 28 (2013) 670–675. https://doi.org/10.1080/10426914.2012.727121.

[126] R.P. Parida, B. Parida, R.K. Bhuyan, S.K. Parida, Structural, mechanical and electric properties of La doped BNT-BFO perovskite ceramics, Ferroelectrics. 571 (2021) 162–174. https://doi.org/10.1080/00150193.2020.1853751.

[127] M. Rabiei, A. Palevicius, A. Monshi, S. Nasiri, A. Vilkauskas, G. Janusas, Comparing Methods for Calculating Nano Crystal Size of Natural Hydroxyapatite Using X-Ray Diffraction, Nanomater. 10(9) (2020) 1627. https://doi.org/10.3390/nano10091627.

[128] S. Kumar, P. Sharma, V. Sharma, CdS nanopowder and nanofilm: Simultaneous synthesis and structural analysis, Electron. Mater. Lett. 9 (2013) 371–374. https://doi.org/10.1007/s13391-013-2151-1.

[129] M. Doumeng, L. Makhlouf, F. Berthet, O. Marsan, K. Delbé, J. Denape, F. Chabert, A comparative study of the crystallinity of polyetheretherketone by using density, DSC, XRD, and Raman spectroscopy techniques, Polym. Test. 93 (2021) 106878. https://doi.org/10.1016/j.polymertesting.2020.106878.

[130] R.B. Peter J. Goodhew, John Humphreys, Electron Microscopy and Analysis, 2000.

[131] M. Ezzahmouly, A. Elmoutaouakkil, M. Ed-Dhahraouy, H. Khallok, A. Elouahli, A. Mazurier, A. ElAlbani, Z. Hatim, Micro-computed tomographic and SEM study of porous bioceramics using an adaptive method based on the mathematical morphological operations, Heliyon. 5 (2019). https://doi.org/10.1016/j.heliyon.2019.e02557.

[132] J.I. Goldstein, D.E. Newbury, J.R. Michael, N.W.M. Ritchie, J.H.J. Scott, D.C. Joy, Scanning Electron Microscopy and X-Ray Microanalysis, Springer, 2003.

[133] B.J. Inkson, 2 - Scanning electron microscopy (SEM) and transmission electron microscopy (TEM) for materials characterization, in: G. Hübschen, I. Altpeter, R. Tschuncky, H.-G.B.T.-M.C.U.N.E. (NDE) M. Herrmann (Eds.), Woodhead Publishing, 2016: pp. 17–43. https://doi.org/10.1016/B978-0-08-100040-3.00002-X.

[134] C.B. Carter, D.B. Williams, Transmission Electron Microscopy Diffraction, Imaging and spectroscopy, Springer, 2016.

[135] D.P.E. Dickson, F.J. Berry, Principles of Mössbauer spectroscopy, in: D.P.E. Dickson, F.J. Berry (Eds.), Mössbauer Spectrosc., Cambridge University Press, Cambridge, 1986: pp. 1–16. https://doi.org/DOI: 10.1017/CBO9780511524233.002.

[136] E. Murad, Chapter 2.1 - Mössbauer Spectroscopy, in: F. Bergaya, G.B.T.-D. in C.S. Lagaly (Eds.), Handb. Clay Sci., Elsevier, 2013: pp. 11–24. https://doi.org/10.1016/B978-0-08-098259-5.00003-2.

[137] R.J. Hemley, V. V Struzhkin, R.E. Cohen, G. Shen, 2.13 - Measuring High-Pressure Electronic and Magnetic Properties, in: G.B.T.-T. on G. (Second E. Schubert (Ed.), Elsevier, Oxford, 2015: pp. 313–349. https://doi.org/10.1016/B978-0-444-53802-4.00038-5.

[138] P. Eaton, P. West, Atomic Force Microscopy, At. Force Microsc. 9780199570 (2010) 1–256. https://doi.org/10.1093/acprof:oso/9780199570454.001.0001.

[139] M. Raimondo, C. Naddeo, L. Vertuccio, K. Lafdi, A. Sorrentino, L. Guadagno, Carbon-Based Aeronautical Epoxy Nanocomposites: Effectiveness of Atomic Force Microscopy (AFM) in Investigating the Dispersion of Different Carbonaceous Nanoparticles, Polym. 11 (2019). https://doi.org/10.3390/polym11050832.

[140] V. Sudarsan, Chapter 4 - Materials for Hostile Chemical Environments, in: A.K. Tyagi, S.B.T.-M.U.E.C. Banerjee (Eds.), Elsevier, Amsterdam, 2017: pp. 129–158. https://doi.org/10.1016/B978-0-12-801300-7.00004-8.

[141] Atomic Force Microscopy Peter Eaton and Paul West, MRS Bull. 39 (2014) 379. https://doi.org/10.1557/mrs.2014.72.

[142] S.D. Connell, G.R. Heath, J.A. Goodchild, Quantitative Analysis of Structure and Dynamics in AFM Images of Lipid Membranes BT - Atomic Force Microscopy: Methods and Protocols, in: N.C. Santos, F.A. Carvalho (Eds.), Springer New York, New York, NY, 2019: pp. 29–44. https://doi.org/10.1007/978-1-4939-8894-5_2.

[143] R.L. Sakaguchi, J.M.B.T.-C.R.D.M. (Thirteenth E. Powers, eds., Chapter 4 - Fundamentals of Materials Science, in: Mosby, Saint Louis, 2012: pp. 33–81. https://doi.org/10.1016/B978-0-323-08108-5.10004-0.

[144] W.C. Oliver, G.M. Pharr, An improved technique for determining hardness and elastic modulus using load and displacement sensing indentation experiments, J. Mater. Res. 7 (1992) 1564–1583. https://doi.org/10.1557/JMR.1992.1564.

[145] E.W. Washburn, Note on a Method of Determining the Distribution of Pore Sizes in a Porous Material, Proc. Natl. Acad. Sci. 7 (1921) 115 LP – 116. https://doi.org/10.1073/pnas.7.4.115.

[146] H.M. Rootare, A Review of Mercury Porosimetry BT - Advanced Experimental Techniques in Powder Metallurgy: Based on a Symposium on Advanced Experimental Techniques in Powder Metallurgy sponsored by the Institute of Metals Division, Powder Metallurgy Committee, held at , in: J.S. Hirschhorn, K.H. Roll (Eds.), Springer US, Boston, MA, 1970: pp. 225–252. https://doi.org/10.1007/978-1-4615-8981-5_9.

[147] C.A. León y León, New perspectives in mercury porosimetry, Adv. Colloid Interface Sci. 76 (1998) 341–372. https://doi.org/10.1016/s0001-8686(98)00052-9.

[148] K.K. Aligizaki, Pore Structure of Cement-Based Materials: Testing, Interpretation and Requirements (1st ed.) Chapter 3 Mercury intrusion porosimetry, 2004. https://doi.org/10.1201/9781482271959-14.

[149] S. Hong, K. de Bruyn, E. Bescher, C. Ramseyer, T.H.-K. Kang, Porosimetric features of calcium sulfoaluminate and Portland cement pastes: testing protocols and data analysis, J. Struct. Integr. Maint. 3 (2018) 52–66. https://doi.org/10.1080/24705314.2018.1426168.

[150] P. Nugent, 18 - Rotational Molding, in: M.B.T.-Applied Plastic Engineering Handbook (Ed.), Plast. Des. Libr., William Andrew Publishing, Oxford, 2011: pp. 311–332. https://doi.org/10.1016/B978-1-4377-3514-7.10018-2.

[151] S.U. Rawal, M.M. Patel, Chapter 2 - Lipid nanoparticulate systems: Modern versatile drug carriers, in: A.M.B.T.-L.N. for D.T. Grumezescu (Ed.), William Andrew Publishing, 2018: pp. 49–138. https://doi.org/10.1016/B978-0-12-813687-4.00002-5.

[152] V.S. Kulkarni, C. Shaw, Chapter 11 - Miscellaneous Physical, Chemical, and Microbiological Test Methods, in: V.S. Kulkarni, C.B.T.-E.C. for F. of S. and L.D. Shaw (Eds.), Academic Press, Boston, 2016: pp. 193–221. https://doi.org/10.1016/B978-0-12-801024-2.00011-X.

[153] E.B. J. Ross Macdonald, Impedance spectroscopy Theory , Experiment , and Applications, 2005.

[154] J. Huang, Z. Li, B.Y. Liaw, J. Zhang, Graphical analysis of electrochemical impedance spectroscopy data in Bode and Nyquist representations, J. Power Sources. 309 (2016) 82–98. https://doi.org/10.1016/j.jpowsour.2016.01.073.

[155] W. Choi, H.-C. Shin, J.M. Kim, J.-Y. Choi, W.-S. Yoon, Modeling and Applications of Electrochemical Impedance Spectroscopy (EIS) for Lithium-ion Batteries, J. Electrochem. Sci. Technol. 11 (2020) 1–13. https://doi.org/10.33961/jecst.2019.00528.

[156] J. Aguedo, L. Lorencova, M. Barath, P. Farkas, J. Tkac, Electrochemical Impedance Spectroscopy on 2D Nanomaterial MXene Modified Interfaces: Application as a Characterization and Transducing Tool, Chemosens. 8 (2020). https://doi.org/10.3390/chemosensors8040127.

[157] B.S. Tosun, R.K. Feist, A. Gunawan, K.A. Mkhoyan, S.A. Campbell, E.S. Aydil, Sputter deposition of semicrystalline tin dioxide films, Thin Solid Films. 520 (2012) 2554–2561. https://doi.org/10.1016/j.tsf.2011.10.169.

[158] M. Al-Mansoori, S. Al-Shaibani, A. Al-Jaeedi, J. Lee, D. Choi, F.S. Hasoon, Effects of gas flow rate on the structure and elemental composition of tin oxide thin films deposited by RF sputtering, AIP Adv. 7 (2017) 125105. https://doi.org/10.1063/1.5001883.

[159] P.M. Faia, J. Libardi, Response to humidity of TiO_2:WO_3 sensors doped with V2O5: Influence of fabrication route, Sensors Actuators B Chem. 236 (2016) 682–700. https://doi.org/10.1016/j.snb.2016.05.109.

[160] R. Pasricha, D. Sachdev, Biological characterization of nanofiber composites, 2017. https://doi.org/10.1016/B978-0-08-100173-8.00007-7.

[161] B. Hertzberg, J. Benson, G. Yushin, Ex-situ depth-sensing indentation measurements of electrochemically produced Si-Li alloy films, Electrochem. Commun. 13 (2011) 818–821. https://doi.org/10.1016/j.elecom.2011.05.011.

[162] J. Chen, S.J. Bull, S. Roy, A. Kapoor, H. Mukaibo, H. Nara, T. Momma, T. Osaka, Y. Shacham-Diamand, Nanoindentation and nanowear study of Sn and Ni-Sn coatings, Tribol. Int. 42 (2009) 779–791. https://doi.org/10.1016/j.triboint.2008.10.001.

[163] P. Kringho/j, R.G. Elliman, Diffusion of ion implanted Sn in Si, $Si_{1-x}Ge_x$, and Ge, Appl. Phys. Lett. 65 (1994) 324–326. https://doi.org/10.1063/1.112360.

[164] A. Nikiforov, V. Timofeev, V. Mashanov, I. Azarov, I. Loshkarev, V. Volodin,

D. Gulyaev, I. Chetyrin, I. Korolkov, Formation of SnO and SnO_2 phases during the annealing of $SnO_{(x)}$ films obtained by molecular beam epitaxy, Appl. Surf. Sci. 512 (2020) 145735. https://doi.org/10.1016/j.apsusc.2020.145735.

[165] P.T. Vianco, J.A. Rejent, Dynamic Recrystallization (DRX) as the Mechanism for Sn Whisker Development. Part I: A Model, J. Electron. Mater. 38 (2009) 1815–1825. https://doi.org/10.1007/s11664-009-0879-z.

[166] J. Smetana, Theory of Tin Whisker Growth: "The End Game," IEEE Trans. Electron. Packag. Manuf. 30 (2007) 11–22. https://doi.org/10.1109/TEPM.2006.890645.

[167] D. Bunyan, M.A. Ashworth, G.D. Wilcox, R.L. Higginson, R.J. Heath, C. Liu, Tin whisker growth from electroplated finishes – a review, Trans. IMF. 91 (2013) 249–259. https://doi.org/10.1179/0020296713Z.000000000119.

[168] A.T. Wu, Y.C. Ding, The suppression of tin whisker growth by the coating of tin oxide nano particles and surface treatment, Microelectron. Reliab. 49 (2009) 318–322 https://doi.org/10.1016/j.microrel.2008.11.002.

[169] S. Jakhar, S. Duhan, S. Nain, Facile hydrothermal synthesis of mesoporous WO_3 /KIT-6 nanocomposite depicting great humidity sensitive properties, Mater. Res. Innov. (2021) 1–11. https://doi.org/10.1080/14328917.2021.1940668.

[170] H. Kakiuchi, H. Ohmi, M. Harada, K. Yasutake, Formation of silicon dioxide layers at low temperatures (150-400°C) by atmospheric pressure plasma oxidation of silicon, Sci. Technol. Adv. Mater. 8 (2007) 137–141. https://doi.org/10.1016/j.stam.2006.12.006.

[171] T. Krishnakumar, R. Jayaprakash, V.N. Singh, B.R. Mehta, A.R. Phani, Synthesis and Characterization of Tin Oxide Nanoparticle for Humidity Sensor Applications, J. Nano Res. 4 (2009) 91–101. https://doi.org/10.4028/www.scientific.net/JNanoR.4.91.

[172] B.C. Yadav, R. Srivastava, C.D. Dwivedi, Synthesis and characterization of ZnO–TiO_2 nanocomposite and its application as a humidity sensor, Philos. Mag. 88 (2008) 1113–1124. https://doi.org/10.1080/14786430802064642.

[173] N. Kumar, P. Sanguino, S. Diliberto, P. Faia, B. Trindade, Tailoring thin mesoporous silicon-tin films by radio-frequency magnetron sputtering, Thin Solid Films. 704 (2020). https://doi.org/10.1016/j.tsf.2020.137989.

[174] F. Zhang, E. Burkel, Novel Titanium Manganese Alloys and Their Macroporous Foams for Biomedical Applications Prepared by Field Assisted Sintering, in: 2011. https://doi.org/10.5772/12874.

[175] N. Kumar, P. Sanguino, S. Diliberto, P. Faia, B. Trindade, Tailoring thin mesoporous silicon-tin films by radio-frequency magnetron sputtering, Thin Solid Films. 704 (2020). https://doi.org/10.1016/j.tsf.2020.137989.

[176] E. Crandall, Factors Governing Tin Whisker Growth, (2013). https://doi.org/10.1007/978-3-319-00470-9.

[177] L. Juhász, A. Vass-Varnai, V. Timár-Horváth, M.P.Y. Desmulliez, R. Dhariwal, Porous Alumina Based Capacitive MEMS RH Sensor, DTIP MEMS MOEMS. abs/0805.0 (2008).

[178] N. Kumar, M. Evaristo, B. Trindade, P. Faia, Humidity sensing properties of thin silicon-tin films prepared by magnetron sputtering, Sensors Actuators B Chem. 321 (2020). https://doi.org/10.1016/j.snb.2020.128554.